

TWISTED AND COILED POLYMER MUSCLES AND STRUCTURES
FOR ROBOTICS APPLICATION

by

Lianjun Wu



APPROVED BY SUPERVISORY COMMITTEE:

Yonas Tadesse, Chair

Dong Qian

Robert D. Gregg

Hongbing Lu

Ray H. Baughman

Copyright © 2017

Lianjun Wu

All Rights Reserved

*This dissertation
is dedicated to my wife and my parents,
who have always supported me.*

TWISTED AND COILED POLYMER MUSCLES AND STRUCTURES
FOR ROBOTICS APPLICATION

by

LIANJUN WU, BS, MS

DISSERTATION

Presented to the Faculty of
The University of Texas at Dallas
in Partial Fulfillment
of the Requirements
for the Degree of

DOCTOR OF PHILOSOPHY IN
MECHANICAL ENGINEERING

THE UNIVERSITY OF TEXAS AT DALLAS

December 2017

ACKNOWLEDGMENTS

I would like to offer my deep gratefulness and sincere appreciation to my advisor, Dr. Yonas Tadesse, for his consistent support and guidance throughout the course of my research study. I am very thankful to him for his encouragement and invaluable suggestions. I am also particularly thankful to Dr. Monica Jung de Andrade, and Dr. Carter Haines for their motivation, invaluable help and discussion. I would also like to thank my committee members: Dr. Ray Baughman, Dr. Hongbing Lu, Dr. Robert D. Gregg and Dr. Dong Qian for their comprehensive and insightful comments.

Special thanks to my wife Xuemin Wang and my son Ethan Wu, for their unconditioned love and support of my life.

Many friends have been exceptionally supportive and helpful, in particular the group members in Humanoid, Biorobotics and Smart System (HBS) Lab: Lokesh Saharan, Akshay Potnuru, Mohsen Jafarzadeh, Farzad Karami, Armita Hamidi and Yara Almubarak.

I would like to thank the Department of Mechanical Engineering at The University of Texas at Dallas and the Office of Naval Research (ONR) for the financial support under the grant number N00014-15-1-2503.

November 2017

TWISTED AND COILED POLYMER MUSCLES AND STRUCTURES
FOR ROBOTICS APPLICATION

Lianjun Wu, PhD
The University of Texas at Dallas, 2017

Supervising Professor: Dr. Yonas Tadesse

New actuator technologies play a significant role to develop a lightweight, cost-effective, high performance and biomimetic robotic system. In 2014, Haines et al. [Artificial muscles from fishing line and sewing thread. *science*, 343(6173), pp.868-872] demonstrated the transformation of polymer fibers from fishing line and sewing thread into artificial muscles by twisting & coiling and heat treatment process, which contract in response to thermal or electrothermal stimuli. The twisted and coiled polymer (TCP) muscles can generate giant stroke, demonstrate high energy and power densities, operate silently, and are of great interest for robotics application.

This work presents an extensive study of the TCP muscles using experimental methods to establish the relationship of the characteristics of the muscles in response to input parameters such as power, pre-stress, and stiffness. The experimental results in the time domain were evaluated using thermo-electric and thermo-mechanical models. A new artificial muscle mandrel-coiled fabrication apparatus was designed and developed to produce TCP muscles from fishing line and resistance wire. The new fabrication method enables twisting of the polymer fiber without adding twist into the resistance wire. Isotonic test and spring-load test characterization of TCP muscles were

conducted to investigate the performance of TCP muscles. In the two test methods, the effect of power input, frequency, external load, and pre-stress on the actuation stroke and the pulling force of the artificial muscle were investigated. It was shown that a quick contraction (within 1 s) can be achieved without sacrificing actuation stroke by using short pulse with high electrical power. The full characterization of TCP muscles provides a guideline for actuator development. In this work, three novel applications of TCP muscle were demonstrated for the first time. The first one is a reconfigurable robot with icosahedral tensegrity structure that was developed using TCP muscles from sewing thread. Rolling motion of the tensegrity robot under a contact pattern 2 (contact with a ground in a non-regular, isosceles triangle) was successfully demonstrated. The second one and important contribution is a compact and low-cost humanoid hand that was powered by nylon artificial muscles made from multifilament nylon 6 sewing thread. Two different designs were presented along with the essential elements consisting of actuators, springs, tendons and guide systems. The hand design utilized a bioinspired design approach by utilizing agonist and antagonist actuation system. A kinematic model for the flexor tendons was developed to simulate the flexion motion and compared with experimental results. Grasping of various objects was demonstrated within 1 s using the robotic hand showing an array of functions similar to a natural hand. The third one is a modular musculoskeletal system based on ball and socket joint for bio-inspired robotic system. For this purpose, 3D printed bone-like structure and TCP muscles were embedded within elastomeric skin to mimic natural joints. 3D printing and casting were primarily used for manufacturing the musculoskeletal system and the experimental results showed that the bio-inspired ball and socket joint could deliver a very good dynamic response, promoting TCP muscle application in musculoskeletal system and other biologically inspired robotic system.

TABLE OF CONTENTS

ACKNOWLEDGMENTS	v
ABSTRACT	vi
LIST OF FIGURES	xii
LIST OF TABLES	xxi
CHAPTER 1 INTRODUCTION AND BACKGROUND.....	1
1.1 Introduction.....	1
1.2 Shape Memory Alloy.....	2
1.3 Shape Memory Polymer	5
1.4 Pneumatic Artificial Muscle (PAM).....	6
1.5 Twist and Coiled Polymer (TCP) Muscles	7
1.6 Objectives and Dissertation Outline	10
1.6.1 Objectives.....	10
1.6.2 Dissertation Outline and Acknowledgments.....	11
CHAPTER 2 FABRICATION AND CHARACTERIZATION OF TCP MUSCLE	13
2.1 Introduction.....	13
2.2 Self-coiled TCP Muscle.....	13
2.3 Mandrel-coiled TCP Muscle.....	17
2.3.1 Twist Insertion.....	22
2.3.2 Incorporation of the Resistance Wire.....	23
2.3.3 Mandrel Coiling	24
2.3.4 Thermal Annealing.....	25

2.4	Experimental Methods of TCP Muscles' Characterization	26
2.4.1	Isotonic Test of TCP muscle	26
2.4.2	Spring-load Test of TCP muscle	28
2.5	Modeling of The Electrical Resistance of 1-ply TCP Muscle	29
2.5.1	Muscle Preparation (1-ply TCP muscle).....	31
2.5.2	Experimental Method.....	31
2.5.3	Experimental Results and Discussion (1-ply TCP muscle)	33
2.5.4	Thermomechanical Characterization of 1-ply TCP Muscle.....	37
2.5.5	Thermoelectric Characterization of 1-ply TCP Muscle	39
2.5.6	Summary on The Study of Electrical Resistance of 1-ply TCP Muscle	40
2.6	Summary	41
CHAPTER 3 A RECONFIGURABLE ROBOT WITH TENSEGRITY STRUCTURE USING NYLON ARTIFICIAL MUSCLE.....		43
3.1	Introduction.....	43
3.2	Design and Method.....	44
3.2.1	Materials.....	44
3.2.2	Strut Design.....	45
3.2.3	Prototype	46
3.2.4	Transition of Gravitational Potential Energy of The Tensegrity Robot.....	49
3.3	Experimental Method and Simulation	50
3.3.1	Experimental Method.....	50
3.3.2	Simulation	53
3.4	Results and Discussion	57

3.5	Summary	61
CHAPTER 4 COMPACT AND LOW COST ROBOTIC HAND POWERED BY TCP MUSCLE		62
4.1	Introduction.....	62
4.2	Design Approach	67
4.2.1	Human Hand Anatomy.....	67
4.2.2	Biologically Inspired Agonist-antagonist Arrangement	69
4.3	Modeling and Analysis	74
4.3.1	Finger Kinematics	74
4.3.2	Stress and Deformation Simulation.....	78
4.4	Muscle Characterization	81
4.4.1	Isotonic Test Characterization.....	81
4.4.2	Spring-load Test Characterization.....	84
4.5	Index Finger Characterization.....	87
4.6	TCP Hand Grasping Experimental	91
4.7	Robotic Finger Actuated by Mandrel-Coiling Fishing Line Muscle via Fluidic method	93
4.8	Summary	97
CHAPTER 5 MUSCULOSKELETAL SYSTEM FOR SOFT ROBOTICS		100
5.1	Introduction.....	100
5.2	Design	104
5.2.1	Anatomy of the Human Shoulder.....	104
5.2.2	Biologically Inspired Joint Design.....	105

5.2.3 Kinematics of the Musculoskeletal System	108
5.3 Manufacturing Method and Description	113
5.4 Experimental Methods	116
5.4.1 Joint Stiffness and Muscle Stiffness.....	116
5.4.2 Muscle Characterization.....	118
5.4.3 Characterization of Musculoskeletal System	124
5.5 Power Source Design.....	130
5.6 Summary	134
CHAPTER 6 CONCLUSION AND FUTURE WORK.....	136
6.1 Conclusion	136
6.2 Future Recommendations	143
REFERENCES	145
BIOGRAPHICAL SKETCH	160
CURRICULUM VITAE.....	161

LIST OF FIGURES

1.1.	3D stress-strain-temperature diagram of SMA phase transformation [6].....	3
1.2.	A representative 3-D plot for presenting thermomechanical cycles for an example of a shape memory polymer [27].	6
1.3.	Schematic diagram of the actuation principle of PAM in its resting (a) and actuated (b) configurations.....	7
2.1.	Two coiled artificial muscle structures: (a) A self-coiled artificial muscle from twist induced coiling; (b) A mandrel-coiled artificial muscle obtained by wrapping around a rod of a certain diameter.	13
2.2.	Schematic diagram of the fabrication process for TCP muscles: (a) The top end of the precursor fiber is attached to a motor and a deadweight is suspended at the bottom end to keep the precursor fiber straight and taut. (b) Twist is inserted in the fiber by rotating the motor in a counterclockwise direction. (c) Continuous, regular coils emerge throughout the thread length to form a 1-ply TCP muscle. (d) A 1-ply muscle is annealed by electro-thermal heating by applying power, P_A , across terminals. (e) After annealing, the muscle is trained by electro-thermal heating by applying power, P_T . (f) Plying two 1-ply muscles together in a clockwise direction to form a 2-ply muscle and obtain a structure as in (g). (h) The unloaded length without lifting weight and (i) The loaded configuration is shown. (j)After annealing and training, the 1-ply TCP muscle is tested by applying powering voltage, P_p , showing the contraction of (i), and (k) SEM image of 1-ply muscle.	15
2.3.	(a) Magnified view of circle in (c), (b) SEM image of a fabricated 1-ply muscle, (c) SEM image of a fabricated 2-ply muscle, and (d) SEM image of a fabricated 3-ply muscle.	17
2.4.	SEM image of the defected 1-ply TCP muscle from silver-plated sewing thread.....	19
2.5.	(a) The home-made experimental setup; (b) Forming the mandrel-coiling muscle from twisted fiber with heating wire wrapped around via the rotation of the stepper motor. (c) The magnified view of the muscle in (b); The resulting mandrel-coiling muscle after annealing.	23
2.6	Schematic diagram of the muscle fabrication. (a) Wrapping the resistance wire around the twisted fiber. (b) Forming the mandrel-coiling muscle from the twisted fiber with resistance wire as made in (a) by wrapping it around the rod. (c) The working principle of muscle; Left of (c) the muscle at rest when hanging a weight to the bottom; Right of (c) the muscle contracts upon receiving Joule heat.	25

2.7.	Schematic diagram of the experimental setup for characterization of the Fishing Line TCP muscle in isotonic test.....	27
2.8.	Schematic diagram of the experimental setup for determining the characterization of the muscle and in the detail an optical micrograph of a 3.33-mm-diameter coil formed by inserting twist in the 860- μ m-diameter monofilament fiber and wrapping the twisted, non-coil fiber around a 1.6 mm diameter steel rod.	28
2.9.	Schematic diagram of the experimental setup for characterization of the Fishing Line TCP muscle in spring-load test.....	29
2.10.	The relation among the state variables of TCP muscles	33
2.11.	The measured parameters of 1-ply TCP muscle from silver-plated sewing thread (a diameter of 0.8 mm and a length of 129 mm measured under a 0.26 N pre-stress) including current (a), voltage (b), temperature (c), force (d) and displacement (e).	35
2.12.	The resistance profile of 1-ply TCP muscle in the time domain.	36
2.13.	Geometrical model of a 1-ply TCP muscle. (a) stretched coils under a pre-tension, and current travels in a route as indicated by the red lines. (b) coils start contacting with each other at the temperature T_C and current travels in a direction as indicated by the red lines. (c) the swelling state of TCP muscle after the temperature reaches over T_C and the current passes through TCP muscle as shown in the red lines.....	37
2.14.	The comparison of displacement between simulated results and experimental data....	39
2.15.	The comparison of temperature between simulated results and experimental data.....	41
3.1.	The tensegrity prototype: (a) The icosahedron tensegrity robot constructed with 2-ply muscles and aluminum struts; (b) The 2-ply TCP muscle magnified view and (c) The tensegrity after being folded into a flat configuration by pushing the structure downwards to the ground.....	45
3.2.	The two prototypes of a 6-strut tensegrity structure. Left: The second prototype made of aluminum tube and TCP muscles. Middle: The first prototype fabricated using 3D printer using ABS material. Left Top: The detailed view of connection in a vertex of the second prototype. Left Bottom: The detailed view of one end of the strut of the first prototype.....	47
3.3.	Prototype of a 6-strut tensegrity robot. (a) The prototype consists of 6 aluminum tube and 24 TCP muscles. Two styrofoam balls are attached to both ends of each aluminum tube, and (b) Numbers are labeled on individual vertices of the tensegrity robot prototype.....	49

3.4.	Contact conditions between the floor and the tensegrity structure. Red lines represent closed base triangles and isosceles triangles, respectively. (a) Pattern 1. (b) Pattern 2.	49
3.5.	The stiffness study of 2-ply muscle at different static loads.....	51
3.6.	Actuation as a function of time for different values of pulsed power input for a 2-ly muscle under a load of 50 gram.....	52
3.7.	Mechanical response in an isotonic test of 2-ply TCP muscle at constant load 50 g. (a) Tensile actuation (% of loaded length), (b) Voltage, (c) Current, (d) Temperature.	54
3.8.	The two contact patterns with the ground in the NTRT simulator: (a) Contact pattern 2 (non-regular triangle) of default icosahedron, (b) Contact pattern 1 (regular triangle) of the default icosahedron, (c) Contact pattern 2 of our tensegrity robot and (d) contact pattern 1 of our tensegrity robot. Blue arrows show contact points with the ground.	55
3.9.	The rolling motion actuation pattern: (a) The contact pattern 2, (b) Actuator (2, 4) shown in the red block actuated, (c) Actuator (2, 3) shown in the red block actuated, (d) The pulsed input power provided to the actuator (2, 3) and actuator (2, 4).....	58
3.10.	Snapshots extracted from video of the tensegrity robot during rolling: (a) Initially at rest, (b), (c) and (d) deformation and rotation, (e) Recovery to the final state of the rolling motion. The power is on from $t = 0.0$ s to $t=1.0$ s; After $t=1.0$ s, the power is turned off. Note: The red round marker is attached to a ball for comparison purpose.	59
3.11.	(a) The position in the initial contact pattern 1. (b) The power input profile for each first column actuator pairs in Table 3.3. (c) The power input profile for each second column actuator pairs in Table 3.3.....	60
3.12.	Payload capacity of the 6-strut tensegrity robot when a dead weight is suspended in the central region: (a) No payload, (b) 200 g, (c) 300 g, (d) 400 g, (e) 500 g and (6) 700 g. The last three masses made the structure have a slack in the some of the cables.	60
4.1.	The 7-year-old child-sized humanoid robot HBS-1: (a) Comparison of HBS-1 and an 8-year-old child, (b) Front view of HBS-1 and (c) Side view. All dimensions are in millimeters (mm).	63
4.2.	X-ray image of a human hand.....	68

4.3.	Schematic diagrams of the finger actuation systems, where L_1, L_2, L_3 are the length of each phalange. (a) Isometric view of design I, (b) A 3-ply flexor muscle with torsional springs employed in design I, (c) Isometric view of design II, and (d) An agonist-antagonist actuator configuration containing 2-ply actuators, extension springs and pulley employed in design II.	71
4.4.	The schematic diagram of flexion-extension movement of the TCP hand in design II. (a) The fully extended state, (b) When the flexor muscle contracts upon heating and stretches the extension spring, and (c) The extensor muscle contracts upon heating, the extension spring contracts when the flexor muscle undergoes natural cooling, and the finger returns to its original position.	72
4.5.	TCP hand prototypes: (a) The first prototype (Design I) comprising the TCP actuators in comparison to a hand of an 8-year-old child; (b) The second prototype (Design II) consisting of the TCP actuators, silicone skin in the palm and soft finger-pads in the fingers; (c) Optical micrographs of the artificial muscles studied in this work, 2-ply TCP muscle; (d) 3-ply TCP muscle. The bar scales are 1 mm long; (e) The second prototype without the silicone skin on the palm and its dimensions.	73
4.6.	Kinematic model of the finger: (a) schematic diagram, (b) inset of the joint at DIP, (c) inset of the joint at PIP, and (d) inset of the joint at MCP. (The solid and dashed golden lines represent the tendon during flexion and the initial fully extended state, respectively.	77
4.7.	SolidWorks™ 2014 simulations of the displacement of a 3D printed cantilever beam (ABS material) loaded with a tip mass. (a) Schematic diagram and 3D printed cantilever with Normal and Sparse high-density printing options, (b) displacement of the cantilever for tip mass load—experimental and simulation results, (c) displacement contour plot-simulation and (d) stress along the cantilever beam-simulation at 40gm tip load.	79
4.8.	Simulations of index finger entirely 3D printed with ABS material (including the pins)- loaded with a force of 1N applied at: (a) the DIP, (b) the PIP, and (c) the MCP. (1) Von Mises stress, (2) Magnified view of the Von Mises stress in the pin, (3) Displacement, and (4) Schematic diagram.	80
4.9.	Tensile actuation study for an applied electrical power per length of the TCP muscles (square-wave input, 36% duty cycle; a period of 70 s) under a 200-gram load: (a) A 2-ply TCP muscle, unloaded length of 235 mm and 1.2 mm in diameter; (b) A 3 ply TCP muscle, unloaded length of 235 mm and 1.4 mm in diameter; and (c) Experimental setup used to determine the TCP muscles tensile actuation. The yellow shaded regions represent the heating stages.	82

4.10.	Tensile actuation as a percent of the loaded length of a 2-ply TCP muscle in an isotonic test at three different current input.	83
4.11.	Relationship between the temperature and the tensile actuation of a 2-ply TCP muscle. The blue lines represent the cooling stage, and the red lines represent the heating stage.	84
4.12.	Study of the influence of applied electrical power per length of the muscle (square-wave input, 36% duty cycle, a period of 70 s) on the force generation against a passive spring of stiffness of 50 N/m: (a) 2-ply, unloaded length 235 mm, diameter of 1.4 mm (a prestress of 1.7 N); (c) Experimental setup used for testing the force output. The yellow shaded regions represent the heating stages. Note that the force output is not dependent on the muscle length but it depends on the diameter of the muscle and applied power.	85
4.13.	Pulsed actuation results for a 2-ply TCP muscle at different power inputs: (a) Contraction of 2-Ply muscle, an unloaded length of 235 mm, diameter of 1.2 mm, under a 50-gram load and obtained from experimental setup shown in Figure 2.7. (b) The input voltage waveform of the 2-ply muscle with a pulse duration of 1s and square wave input. (c) Force generation of a 2-ply TCP muscle of unloaded length 235 mm and diameter 1.2 mm for a pulse duration of 1 s with peak power input (the same pulse power input profile as in Figure (b) against a passive spring load (spring stiffness of 20 N/m) obtained from experimental setup shown in Figure 2.9.....	87
4.14.	Tendon displacement and angle relationship of the index finger of design I: (a) the simulated and (b) experimental values and the linear trend lines.	88
4.15.	Characterization of the index finger of the prototype hands during flexion motion: (a) Comparison of experimental and simulated angular displacement of the joints in the index finger of design I (muscle's length of 100 mm) at low step input power 0.32 W/cm for 45 s. (b) Comparison of experimental and simulated joint trajectories of the index finger of design I; Inset: The humanoid hand prototype of design I with trajectories. (c) Experimental angular displacement of the joints in the index finger of design II (muscle length of 274 mm) at high pulsed power input of 2.12 W/cm for 1 s. (d) Experimental joint trajectories of the index finger of design II. Inset: The humanoid hand prototype of design II with trajectories. The experimental data were collected from high-speed camera data and processed in PCC software, and the theoretical data were obtained from Eq.4.1- 4.4 using Matlab.	90
4.16.	Angular displacement of the index finger in design II during the continuous cycle of flexion-extension. The narrow yellow shaded regions represent the heating stages of 1 s duration for flexor muscle at 2.12 W/cm; The wide yellow shaded regions represent the heating stages of 5 s duration for extensor muscle at 0.25 W/cm.	91

4.17.	Grasping configurations on the TCP hand -prototype II: (a) forceps, (b) silicone tube, (c) screwdriver, (d) cylinder, (e) ping-pong, (f) sphere, (g) disk, (h) thread spool, (i) syringe, (j) cone, (k) stapler, (l) super glue. Gravity is in the same direction for all images as shown in (a).....	92
4.18.	Hydrothermal actuation of a coiled 3.33-mm-diameter nylon 6 fishing line lifting a 200-gram load by 22% when switched between 21 °C water and 99 °C water manually.	94
4.19.	Tensile actuation for a coiled fishing line muscle as a function of the temperature of the hot water used to produce muscle contraction. A 200-gram weight was raised during muscle contraction.....	94
4.20.	(a) Coiled fishing line actuator concept and (b) the assembled coiled fishing line actuator. (c) Schematic diagram of the experimental setup to test the performance of the coiled muscle in the application of robot hand and (d) picture of the laboratory experimental setup.	96
4.21.	(a) Initial position of the index finger before actuation and (b) Final position of the index finger after actuation.	97
5.1.	Musculoskeletal system in different species.....	103
5.2.	Structure of shoulder joint [169].....	105
5.3.	MS prototype in design I based on 3D printed ball and socket joint with stabilization element made of silicone: (a) CAD Design and (b) Prototype integrated with TCP muscles. The bar scale is 1 mm long.	106
5.4.	(a) Schematic diagram of MS prototype in design II based on ball-and-socket joint structure using bioinspired antagonistic pairs of muscles. (b) The musculoskeletal system under actuated state, and (c) The final fabricated prototype of MS.	107
5.5.	Muscle structures and implementation in musculoskeletal system. (A) A scanning electron microscope (SEM) image of TCP _{NC} ^{FL} muscle. (B) Optical images of TCP _{NC} ^{FL} muscle. (C) Electrothermal actuation of TCP _{NC} ^{FL} muscle lifting a 100-gram load by 53% actuation stroke at a constant current 0.22A for a period of 6 seconds.	108
5.6.	Modeling of the ball and socket joint (MS prototype in design I). (a) configuration of the prototype during bending motion about z axis and (b) schematic diagram of the bending motion, (c) the prototype during twisting motion about y-axis and (d) the top view of the joint during twisting motion.	110

5.7.	Position diagram of the MS.	112
5.8.	Dexterous workspace of the musculoskeletal system.	113
5.9.	Manufacturing steps for creating of ball-and-socket joint: (a) 3D printed joint assembly mode, (b) surface polishing and adding grease into the clearance, (c) section view. (d) injecting the mixture of silicone, and (e) mold removed.	114
5.10.	The ball-and-socket joint and mold in (a) was 3D printed using ABS plus material; The silicone ligament and one pair of channels were fabricated from step (b) to (c); The other pair of channels as shown in (e) could be added in step (d) from parts shown in step (c); Performing step (f) twice, a silicone layer was introduced to cover the top and bottom plates and secure the connection between four channels and the joint; (g) shows the final fabricated prototype.	115
5.11.	Schematic diagram of the experimental setup to characterize the stiffness of the joint (a) and muscle (b).	117
5.12.	The measurement of force during stiffness test;	118
5.13.	Mechanical response of TCP_{NC}^{FL} muscle in an isotonic test fabricated from an 860-um-diameter nylon 6 monofilament that was mandrel coiled incorporating an 80-um-diameter resistance wire in a double spacing, which resulted in spring index of 5.2: (a) the measured force profile, (b) the measured voltage profile, (c) the measured absolute displacement profile, (d) tensile actuation stroke, as a percent of the loaded muscle length, (e) the measured temperature profile characteristics measured at different pre-stress levels,	120
5.14.	Average tensile actuation as a percent of the loaded length, the absolute contraction displacement during actuation, the loaded length and temperature of a TCP_{NC}^{FL} muscle fabricated from an 860-um-diameter nylon 6 monofilament that was mandrel coiled incorporating an 80-um-diameter resistance wire in a double spacing, which resulted in spring index of 5.2, in an isotonic test versus different load.	121
5.15.	Characteristics of TCP_{NC}^{FL} muscle fabricated from an 860-um-diameter nylon 6 monofilament that was mandrel coiled incorporating an 80-um-diameter resistance wire in a double spacing, which resulted in spring index of 5.2, against a passive spring of stiffness of 133 N m^{-1} under different pre-stress: (a) the measured force profile, (b) the measured voltage profile, (c) the measured absolute displacement profile, (d) tensile actuation stroke, as a percent of the loaded muscle length, and (e) the measured temperature profile characteristics measured at different pre-stress levels.	123

5.16.	Average tensile as a percent of the loaded length, the absolute contraction displacement during actuation, the loaded length and maximum force of a TCP _{NC} ^{FL} muscle fabricated from an 860-um-diameter nylon 6 monofilament that was mandrel coiled incorporating an 80-um-diameter resistance wire in a double spacing, which resulted in spring index of 5.2, in a spring load test against a passive spring of stiffness of 133 N m ⁻¹ versus different pre-stress.....	124
5.17.	Pulsed actuation results for fishing line TCP muscle at different current. (a) Contraction absolute displacement of a fishing line TCP, (b) Tensile actuation as a percent of the loaded muscle length, (c) The measured force profile and (d) the measured temperature profile.	126
5.18.	Bending test of the MS joint (Design I): (a) Initial position (no actuation, (b) The maximum angle bending towards to the right side (the muscle in the blue block was actuated, and θ represents the angle measured in the test), (c) The maximum angle bending towards to the left side (the muscle in the blue block was actuated).	127
5.19.	The angular displacement during the bending test of the joint integrated with TCP muscles (yellow highlighted regions indicate that the power is on).	127
5.20.	Rotation test about y-axis by twisting the ball-and-socket joint in Design I: (a) The initial state after twisting the ball-and-socket joint manually. (b) The final position after the rotation by actuating all the muscles, and (c) The twisted ball-and-socket joint as seen from side view.....	128
5.21.	Performance of MS prototype (Design II): (A) Musculoskeletal system Bending motion (Regular actuation with long duration 30 s, and cooling time is 100s); (B) Pulse actuation with short duration 1s, and cooling time is 100s. (C) Pulse actuation with short duration 1s, and cooling time is 30 s. The insets show the bending angle of the musculoskeletal skeletal system in the end of each actuation cycle.....	131
5.22.	The bending motion of the musculoskeletal system (design II)..	132
5.23.	Concept design of MS which is operable in a cordless mode.....	133
5.24.	(a)The tensile actuation of a 2-ply TCP muscle (63 mm in length) at constant 100-gram load; (b) The measured voltage at a constant current input (0.37A).	134
6.1.	Overview of Chapter 2: Schematic diagram of self-coiled muscle (A) and mandrel-coiled muscle (B) fabrication setup, and (C) The resistance change of 1-ply TCP muscle in spring-load test, along with other state variables.	138
6.2.	Overview of Chapter 3: (A) Tensegrity prototype, (B) Stiffness and (C) tensile actuation of 2-ply muscle.....	139

6.3.	Graphical abstract of Chapter 4: (A) Schematic diagram of the finger actuation system. (B) Kinematic model of the finger. (C) Tensile actuation vs load at three different current input. (D) Stress analysis of the finger. (E) Tensile actuation and pulling force in pulsed actuation and (F) Grasping of various objects.	141
6.4.	Overview of Chapter 5: Muscle structures and implementation in musculoskeletal system. (A) SEM image of TCP_{NC}^{FL} muscle. (B) Electrothermal actuation of TCP_{NC}^{FL} muscle lifting a 100-gram load by 53% actuation stroke. (C) Schematic diagram of the musculoskeletal system based on ball-and-socket joint structure using bioinspired antagonistic pairs of muscles. (D) The prototype of the musculoskeletal system. (E) Dexterous workspace of the musculoskeletal system. Mechanical performance of the TCP_{NC}^{FL} muscle in an isotonic test (F) and in a spring load test (G).	142

LIST OF TABLES

2.1.	Muscles used for the robotic hands.....	17
2.2.	Model parameters of K_1 and K_2 for all tests.	40
3.1.	The properties of the tensegrity structure	48
3.2.	Parameters of the NTRT default structure and our tensegrity robot.....	56
3.3.	Actuator pairs tested to cause transition from contact pattern 1 (8,11,6).	58
4.1.	Characteristics of some robotic (R) and prosthetic (P) hands/fingers.	65
4.2.	The comparison of TCP and other robotic hand/finger	73
4.3.	The various objects the TCP hand could grasp.....	93
5.1.	The specification of the selected battery.....	134

CHAPTER 1

INTRODUCTION AND BACKGROUND

This dissertation focuses on a new class of artificial muscles (twisted and coiled polymer muscles) and explores their applications in robotics, including (1) a reconfigurable robot with icosahedral tensegrity structure, (2) a compact and low cost robotic hand and (3) a musculoskeletal system for bio-inspired robotics systems. The dissertation consists of six chapters. In this chapter, different actuator technologies, such as shape memory alloy, shape memory polymer, pneumatic artificial muscle and twisted and coiled polymer muscle, are discussed. Finally, this chapter gives the objectives of the study and an outline of the dissertation.

1.1 Introduction

The emergence of unique actuator technologies has pushed the development of robotics, enabling new capabilities and features. Most of the robots have some type of actuation systems, and actuator is one of the key components in the robots that determines the performance such as form factor, weight, degree of freedom, force, speed and cost. For biomimetic robotic system, we mainly focus on the utilization of new actuator technologies that have muscle-like forms and associated technologies to create articulated movements. This chapter presents a brief introduction of a number of promising actuator technologies and the development of the state of art robots based on those actuators. The actuator technologies covered in the section include shape memory alloy, shape memory polymer, pneumatic artificial muscle, and twisted and coiled polymer muscle. The following sections summarize the history, development and the current research activities of the aforementioned actuator technologies and their application in robotics.

1.2 Shape Memory Alloy

Shape memory alloy (SMA) was first discovered by Arne Olander in 1932 [1]. The recognition of the importance of shape memory alloys can be tracked back to 1963 as William Buehler and Frederick Wang discovered that a nickel titanium alloy (NiTi) showed a shape memory effect (SME) when subjected to loading and heating conditions [2]. This effect can be described as the ability to return to the original shape from a deformed shape. Since then, researchers have been exploring different alloys which could also exhibit the shape memory effect, such as copper based alloys (CuZn and CuAl). By tailoring the constituent materials of NiTi based shape memory alloys through varying the concentration of nickel to titanium, along with other elements such as copper and iron, researchers were able to obtain a wider operating temperature range and a better mechanical response.

SMA exhibits two transformation phases with three distinct crystal structures (i.e. twinned martensite, detwinned martensite and austenite), which depend on temperature or magnetic field [3]. Shape memory effect is a transformation phenomenon observed in shape memory cycle. The martensite structure exists in low temperature and the austenite structure is dominant in higher temperature. The transformation from martensite to the austenite phase takes place when the SMA is subjected to heat. Figure 1.1 shows the 3D stress-strain-temperature diagram of SMA phase transformation. During the heating process, the material starts to change from martensite to austenite at austenite-start-temperature (A_s) and is complete when it reaches the austenite-finish-temperature (A_f). Once the SMA experience a temperature between A_s and A_f , it shows a phenomenon of contraction in length, i.e. an intention to recover into its original form. During the cooling, when the temperature decreases below martensite-start-temperature M_s , the austenite

begins to transform to the martensite to revert the phase transformation until the temperature reaches martensite-finish-temperature M_f , where the transformation is complete. However, the SMA may lose the shape memory effect and undergo permanent deformation if SMA reaches a critical high temperature called M_d [4].

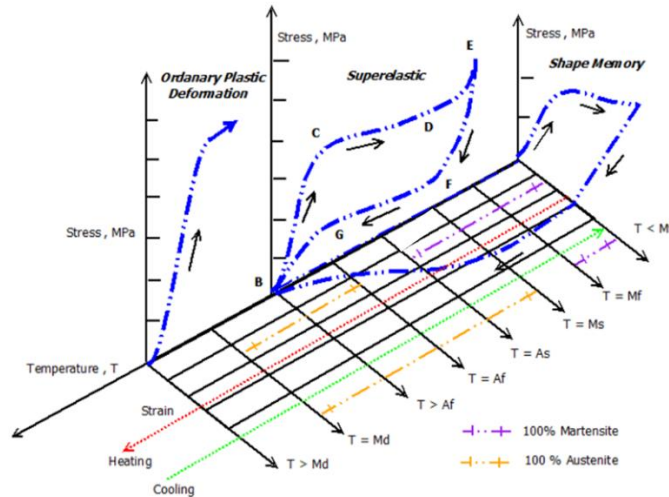


Figure 1.1. 3D stress-strain-temperature diagram of SMA phase transformation [5].

SMA's are characterized by their hysteretic behavior as can be seen in Figure 1.1. Hysteresis is generally defined as temperature difference between the temperatures where material reaches 50% austenite phase from full martensite phase upon heating and 50% martensite upon cooling from full austenite phase [6]. This limits their application especially where precise control is required. The hysteresis loop makes the control of SMA's quite difficult. Hysteresis is one of SMA's design challenges. Other challenges include a fairly small effective strain, low actuation frequency, and low energy efficiency.

Joule heating is a widely used heating source to power SMA's. The electrical resistivity of NiTi increases by more than 20% during the phase transformation in the shape memory cycle [7] and

the change of resistivity is a complicated non-monotonic function of temperature over a wide temperature range. However, researchers found a way to implement control over SMA actuator effectively in a specific temperature band (usually within the range of phase transformation temperature). The response time (contraction) of SMA is determined by power consumption (the supplied energy and heating time), which can be significantly improved by using large magnitude of power pulses. The restricting factor of SMAs is the low operational frequency, a result of the time required for heating and cooling. This problem could be improved by active cooling techniques [8-10].

The SMAs come in a wide range of shape and size, which suit them for a diverse range of applications. A review of the development of SMAs and their application can be found in [6, 11]. For robotic system, SMAs are extensively used as micro-actuators or artificial muscles. The benefits of SMAs are compact size, high force-to-weight ratio and silent operation (no noise during actuation). Thermally driven SMA muscles, nonetheless, are widely deployed in humanoid hands. A number of robotic/prosthetic hands have been also constructed based on SMA actuators. For instance, Villoslada, et al. [12] presented a new design of SMA actuator for a wrist exoskeleton. The new design enables the new actuator to bend up to 180° and can accommodate several loops of SMA wire to provide a great linear displacement. She et al. [13] developed a soft five-fingered robotic hand embedded with an antagonistic pair of SMA strips. Andrianesis and Tzes [14] demonstrated the implementation of SMA actuators in a multifunctional prosthetic hand. Bergamasco et al. [15] presented a shape memory alloy based artificial hand in which coil-type SMA springs were located inside the structure of the proximal phalanx. Dilibal et al. [16] performed a successful set of experiments testing a three fingered SMA robot hand, which utilized

rectangular nickel-titanium sheets. Price et al. [17] developed a three-fingered robot hand for prosthetic application using shape memory alloy actuators. Laurentis et al. [18] focused on mechanical design of a SMA actuated prosthetic hand with five fingers and 20 DOF. Other applications of SMAs in robotics include the development of crawling robot [19, 20], bat robot [21], soft robot arm [22], caterpillar robot [23] and starfish robot [24].

1.3 Shape Memory Polymer

Shape memory polymers (SMPs) are another class of smart materials that have the ability to recover to their previous form due to certain external stimuli such as heat, light or solvent exposure. More specifically, SMPs can be manipulated and stored in temporary shapes under certain conditions by vitrification or crystallization. Vitrification is the transformation of a substance into a non-crystalline amorphous solid. When an external stimulus is applied, the material changes its shape to the original, equilibrium and stress-free condition. However, the principle of the deformation mechanism differs dramatically from those of SMAs.

In shape memory polymer, the shape memory effect can be revealed through the evolution of tensile stress, tensile elongation and temperature during thermomechanical cycling [25]. This behavior can be depicted as shown in Figure 1.2. SMP exists in a rubbery, elastic state at an elevated temperature (T_d) which is higher than the SMP transition temperature (T_{trans}). At the beginning, the elastic state is deformed to a certain strain upon applied load. The obtained deformation can be fixed during subsequent cooling under constant stress to a temperature (T_f). During this stage, the material exists in a more rigid state (the semicrystalline state) as the recovery of the polymer chains is prohibited by material immobilization, and the energy is stored as latent

strain energy. Therefore, upon release of stress at T_f , a minor strain decrease may occur. In general, a subsequent temperature increases up to a temperature greater than T_{trans} without any stress will lead to a shape recovery. During this stage, the strain or shape will return to equilibrium shape due to the regained chain mobility.

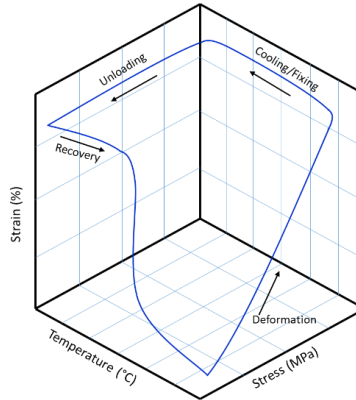


Figure 1.2. A representative 3-D plot for presenting thermomechanical cycles for an example of a shape memory polymer [26].

In the past several years, shape memory polymers have attracted significant research activities on different aspects, such as the elucidation of new composites to tailor the material property [27-31], the exploration of new shape fixing and recovery mechanism [32-36], and emergence of diverse applications [37-40]. However, shape memory polymers' response time is slow.

1.4 Pneumatic Artificial Muscle (PAM)

Pneumatic artificial muscles are actuators in a cylindrical shape mainly made of a flexible and inflatable membrane. PAMs comprise of a flexible reinforced closed membrane, which contributes the compliant behavior. The membranes are usually made from pure rubber latex, reinforced by fibrous filaments. The actuation principle of PAM is quite simple, as shown in Figure 1.3. PAMs contract in lengthwise direction and expand in radial direction in response to pressure input.

Thereby, PAMs are able to deliver a pulling force. The generated force depends on the shape and size, the rate of pressure input and flow rate. PAMs usually require an energy source such as a compressor to force the gas into the actuators to create a pressure difference between the inside gas and the ambient environment. The requirement of a compressor makes these actuators less attractive for robotics, particularly for portability.

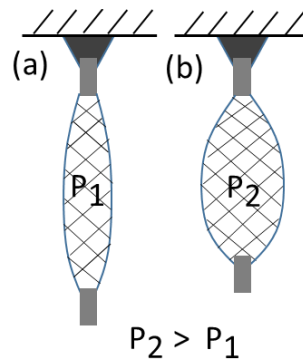


Figure 1.3. Schematic diagram of the actuation principle of PAM in its resting (a) and actuated (b) configurations.

A review of the pneumatic artificial muscles as actuators for robotics can be referred in [41]. Yang et al. developed a novel bio-inspired robotic finger which is composed of a pneumatic actuator and a multi-material substrate [42]. Another pneumatic based hand developed by Deimel and Brock [43] exhibited a robust grasping performance and showed a high degree of compliance. Wakimoto et al. [44] explored a new concept of pneumatic artificial muscle with a pressure-sensing ability.

1.5 Twist and Coiled Polymer (TCP) Muscles

Twisted and coiled polymer (TCP) muscles are another type of artificial muscles that can be thermally driven to produce giant stroke and large pulling force. The spring-like artificial muscles are highly stretchable, compliant and of great interest for a wide range of applications in robotics.

In 2014, Haines et al. [45] demonstrated the transformation of polymer fibers used for fishing line and sewing thread into artificial muscles, which contract in response to hydro-thermal, electro-thermal actuation or photothermal actuation. Such muscles are low cost and easy to manufacture by a continuous process, and can be fabricated from a wide range of precursor materials, including nylon 6,6 multifilament sewing thread and nylon 6 monofilament fishing line. These muscles can be prepared by inserting twist into a precursor polymer fiber, followed by thermal treatment. Although the untwisted fiber can achieve 4% strain (similar to SMAs), twist insertion to produce fiber coiling allows small strain induced by anisotropic thermal expansion to be transformed into a large tensile contraction along the length of the coiled fiber [46].

Two different muscle fabrication methods were reported and widely used in the literature. The first method is based on direct self-coiling (twist-induced coiling) to produce artificial muscle, and the other method is based on mandrel-coiled approach. Self-coiled artificial muscles result from nucleation of coils through the length of the precursor fiber once the fiber reaches maximum twist density. The mandrel-coiled artificial muscles differ in terms of coil formation. It is made by wrapping the twisted fiber (but not coiled) over a mandrel. One necessary step to form mandrel-coiled muscles is thermal annealing which is needed to lock the shape of the muscle. Usually, it will take up to two hours at 210°C to perform the annealing steps depend on the material properties of precursor fiber. The artificial muscle can deliver tremendous tensile/contractile stroke and pulling force. Users can control the level of stroke amplification by adjusting the twist insertion in the fiber, the spring index (the ratio of mean coil diameter to the fiber diameter) and power input. If a fiber is simply twisted and coiled with a spring index of 1.7, it can provide stroke up to 20% at nominal stress greater than 35 MPa [45]. Scaling up of the muscle can also deliver different

amount of pulling force. In addition to giant stroke, high energy and power densities, muscles contraction can be attained at silent operation (without noise). Other impressive advantages of TCP muscles are the compact size and minimal or no hysteresis compared with large hysteresis of SMAs. TCP muscles (~\$5/kg for fishing lines precursor fiber) are also much cheaper than the SMAs [47] (more than \$3,000/kg for Flexinol wire of diameter 0.13 mm). In general, silver coated nylon precursor material is higher in cost compared with fishing line. Hysteresis in TCP muscles may be observed if the muscles are under isothermal loading conditions during tensile test [48]. However, hysteresis of TCP muscles made of nylon 6,6 monofilament was reported to be negligible in [45] in isotonic test. Specifically, Haines et al. [45], showed that the hysteresis for 127 μ m-diameter nylon 6,6 monofilament is less than 1.2°C hysteresis compared to 27°C hysteresis for NiTi shape memory alloy muscle.

The convenient availability of those precursor materials, easiness of artificial muscle fabrication technique and the resulting high-performance lead to a very promising actuator/sensor for various applications. In [49], Weijde et.al explored the possibility of deploying the twisted and coiled polymer muscle as a sensor. The sensing principle was based on self-sensing via electrical impedance to predict the deflection, force and temperature. The experimental results revealed the suitability of the sensing principle in the Joule-heated twisted and coiled polymer muscle. The polymer artificial muscle can even be used as a healing-on-demand composites in [50] which consists of other components such as thermoset host and thermoplastic particle. It is reported that the composites can achieve higher healing efficiency at free boundary condition (60%) than that at fixed boundary condition (54%). The authors envision that the polymer artificial muscle will promote the development of new device for the next generation healing-on-demand polymer

composite. Kim et.al put an effort on energy harvester based on the polymer artificial muscle [51]. The principle is to utilize the fluctuation in air temperature to actuate a 27 μm -diameter coiled nylon muscle which drives the rotation of a magnetic rotor. An average output electrical power of 124 W per kg of the muscle was reported. Almubarak and Tadesse [52] presented an interesting work which utilized TCP muscles embedded in silicone elastomer for soft robot applications. Saharan et al. [53] developed an orthotic hand powered by TCP muscles and demonstrated the hand versatile manipulation capabilities.

1.6 Objectives and Dissertation Outline

1.6.1 Objectives

The aim of this study is to evaluate TCP muscle's performance for use in robotics and correlate its relationship with process parameters. In our case, the process parameters include voltage, current, temperature and load conditions. The mechanical performance is usually evaluated in terms of tensile actuation and force. The other objective is also to develop and characterize novel TCP muscles and to bridge the gap between the new TCP muscles and their robotics application. The objectives of the research are summarized as follows:

- Development of a novel muscle fabrication setup to produce mandrel-coiled TCP muscle from fishing line and resistance wire, enabling the Joule heating actuation and hence use for robotics application.
- Development of an automated experimental setup to fully characterize the TCP muscles, and obtain time domain response of the actuators.

- Development of a model of TCP muscle to predict the actuation performance, providing some insights from TCP muscle control aspects.
- Study of the TCP muscle resistance change during electro-thermal actuation, presenting for the first time the electrical properties of TCP muscle.
- Demonstration of a novel application of TCP muscle into a reconfigurable robot based on tensegrity and characterization of the integrated system.
- Design and development of a novel humanoid hand utilizing TCP muscles and critical analysis of the robotic hand performance.
- Design, fabrication and characterization of musculoskeletal system based on ball-and-socket joint using TCP muscle for advanced bio-mimetic robots.

1.6.2 Dissertation Outline and Acknowledgments

An extensive study has been carried out on a novel TCP muscle in this dissertation to bridge the gap in integrating TCP muscles and robotic systems. The dissertation is divided into six chapters. In the present chapter, a brief introduction of other smart actuator technologies, and TCP muscles are described. The scientific impact and the need to further understand the new artificial muscle to utilize their full potential towards robotics are highlighted. It also covers the objectives of the study, detailing the specific goals of the dissertation and efforts to advance the progress on exploring the new artificial muscles as actuators for robotics application. Chapter 2 introduces the fabrication methods of the new artificial muscles, explains the full characterization of TCP muscles to further understand the muscle, and discusses the study of the resistance change of TCP muscle. Chapter 3 shows for the first time, a novel application of TCP muscle in a reconfigurable robot with

tensegrity structure. Chapter 4 discusses the design and development of a humanoid hand powered by TCP muscles based on agonistic-and-antagonistic arrangement. Numerous time domain experimental results of 2-ply and 3-ply TCP muscles (self-coiled) are presented. Chapter 5 demonstrates the application of TCP muscles to musculoskeletal system based on ball-and-socket joint. In this chapter, a mandrel-coiled actuator is briefly explained along with unique characteristic curves of the actuator. The last chapter makes a conclusion of the study, along with discussions on future work.

Chapter 2 and Chapter 4 contain material from the following source: © IOP Publishing. Reproduced with permission, (Wu, Lianjun, et al. "Compact and low-cost humanoid hand powered by nylon artificial muscles." *Bioinspiration & Biomimetics* 12.2 (2017): 026004.), (February 2017), DOI:10.1088/1748-3190/aa52f8. Chapter 4 also contains material from the following two sources © SPIE. Reproduced with permission, (Wu, Lianjun, et al. "Nylon-Muscle-Actuated Robotic Finger." *Proc. of SPIE Vol. 9431.*) (April 2016), DOI:10.1117/12.2084902; © MDPI. Reproduced with permission, (Wu, Lianjun, et al. "HBS-1: a modular child-size 3D printed humanoid." *Robotics* 5.1) (January 2016), DOI:10.3390/robotics5010001. Chapter 3 contains material from the following source: © SPIE. Reproduced with permission, (Wu, Lianjun, et al. "A reconfigurable robot with tensegrity structure using nylon artificial muscles." *Proc. of SPIE Vol. Vol. 9799.* 2016.), (April 2016), DOI: 10.1117/12.2219641. Chapter 5 contains material from the following source: © ASME. Reproduced with permission, (Wu, Lianjun, and Yonas Tadesse. "Musculoskeletal System for Bio-Inspired Robotic Systems Based on Ball and Socket Joints." ASME 2016 International Mechanical Engineering Congress and Exposition. American Society of Mechanical Engineers.), (April 2016), DOI: 10.1115/IMECE2016-67394. All rights reserved.

CHAPTER 2

FABRICATION AND CHARACTERIZATION OF TCP MUSCLE

2.1 Introduction

Based on fabrication methods, polymer artificial muscles can be characterized into two types, namely self-coiled and mandrel-coiled muscles as shown in Figure 2.1. Self-coiled muscles are those that form the coils due to extreme twist. In mandrel-coiled muscles, the twisted precursor materials (without coil nucleation) are wrapped around a mandrel of a certain diameter to form the coils. The mandrel-coiled muscles can be further divided into another two forms: homochiral and heterochiral coils. In homochiral coils, the twist insertion and wrapping are performed in the same direction similar to that in self-coiled muscles. However, a heterochiral coil is made in the opposite direction between twist insertion and wrapping. A homochiral coil contracts in length when heated. A heterochiral coil expands in the lengthwise direction when heated.

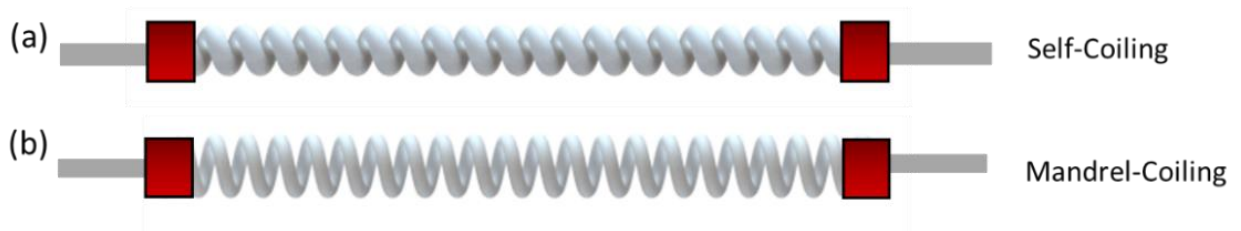


Figure 2.1. Two coiled artificial muscle structures: (a) A self-coiled artificial muscle from twist induced coiling; (b) A mandrel-coiled artificial muscle obtained by wrapping around a rod of a certain diameter.

2.2 Self-coiled TCP Muscle

TCP muscles from sewing thread such as silver coated nylon can be categorized as self-coiled muscles, and the details of producing the self-coiled artificial muscles will be discussed in this

section. In this study, the TCP muscles were fabricated from conductive sewing thread (silver coated nylon 6,6 precursor), manufactured by Shieldex Trading, Inc. (Shieldex PN#260151023534oz, nominal diameter of 0.2 mm, electrical resistance of 0.50 Ω /cm, 136 number of filaments and linear density of 1.3 mg/cm). The investigated TCP muscles consist of a multifilament silver-coated nylon 6,6 sewing thread. Such muscles are easy and inexpensive to manufacture by a continuous process. Figure 2.2 illustrates the muscles fabrication process including twist insertion (a-b), coiling (c), annealing (d), training (e), plying (f-g) to make different types of muscles (2-ply muscles shown in (g)) and final actuation testing (h-j). In the previous similar work [45, 54], thermal annealing was performed in a furnace while the muscles were kept under tension. In Ref [55], the muscles were subjected to 1 hour on-frame thermal annealing in air at 150°C. In this study, the muscles were annealed electro-thermally (Joule heating) while tethered and hooked at one end with a load to keep under a pre-stress. The electro-thermal heating refers to the application of electrical power to the muscles, which results in heating as shown in Figure 2.2 (j). The amplitude of power determines the magnitude of temperature rise in the muscles and hence the stroke of the muscles.

There are two major material processing steps of the precursor material for making artificial muscle. The first one is *Twist insertion, coiling and plying*. The second one is *Annealing and training*.

(a) Twist Insertion, coiling and plying

Twist insertion into the precursor Ag-plated nylon 6,6 thread up to coiling (Figure 2.2(a) and Figure 2.2(b)) is the first step in polymer artificial muscle fabrication. Following similar procedure reported in [45], TCP muscles are fabricated by attaching one end of the sewing thread to a motor

and hanging a hooked weight from the other end to keep the precursor fiber straight and taut. The sewing thread (precursor material) is tethered at the bottom end to prevent torsional rotation of this end. The importance of selecting an appropriate weight is worth mentioning because the thread

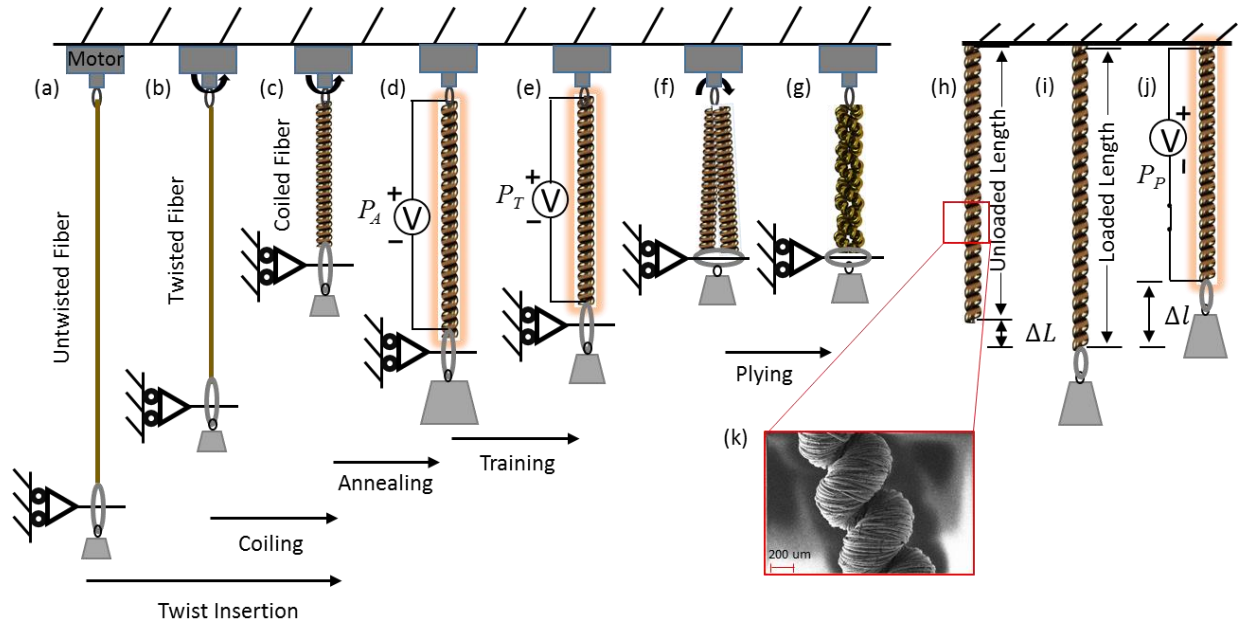


Figure 2.2. Schematic diagram of the fabrication process for TCP muscles: (a) The top end of the precursor fiber is attached to a motor and a deadweight is suspended at the bottom end to keep the precursor fiber straight and taut. (b) Twist is inserted in the fiber by rotating the motor in a counterclockwise direction. (c) Continuous, regular coils emerge throughout the thread length to form a 1-ply TCP muscle. (d) A 1-ply muscle is annealed by electro-thermal heating by applying power, P_A , across terminals. (e) After annealing, the muscle is trained by electro-thermal heating by applying power, P_T . (f) Plying two 1-ply muscles together in a clockwise direction to form a 2-ply muscle and obtain a structure as in (g). (h) The unloaded length without lifting weight and (i) The loaded configuration is shown. (j) After annealing and training, the 1-ply TCP muscle is tested by applying powering voltage, P_P , showing the contraction of (i), and (k) SEM image of 1-ply muscle.

tends to snarl prior to coiling under too little weight and break during coiling under excessive weight. Typically, a 150-gram mass is attached at the end of a precursor multifilament to make a 1-ply TCP muscle. In Figure 2.2(c), the twisted nylon fiber forms continuous, regular coils throughout the thread length when twisted beyond a critical twist density (around 2,430 turns/m),

which is expressed in terms of inserted twist turns per length of precursor fiber. Subsequent untwist can be performed if the coils are so dense that inter-coil contact interferes with muscle contraction when under the targeted range of mechanical loads. In preparing the actuators, care was taken to insert twist into the commercial fibers only to the point of full-length coiling under the applied weight. The ratio of initial, non-twisted fiber length to coiled non-annealed length for the investigated TCPs is around 3.52. To explore the actuation forces, then two 1-ply muscles were plied (as shown in Figure 2.2(f)) to make a 2-ply muscle as illustrated in Figure 2.2(g). A 3-ply muscle can be similarly fabricated by plying three 1-ply muscles.

(b) Annealing and training

In Figure 2.2(d), the muscles were annealed (2 cycles, < 30 s each) by electro-thermal heating above 105°C. To do this, a power of 0.59 W/cm and 0.43 W/cm at the first and second cycle, respectively, was used for 2-ply muscle preparation, while a 0.65 W/cm and 0.59 W/cm was used for 3-ply muscle (typically, considering unloaded non-annealed length). During this step, a dead weight was hooked, typically 350 g and 500 g for 2-ply and 3-ply coiled yarns, respectively. These processes enable the muscles to actuate reversibly and obtain a good inter-coil spacing. After annealing, in Figure 2.2(e), the muscles were trained (at least ten cycles, <30 s each) by electro-thermally heating at 0.2 W/cm and 0.3 W/cm for 2-ply and 3-ply coiled yarns respectively, under the targeted range of mechanical load. Figure 2.3 shows the SEM images of 1-ply, 2-ply and 3-ply samples of the fabricated artificial muscles. From Figure 2.3(a), it can be seen that some defects of the silver-plated layer occur at the surface of the polymer muscle. High power pulsed test can lead the flaking of silver from the polymer muscle more easily. Table 2.1 provides the properties of the artificial muscles that were prepared for robotic hand design and development.

Table 2.1. Muscles used for the robotic hands.

	Number of filaments	Linear density (mg/cm)	Electrical resistance (Ω/cm)	Total outer coiled diameter, D (mm)	Power regular for actuation (W/cm)	Actuation (%)
2 -Ply	272 (2n)	8.3 (± 0.5)	0.60 (± 0.06)	1.24 (± 0.02)	0.18-0.25	8.0-14.0
3 -ply	408 (3n)	12.5 (± 0.3)	0.43 (± 0.04)	1.41 (± 0.02)	0.21-0.33	9.0-13.0

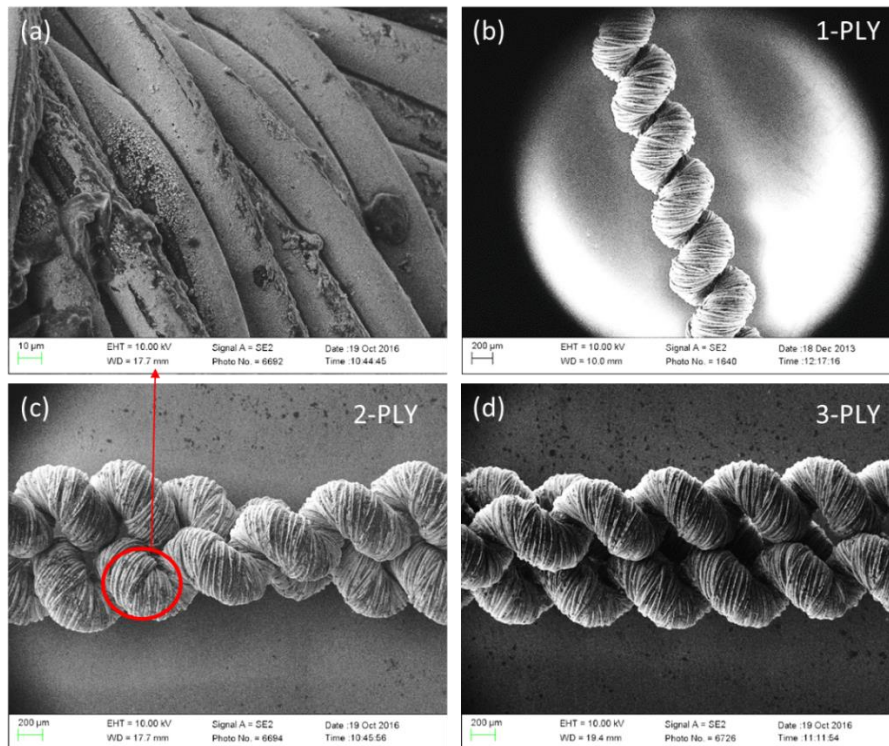


Figure 2.3. (a) Magnified view of circle in (c), (b) SEM image of a fabricated 1-ply muscle, (c) SEM image of a fabricated 2-ply muscle, and (d) SEM image of a fabricated 3-ply muscle.

2.3 Mandrel-coiled TCP Muscle

Artificial muscles produced from sewing thread with conductive silver coating mentioned in the previous section is widely used due to the easiness of delivering heat to muscles via electro-thermal

actuation. Although TCP muscles made from sewing thread are easy to actuate via electro-thermal heating, the silver coating, that is needed for Joule heating, increases the cost of the precursor material compared with its counterpart fishing line. Moreover, our high current pulses tests showed that extremely high power within short period may lead to the degradation of the muscles life cycles due to flaking of silver from the nylon surface which affects electro-thermal actuation as shown in Figure 2.4. The bright regions of a 1-ply TCP muscle in Figure 2.4 indicate those area where the silver-plated layer flaked from the polymer surface. The higher power supplied to the TCP muscle caused the muscle to lose conductivity. On the other hand, fishing line muscles are cost efficient, as the precursor material is not manufactured with a conductive coating. They can be actuated by hot air or water. When a muscle is actuated by water, it is called hydrothermal actuation. For mandrel-coiled muscles without heating wire, a fluidic actuation method is a good option to deliver heat to muscles. Mandrel-coiled muscles (made from monofilament nylon 6 fishing line) via hydro-thermal actuation can deliver a much higher actuation stroke than self-coiled muscles (made from multifilament nylon 6,6 sewing thread with silver plated) via electrical-thermal actuation. However hydro-thermal actuation requires complicated fluidic circuits and pipes, thus inhibiting the wide application of mandrel-coiled muscles. There are some solutions to overcome those issues. The flaking problem in silver-coated TCP muscles can be avoided by working at a lower temperature, but this limits the frequency of the actuator. Another alternative approach is to replace the silver coating with other conductive element such as resistance wire that is plied with the polymer yarn. In general, the incorporation of a heating element will provide the advantage of convenient electro-thermal actuation by Joule heating. Carbon multiwalled nanotube (MWNT) was selected as electronic conductor [45], however, the procedure is relatively

complicated and produces high linear resistances (10 to 100 volts per centimeter of muscle length). For this reason, a novel apparatus was developed to create mandrel-coiled artificial muscles from fishing line and a resistance wire. To incorporate a resistance wire into the mandrel-coiled muscle is not trivial. The developed device will facilitate the fabrication of mandrel-coiled muscle with resistance wire. The manufacturing method described in this section enables researchers to fabricate muscles having identical and repeatable characteristics easily.

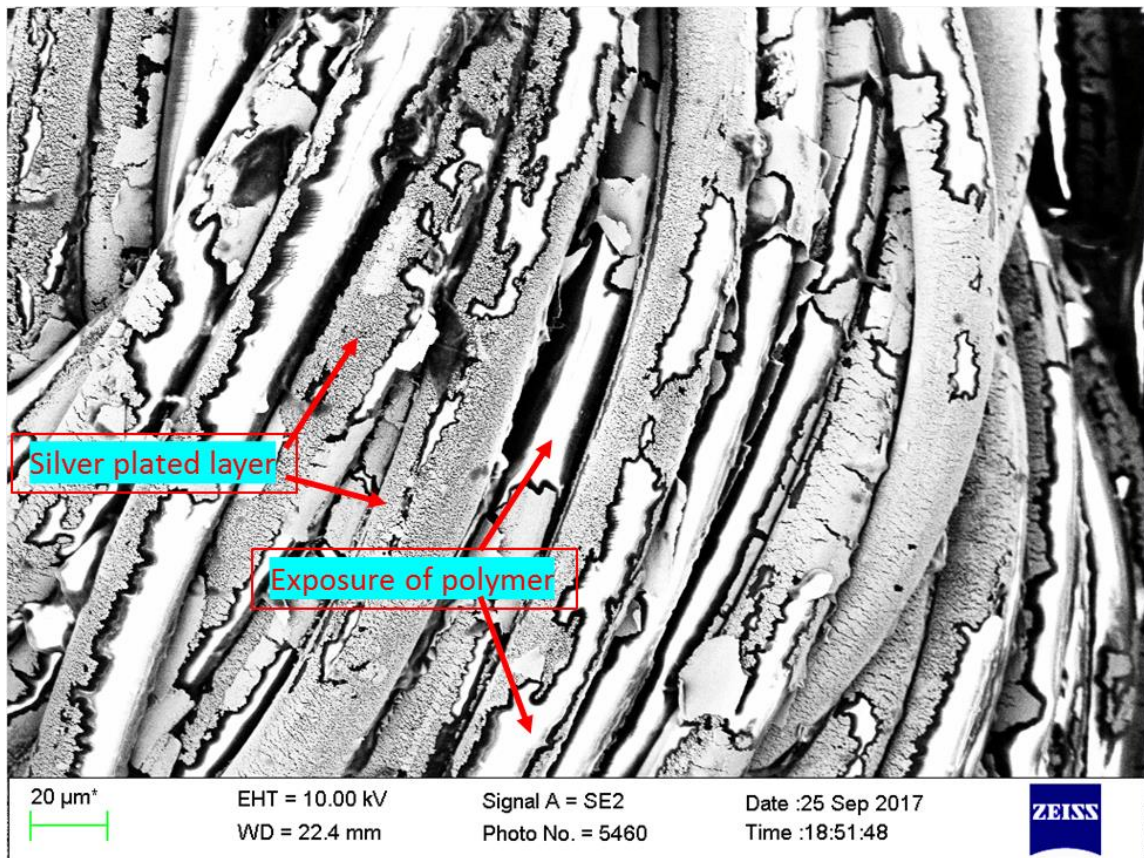


Figure 2.4. SEM image of the defected 1-ply TCP muscle from silver-plated sewing thread.

First, the fabrication approach of a mandrel-coiled muscle without resistance wire is briefly discussed. To fabricate the muscle, a commercially purchased nylon 6 fishing line (EagleClaw 8lb, 80lb monofilament) with 860 μm diameter was selected as the precursor material. This precursor

fiber was converted to an artificial muscle by twisting and then wrapping the twisted fiber around a mandrel to form a coil. To accomplish this, the following muscle fabrication procedure was used, which is similar to that previously described [45]. One end of the fishing line was attached to the shaft of a rotational motor and the other end was suspended with a 500-gram weight, which was tethered so it could not rotate. The choice of this weight is important, because the fishing line tends to snarl prior to coiling under too little tensile load and break during coiling under excessive load. Then the muscle was obtained by wrapping the twisted, non-coiled fiber around a 1.6 mm diameter steel rod. In order to obtain inter-coil spacing and set the structure, the sample was fixed at constant length for heat treatment. While tethering the two fiber ends so that untwist could not occur, the coiled fiber was thermally annealed for 1 hour and 30 minutes at 180 °C to set the inserted twist. The final outer diameter of the coiled fiber was 3.3 mm.

As a non-conductive material, a fishing line muscle can be actuated via the hydrothermal actuation method; however, the method requires multiple heating components like hot water reservoir and fluid pump [56]. This method is not as convenient as electrothermal actuation. In a related work, Semochkin introduced a device for producing TCP muscles from nylon 6 fishing line and copper wire with a diameter of 140 μm [19]. Instead of silver plating or deposition of nanotube sheet around the fishing line, twisting the resistance wire and fishing line together directly is also used to produce artificial muscles. Xiang et al. [57] demonstrated a new SMA-Fishing-Line actuator by twisting shape memory alloy (a diameter of 140 μm) and fishing line (a diameter of 520 μm). Weijde et al. [58] fabricated a TCP muscle by twisting a 200 μm diameter iron wire. Following the same approach, Arakawa et al. [59] also produced nylon thread with a 200 μm diameter nichrome wire. However, the resistance wire should have negligible mechanical

effect on the actuation of the substrate fishing line fiber, for this purpose, a thin resistance wire with a diameter $80\ \mu\text{m}$ is selected as conductive material. During the twist insertion procedure, the resistance wire (the tensile strength 690 Mpa) broke frequently due to the twist insertion into the resistance wire. Our unique approach is to incorporate the resistance wire around the twisted fiber without adding any twist to the resistance wire.

Here, the new manufacturing method to produce mandrel-coiled TCP muscle with resistance wire is discussed. In general, the incorporation of a heating element will provide the advantage of convenient electro-thermal actuation by Joule heating. The novel fabrication setup can yield a better actuator, for several reasons. First, it will enable the actuation of TCP muscle from fishing line (nonconductive) via electro-thermal actuation. Second, without adding twist to resistance wire enables the use of a very thin resistance wire. If twists were inserted into the resistance wire, the resistance wire would break during the fabrication procedure. This is one of the main reasons why we avoid adding twist in the resistance wire. Third, the fabrication process using very thin resistance wire will have negligible mechanical effect on the actuation of the actuation stroke. Lastly, the resistance of TCP muscle will no longer change significantly with the increase of temperature. The aim of the developed device is to facilitate the fabrication of mandrel-coiled muscle with resistance wire. The materials consist of a monofilament nylon 6 precursor material ($860\ \mu\text{m}$ diameter Eagle Claw monofilament fishing fine) and nickel chromium wire with $80\ \mu\text{m}$ diameter (Stock number: 8880K87 from McMaster.com). It is difficult to wind the resistance wire around the fishing line manually. Using the nickel-chromium wire to heat the fishing line muscle requires uniform and extensive surface contact between the fishing line and heating wire without sacrificing the mechanical properties of the fishing line itself. This challenge can be addressed by

wrapping a very thin nickel-chromium wire around the precursor material in a small pitch at a constant speed. The easy-to-form nickel chromium alloy wire can act like a soft bend-and-stay wire so that it can provide a conformal conductive layer.

The home-made experimental setup in Figure 2.5 is made of commercial available electronic and mechanical components, which enables others to replicate and use the device easily. The setup consists of 3 stepper motors, one linear motion slide and one carriage which will guide the wrapping of heating wire. Namely, three stepper motors NEMA 17 (holding torque 55 N.cm), Nucleo-F401RE development board, Nucleo-IHM03A1 stepper motor driver expansion board, and one power supply (Model: Topward 6306A) are the electronic components. There are mainly four steps involved in producing the mandrel-coiled fishing line muscle. The first step is to insert twist into the precursor material. The second step is to wind the heating wire around the twisted fiber. The third step is to wrap the twisted fiber with heating wire around a mandrel. The final step is to lock the shape of the muscle by annealing at around 180°C in a furnace.

2.3.1 Twist Insertion

For fabricating the muscles, a certain length of fishing line needs to be cut to fit the traveling range of the linear motion slide. For the setup, a 145-cm long fishing line was cut from the pool of the fishing line. One end of the fishing line was attached to the top stepper motor 1(MT1) using a safety pin, while the other end was suspended with a 500-gram load to keep the fiber under tension. Besides the load, a stopper, which can prevent the fiber from untwisting, was also placed at the bottom of the load. Subsequently, the motor was turned on to rotate in the direction in which the right-hand fingers curl when the right thumb points upwards to MT1. During this process of twist

insertion, the fiber was twisted and shrunk in length, and as a result, the load moved up. The motor was stopped, and the process ended when the first coil formed along the fiber.

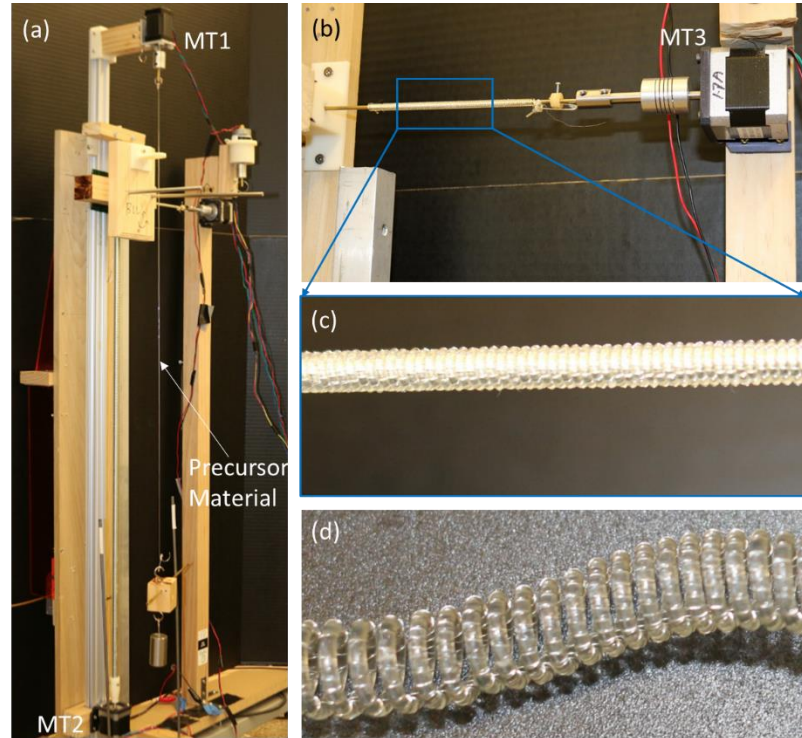


Figure 2.5. (a) The home-made experimental setup; (b) Forming the mandrel-coiling muscle from twisted fiber with heating wire wrapped around via the rotation of the stepper motor. (c) The magnified view of the muscle in (b); The resulting mandrel-coiling muscle after annealing.

2.3.2 Incorporation of The Resistance Wire

The next step is to incorporate the resistance wire into the muscle by wrapping the nichrome around the twisted fiber as shown in Figure 2.6(a). In this step, the stopper used in the previous step was removed, and a new untwisted precursor fishing line fiber was attached to the bottom of the twisted fishing line fiber. The 500-gram load was released from the twisted fiber and attached to the bottom of the new untwisted fiber. The length of the new untwisted fiber was determined such that the attached load would be in contact with the ground to secure and also enable the rotation of the

twisted fiber to wrap the heating wire around the fiber. The carriage on the linear motion slide driven by MT2 was moved to the starting position, which was close to MT1. Next, the resistance wire pool was placed on the pool holder. One end of the heating wire was then attached to MT1. The resistance wire was routed around a guide rod. A 20-gram load was hung on the heating wire to keep it taut during the wrapping process, and provide a uniform and constant wrapping angle. MT1 was rotated following previous direction and the carriage on the linear motion slide started to move downwards slowly at a constant speed, thereby creating a uniform wrapping of the heating wire around the twisted fiber. The pitch in the wrapped heating wire could be adjusted by controlling the rotating speed of the top MT1 and bottom MT2.

2.3.3 Mandrel Coiling

The third step is to wrap the twisted fiber with resistance wire around a mandrel as shown in Figure 2.6(b). After incorporating the nichrome wire, the weight at one end of the twisted fiber was maintained, and the safety pin attached to the other end of the fiber was passed through a hole in a locker located at the end of the mandrel close to MT3 so that the twisted fiber is firmly attached to the rod. Once the muscle was fixed at one end of the rod, the motor (MT3) was turned on to allow the twisted fiber to wrap or coil around the mandrel. In this step, the rotating direction of MT3 determines whether the fabricated muscle contracts or expands. If MT3 rotated in the same direction as the direction of twist, then the muscle would contract along the lengthwise direction when heated. On the contrary, if MT3 rotated in the opposite direction, the muscle would expand along the lengthwise direction. Additionally, in this step, the diameter of the rod determines the spring index of the muscle. Therefore, by changing the diameter of the rod, muscles of different diameters and spring indices could be created.

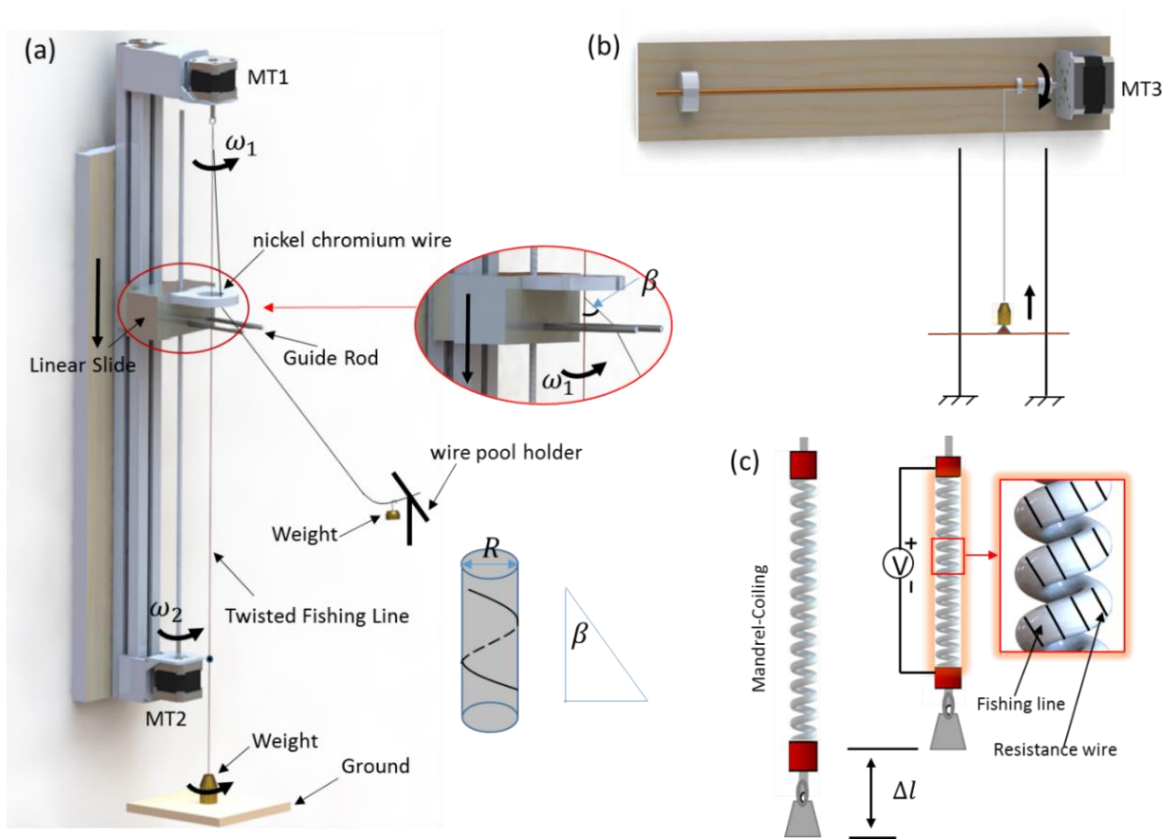


Figure 2.6 Schematic diagram of the developed muscle fabrication. (a) Wrapping the resistance wire around the twisted fiber. (b) Forming the mandrel-coiling muscle from the twisted fiber with resistance wire as made in (a) by wrapping it around the rod. (c) The working principle of the muscle; Left of (c) the muscle at rest when hanging a weight to the bottom; Right of (c) the muscle contracts upon receiving Joule heat.

2.3.4 Thermal Annealing

The final step is to retain the shape of the muscle by annealing the muscle in a furnace. After the twisted fiber with the nichrome wire was uniformly wrapped or coiled along the rod, the rod was detached from MT3 and placed in an aluminum frame to keep intact during annealing. To prevent the unwrapping of the fiber, two clamps were used to fix both ends of the muscle. The furnace was preheated to 180°C and the whole frame was then kept in the furnace for one and half hours. The annealing temperature depends on the chosen fiber, and should be above the maximum actuation

temperature, but below the melting point (around 250°C). Figure 2.6(c) shows the working principle of the fabricated muscle. The muscle contracts once it receives the Joule heat via electrothermal actuation.

2.4 Experimental Methods of TCP Muscles' Characterization

2.4.1 Isotonic Test of TCP Muscle

An experimental setup was developed to characterize the actuation behavior of twisted and coiled polymer muscle (TCP muscle) from multifilament silver-plated sewing thread, and mandrel-coiled muscle from monofilament fishing line under different load conditions and different temperature in isotonic test. Here, the experimental setup was briefly described.

For TCP muscle (silver-plated sewing thread, Joule-heat actuation), the experimental setup consists of laser displacement sensor (Keyence LK-G152), a power supply (BK Precision 1687B), linear motion stage, National Instruments data acquisition system with a computer interface and LabVIEW program. Schematic diagram of the experimental setup is shown in Figure 2.7. TCP muscle with ring terminals was attached to the one end of the linear motion slide. A reflecting tape was attached to the rectangular holder mounted on the other end of the linear motion slide. Then laser sensor position was adjusted to detect the linear displacement of the linear motion slide which reflects the lengthwise contraction of TCP muscle upon heating. The state vector input and output, namely voltage, current, temperature and displacement were connected to the NI DAQ for further data analysis. The sampling rate was set as 1k Hz in the experiment. The time domain response of displacement and temperature for various input power was measured using the laser displacement sensor and thermal couple respectively. The experimental data was measured by varying the power

input and the attached load. The power input waveforms were programmed and defined in a power supply (BK Precision 1687B). Here and elsewhere, input power is the peak electrical power given per length of muscle under loaded condition. Tensile actuation was calculated as the ratio of the amount of contraction to the loaded length of the muscle.

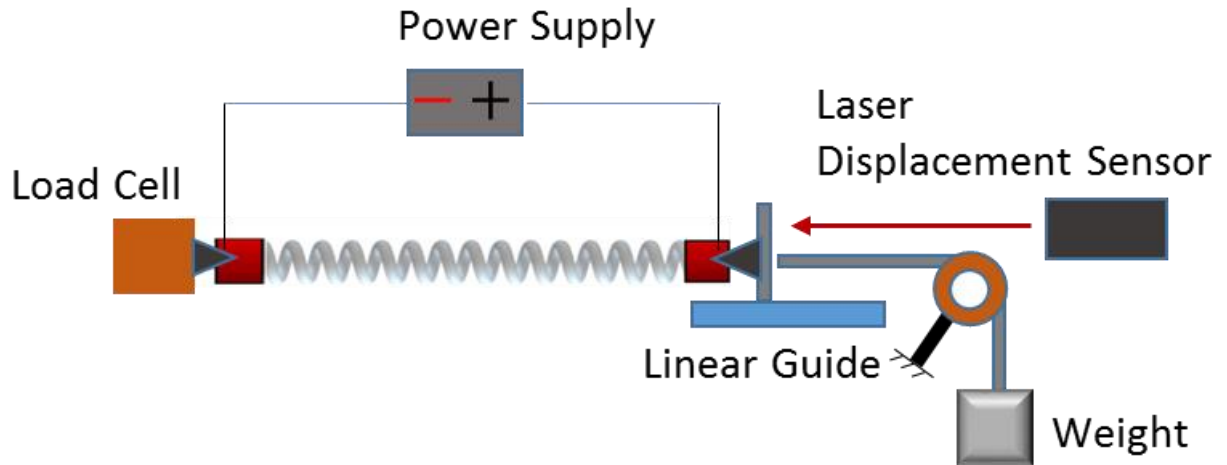


Figure 2.7. Schematic diagram of the experimental setup for characterization of the Fishing Line TCP muscle in isotonic test.

For TCP muscle (Mandrel-coiled fishing line muscle, hydrothermal actuation), the experimental setup used for characterization of actuation is described here. A block diagram of the experimental setup is shown in Figure 2.8. The coiled fishing line muscle was tethered via a crimp. One terminal of the muscle was attached to the support while the other end was pre-strained with the load. A black tape was glued to the dead weight for tracking purpose. In this experiment, the muscle with a 128-mm length was used for the test and a syringe was used to inject hot water through a tube where the muscle is housed and inject cold water (coolant) to reverse the actuation. A fast camera (Phantom Miro eX2) was used to record the linear displacement of the coiled fishing line muscle.

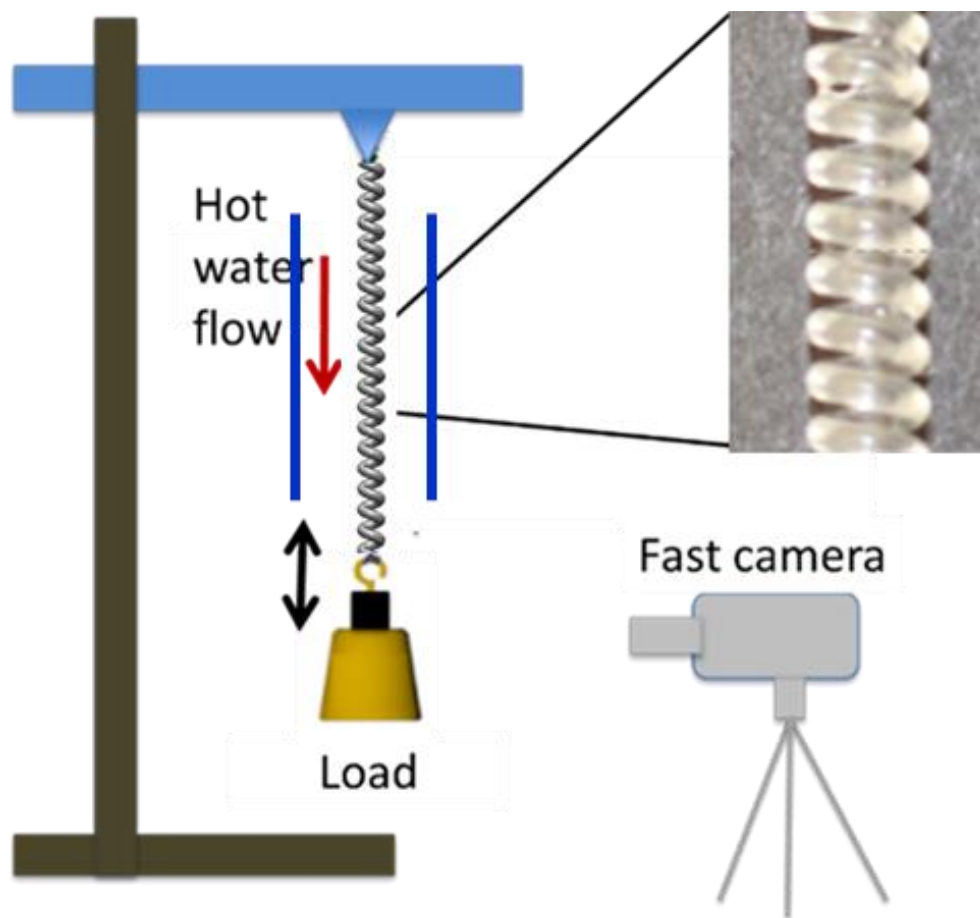


Figure 2.8. Schematic diagram of the experimental setup for determining the characterization of the muscle and in the detail an optical micrograph of a 3.33-mm-diameter coil formed by inserting twist in the 860- μm -diameter monofilament fiber and wrapping the twisted, non-coil fiber around a 1.6 mm diameter steel rod.

2.4.2 Spring-load Test of TCP Muscle

The performance of TCP muscle in varying load condition is also of interest for practical application. In most of the practical applications, the load is not always constant. The isotonic test will only give a direct understanding of the performance of TCP muscle in the constant load condition. Thus, this section, presents the design of the experiment to characterize TCP muscle in a spring-load condition where the muscle works contract against a linear spring. The experiment

also gives an idea how much force the TCP muscle generates. The experimental setup used for spring-load test is depicted in Figure 2.9. The setup also consists of laser displacement sensor (Keyence LK-G152), a power supply (BK Precision 1687B), linear motion stage, National Instruments data acquisition system with a computer interface and LabVIEW program. Unlike the isotonic test, the muscle in this test experiences variable load instead of constant load. The tensile actuation is highly dependent on the selection of the linear spring. The aim of choosing an appropriate spring is to reproduce the load condition from the practical application. In order to investigate the effect of pre-stress on the mechanical performance of TCP muscle, the position of the load cell can be adjusted to provide different pre-stress for this purpose.

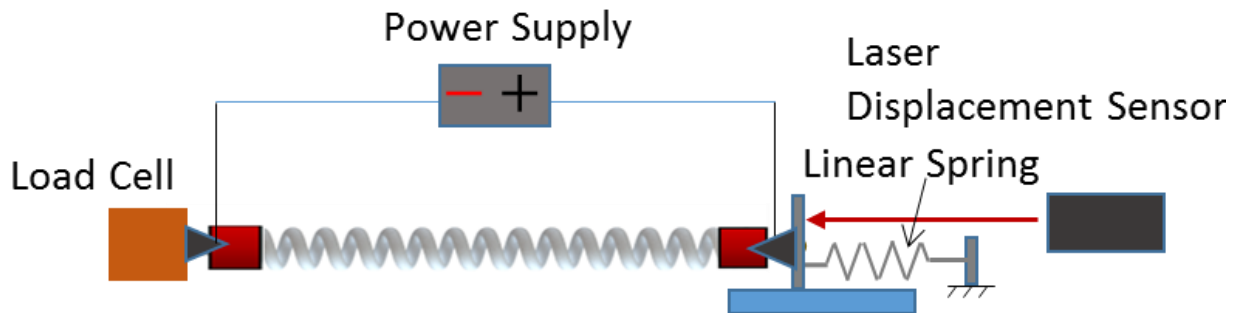


Figure 2.9. Schematic diagram of the experimental setup for characterization of the Fishing Line TCP muscle in spring-load test.

2.5 Modeling of The Electrical Resistance of 1-ply TCP Muscle

The twisted and coiled polymer (TCP) muscle possesses many physical properties, such as large reversible contraction capability and high mechanical power output. The other advantages of TCP muscle are easiness of fabrication, low-cost precursor material, diverse actuation strategies, and long-life cycles. Electro-thermal actuation is one of the popular convenient ways to deliver Joule heating to actuators. The precursor material nylon 6 sewing thread fiber comes with a silver-plated

layer. This silver-plated layer enables current to pass through the fabricated muscle, resulting in heat generation within the muscle. Thus, the investigation of the resistance of TCP muscle is of great interest for control purpose and development of TCP based sensor.

Sensor is a potential application of TCP material. Sensors can be categorized as mechanical sensor [60, 61], thermal sensor [62, 63], and chemical sensor [64, 65] according to their sensing criteria. A self-sensing capability can enable the development of TCP muscle as a sensor [49]. A self-sensing feature will also enable closed-loop control system, eliminating the extra cost of an off-board sensor. To address the control issue of TCP muscle, rapidly increasing efforts have been carried out [57, 66-69]. However, the self-sensing properties of TCP muscle hasn't been explored widely. In addition, the discussion of changes in resistance of TCP muscle during electro-thermal actuation has received little attention. Weijde et.al [49] explored the possibility of deploying the twisted and coiled polymer muscle as a sensor based on its self-sensing capability. The sensing principle was based on self-sensing via electrical impedance to predict the deflection, force and temperature. The experimental results revealed the suitability of the sensing principle in the Joule-heated twisted and coiled polymer muscle. In [70], Zhao and Abbas investigated the TCP muscle application as a sensor by embedding it into a 3D printed soft manipulator to create a soft sensor. Basically, the authors characterized the relationship between the resistance and displacement of the TCP muscle under non-actuated state.

In this section, the study on resistance change of 1-ply TCP muscle is described. The aim is to investigate the change of electrical resistance of TCP muscle at different actuated state via a series of experiments and to propose a geometrical model to better understand the self-sensing principle of TCP muscle. The TCP muscle was produced in a similar manner as in [71], and 1-ply muscle,

the simplest spring structure was chosen for the study in this work, to eliminate the complex structure of 2-ply TCP muscle and avoid the inter-lock of coils for simplification purpose.

2.5.1 Muscle Preparation (1-ply TCP Muscle)

Different kinds of materials listed in supplementary material of [45] can be used to fabricate the TCP muscle, among which fishing line and sewing thread are commonly used due to their convenient availability. In this study, a conductive sewing thread from Shieldex Trading, Inc. (Shieldex PN#260151023534oz, nominal diameter of 0.2 mm, electrical resistance of 0.50 Ω /cm, 136 number of filaments and linear density of 1.3 mg/cm) was selected as the precursor material. The precursor material has multifilament nylon 6,6 plated with silver.

In this study, the electrical resistance of a 1-ply TCP muscle during actuation was studied. TCP muscles were fabricated via directly over-twisting the precursor materials following the approach in Figure 2.1. The muscles were annealed electro-thermally (Joule heating) under a 200-gram weight via delivering electrical power to the muscles from a power supply. The selection of power has a critical effect on the performance of TCP muscle. The value of power input determines the magnitude of temperature rise in the muscles and hence the actuation strain of the muscle. The last step to complete the fabrication is to train the muscle at the target load condition for intended applications. When TCP muscle exhibits consistent actuation strain, the TCP muscle is considered ready for further test.

2.5.2 Experimental Method

To characterize the electrical resistance change and understand the performance of the 1-ply TCP muscle, here several tests were carried to acquire data on temperature, displacement, force, voltage

and current of the TCP muscle. The relationship among those state variables of TCP muscles can be described in Figure 2.10. The power input (here the constant current) determines the temperature rise during the heating time. The heat is the driving source for the TCP muscles, thus temperature variation will determine the resistance change, the pulling force and the actuation stroke. The pulling force and actuation stroke will influence each other depending on the target external load condition. Electrical resistance is mainly affected by temperature and actuation stroke which affects the structure of the TCP muscle. The simplified schematic diagram of the experimental setup is shown in Figure 2.9. The experimental setup consists of 4 parts: a programable power supply, a characterizing system (sensors and pre-load), a device to measure the voltage and current, and a data acquisition system. The muscle here works against a linear spring with a stiffness 50 N/m. In this study, 1-ply TCP muscle with a diameter of 0.8 mm (twisting speed 600 rpm), were tested at different values of power. The ends of the TCP muscle were clamped using two ring circular 16-20AWG crimp (Digi-key # A118933CT-ND). Then one crimp was connected to the linear guide which was connected to the linear spring. The other crimp was connected to the force sensor. The loaded length at the stretched state under a 0.26 N pre-stress is 129 mm. Electrical resistance was calculated based on Ohm's Law. A type-E thermocouple was also added to the 1-ply muscle (close to the middle point of the muscle) to measure the temperature rise during the heating stage and temperature decrease during cooling stage. The tests were performed at different values of power. In each experiment, constant current input was applied to the TCP muscle to generate the heat, and the current was varied from 0.15 A to 0.42A, with an incrementation of 0.03A. For each experiment after switching current input, the muscle was trained in the new power setting to obtain consistent actuation strain. Each test has 3 continuous cycles.

For all experiments, the power-on time (heating time) was 14 s and the power-off time (cooling time) was 30 s (duty cycle 32%), a period of total 44 s. The experimental data was synchronized and stored in the master PC.

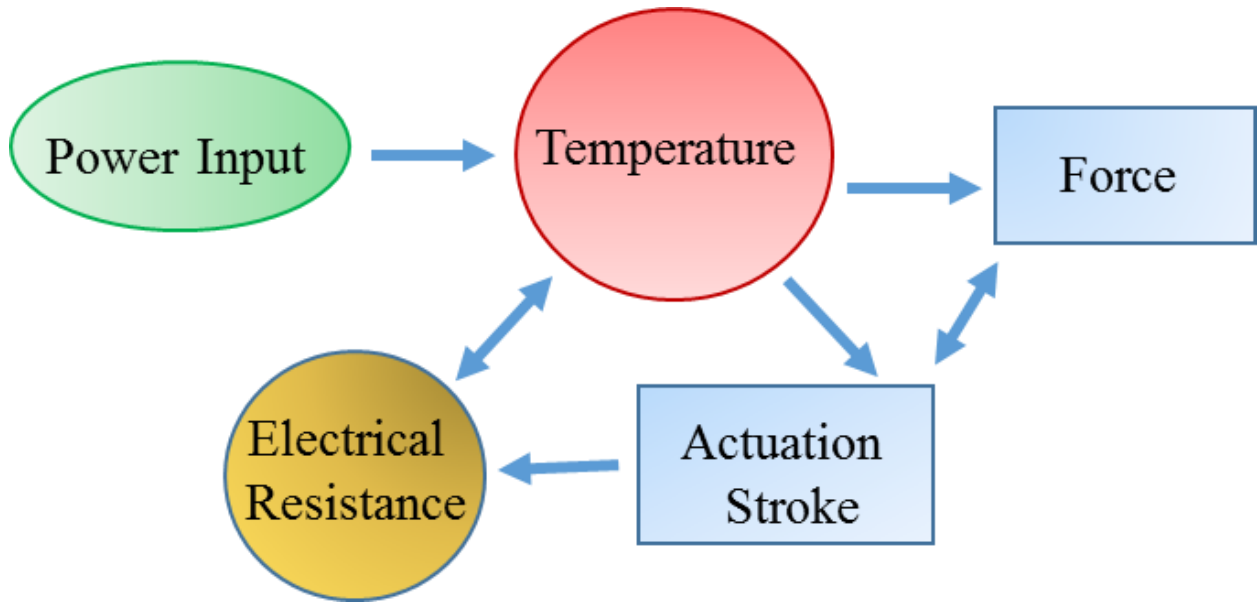


Figure 2.10. The relation among the state variables of TCP muscles

2.5.3 Experimental Results and Discussion (1-ply TCP Muscle)

In this section, first the experimental results are presented and analyzed, and current different approaches to model electrical resistance properties of TCP muscle will be discussed. The last discussion focuses on a geometrical model to explain the variation of the resistance change in TCP muscle under actuated state. Figure 2.11 shows the measured parameters of TCP muscle during actuation. As shown in Figure 2.11(a), the current input is set as a constant value and the sequence of the step current was programmed in the power supply. The voltage in Figure 2.10(b) shows the measured voltage between the two ends of the TCP muscle. Figure 2.11(c) illustrates the temperature variation measured from the surface of TCP muscle. As seen in Figure 2.11(d), the

pulling force of the TCP muscle during actuation is measured from the load cell. Figure 2.11(e) shows the displacement of the TCP muscle in the test.

Figure 2.12 shows the electrical resistance change in the time domain. The result reveals that the electrical resistance of TCP muscle experienced a very significant change. It can also be observed that the significant change of resistance of TCP muscle is highly repeatable during the change of temperature within the three cycles in the test. In [57, 67], the electrical resistance is treated as a constant value. In [49], the electrical resistance is assumed to have the following form:

$$R(\Delta x, T) = \rho_x \Delta x + \rho_T T + \rho_0 \quad (2.1)$$

Where ρ_x , ρ_T are coefficients for displacement Δx and temperature T , and ρ_0 is a constant value. Referring Figure 2.12, the resistance profile at the step current of 0.15A, 0.18A, 0.21A and 0.24A can use the equation 2.1 to describe the changes. However, starting from the case of current 0.27A to 0.42A, the resistance experienced a peak value and then decreased after the peak value. Here a geometrical model as shown in Figure 2.13 was provided to explain the phenomena of resistance change.

From the literature, it was reported that the electrical resistance of TCP muscle can be used to predict the strain [70]. However, the challenge of using the self-sensing capabilities arises from the fact the nonlinear relationship between electrical resistance, temperature and actuation strain, especially within high temperature range. Here the aim is to explain the underlying process behind the change of electrical resistance. The geometrical model as shown in Figure 2.13 can help describe the structural change of the TCP muscle to understand the phenomena of resistance change. As shown in Figure 2.13, the 1-ply muscle undergoes a structure change during heating stage. In Figure 2.13(a), the TCP muscle is pre-stretched to a point at a certain pre-tension,

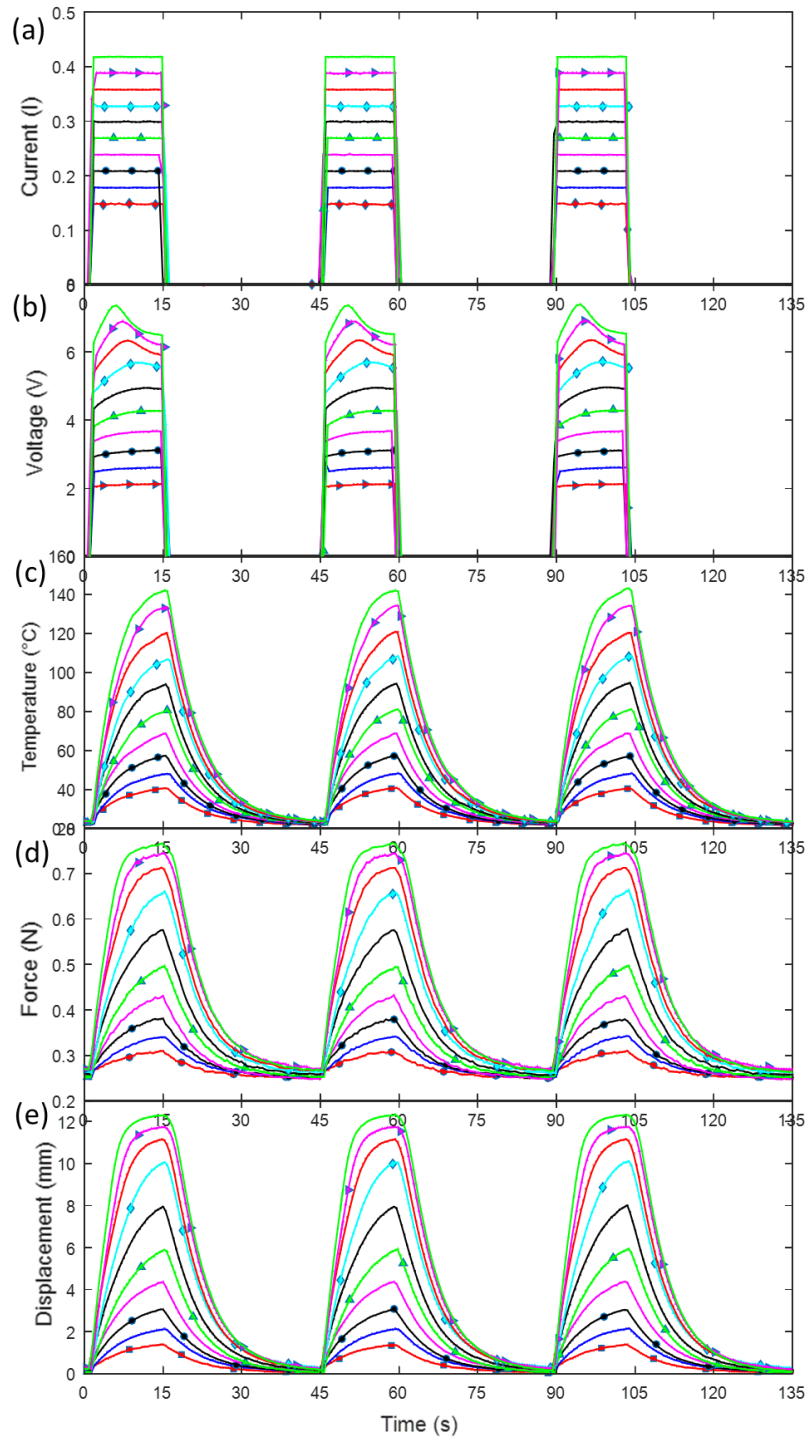


Figure 2.11. The measured parameters of 1-ply TCP muscle from silver-plated sewing thread (a diameter of 0.8 mm and a length of 129 mm measured under a 0.26 N pre-stress) including current (a), voltage (b), temperature (c), force (d) and displacement (e).

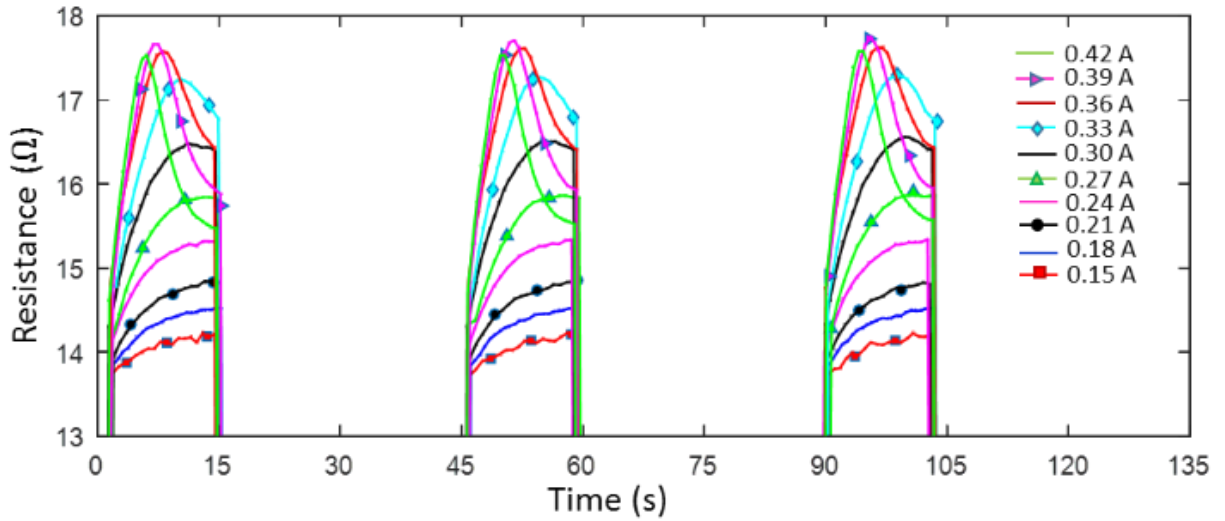


Figure 2.12. The resistance profile of 1-ply TCP muscle in the time domain.

resulting in a gap between neighboring coils. As the TCP muscle is stretched, the gap will increase and the average cross section area will decrease. There is no direct contact between neighboring coils. In this stage, the TCP muscle can be treated as an electrical wire which has a diameter of d_1 in a spiral structure. Once the TCP muscle receives Joule-heating, the temperature arises and the muscle starts to contract in the lengthwise direction. The gap of neighboring coils will decrease until the temperature reaches T_c (contact temperature), when the coils touch each other. After the coils start contacting with each other, the TCP muscle can be assumed as an electrical wire with a diameter of D_2 . After the temperature goes above T_c , the muscle expands in a radial direction and the contact between neighboring coils is become more extensive and sufficient. At this point, a saturation of contraction occurs in the TCP muscle as there is no more space for the longitudinal shrinking. The TCP muscle can be treated as an electrical wire with a diameter of D_3 . The above-mentioned structure evolution may explain why equation 2.1 does not hold true at very high temperature as shown in Figure 2.12.

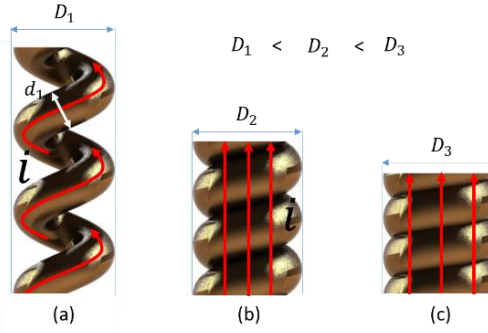


Figure 2.13. Geometrical model of a 1-ply TCP muscle. (a) the stretched coils under a certain pre-tension, and the current travels in a route as indicated by the red lines. (b) the coils start contacting with each other at the temperature T_c and the current travels in a direction as indicated by the red lines. (c) the swelling state of TCP muscle after the temperature reaches over T_c and the current passes through TCP muscle as shown in the red lines.

2.5.4 Thermomechanical Characterization of 1-ply TCP Muscle

Based on the measured state variables of the 1-ply TCP muscle, Figure 2.11 shows the temperature profile shifts upwards with the increase of power, as is true for displacement and force profile, indicating the temperature is the key driving source for the TCP muscle. Here, the thermo-mechanical model and thermo-electric model were further developed based on the prior works reported in [57, 72] to identify the relationship among all the state variables of the TCP muscles, which consist of displacement, force, temperature, voltage, and current. Using the following thermo-mechanical model equation, the force, displacement, temperature and initial force/pre-stress can be correlated.

$$F = kx + b\dot{x} + c(T - T_0) + F_0 \quad (2.2)$$

where k is the equivalent stiffness of the serially connected TCP muscle at the actuated state and the linear passive spring, x is the measured displacement of the TCP muscle in the test, b is the damping factor of the TCP muscle, \dot{x} is the moving speed of TCP muscle, and c is the thermal

constant. T_0 and F_0 are the initial TCP temperature which is the room temperature and the pre-stress of the TCP muscle in the test. k is determined using the linear fit between the force and displacement profile shown in Figure 2.11 and has a value of 40 N/m. The value of b is set as 0.7 N · s/m within the range in the reference [67]. For the case of test at current 0.42A, c is determined by fitting the experimental data of force vs displacement and has a value of 0.1 mN/°C, then c is used in the rest of tests.

Equation 2.2 can be solved using forward Euler method, and the form of equation 2.2 can be rewritten as

$$F_n = kx_n + b \frac{x_{n+1} - x_n}{\Delta t} + c(T_n - T_0) + F_0 \quad (2.3)$$

$$\Delta t = t_{n+1} - t_n$$

The displacement can be described by rearranging equation 2.3 into the following:

$$x_{n+1} = x_n + (t_{n+1} - t_n)[F_n - F_0 - c(T_n - T_0) - kx_n]/b \quad (2.4)$$

From equation 2.4, the simulated displacement can be predicted from the force and temperature profiles. Figure 2.14 presents the comparison between the simulated results and experimental data. The simulation was performed through all the 10 group of experiments where the step current started from 0.15A to 0.42 A, with an equal incrementation of 0.03A. All the state variables of TCP muscle were obtained from synchronized measurement. A remarkable feature in Figure 2.14 is that the simulated results are in a very good agreement with the experimental data. The maximum error occurs at the current of 0.24A. This result indicates that the developed model can govern and predict the dynamic behavior of 1-ply TCP muscle in a very good manner in the test rig shown in Figure 2.9.

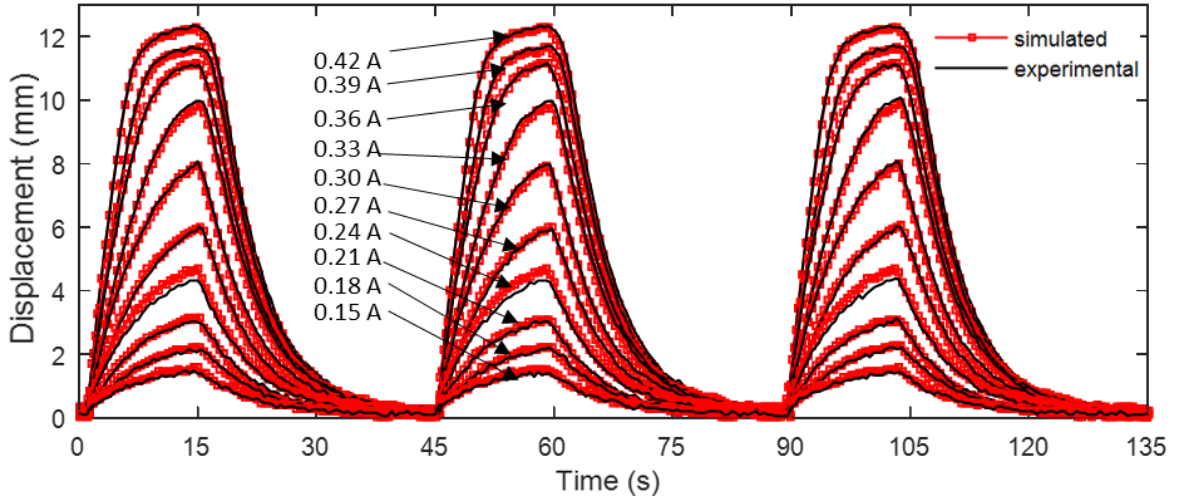


Figure 2.14. The comparison of displacement between simulated results and experimental data.

2.5.5 Thermoelectric Characterization of 1-ply TCP Muscle

In the study, step currents passing through the silver-plated TCP muscle result in elevation of temperature. Temperature can be modeled using the following thermo-electric equation.

$$\frac{dT}{dt} = K_1(T_0 - T) + K_2U(t)I(t)$$

$$K_1 = \frac{hA_c}{mC_p} \quad (2.5)$$

$$K_2 = \frac{1}{mC_p}$$

K_1 and K_2 are the model parameters, which need identification from experiments. h is the convective heat transfer coefficient, A_c is the surface area of the 1-ply TCP muscle. m is the mass of the 1-ply TCP muscle. C_p is the specific heat capacity of the 1-ply TCP muscle. The parameters used are listed in Table 2.2. K_1 is estimated from parameters C_{th} and λ in [67] and determined by fitting the simulated results with experimental data. K_2 is obtained by trial and error.

Table 2.2. Model parameters of K_1 and K_2 for all tests.

	Step Current (A)	K_1	K_2	Max Temperature (°C)
Test 1	0.15	0.145	10.1	41
Test 2	0.18	0.145	9.6	48
Test 3	0.21	0.145	9.3	57
Test 4	0.24	0.145	9.0	69
Test 5	0.27	0.145	8.7	81
Test 6	0.30	0.145	8.3	94
Test 7	0.33	0.145	7.9	108
Test 8	0.36	0.145	7.6	120
Test 9	0.39	0.145	7.5	134
Test 10	0.42	0.145	7.1	142

Following the similar approach, equation (2.5) can be rewritten as

$$\frac{T_{n+1} - T_n}{\Delta t} = K_1(T_0 - T_n) + K_2 U_n I_n \quad (2.6)$$

$$T_{n+1} = T_n + (t_{n+1} - t_n)[K_1(T_0 - T_n) + K_2 U_n I_n] \quad (2.7)$$

Equation (2.7) was utilized to predict the temperature based on voltage and current profiles. Figure 2.15 shows that the simulated results of temperature match the experimental data with a very high accuracy. The maximum error occurs in the case of current at 0.42A, above which the TCP muscle may get damaged. The high current results in a very high temperature in the 1-ply muscle and may initiate the structural change within the muscle that might cause the error. Therefore, the thermo-electric model can be utilized to characterize the behavior of TCP muscle. In this model, the power input was calculated in a way to avoid using the electrical resistance.

2.5.6 Summary on The Study of Electrical Resistance of 1-ply TCP Muscle

In this section, a group of 10 experiments by varying the step current was performed to investigate the resistance change of 1-ply TCP muscle and to generate high quality data from carefully

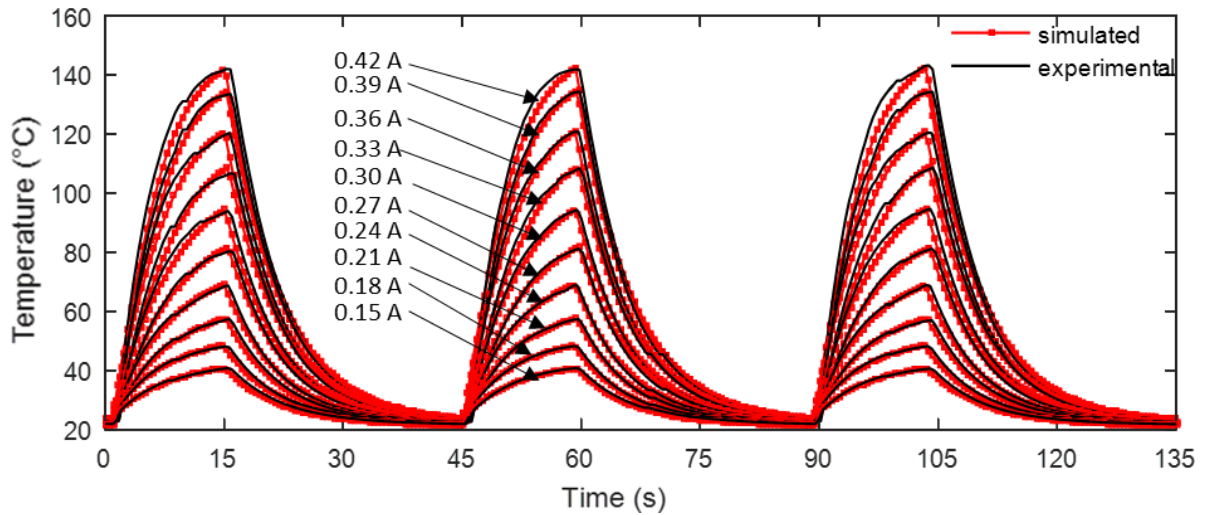


Figure 2.15. The comparison of temperature between simulated results and experimental data.

designed characterization setup. All the state variable of TCP muscle including current, voltage, temperature, force and displacement were collected from the experiments. A thermo-mechanical model and thermo-electric model were investigated and validated using the obtained experimental data. In the models, the mechanical performances (force and displacement) of 1-ply TCP muscle are determined by the rise in temperature of the muscle and the load condition. The temperature is determined by the resistance, power magnitude, heat transfer coefficient and specific heat capacity. The comparison between simulated results and the experimental data using those two models shows a high degree of accuracy. The resistance profile of 1-ply TCP muscle obtained from the experiment was also presented. A geometrical model was also presented to describe the structural change of the TCP muscle to understand the phenomena of resistance change.

2.6 Summary

In this chapter, the fabrication methods of twisted and coiled polymer (TCP) muscles were presented and discussed. Two categories of self-coiled and mandrel-coiled TCP muscles are

explained. TCP muscle from the silver-plated multifilament nylon 6,6 sewing thread fiber are usually made using self-coiled method. The silver-plated layer of the sewing thread fiber enables current to pass through the muscle via electro-thermal actuation. The nonconductive monofilament nylon 6 fishing line can be produced via self-coiled method as well as via mandrel-coiled method. Self-coiled muscles in general can produce higher pulling force and less tensile actuation than that of mandrel-coiled muscles. Among the actuation strategies, electrothermal actuation is widely used in silver-plated TCP muscles due to the easiness of delivering heat to muscles. To enable the electro-thermal actuation of nonconductive TCP muscles from fishing line, a novel experimental apparatus was developed to incorporate resistance wire into TCP muscles from fishing line. Isotonic test and spring-load test were designed to fully characterize the mechanical performance of different types of TCP muscles. The aim of isotonic test was to investigate tensile actuation against a constant load. The purpose of spring-load test was to explore the pulling force and tensile actuation against a linear spring. Further modeling of the electrical resistance of TCP muscle from silver-plated sewing thread was presented and discussed. A group of 10 experiments by varying the step current was performed to investigate the resistance change of 1-ply TCP muscle in spring-load test and to generate high quality data from carefully designed characterization setup. Thermo-mechanical and thermo-electric models were investigated and validated using the obtained experimental data. The comparison between simulated results and the experimental data using those two models shows a high degree of accuracy. The resistance profile obtained from the experiment was also presented and a geometrical model was proposed to describe the structural change of the TCP muscle to understand the phenomena of resistance change.

CHAPTER 3

A RECONFIGURABLE ROBOT WITH TENSEGRITY STRUCTURE USING NYLON

ARTIFICIAL MUSCLE

3.1 Introduction

The word tensegrity comes from “tensional integrity” [73] and comprises tensile (cables or tendons) and compressive (bars or struts) elements. Such compliant tensegrity structures are characterized by lightweight, easy deployability and mechanical stability. Tensegrity structure was initially studied in the 1960s [73, 74]. However, it was only in the last 19 years that researchers used the principles of tensegrity applied to robotics [75] with an ever-increased interest towards space applications [76]. Dynamic analysis, design problems and shape control for tensegrity structures were presented in review articles [77, 78]. A tensegrity structure always intends to reach an equilibrium configuration due to a balanced force between the tensile and compressive elements. Crawling [79] and rolling [80, 81] have been the most explored methods of locomotion used in tensegrity robots. When an external load is applied to a tensegrity structure, all components are exposed to axial force, where the struts bear compressive forces and the cables bear tensile forces. This enables the structure to have naturally compliant mechanism enabling the tensegrity structure to withstand an impact or survive from significant force by absorbing shock. Other advantages of those naturally compliant tensegrity structures or robots are: self-sustainability, lightweight, robust, energy-efficient and capable of wide-range of motions [82].

In a tensegrity robot, there are three methods of changing shapes: (a) deformation of a strut component, (b) deformation of a string component and (c) deformation of two struts, two cables

or a strut and a cable. Different ways of shape changing require different actuation technologies. In method (a), to change strut's length, various actuators such as pneumatic cylinders [83] or motors can be used [84, 85], which are responsible for altering the strut length to cause the deformation of the structure. In method (b), other possible physical designs involve different ways of changing the cable's length, such as dynamic cable twist, shape memory alloys (SMAs) [79, 86, 87], tendons driven by motor [88, 89], elastomers [90], which can be used to deform the effective rest length of the cables. In method (c), a redundant actuator is required to alter the distance between the two struts, two cables or a strut and cable.

3.2 Design and Method

In this section, the mechanical design of the tensegrity icosahedron robot will be presented. Icosahedron robot is a 6-strut robot with 24 tensional elements, whose shape resembles a sphere. The benefits of choosing the icosahedron shape are: (1) ability for rolling locomotion due to the spherical shape; (2) easiness of building due to the relatively simple structure; (3) reconfigurability of being folded into a flat shape as shown in Figure 3.1(c). Figure 3.1(a) shows the photograph of the tensegrity structure integrated with 2-ply TCP muscles, Figure 3.1(b) shows a zoomed portion of the TCP muscle and Figure 3.1(c) shows the collapsed state of the tensegrity structure when pressed by a hand.

3.2.1 Materials

The twisted and coiled polymer (TCP) muscle is made of sewing thread with a conductive silver coating. The conductive sewing thread manufactured by Shieldex Trading, Inc. (Shieldex PN#260151023534oz) was selected for the present study. 2-ply TCP muscles were annealed at

current 0.8A for 5 s under 500 g with 12 cycles and the training was done using 50 g weight and 12 cycles by applying current 1.8A for 1 s. Then after the muscles were assembled to the tensegrity, another 3 cycles of muscle training at pulsed power input of 1.8 A were applied to all the muscles to ensure the muscles have almost the same length and deliver consistent performance.

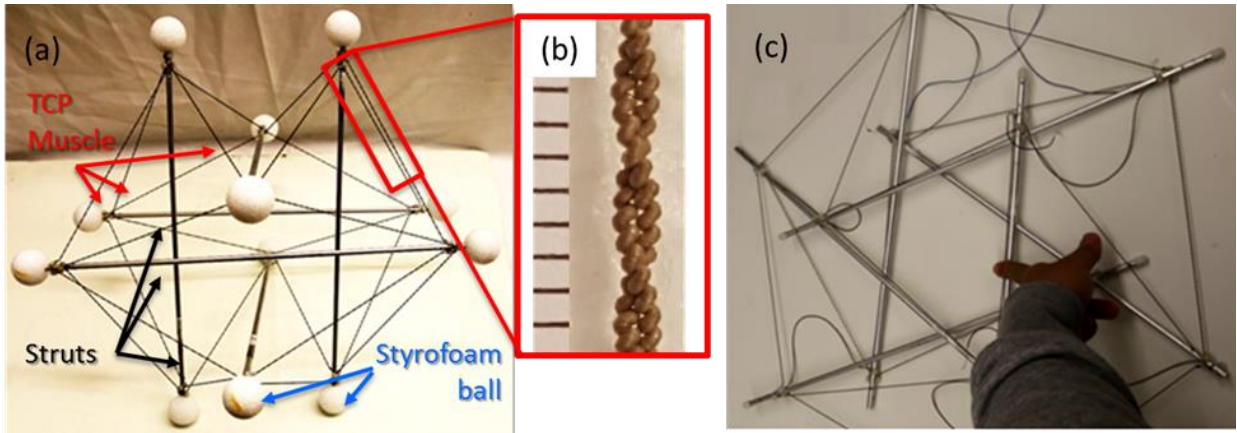


Figure 3.1. The tensegrity prototype: (a) The icosahedron tensegrity robot constructed with 2-ply muscles and aluminum struts; (b) The 2-ply TCP muscle magnified view and (c) The tensegrity after being folded into a flat configuration by pushing the structure downwards to the ground.

3.2.2 Strut Design

The tensegrity robot prototype consists of 24 TCP muscles and 6 rigid struts. The struts serve as compressive elements and determine the overall size of the structure. In the structure, the rod lengths are selected to have 420 mm in length and diameter of 5.6 mm. The aim is to provide large enough space for the payload at the center. Another reason for selecting an appropriate length is to have a relatively large shape deformation that is determined by the stroke of the actuators. The characteristic of the muscles will be discussed later. Generally, the contraction length is determined by the type of muscle, the muscle length and the load condition. A relatively large strut length

means, a relatively longer muscle required to make the structure, thereby generating relatively large structural deformation of the tensegrity robot.

The struts account significantly for the major mass of the structure, compared with the weight of actuators, nylon screws, nuts and washers. In other proposed structures, materials such as bamboo [91, 92], carbon fiber [84, 93] and wood [82] are chosen for the strut (rod) material. In order to form the basis of lightweight for the tensegrity structure while maintaining body size, aluminum tubes are selected as the rod materials. The benefits of choosing aluminum tubes include lightweight and easy machinability. Therefore, aluminum materials were used as the rod structure for the robot. The aluminum tubes were cut into the same length of 420 mm. Holes were created at the ends of the rod for muscle attachment.

3.2.3 Prototype

In order to develop a rolling tensegrity robot, firstly a modular tensegrity that is 3D printed was realized for rapid experimentation and the design of the system was carried out using CAD packages. Hence, in the first prototype, the rods of the structure were designed and fabricated entirely by 3D printing using the Stratasys Fortus 250mc 3D printer and Acrylonitrile Butadiene Styrene (ABS) material. The maximum part size the printer can handle is 10" × 10" × 12" (254 x 254x 305 mm), which limits the overall size of the structure. The ABS is a thermoplastic material with yield strength of 31 MPa and volume resistivity of 2.5×10^{15} - 5.0×10^{16} Ω -cm [31]. Another limiting feature of the Stratasys Fortus 250mc 3D printer is the size of the minimum printable feature, which is around 0.178 mm (0.007"), the size for the thickness of one layer of ABS Plastic. This restricted the amount of detail that can be produced. The strength of the hook at the end of the rod as shown in Figure 3.2 was not so strong, and it was broken quite few times. However, the

design helped study various configurations quickly and identify the issues associated with 3D printing for such robots.

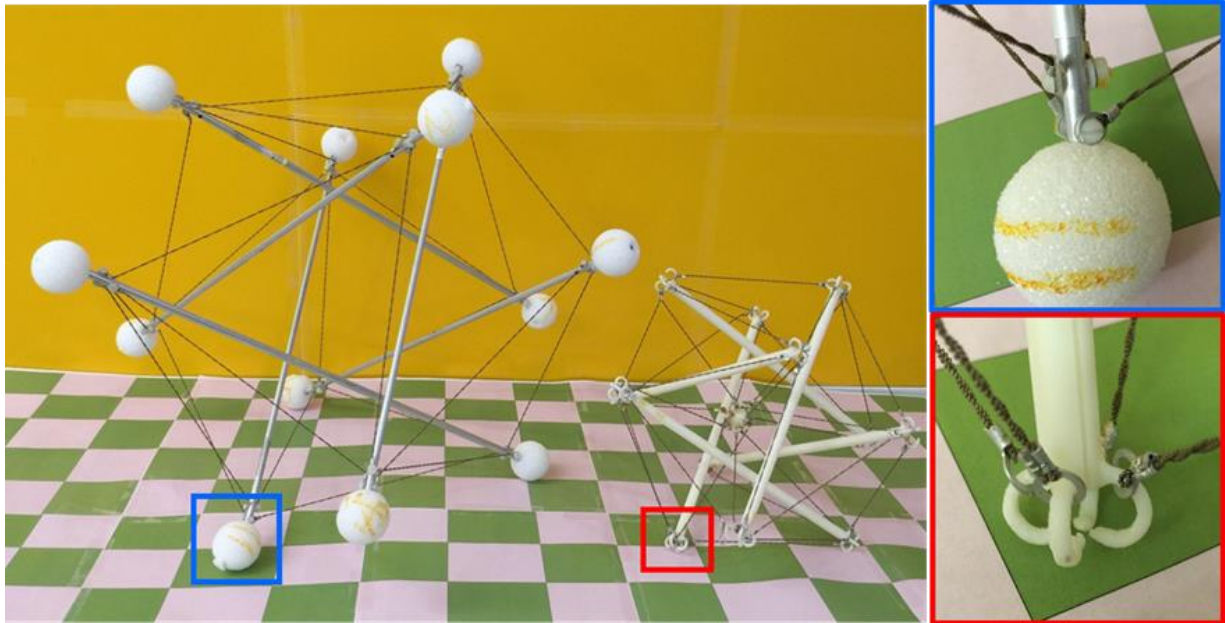


Figure 3.2. The two prototypes of a 6-strut tensegrity structure. Left: The second prototype made of aluminum tube and TCP muscles. Middle: The first prototype fabricated using 3D printer using ABS material. Left Top: The detailed view of connection in a vertex of the second prototype. Left Bottom: The detailed view of one end of the strut of the first prototype.

A lesson learned from the 3D printed tensegrity structure was that the hook was not practical for the tensegrity as it sometimes got broken, and not ideal for rolling motion due to the shape. The second prototype was made out of aluminum tube, 2-ply TCP muscles, nylon screws, nuts and washers as the mechanical components. Nylon screws, nut and washers were used to avoid short-circuit and, thus allow individual recruitment of the TCP muscles. Figure 3.2 shows the two prototypes of the tensegrity robots. The second prototype as shown in Figure 3.2 (left side), which is the focus in this chapter, has a total weight of 69 g. The structure has six struts of 420 mm in length are made of aluminum tube, and two styrofoam balls of diameter 36 mm were attached to

the both ends of each strut. TCP muscles are used as actuators and as cables. Selection of the muscles length and pre-tension are critical to the tensegrity performance. The muscles were fabricated and prepared with the same length. Then after the muscles were assembled to the tensegrity, another 3 cycles of muscle training at pulsed power input of 1.8 A were applied to all the muscles to ensure the muscles have almost the same length and deliver consistent performance. After the training, the muscle performance was measured again; the actuators generated a stroke of 12% at a pulsed actuation for 1 s. Each rod weighs 5 g and has a length of 42 cm. 3 pairs of the same length and parallel aluminum tube, together with 24 muscles with the same length are utilized to maintain the equilibrium shape of the robot. The properties of the tensegrity structure are summarized in Table 3.1.

In order to give a geometric description of the tensegrity, in Figure 3.3(a), numbers are labeled on individual vertices of the tensegrity robot. As illustrated in Figure 3.3(b), the corresponding vertex number is attached to the prototype. Then, the components in the tensegrity can be represented by a pair of vertices. Figure 3.4 shows two contact patterns with the ground surface: one is regular triangle, which has three actuators while the other one is non-regular, isosceles triangle that has two actuators.

Table 3.1. The properties of the tensegrity structure

Total robot mass	69 g	Maximum payload without deforming	300 g
Rod length	420 mm	Rod diameter	6 mm
Rod Mass	5 g	Number of Aluminum rods	6
Muscle rest length	210 ± 5 mm	Number of TCP muscles	24
Muscle Stiffness	98.85 N/m	Mass of each muscle	0.47 g
Styrofoam Ball	0.75 g	Number of Styrofoam Balls	12

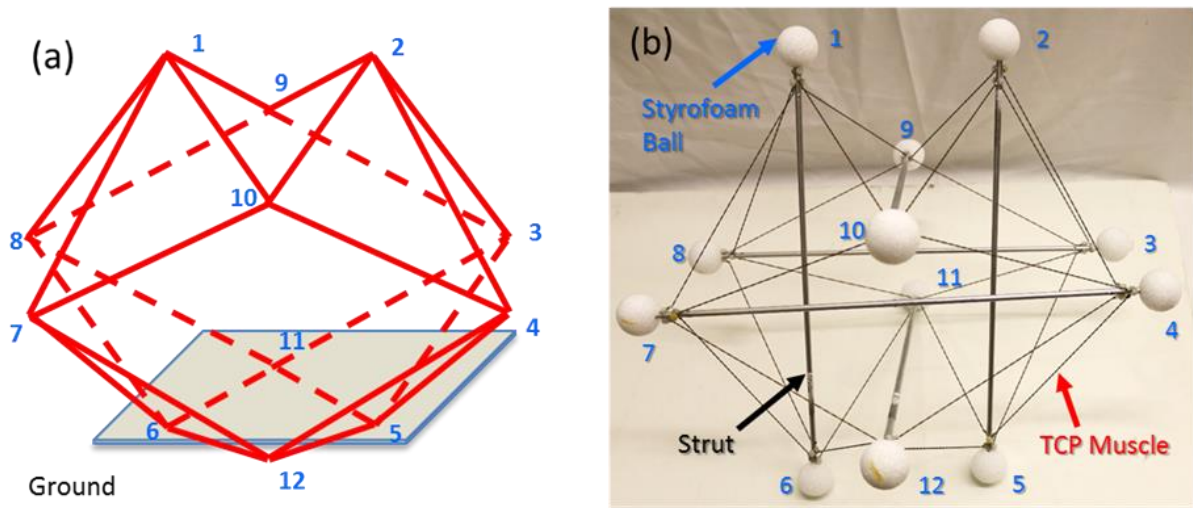


Figure 3.3. Prototype of a 6-strut tensegrity robot. (a) The prototype consists of 6 aluminum tube and 24 TCP muscles. Two styrofoam balls are attached to both ends of each aluminum tube, and (b) Numbers are labeled on individual vertices of the tensegrity robot prototype.

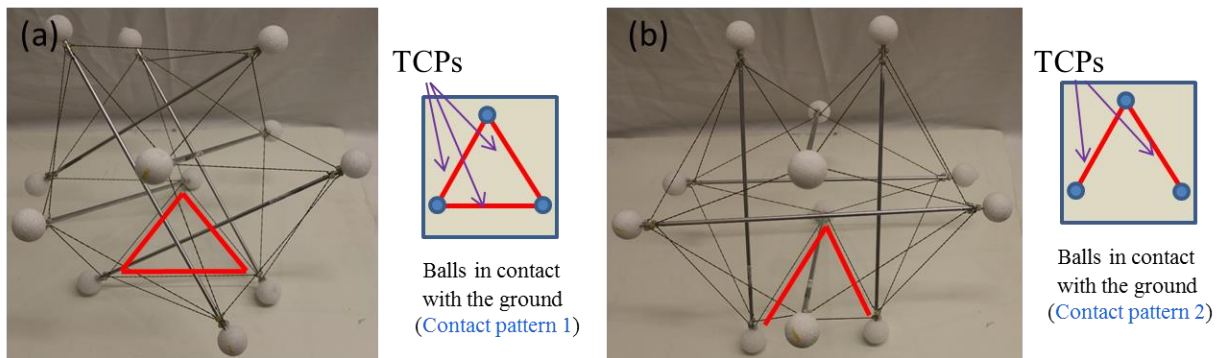


Figure 3.4. Contact conditions between the floor and the tensegrity structure. Red lines represent closed base triangles and isosceles triangles, respectively. (a) Pattern 1. (b) Pattern 2.

3.2.4 Transition of Gravitational Potential Energy of the Tensegrity Robot

Here, the principle of rolling motion will be briefly explained based on the assumption that the tensegrity robot lies on a flat ground. One of the key factors affecting the rolling motion is gravitational potential energy during transition. The tensegrity robot moves by applying a change

in gravitational potential energy that can be accomplished by contracting the muscle length in the structure. As the struts account for the major weight of the tensegrity structure, the gravitational potential energy can be calculated from equation 3.1 following the description in ref. [79], ignoring the potential energy of muscles:

$$E_g = \sum_{i=1}^N (m_i g h_i) \quad (3.1)$$

Where m_i and h_i represent the mass and height of the center of mass of the i^{th} strut, g is the gravitational constant. In the naturally stable state, the gravitational potential energy of the tensegrity energy reaches to its minimum. By applying power into a muscle, the muscle length contracts, resulting in unbalanced force within the structure and gradient changes in gravitational potential energy. Due to the nonlinear coupling between the components, the force generated by the muscles propagates through the entire structure. The unbalanced force generates a moment of gravitational force around the contacting area, causing the robot to move on the ground. Then, the tensegrity rolls over to the other side. Stopping the power, the muscle returns to its rest length and the gravitational potential energy of the structure reaches its minimum again at the new contact configuration. Then, the actuation procedure completes one rolling motion. A successive application of power to certain muscles enables a continuous rolling motion of the tensegrity robot on the ground.

3.3 Experimental Method and Simulation

3.3.1 Experimental Method

The prototype of the six struts tensegrity structure was used as the experimental platform. The

tensegrity robot made of aluminum struts and TCP muscles is discussed based on experimental results to validate the ability of shape changing and rolling motion. Due to its shape deforming ability, it has a potential application as rolling robot, which can navigate rugged terrains that are difficult for wheeled vehicles. Figure 3.5 shows the extension of a 2-ply muscle at different static load, showing the stiffness of the muscle. It can be seen that the extension of the 2-ply muscle has a linear relationship with the corresponding static load and indicates a static stiffness of 98.85 N/m. The information in Figure 3.5 is important for selecting an appropriate length of the TCP muscles during the integration in the tensegrity structure. If the muscles that connect struts are too short, they will be highly extended from the rest length when assembled to the structure, thus resulting a high pre-tension in the structure. If too high pre-tension

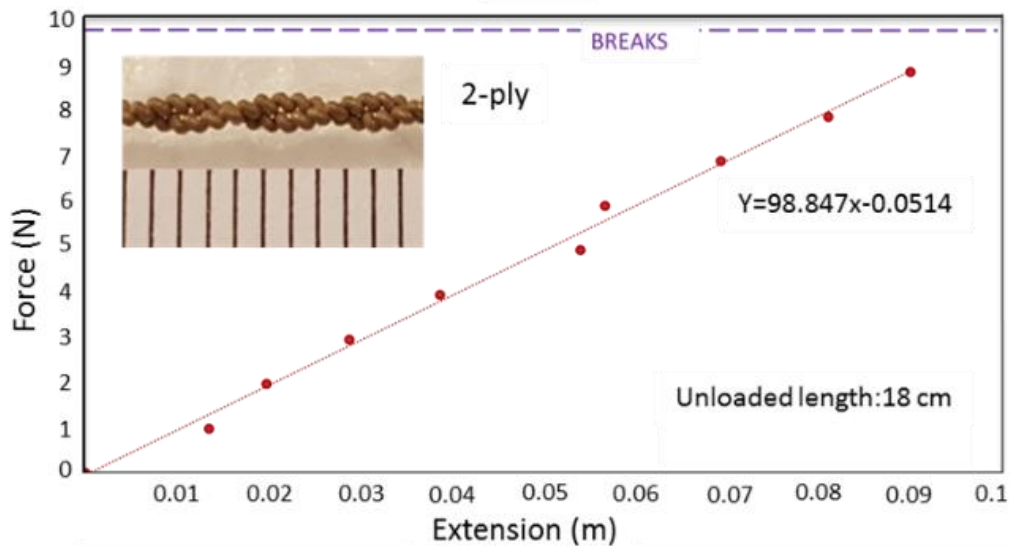


Figure 3.5. The stiffness study of 2-ply muscle at different static loads.

exists in the structure, upon receiving heat, the muscle will contract generating excessive force in the muscle depending the type of input power. From experiments, it was found that a pulsed power caused damage to the muscle for a highly pre-tensioned muscle in the tensegrity. The solution is

to avoid this by adjusting the pre-tension to an appropriate value which was 21 ± 0.5 mm, meanwhile maintaining the basic shape of the tensegrity. Figure 3.6 shows that a pulsed actuation at power of 1.87 W/cm for 1 s can generate a maximum actuation of $\sim 15\%$ stroke in the muscle. The test was performed using the experimental setup shown in Figure 2.7. The displacement was measured using the laser displacement (Keyence LK-G152). Depending on the applied power, a pulse voltage for 1 s, the actuation stroke realized was between $\sim 11.5\%$ to 15.5% . This test was performed by mounting a 50-gram load at the end of the muscle and applying electrical power across the terminals.

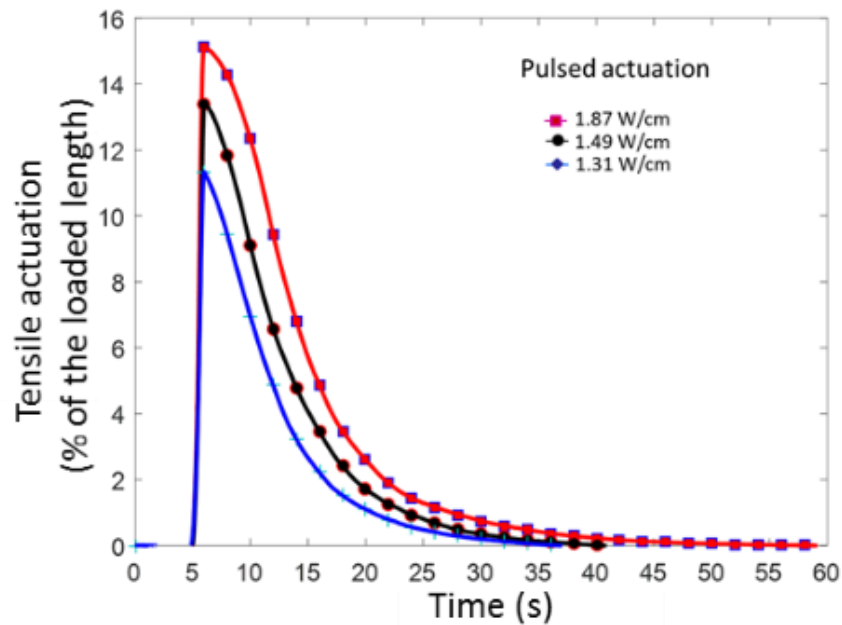


Figure 3.6. Actuation as a function of time for different values of pulsed power input for a 2-ply muscle under a load of 50 gram.

Figure 3.7 shows the measured state variables of a 2-ply TCP muscle at a constant 50-gram load. In this test, three different square-wave current inputs (0.66A, 0.60A and 0.55A; 36% duty cycle and a period of 70 s) were used. In Chapter 2, it was noticed that a significant change of

resistance in 1-ply TCP muscle occurred at high temperature range. In case of 2-ply TCP muscle, the resistance change was also observed when the muscle was subjected to the power of 0.25 W/cm (0.66 A). Using the current 0.66A, the maximum temperature was measured around 140 °C. It was also obvious that the higher current resulted in higher temperature which provided higher tensile actuation.

3.3.2 Simulation

The NTRT (NASA Tensegrity Robotics Toolkit) simulator was used to simulate the rolling motion discussed above. The NTRT is a Linux based simulator built specifically to help better understand the various tensegrity structures. It runs on top of the Bullet Physics Engine [94], which is used by numerous games for realistic physics interaction. The simulator is created using C++ and MATLAB programs and contains modules, which makes it comparatively easy to develop complex geometries. The Bullet Physics Engine currently does not support realistic model for cables [95]. Thus in the simulator, spring-cable assemblies are treated as two point tensional elements which apply directional forces to rigid bodies [95].

The software model of the robot helped better understand the movement of all the elements with respect to each other. As discussed earlier, a six-strut tensegrity icosahedron consists of eight regular triangles and twelve non-regular isosceles triangles. These regular triangles present a challenge during locomotion as the regular triangles being very stable on the ground, require more energy to destabilize and move. To study the effects of various configurations, we used simulating parameters similar to our tensegrity structure properties (mass, length, density, surface conditions, etc.) in the NTRT simulator and attempt to emulate the geometry, actuation policy, and rolling motion.

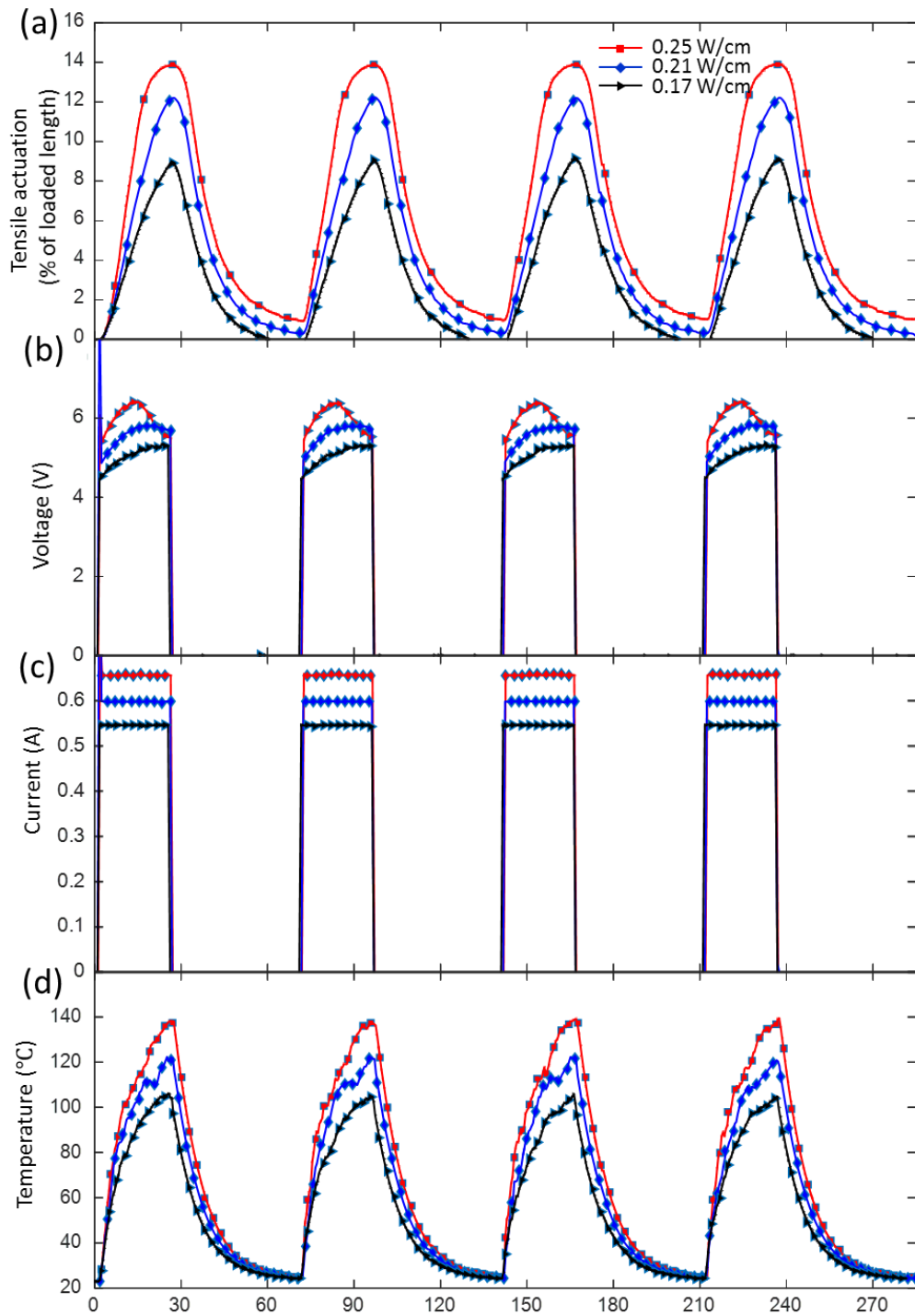


Figure 3.7. Mechanical response in an isotonic test of 2-ply TCP muscle at constant load 50 g. (a) Tensile actuation (% of loaded length) output, (b) Voltage input to the muscle, (c) Current input to the muscle, (d) Temperature rise in the muscle.

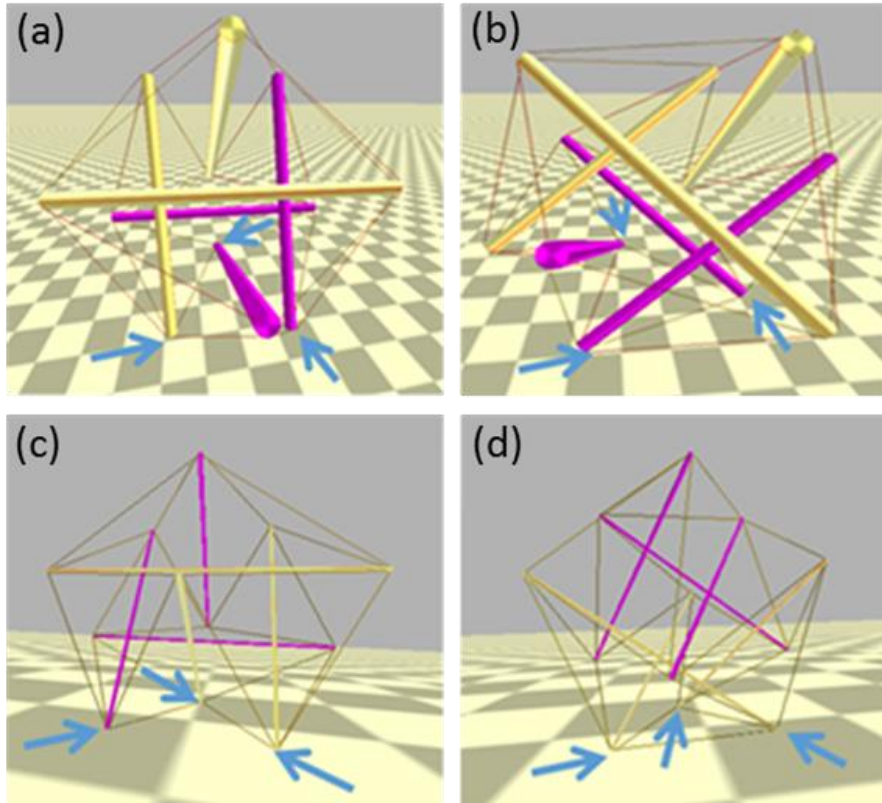


Figure 3.8. The two contact patterns with the ground in the NTRT simulator: (a) Contact pattern 2 (non-regular triangle) of default icosahedron, (b) Contact pattern 1 (regular triangle) of the default icosahedron, (c) Contact pattern 2 of our tensegrity robot and (d) contact pattern 1 of our tensegrity robot. Blue arrows show contact points with the ground.

Figure 3.8(a) and Figure 3.8(b) show the default icosahedron structure available in the NTRT simulator at rest on the non-regular triangle and the regular triangle (i.e. contact pattern 2 and 1) respectively. Figure 3.8(c) and Figure 3.8 (d) show the virtual structure designed according to the geometry and mass properties of our tensegrity robot. Table 3.2 shows the default parameters and the one used for our robot. The Figure 3.8(c) shows the structure at rest on a non-regular triangle, while in Figure 3.8(d) the structure rests on a regular triangle. Moving from contact pattern 2 to 1 (i.e. from non-regular to regular triangle) was comparatively easier and was experimentally validated, as compared to contact pattern 1 to 2 (regular to irregular). While the robot is in pattern

2 contact with the ground, a force was applied to the tip of the uppermost strut and the configuration changed to pattern 1 easily (From Figure 3.8(c) to Figure 3.8(d)). However, the reverse motion (i.e. contact pattern 1 to 2) was difficult, meaning it required a large force during simulation. The force was applied by dragging with a computer mouse on the graphic window.

The first column of Table 3.2 shows the various parameters which were given as input to the simulator. The values in the second column are the values of the default geometry available in NTRT while the last column lists the parameters of our tensegrity robot using TCP. In the last column, the value of damping of the muscle was considered 1% of the stiffness and target velocity was assumed so as to provide a model that can be regenerated in the simulator.

Table 3.2. Parameters of the NTRT default structure and our tensegrity robot.

Parameters	Default NTRT structure	Tensegrity Robot using TCP
Density of the rod material (kg/decimeter ³)	0.825	2.7
Radius of the rods (decimeter)	0.31	0.03
Stiffness of the cables/muscles (kg/sec ²)	613	98
Damping of the cables/muscles (kg/sec)	200	0.98
Rod length (decimeter)	15	4.2
Rod space (space between two rods) (decimeter)	7.5	1.7
Friction	0.99	0.99
Roll Friction	0.01	0.01
Restitution	0	0
Pretension (kg*decimeter/s ²)	2452	30
Max Tension (kg*decimeter/s ²)	100,000	100
Target Velocity (decimeter/s)	10,000	0.24

3.4 Results and Discussion

Controlling tensegrity robots is a big challenge for the desired movement due to the nonlinear coupling effects. As an effort to achieve the rolling motion, the same length aluminum tube and the same length muscles enable the shape of the current prototype look similar to that of a regular icosahedron. Recalling that there are two contact patterns of the tensegrity robot with the ground: contact pattern 1 (regular triangle) and contact pattern 2 (non-regular triangle). Figure 3.9(a)-(c) show the actuation policies for the tensegrity structure in contact pattern 2, by actuating the actuator in the red block individually. Figure 3.9(d) shows the pulsed power input given to the muscle shown in Figure 3.9(b) and Figure 3.9(c) to achieve the rolling motion transition from contact pattern 2 to contact pattern 1 (not continuous rolling motion, but one step). The duration of the pulse actuation was 1 second, and after that the power was turned off for natural cooling of the muscle in the air. The cooling time the muscle was around 35 second and it is not shown in the figure.

Figure 3.10 shows successive images of experimental rolling motion which was implemented by actuating the muscle shown in Figure 3.9(b). These images were taken from a video recorded during the rolling motion. The structure rolls to the left completing the motion in 2 seconds. Similar rolling motion can be obtained by actuating the muscle shown in Figure 3.9(c). As shown in Figure 3.10, the rolling motion was successfully demonstrated for one step under contact pattern 2. Table 3.3 shows the actuation policies tested for the rolling motion from the initial contact pattern 1 (regular triangle). The structure was tested by giving a pulsed power for one single muscle and the other muscle was actuated by regular actuation method for 5 seconds as shown in Figure 3.11(c). In Table 3.3, the actuator pairs in the first column received a pulsed actuation whose power input

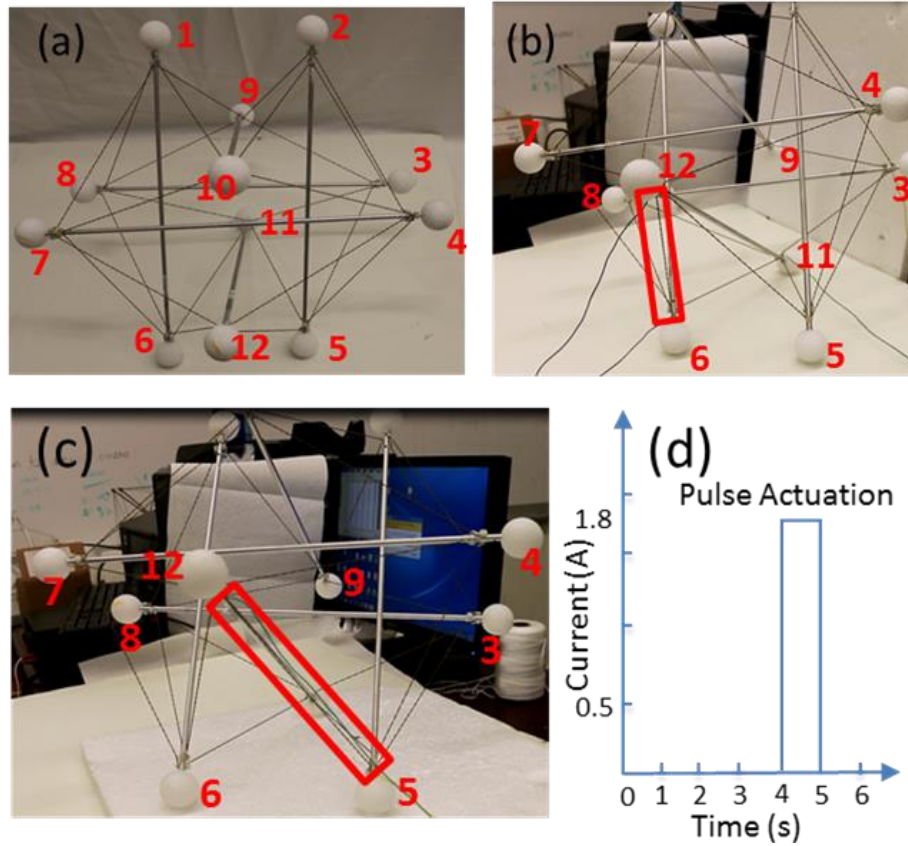


Figure 3.9. The rolling motion actuation pattern: (a) The contact pattern 2, (b) Actuator (2, 4) shown in the red block actuated, (c) Actuator (2, 3) shown in the red block actuated, (d) The pulsed input power provided to the actuator (2, 3) and actuator (2, 4).

Table 3.3. Actuator pairs tested to cause transition from contact pattern 1 (8,11,6).

Actuator pairs	
(4,5)	—
(4,5)	(8,11)
(3,5)	—
(3,5)	(8,11)
(8,11)	—
(5,11)	(8,11)
(3,11)	(8,11)
(1,8)	(8,11)
(1,8)	(8,9)

profile is shown in Figure 3.11 (b). The second column in actuator pairs received regular actuation whose power input profile is shown in Figure 3.11(c). The combination of the two actuated muscles resulted in a good shape deformation but couldn't generate the rolling motion. It was confirmed experimentally that contact pattern 1 (regular triangle) was more stable than contact pattern 2 (non-regular triangle) because contact pattern 1 has a larger contact area with the ground.

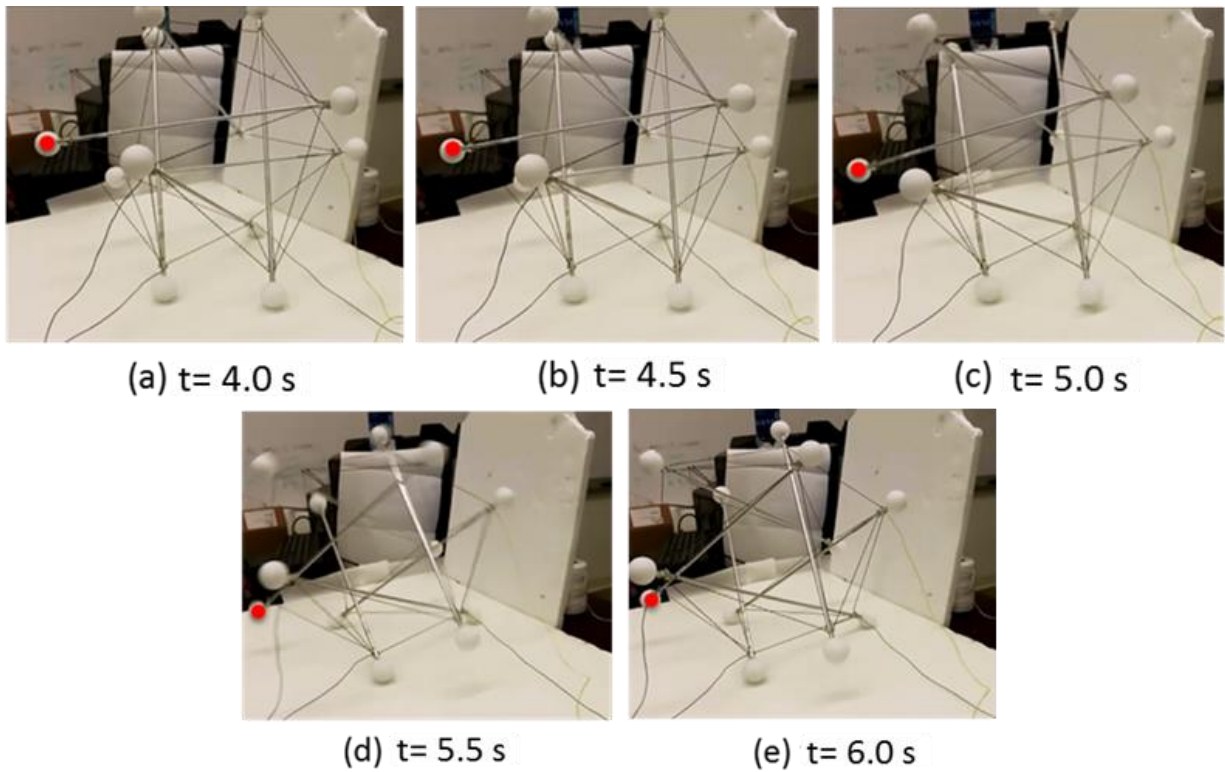


Figure 3.10. Snapshots extracted from video of the tensegrity robot during rolling: (a) Initially at rest, (b), (c) and (d) deformation and rotation, (e) Recovery to the final state of the rolling motion. The power is on from $t = 0.0$ s to $t = 1.0$ s; After $t = 1.0$ s, the power is turned off. Note: The red round marker is attached to a ball for comparison purpose.

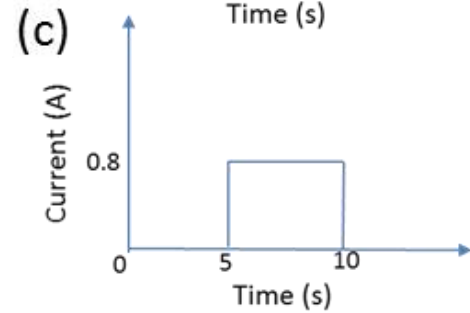
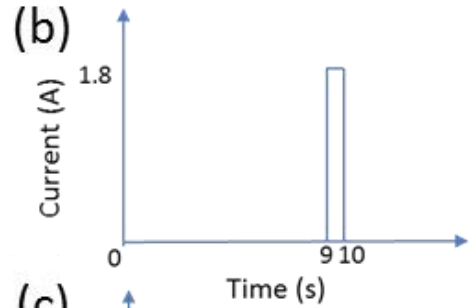
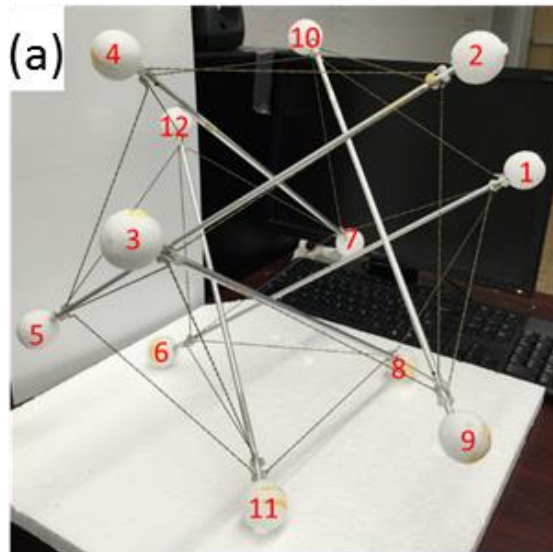


Figure 3.11. (a) The position in the initial contact pattern 1. (b) The power input profile for each first column actuator pairs in Table 3.3. (c) The power input profile for each second column actuator pairs in Table 3.3.

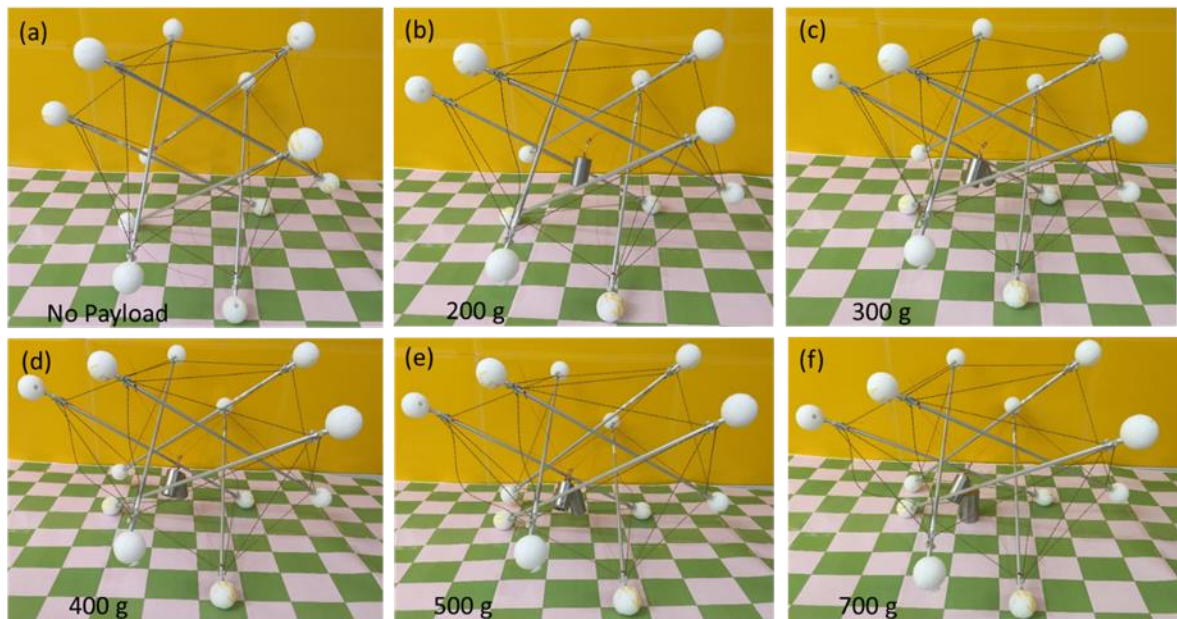


Figure 3.12. Payload capacity of the 6-strut tensegrity robot when a dead weight is suspended in the central region: (a) No payload, (b) 200 g, (c) 300 g, (d) 400 g, (e) 500 g and (f) 700 g. The last three masses made the structure have a slack in the some of the cables.

The payload capacity of the tensegrity robot was determined by mounting calibrated weight in the central region and observing the deformation of the structure. Slight deformation of the structure was observed when the load was increased until 300g. However, when the load was increased further to 400, 500 and 700g, observable slacking in some of the TCPs were noticed as shown in Figure 3.12.

3.5 Summary

In this chapter, a tensegrity robot based on 2-ply TCP muscles for large shape deformation was presented and rolling motion under a contact pattern 2 (contact with a ground in a non-regular, isosceles triangle) was also demonstrated. The mechanical design of the tensegrity robot, the muscle fabrication procedure and the performance of the muscle were described. The 2-ply TCP muscles were tested and could produce around 15% tensile actuation at an input pulsed power of 1.87 W/cm for 1 s actuation. For regular actuation, the 2-ply TCP muscle could produce around 14% tensile actuation at an input power of 0.25 W/cm for 25 s actuation. A total of twenty-four 2-ply TCP muscles and six aluminum rods were used to create the tensegrity structure. The tensegrity structure was very light and only had a mass of 69 g. The load carrying capacity was also evaluated. It can carry five times heavier load without any noticeable deformation. Contact conditions of the tensegrity robot, the principle of the rolling motion and the performance of the tensegrity robot were further discussed. Future work includes the exploration of actuation policies to recruit several muscles simultaneously and in combination for the contact pattern 1. In addition to the actuation policies, the mechanics and controller design and other mechatronic components will be incorporated for further investigation.

CHAPTER 4

COMPACT AND LOW COST ROBOTIC HAND POWERED BY TCP MUSCLE

This chapter focuses on design, fabrication and characterization of a biomimetic, compact, low-cost and lightweight 3D printed humanoid hand (TCP Hand) that is actuated by twisted and coiled polymeric (TCP) artificial muscles. The five-fingered humanoid hand is under-actuated and has 16 degrees of freedom (DOF) in total (15 for fingers and 1 at the palm). In the under-actuated hand designs, a single actuator provides coupled motions at the phalanges of each finger. Two different designs are presented along with the essential elements consisting of actuators, springs, tendons and guide systems. Experiments were conducted to investigate the performance of the TCP muscles in response to the power input (power magnitude, type of wave form such as pulsed or square wave, and pulsed duration) and the resulting actuation stroke and force generation. A kinematic model of the flexor tendons was developed to simulate the flexion motion and compared with experimental results. For fast finger movements, short high-power pulses were employed. Finally, grasping of various objects was demonstrated successfully using the humanoid TCP hand showing an array of functions similar to a natural hand.

4.1 Introduction

While humanoids are yet to be deployed widely in daily life, their development is projected to be used in household and personal assistance. Such robots require significant amounts of research and development before gaining market acceptance. Development challenges for this technology include design and manufacture of high-performance actuators to empower humanoid robots. Figure 4.1 shows the efforts of HBS lab in this area. In HBS lab, a humanoid was fabricated

entirely by 3D printing technology [96]. The robot size was based on the anatomy of a 7-year-old child. The figure shows the relative size of HBS-1 robot compared with an 8-year-old child. Dynamixel servo motors, SMAs and TCP muscles were used for actuation. This resulted in 51 DOF for movements of joints. Dynamixel servomotors, costing approximately \$500 each, were used for some joints requiring large torque (especially at the knee, hip and waist), and accounted for the major cost of the robot. The overall material cost of the robot is approximately \$10,000. The first version of the hand is actuated by shape memory alloy (SMA) actuator [47]. The robotic hand, however, is actuated by economical TCP muscles, which is the focus of this chapter.

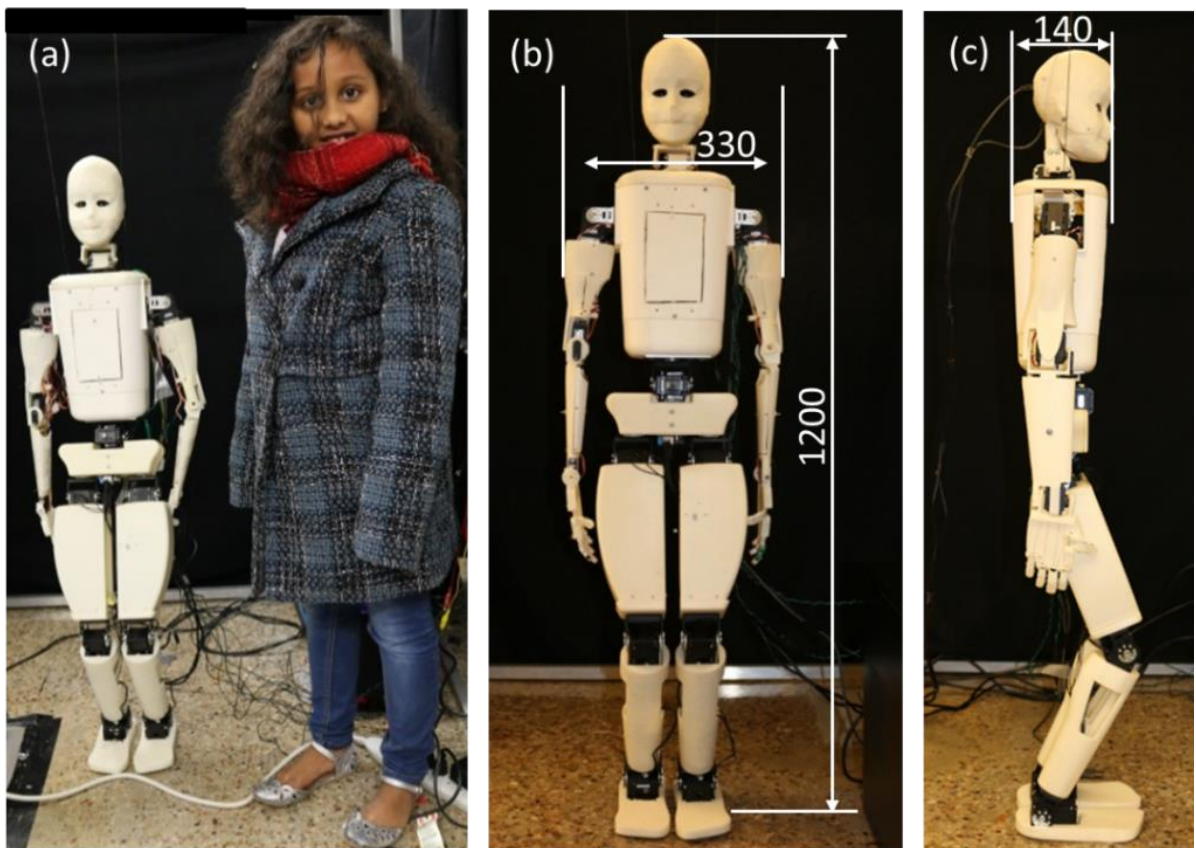


Figure 4.1. The 7-year-old child-sized humanoid robot HBS-1: (a) Comparison of HBS-1 and an 8-year-old child, (b) Front view of HBS-1 and (c) Side view. All dimensions are in millimeters (mm).

Multi-fingered robotic/prosthetic hands have been designed and studied extensively, and one ultimate goal of developing such hands is to achieve dexterous manipulation. Researchers have used the human hand as a model for recreating functional robotic hands. Core aspects of the design and manufacturing of robotic hands include the capability to hold different objects skillfully, size & weight of the actuator system, ease of fabrication, degree of freedom and overall cost. Multiple laboratories have developed robotic/prosthetic hands [97-101], which are capable of grasping various objects. Industrial efforts also have found their way to the marketplace [102-104]. A summary of robotic/prosthetic hand designs developed using various actuation technologies, degrees of freedom and transmission mechanism is shown in Table 4.1. Conventional actuation technologies such as electromagnetic [97, 99-101, 105-107], hydraulic/fluidic [108, 109] and pneumatic [110, 111] systems have been extensively explored to make functional devices and help human beings in daily life. Electrical motors, together with a diverse collection of approaches to finger actuation, have been used in [112-115] to provide precise positioning. 3D printed robotic hand actuated by twisted strings via electric motors was presented in [116]. Further, the mechanical design, hand control and grasping performance are presented in review articles [117-120].

In addition to actuation units that use motors, cables, gears and other transmission systems, low profile actuators such as shape memory alloy (SMA) wires are good candidates as actuators for compact designs [121, 122]. However, cylindrical SMA provides limited strain of 4% that requires significant length of the actuator to achieve hand flexion [47]. Although SMA muscle benefits from features such as compact size, high force-to-weight ratio and silent operation, major drawbacks restricting its application include low power efficiency, hysteresis, high cost and low operational frequency. This hysteresis makes the control of SMAs quite complicated. The low

operational frequency, a result of the time required for heating and cooling, could be improved by active cooling techniques [8]. Thermally driven SMA muscles, nonetheless, are widely deployed in humanoid hands [17, 18, 123-126].

Table 4.1. Characteristics of some robotic (R) and prosthetic (P) hands/fingers.

Type of Actuator	Motion Transmission Mode	No. of actuators	Fingers return motion via.	No. of fingers	Joints at thumb	Thumb abduction & adduction / DOF	Total DOF	Name/ Developer
Electrical motors	Flexible driven train (flex shaft)	14	Actuator	5	3	Yes/3	14	Robonaut hand (R) [107]
Electrical motors	Tendon-like driven mechanism	19	Torsional springs	5	4	Yes/4	19	DART hand (R) [101]
Electrical motors	Gear driven mechanism	12	Actuator	4	3	Yes/3	12	NAIST hand (R) [105]
Electrical motors	Tendon-like driven mechanism	16	Helical springs	5	3	Yes/4	16	UB Hand 3 (R) [106]
Electrical motors	Linkage mechanism	5	Actuator	5	3	No/1	5	HIT-DLR hand (P) [115]
Fluidic actuators	Hinge structure	18	Elastomeric spring	5	3	Yes/4	13	Karlsruhe Univ., Germany[108]
Pneumatic	Tendon-like driven mechanism	38	Actuator	4	4	Yes/4	19	UTAH/MIT (R) [111]
SMA	SMA wires	9	Actuator	3	2	No/1	8	SMA hand (P) [125]
SMA	SMA plates	2	Actuator	1	-	-	1	Engeberg <i>et al.</i> (R) [126]
Muscles	Tendon	40	Muscles	5	2	Yes/5	23	Human hand [§] (male) [127]
TCP actuators	Tendon-like driven mechanism	10	Actuator/torsional springs	5	3	No/1	16	TCP UTD hand (R) *

[§] Natural hand is presented to compare with robotic hands.

* The robot hand developed in this study at The University of Texas at Dallas (UTD). Note: TCP = Twisted and Coiled Polymer muscle.

The first robotic finger utilizing TCP muscles, which were fabricated from twisted and coiled fishing line fiber, was reported in the 2015 SPIE conference [128]. In that design, a hot and cold water circulation system was used to actuate the artificial muscle hydrothermally, providing fast finger movements. Later on, Yip and Niemeyer [72] developed a robotic hand that was electrothermally actuated by TCP muscles, which were made from metal-coated sewing threads. Another robotic hand based on these muscles was recently reported in [129]. TCP muscles can be applied to many possible applications where large stroke, low material cost, and high specific work capacity are required. In this chapter, a five-finger under-actuated humanoid hand (TCP Hand) was developed and electro-thermally powered by TCP muscles for a child-sized humanoid called HBS-1 [96]. Given the limited volume of the hand and forearm in pediatric model, it would have been difficult to incorporate expensive traditional motors. TCP muscles were preferred over SMA wires due to higher actuation stroke, enabling greater finger motion range from a given muscle length. The negligible hysteresis actuation and small form factor of these muscles are ideally suited for deployment in humanoid hands. As a consequence of the fact that these actuators are thermally driven, Carnot efficiency and thermal management should be considered to avoid thermal accumulation. The efficiency of coiled nylon and polyethylene was reported as 1.08% and 1.32% respectively [45]. The efficiency of such actuators can be mitigated by using a locking mechanism that holds a load without consuming any power as shown in the recent work [130]. The locking mechanism could be made by using springs and sequentially activating and deactivating a group of muscles in the mechanism.

The present research aims to develop a dexterous, compact, lightweight, low-cost humanoid hand powered by TCP muscles. In the following sections, the fabrication method of TCP muscles

is briefly described, and the designs of robotic hand based on TCP muscles are discussed. Then, TCP muscles characterization and performance are investigated, and the kinematics of the TCP hands are explained both theoretically and experimentally. Finally, the grasping capabilities of various objects with different sizes and weights are demonstrated to show the effectiveness of TCP muscles for application in humanoid hand.

4.2 Design Approach

4.2.1 Human Hand Anatomy

In order to design a humanoid or prosthetic hand, the anatomy of a human hand is used as a guide. An X-ray image of an adult human hand is shown in Figure 4.2 to highlight the details of joints and structural arrangements. Because design changes in dimensioning while mimicking the human hand may cause changes in performance, the optimal configuration requires a full understanding of both hand anatomy and hand mechanics. For the purposes of this discussion, all appearances are referenced to the anatomic position when the subject faces the viewer with palms forward. Flexion will be defined as moving a joint toward a more acute angle and extension toward, or beyond, 180 degrees.

Human evolution has resulted in five functioning fingers. For each finger bone, called a phalange (phalanx), the aspect approaching the fingertip is called distal while the opposite end is proximal. The thumb is the shortest finger consisting of only two phalanges, distal and proximal. The second through fifth fingers are comprised of three phalanges named distal, intermediate and proximal. Interphalangeal joints (distal interphalangeal, DIP, and proximal interphalangeal, PIP, joints) flex to grasp and extend to release describing 1 DOF for each joint. The proximal phalanges

form metacarpal-phalangeal joints (MCP) with the metacarpal bones which comprise the flat palm of the hand. Although usually described as having one DOF, the second through fifth MCP joints also display small lateral and medial deviations for the purpose of fanning the fingers, for example, to span many keys while playing a piano chord.

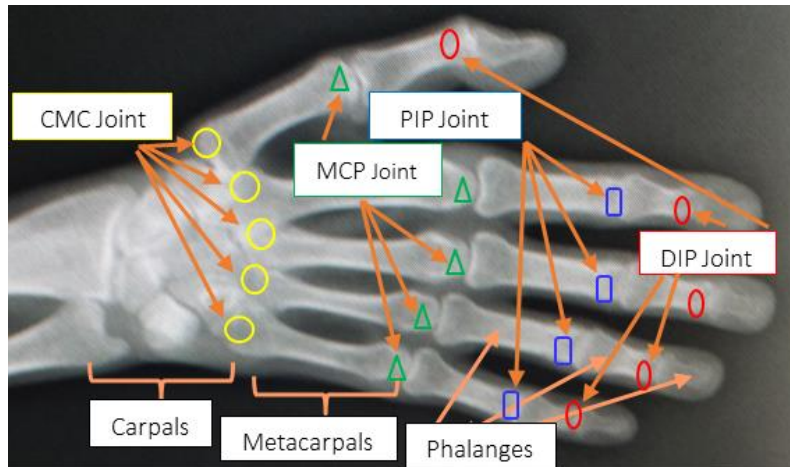


Figure 4.2. X-ray image of a human hand.

The metacarpal bones each form carpal-metacarpal joints (CMC) with one of the four distal row carpal bones among the eight carpal bones which comprise the wrist [34]. For the thumb, the CMC joint has evolved with two degrees of freedom as a result of conformational development of the greater multiangular (trapezium) bone to resemble the compound concave-convex form of a western saddle. This morphology allows not only flexion and extension but also abduction (motion away from the body) and adduction (motion toward the body), giving humans an evolutionary advantage over other creatures that lack a prehensile thumb. The second, third and fourth CMC joints are relatively rigid, but slight movement is seen at the fifth CMC joint to allow for fanning and concavity of the palm in conjunction with the positioning of the first metacarpal. There is little mobility among the wrist bones (carpus). The carpus moves as a block into flexion (anteriorly,

volar) and extension (posteriorly, dorsal). The carpus is able to abduct and adduct slightly, but always remains in the same plane as the radius and ulna, which are the long forearm bones.

The major forces controlling movement of the fingers and the wrist originate in the muscles of the forearm, which morph at their distal aspects into sturdy, inelastic tendons. The tendons terminate at positions of mechanical advantage on each phalanx at its volar and dorsal surface approximately five to twenty millimeters beyond the MCP, PIP and DIP joints. A muscle and tendon unit crossing the palm controls the adduction of the thumb; abduction is affected by a forearm muscle. Wrist flexion and extension are controlled by large proximal forearm muscles yielding one DOF. Small (intrinsic) muscles of the hand contribute to fine motor control.

Rotatory motions such as when working a doorknob or screwdriver requires the hand, wrist and forearm to function as a block. Architectural features such as the unyielding CMC joints and a combination of strong ligaments and bony restrictions at the radio-carpal joint help with this rigidity. The motion derives from muscles mounted on, and at an angle from, the long axes of the forearm bones. Those muscles originate at the volar and dorsal aspects of the ulna and insert on the volar and dorsal aspects of the radius, so as to pull the radius-wrist-hand block into a palm down (pronated) or palm up (supinated) position.

4.2.2 Biologically Inspired Agonist-antagonist Arrangement

The fundamental design goal is to mimic basic capabilities of human hand. Additional design goals are cost-effectiveness, lightweight, and compact size. Our approach in this aim is through developing the tendon-driven agonist-antagonist biomimetic actuation system driven by TCP muscles for the hand of a 7-year-old child robot. The aim is to show that the tendon-driven biomimetic actuation system can address some of the challenges in actuation.

Regarding hand design, this chapter focused on the essential elements and configuration in the TCP hand. Two designs of the mechanical structure and transmission elements were explored, as illustrated in Figure 4.3. The figure shows the schematic diagram of finger designs, including the arrangement of actuation system in agonist and antagonist configurations encompassing springs, tendons, guide ways and actuators housed in the forearm. Based on the fact that PIP and DIP joints of human hand move in near-synchrony [131], the tendon cables were attached to the tip of the distal phalanges allowing flexion of the entire finger. In both designs, the TCP muscles were placed in the forearm connecting the tendon cables and then stretched to a set preload. In design I, Figure 4.3(a) and (b), the preload for 3-ply muscles was provided by torsional springs that were custom made from music wires (K&S Precision Metals, stock #498, with diameter 0.38 mm, spring constant 6.12×10^{-4} Nm/degree). The torsional springs was used in conjunction with the 3-ply actuators for finger extension/flexion. In design II, Figure 4.3(c) and (d), torsional springs were removed, and the preload was provided by the extension spring attached to the TCP muscle. The force required for triggering the finger flexion movement in design I and design II was 2.0 and 0.5 N, respectively. For design I, a 3-ply actuator configuration was preferred since flexor tendons required higher strength to overcome the torsional springs. Therefore 3-ply muscles were employed. However, due to the stiffness of the torsional spring utilized in design I, complete bending motion was not attainable. For design II, the torsional springs were removed, and an agonist-antagonist actuator configuration containing 2-ply actuators was employed. Pulleys were added in design II to use longer muscles to achieve faster actuation and high stroke using pulsed power, which enables the complete bending motion. Many other configurations can be explored and studied, but this study is limited to the two designs, especially focused on design II.

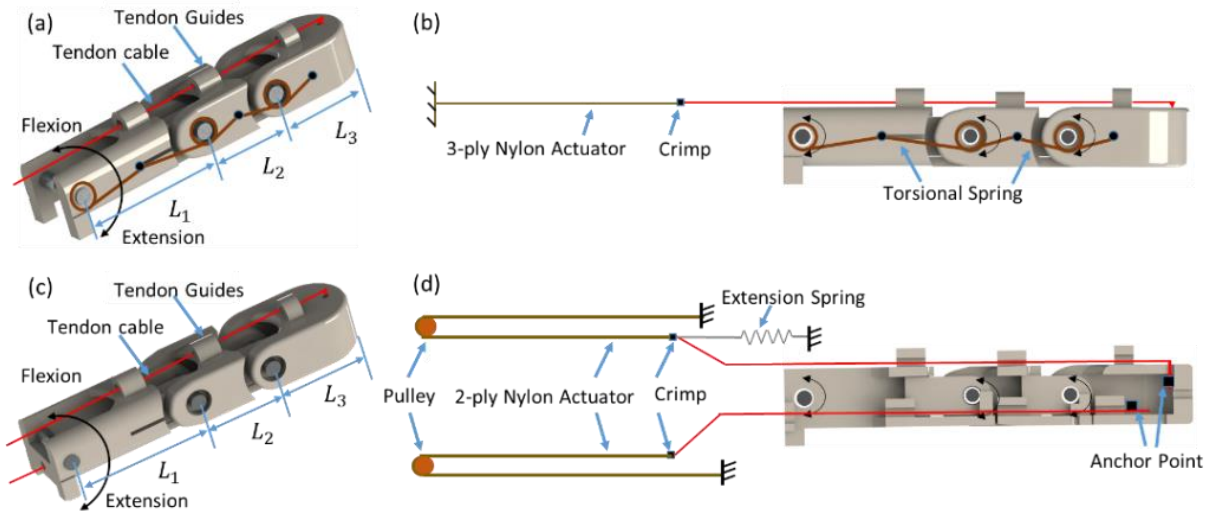


Figure 4.3. Schematic diagrams of the finger actuation systems, where L_1, L_2, L_3 are the length of each phalange. (a) Isometric view of design I, (b) A 3-ply flexor muscle with torsional springs employed in design I, (c) Isometric view of design II, and (d) An agonist-antagonist actuator configuration containing 2-ply actuators, extension springs and pulley employed in design II.

The working principles of the TCP hand in design II are illustrated in Figure 4.4. The fully extended state of the finger is as shown in Figure 4.4(a). When the flexor muscle is actuated as in Figure 4.4(b), it stretches the spring and also rotates the finger. For the return motion (extension), as in Figure 4.4(c), power is given to the extensor muscle. During this time, power is not supplied to the flexor muscle and the muscle undergoes natural cooling, meanwhile the spring returns to its original position. The TCP hands (Figure 4.5) were fabricated using 3D printer (Fortus® 250mc by Stratasys, Ltd), and all five fingers consisting of 3 joints. Figure 4.5 (a) shows the relative size of the TCP hand (design I) compared to the hand of an 8-year-old child. In Figure 4.5(b), a soft finger-pad made from silicone (Ecoflex® 00-30 shore hardness) was included in the TCP hand (design II) to enhance grasping ability. As shown in Figure 4.5(e), the prototype hands have an extra joint, which mimics the carpal-metacarpal joints at the palm.

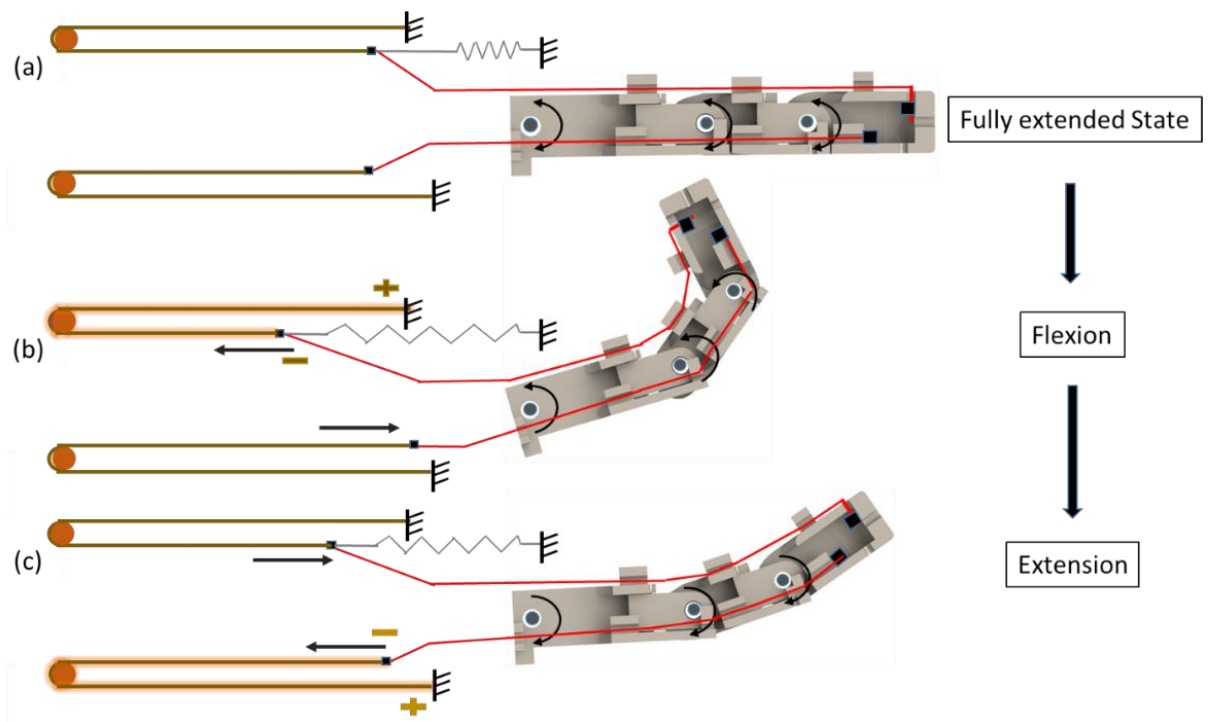


Figure 4.4. The schematic diagram of flexion-extension movement of the TCP hand in design II. (a) The fully extended state, (b) When the flexor muscle contracts upon heating and stretches the extension spring, and (c) The extensor muscle contracts upon heating, the extension spring contracts when the flexor muscle undergoes natural cooling, and the finger returns to its original position.

The overall size of the hand is 122 mm × 64 mm × 14 mm in length, width and thickness, respectively, which is in the range of average hand size of a 7-year-old child [122]. The actuators were located in the forearm and connected to the fingers via tendon strings. The strings were routed along the palmar and dorsal sides of the hands through semicircular guides. In the current configuration, the weight of the humanoid hand (including five fingers, palm, and skin) is 53 g and the forearm weight, including the actuators and pulleys, is 87 g, lighter than those hands reported in [99, 101]. The TCP hand only counts 3.5% and 13.3% of the weight compared to those hands in [99] and [101], as shown in Table 4.2 respectively.

Table 4.2. The comparison of TCP and other robotic hand/finger

	Hand Weight (gram)	Hand overall Size (length×width×height)	Forearm weight	Power Consumption
DART hand [101]	90	180×90×50	960	2.7A; 6.4W
HIT-DLR hand [115]	420	159×79×21	/	5.5W
SMA plate hand[126]	44 per finger	Length 80;	/	20A; 100W
Kurita et al. [99]	3965	200×78×24.6	/	/
TCP hand*	53	122×64×14	87	3A;5.9W

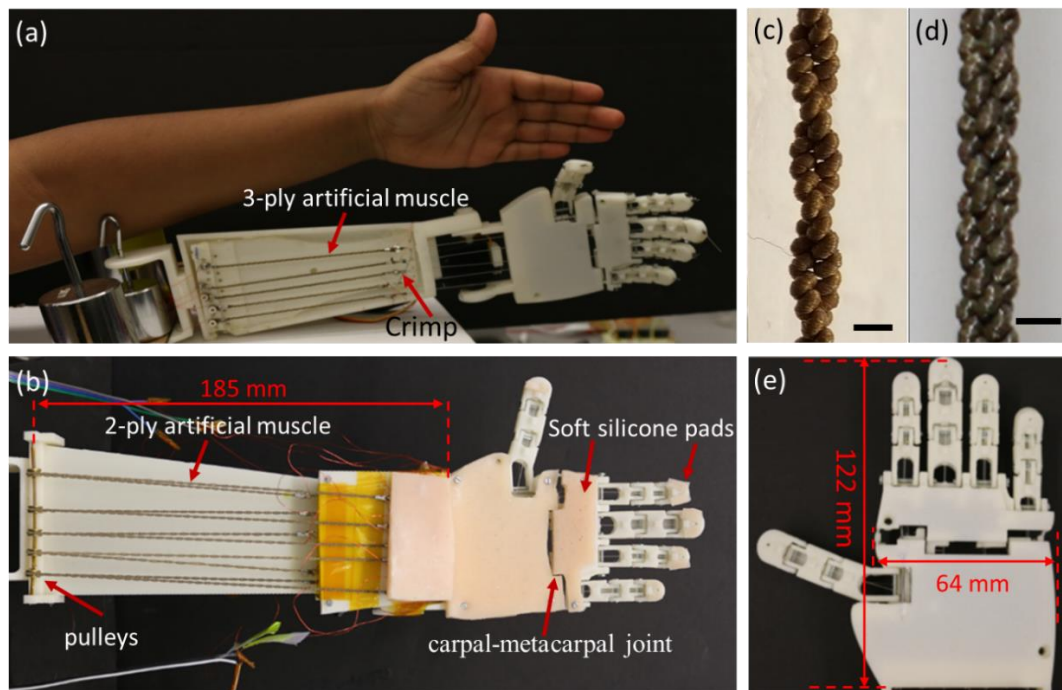


Figure 4.5. TCP hand prototypes: (a) The first prototype (Design I) comprising the TCP actuators in comparison to a hand of an 8-year-old child; (b) The second prototype (Design II) consisting of the TCP actuators, silicone skin in the palm and soft finger-pads in the fingers; (c) Optical micrographs of the artificial muscles studied in this work, 2-ply TCP muscle; (d) 3-ply TCP muscle. The bar scales are 1 mm long; (e) The second prototype without the silicone skin on the palm and its dimensions.

4.3 Modeling and Analysis

4.3.1 Finger Kinematics

A kinematic model of the flexor tendons is developed to describe the multi-joint finger motion and reachable position for potential application in grasping. The dynamic analysis that accounts elastic, viscous and inertial effect is not performed here to limit the scope. In the literature, several design and analysis on robotic fingers have been presented. Secco *et al.* [132] presented a minimum jerk approach for the motion planning of a prosthetic finger. Kim [131, 133] introduced a theoretical model to analyze the joint trajectories of humanoid finger using inter-phalangeal joint coordination. The model was based on human finger joint analysis and found to be useful for design and analysis of humanoid finger. As mentioned in ref. [131] for a human hand, the third link of a finger (distal phalanx) and the second link (middle phalanx) are coupled in most of the voluntary movements. Belter *et al.* [117], presented a review of several prosthetic hands and performance measurements of six commercial prototypes for comparative assessment. The results indicated that three out of the six prototypes (Vincent, iLimb and Bebionic v2) featured a linear relationship between the MCP and PIP. It was stated that each hand had distinct coupling mechanism such as a four-bar linkage or a loop of wires for the coupling and attain fixed relationship between PIP and MCP. Here, the design deployed torsional springs at the joints for the coupling in design I. The analysis followed the approach presented in [131, 133], [134] and assigned the relationship between θ_1 , θ_2 and θ_3 which were defined in Figure 4.6(a) as a linear form :

$$\theta_1 = \lambda_1 \theta_3, \quad \theta_2 = \lambda_2 \theta_3 \quad (4.1)$$

Taking the differential of Eq.4.1, λ_1 and λ_2 are expressed as:

$$\lambda_1 = \frac{\Delta\theta_1}{\Delta\theta_3}, \quad \lambda_2 = \frac{\Delta\theta_2}{\Delta\theta_3}, \quad (4.2)$$

Where $\Delta\theta_1$, $\Delta\theta_2$ and $\Delta\theta_3$ indicate the angular displacement of the MCP, PIP and DIP joints, respectively. Here, $\max \Delta\theta_k = \theta_{k,f} - \theta_{k,i}$, $k = 1,2,3$. The $\theta_{k,f}$, and $\theta_{k,i}$, correspond to the maximum(final) and minimum (initial) motion angles of the joints. The λ_1 and λ_2 are the interphalangeal joint coordination parameters. These parameters are decided in the design of the robotic hands such as joint length and mechanism selection to match closely with human hand. The linear assumption of the joints in two prototypes will be evaluated and discussed in the later section of the chapter.

It should be noted that the nominal resting position of a natural finger is not straight along the palmar plane [135]. The MCP, PIP and DIP joints exhibit a maximum range of motion when passing from full extension to full flexion. To obtain the trajectories of the humanoid hands in both designs, position data was collected experimentally using a high-speed camera (Phantom Miro eX2; PCC software).

The angular displacement of the MCP joint of the robot's index finger is predefined as follows [131]:

$$\Delta\theta_1 = \theta_1 - \theta_{1,i} = (\theta_{1,f} - \theta_{1,i}) \sin\left(\frac{0.5\pi t}{t_f}\right) \quad (4.3)$$

Where the final time parameter t_f was set to be 45 s (similar to the experimentally observed actuation time of the finger in design I when using low-voltage, slow actuation). The final angle $\theta_{1,f}$ and the initial angle $\theta_{1,i}$ were 58° and 28° respectively. The λ_1 and λ_2 were taken as 1.67 and

1.08. Equation (4.2) & (4.1) were used to determine the other angles, the MCP and PIP joints of the finger.

Therefore, using the three joint angles and considering their initial angles, the fingertip trajectories were determined as follows:

$$\begin{bmatrix} x_f \\ y_f \end{bmatrix} = \begin{bmatrix} \cos\theta_1 & \cos(\theta_1 + \theta_2) & \cos(\theta_1 + \theta_2 + \theta_3) \\ \sin\theta_1 & \sin(\theta_1 + \theta_2) & \sin(\theta_1 + \theta_2 + \theta_3) \end{bmatrix} \begin{bmatrix} L_1 \\ L_2 \\ L_3 \end{bmatrix} \quad (4.4)$$

Where x_f and y_f denote the x and y dimensional positions of the fingertip, respectively. L_1 , L_2 and L_3 are the length of each phalange.

Tendon displacement and finger movements during flexion movement can be correlated based on the geometry as shown in the schematic diagram Figure 4.6. The parameter l_i ($i = 1, 2, \dots, 10$) is the length of each section defined in Figure 4.6. The change in length of the tendon (tendon displacement, ΔL) is:

$$\Delta L = l_3 + l_4 + l_6 + l_7 + l_9 + l_{10} - C_1 - C_2 - C_3 \quad (4.5)$$

Where C_i are obtained from cosine law and given as:

$$C_1 = \sqrt{(l_{10} - l'_1)^2 + (l_9 - l'_1)^2 - 2(l_{10} - l'_1)(l_9 - l'_1) \cos(\pi - \theta_1)} \quad (4.6a)$$

$$C_2 = \sqrt{(l_7 - l'_2)^2 + (l_6 - l'_2)^2 - 2(l_7 - l'_2)(l_6 - l'_2) \cos(\pi - \theta_2)} \quad (4.6b)$$

$$C_3 = \sqrt{(l_4 - l'_3)^2 + (l_3 - l'_3)^2 - 2(l_4 - l'_3)(l_3 - l'_3) \cos(\pi - \theta_3)} \quad (4.6c)$$

Considering the small triangles as shown in the insets of Figure 4.6 (b), (c) and (d), the following equations can be established:

$$\begin{bmatrix} l'_1 \\ l'_2 \\ l'_3 \end{bmatrix} = \begin{bmatrix} \tan(\theta_1/2) \\ \tan(\theta_2/2) \\ \tan(\theta_3/2) \end{bmatrix} e \quad (4.7)$$

Where e is the offset distance of the tendon-like string from the rotation axis.

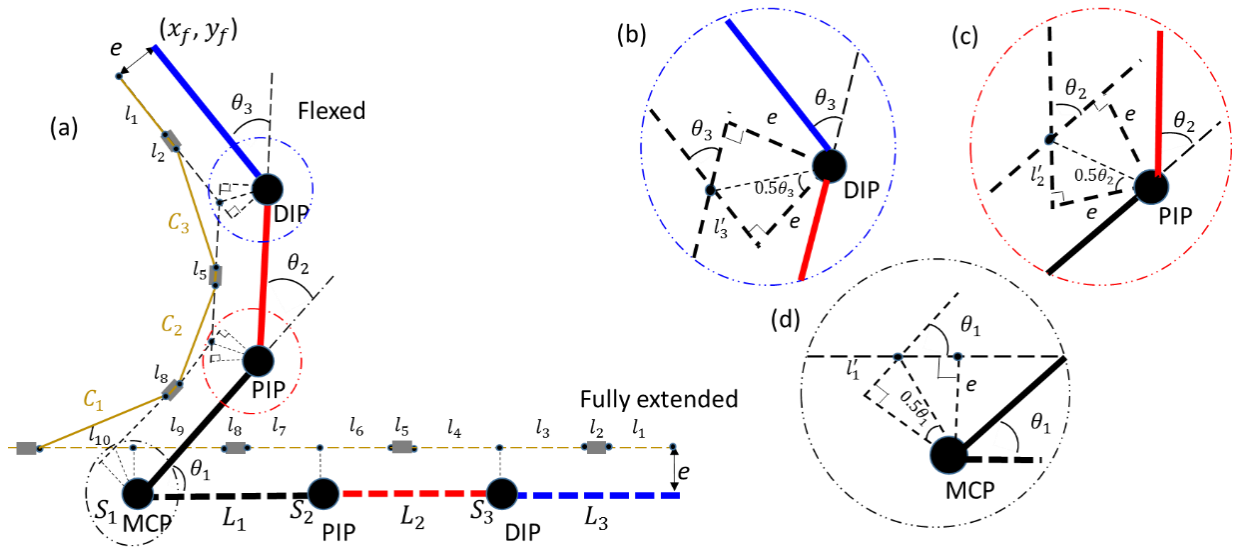


Figure 4.6. Kinematic model of the finger: (a) schematic diagram, (b) inset of the joint at DIP, (c) inset of the joint at PIP, and (d) inset of the joint at MCP. (The solid and dashed golden lines represent the tendon during flexion and the initial fully extended state, respectively).

Equation 4.5-4.7 are nonlinear algebraic equations, and there is no closed form analytical solution that provides the angles for a specific displacement of the tendon. Solving such equations in Matlab/Simulink using tools such as “Fsolve” requires good initial guess and may result in algebraic loop error. However, by assuming the coupled relationship of the angles as described in Equation 4.1 and rewriting θ_3 and θ_2 in terms of θ_1 ($\theta_3 = \theta_1/\lambda_1$, and $\theta_2 = \lambda_2\theta_3 = \lambda_2\theta_1/\lambda_1$) and using the equations 4.5-4.7, the angle for a specific tendon displacement (ΔL) can be solved. A Simulink model was created to solve the equations. Initial guess was used for $\Delta\theta_1$ and the input ΔL was provided by varying from 0 to 6 mm in an increment of 1 mm. Then, a new $\Delta\theta_1$ was obtained that satisfies the Fsolve. The other angles were obtained since λ_1 and λ_2 are known. The results will be discussed in section 4.5.

4.3.2 Stress and Deformation Simulation

Since most parts of the robotic hand are 3D printed using ABS material, we performed finite element analysis. It is important to simulate the strength of the manufactured parts and determine the capabilities. First, a cantilever beam with 100 x 10 x 1 mm, length, width and thickness was 3D printed (ABS material) with two printing options (Normal and Sparse high-density). The normal option fills the part completely with fully dense raster tool paths, and the sparse high-density option minimizes the amount of model material leaving some gaps in the interior regions. Then FEM simulation (Static analysis) was performed by loading the cantilever beam with a tip force corresponding 10, 20, 30 and 40gm loads. SolidWorks™ 2014 was used for the simulation using ABS material library. The model type was linear elastic isotropic. Static simulations were performed by setting the default meshing option. Experiments was also performed on the fabricated cantilever beam (Figure 4.7 (a)) with the same loads as in the simulation and determined the deflection using a camera. The experimental and simulation results of the deflection are close to each other as shown in Figure 4.7(b). The contour plots of displacement and the Von Misses stress of the cantilever beam are shown in Figure 4.7(c) and (d) respectively. As the simulation and experimental results are comparable, one can conclude that similar properties will be shown on other 3D printed parts.

It is also of interest to print the assembly of robotic hand from ABS material and avoid any assembly work. Next, in the stress simulation, the pin connector (1mm in diameter) was assigned with ABS material. A 1N force was applied to various areas of the joints corresponding to DIP, PIP, and MCP joints. It was found that when ABS pin connectors are used at the joints, the stress generated and displacement due to 1N load were 16.8 MPa and 0.12 mm (when the load is at the

DIP section). The safety factor in this case was about 2 (ABS has yield strength of 31 MPa). The displacement, stress and loading conditions of the index finger results are shown in Figure 4.8(a)-(c). The advantages of making the entire finger with 3D printable materials minimize the assembly time and manual operations. However, the strength is compromised somewhat.

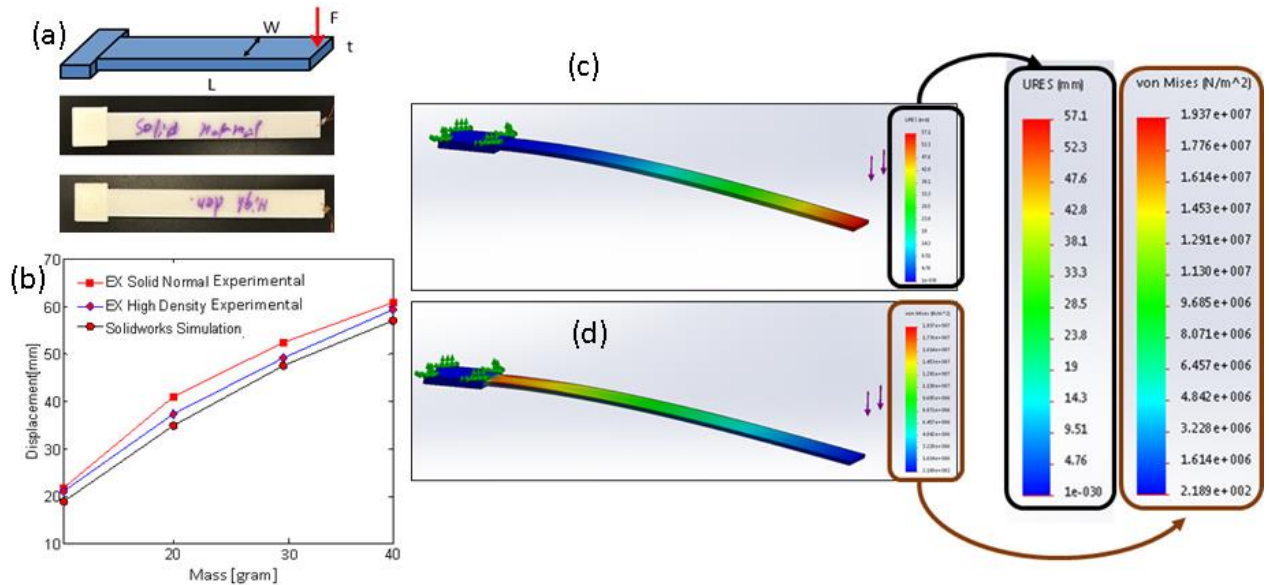


Figure 4.7. SolidWorks™ 2014 simulations of the displacement of a 3D printed cantilever beam (ABS material) loaded with a tip mass. (a) Schematic diagram and 3D printed cantilever with Normal and Sparse high-density printing options, (b) displacement of the cantilever for tip mass load—experimental and simulation results, (c) displacement contour plot-simulation and (d) stress along the cantilever beam-simulation at 40gm tip load.

One concept of design for assembly (DFA) is to minimize the number of parts and fabricate entirely using a 3D printer. However, this notion is often challenged by the capabilities of the current manufacturing paradigm and the strength of the fabricated parts. Nevertheless, the entire robotic hand was supposed to be made with ABS material. The current design uses pins of 1 mm in diameter. As shown in Figure 4.8, it was found that the cylindrical pin connectors made of ABS materials are susceptible to high stress for the intended load-carrying capacity (1N) depending on

the geometry of the index finger under consideration. Further, if the pins were 3D printed, then they would be composed of around 5 layers of ABS plastic. This restricts the amount of detail that will be overcome when new affordable 3D printers with composite materials and high resolution are made available to the market.

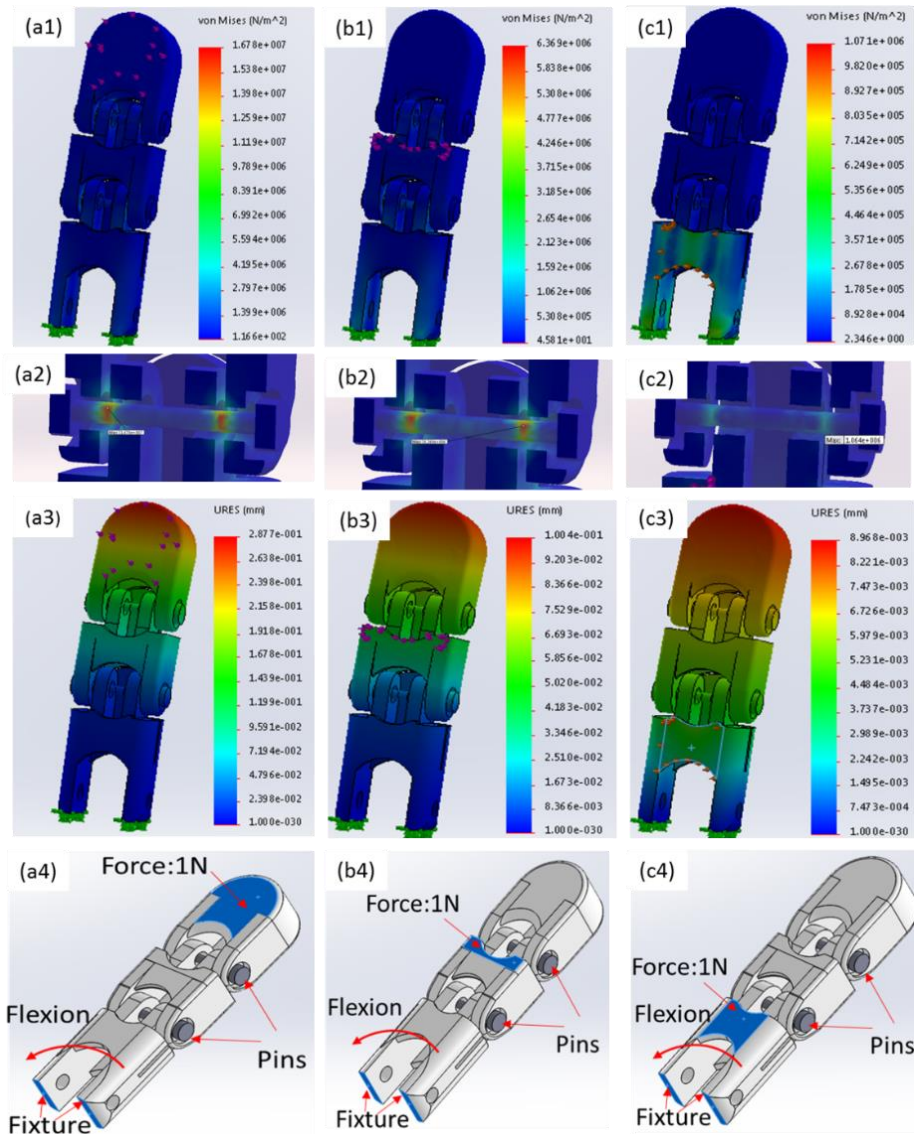


Figure 4.8. Simulations of index finger entirely 3D printed with ABS material (including the pins)-loaded with a force of 1N applied at: (a) the DIP, (b) the PIP, and (c) the MCP. (1) Von Mises stress, (2) Magnified view of the Von Mises stress in the pin, (3) Displacement, and (4) Schematic diagram.

4.4 Muscle Characterization

4.4.1 Isotonic Test Characterization

Lengthwise contractions of TCP muscles upon heating with various magnitudes of power under a 200-gram load condition were investigated (Figure 4.9). 2-ply and 3-ply TCP muscles fabricated at the twising speed of 600 rpm were tested using the experimental setup in Figure 2.7. For this study, a load of 200 g was chosen since this is the appropriate load required to overcome the torsional spring and inherent friction in the robotic hand. In this experiment, the heating time was 25 s and the cooling time was 45 s. The heating time was selected based on the previous experimental observations of temperature change and muscle contraction. It was found that a period of 25 s enables the TCP muscle to contract completely at a constant current 0.6 A under a 200-gram load. After 25 s, the temperature and the actuation stroke of the TCP muscles will not change significantly. Figure 4.9(a) shows the obtained results for a 2-ply TCP muscle under a 200-gram load when a square-wave input power (36% duty cycle and a period of 70 s) was varied between 0.18 W/cm and 0.25 W/cm. The 2-ply TCP muscles achieved an average maximum actuation of almost 14% at 0.25 W/cm applied power. Figure 4.9(b) shows the actuation results for a 3-ply TCP muscle under a 200-gram load when the input power was varied between 0.21 W/cm and 0.33 W/cm. As shown here, a tensile contraction of 13% can be achieved at 0.33 W/cm.

Further, in the isotonic tests, the constant load was varied in a wide range from 50 g to 700 g to investigate the tensile actuation of the 2-ply TCP muscle from sewing thread. In the series of test, the 2-ply TCP muscle was characterized in 3 different currents. Figure 4.10 shows the load dependence of the tensile actuation. The tensile actuation normalized to the loaded muscle length depends mainly on the applied load as the muscle elongates considerably under higher load. The

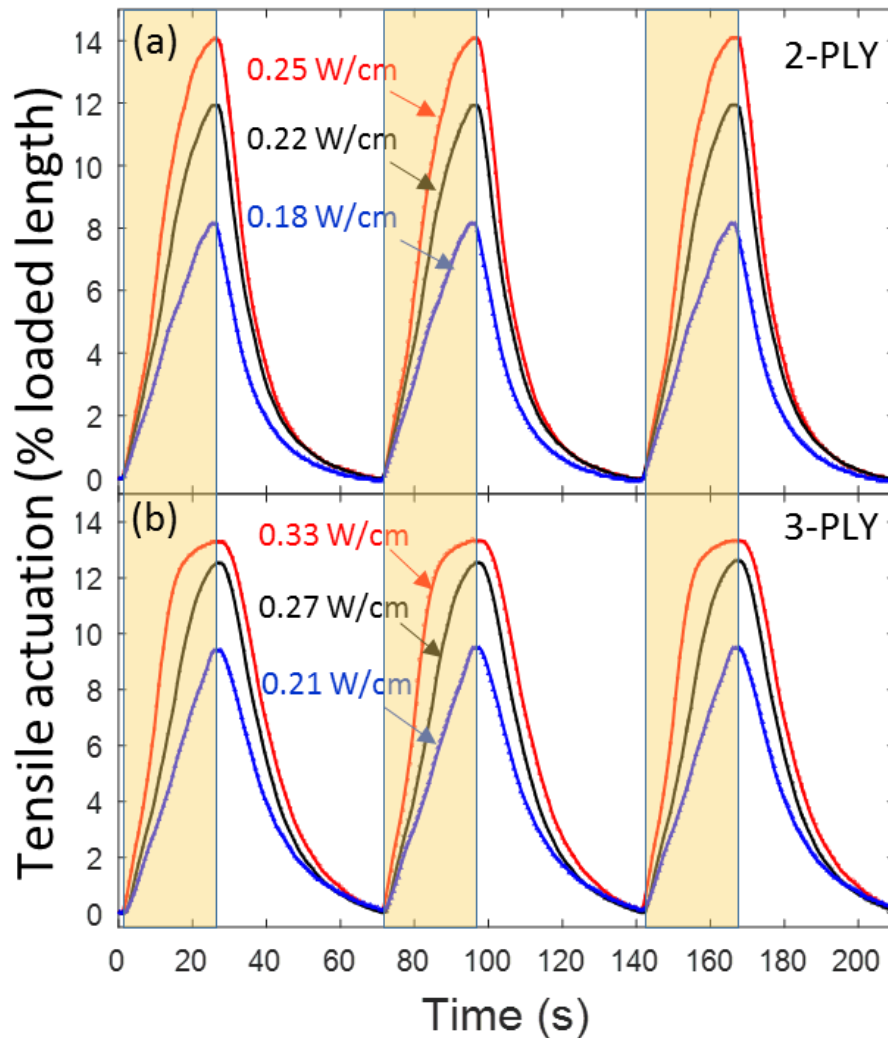


Figure 4.9. Tensile actuation study for an applied electrical power per length of the TCP muscles (square-wave input, 36% duty cycle; a period of 70 s) under a 200-gram load: (a) A 2-ply TCP muscle, unloaded length of 235 mm and 1.2 mm in diameter; (b) A 3 ply TCP muscle, unloaded length of 235 mm and 1.4 mm in diameter; and (c) Experimental setup used to determine the TCP muscles tensile actuation. The yellow shaded regions represent the heating stages.

maximum tensile actuation, realized at a constant current 0.66A, was 15 % stroke. This realized actuation stroke is significant and can be useful in many applications in robotics and other systems.

The optimal load or the lowest applied load which resulted in the maximum displacement or tensile actuation of the investigated muscle was approximately 100 g. From Figure 4.10, it is obvious that larger tensile actuation was realized at higher current. In the case of constant current 0.60A and

0.55A, the optimal load doesn't exist within the range from 50 g to 700 g. The main reason is that lower currents could not produce enough heat to actuate the muscle to realize the full amount of actuation.

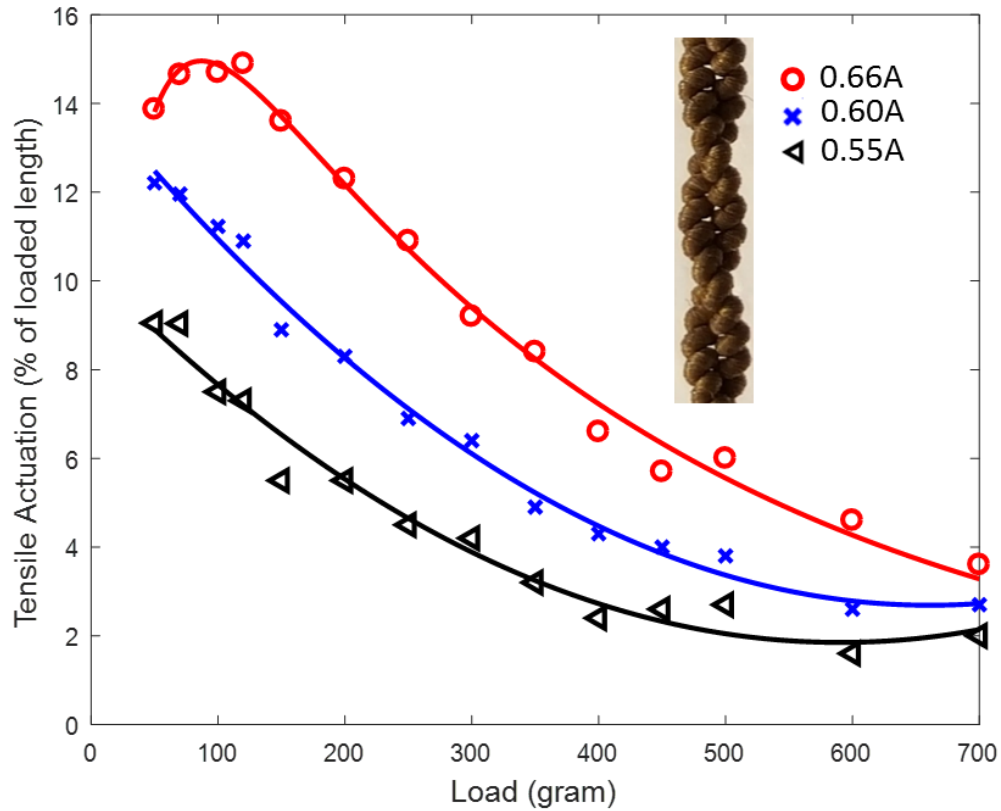


Figure 4.10. Tensile actuation as a percent of the loaded length of a 2-ply TCP muscle in an isotonic test under different load at three different current input.

Figure 4.11 shows the relationship between the temperature and the tensile actuation (of loaded length). Referring the horizontal line, it requires higher temperature to lift a 500-gram load at current 0.66A to generate the same actuation than the case of 100-gram load under the same current 0.66A. For the case of the same 100-gram load at different currents (0.66A and 0.60A), the red line representing the heating stage coincides. The nonlinear dynamics of TCP muscles is also reported in the following work [68, 136, 137].

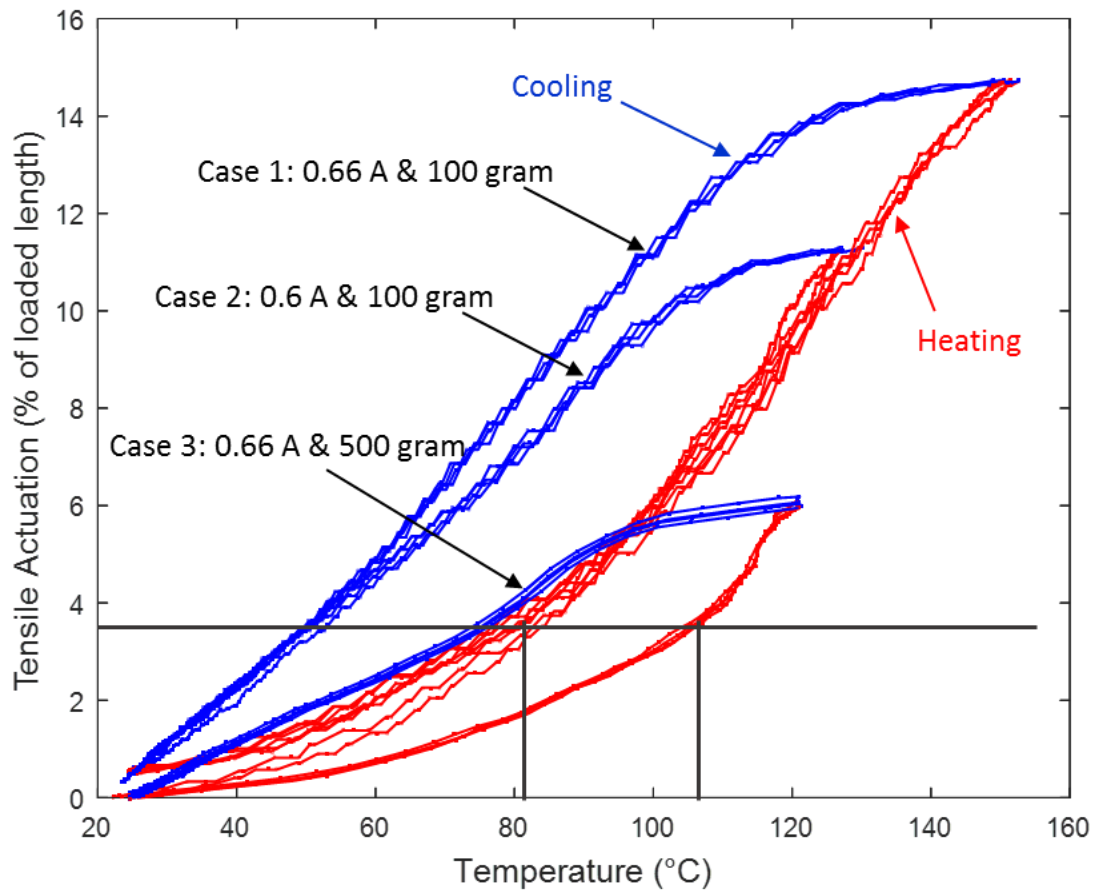


Figure 4.11. Relationship between the temperature and the tensile actuation of a 2-ply TCP muscle via Joule heating and natural cooling. The blue lines represent the cooling stage, and the red lines represent the heating stage.

4.4.2 Spring-load Test Characterization

Experiments were also conducted to investigate the force generated by 2-ply and 3-ply TCP muscles. The force was measured using a load cell (Futek LSB200). Figure 4.12(a) and Figure 4.12(b) show the force generated in response to applied square-wave power. In this experiment, the heating time was 25 s and the cooling time was 45 s. Figure 4.12(a) shows the force generated by a 2-ply TCP muscle by varying the power from 0.17 W/cm to 0.28 W/cm for 3 cycles. The maximum force was around 4.0 N. The same square-wave power input was applied to a 3-ply TCP

muscle, and the input power was varied from 0.20 W/cm to 0.36 W/cm. As shown in Figure 4.12(b), the 3-ply TCP muscle generated a maximum force of around 4.5 N. The experimental setup used for measuring the force generation is depicted in Figure 2.9(c). Both Figure 4.9 and Figure 4.12 show that 2-ply and 3-ply muscles get a higher tensile actuation and a higher force with the increase of power input.

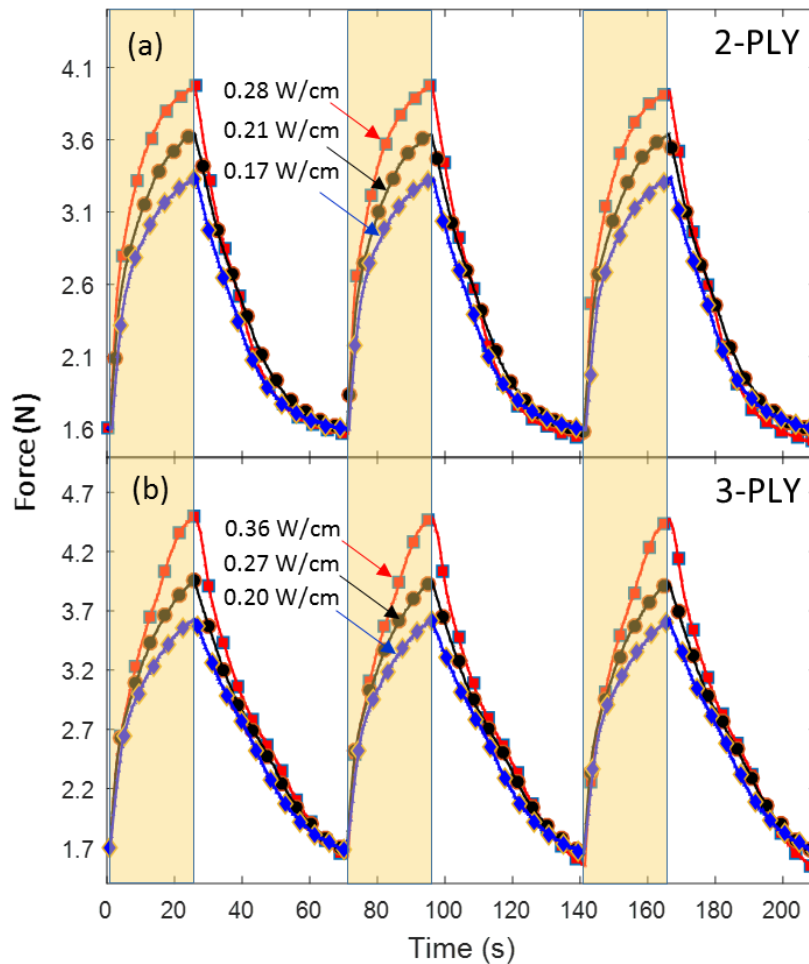


Figure 4.12. Study of the influence of applied electrical power per length of the muscle (square-wave input, 36% duty cycle, a period of 70 s) on the force generation against a passive spring of stiffness of 50 N/m: (a) 2-ply, unloaded length 235 mm, diameter of 1.4 mm (a prestress of 1.7 N); (c) Experimental setup used for testing the force output. The yellow shaded regions represent the heating stages. Note that the force output is not dependent on the muscle length but it depends on the diameter of the muscle and applied power.

To achieve fast actuation, a high-speed actuation of TCP muscle was performed. Here, the study demonstrated that it is possible to reach quick contraction (within 1 s) without sacrificing actuation stroke (Figure 4.13) by using short pulse with high electrical power. The experimental setup used for measurement of tensile actuation and force generation here was the same as shown earlier in Figure 2.7 and Figure 2.9. The voltage was measured using National Instruments data acquisition system (NI 9201) with a computer interface and LabVIEW program at a sampling rate of 1 kHz. Figure 4.13 shows the actuation results of a 2-ply TCP muscle (unloaded length 235 mm) under a 50-gram load when applying two different power input wave forms. The first test was using a low power square wave (0.25 W/cm power for 25 s). The second test was carried out by varying the high-power pulse from 1.75 W/cm to 2.15 W/cm for a short duration of 1 s for all pulsed tests. As shown in Figure 4.13(a), a pulsed power input of 2.15 W/cm for only 1 s results in nearly the same actuation stroke as that achieved by applying square-wave power input (0.25 W/cm for 25 s). From the experimental results, it can be seen that a short pulse with high power improves the actuation frequency of the muscle. In ref. [45], authors reported a 9% stroke while lifting a 300-gram load for a 2-ply, 180 μm diameter silver-plated nylon 6,6 muscle using a 40 ms pulse power. Though the low thermal diffusivity of air limits the cycle rate for passively cooled muscles, employing high thermal diffusivity fluids such as water or helium gas can significantly improve passive cooling. When immersing in water, a coiled, silver-plated, 180- μm -diameter multifilament can be electrothermally actuated at 5 Hz [45]. Figure 4.13(c) shows the results obtained for the force generation of the 2-ply TCP muscle under a spring load and applied pulse power from 1.62 W/cm to 2.24 W/cm. The unloaded length of the muscle used was 235 mm. The maximum force as shown in Figure 4.13(c) is around 0.93 N when tested under a spring load

(stiffness of 20 N/m) which is greater than the force 0.5 N required to trigger finger flexion movement in design II.

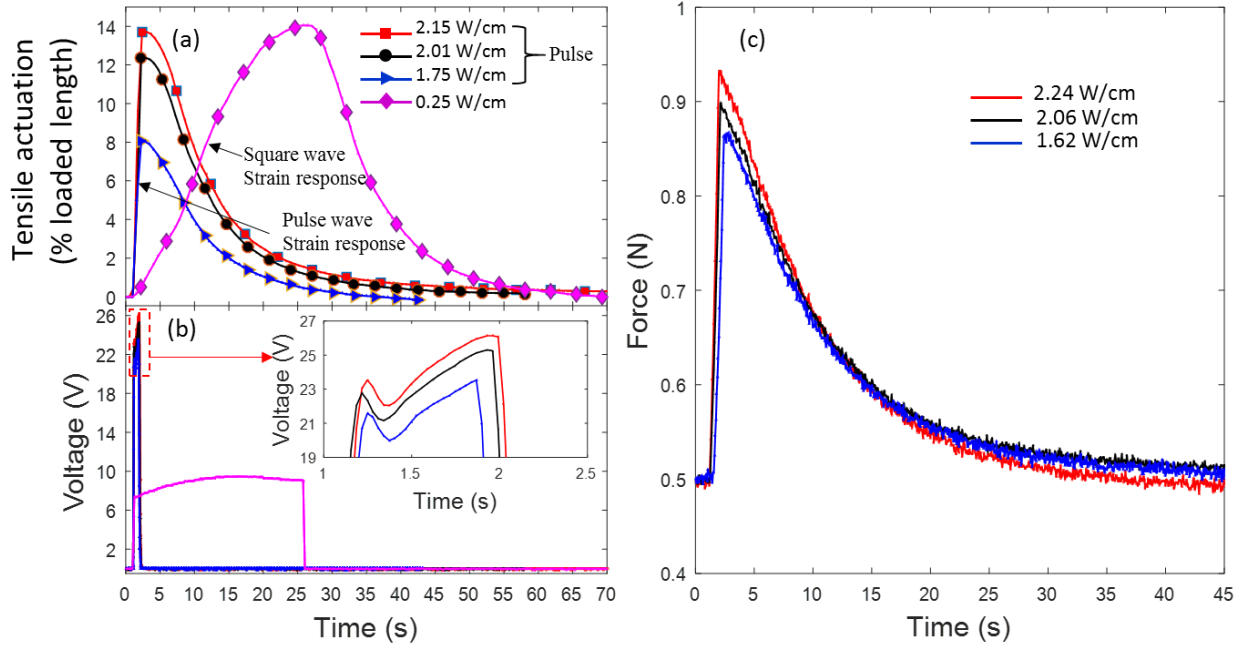


Figure 4.13. Pulsed actuation results for a 2-ply TCP muscle at different power inputs: (a) Contraction of 2-Ply muscle, an unloaded length of 235 mm, diameter of 1.2 mm, under a 50-gram load and obtained from experimental setup shown in Figure 2.7. (b) The input voltage waveform of the 2-ply muscle with a pulse duration of 1s and square wave input. (c) Force generation of a 2-ply TCP muscle of unloaded length 235 mm and diameter 1.2 mm for a pulse duration of 1 s with peak power input (the same pulse power input profile as in Figure (b) against a passive spring load (spring stiffness of 20 N/m) obtained from experimental setup shown in Figure 2.9.

4.5 Index Finger Characterization

The result of the angles for tendon displacement for the index finger in design I is shown in Figure 4.14(a). This result only holds true for coupled relationship of the joint angles. Similar test was carried out for design II, however the linear relationship did not hold true. As discussed earlier, the first prototype has torsional springs at the joints and one actuator per finger. The second

prototype has no torsional springs at the joints and it is actuated in agonist-antagonist manner (two actuators per finger). The phalange lengths of the two prototypes are also slightly different that contribute to the variation. The angular motion of the index finger was measured using a high-speed camera (Phantom Miro eX2; PCC software) by actuating the muscle in the forearm using a power supply (BK Precision 1687B). Figure 4.14(b) shows the experimental tendon displacement vs. angle relationships. As can be seen the relationships between tendon displacements and the angles are linear (regression coefficient R^2 of 0.98~0.99, indicating good correlation). The magnitude of the $\Delta\theta_1$ and $\Delta\theta_2$ has similar values to the simulated in Figure 4.14(a). However, the angle $\Delta\theta_3$ showed slight variation compared with the simulated value. This is due to the linear assumption of the angles relationship in the theoretical description, which indicates dynamic modeling is required to fully understand the system. Therefore, performing several experiments are necessary to determine the relations.

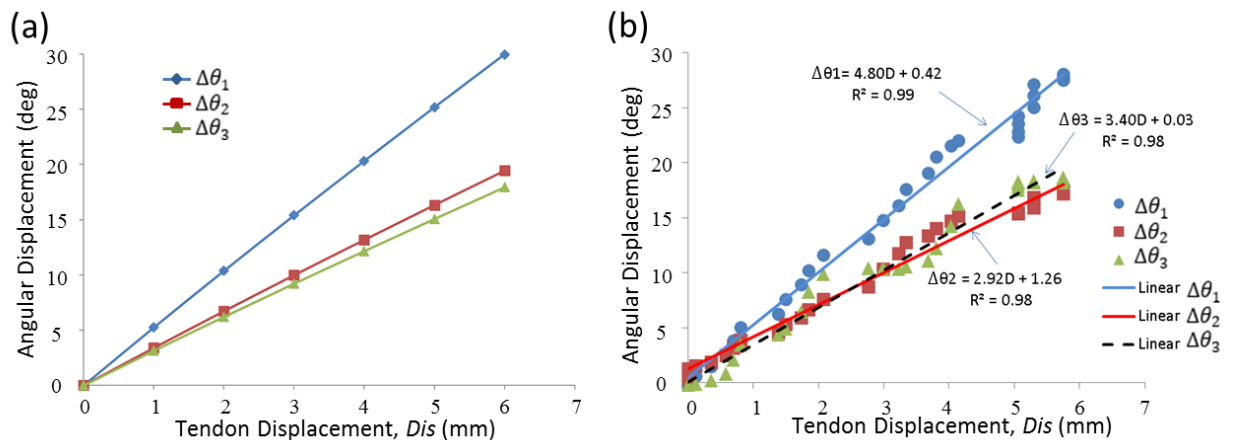


Figure 4.14. Tendon displacement and angle relationship of the index finger of design I: (a) the simulated and (b) experimental values and the linear trend lines.

Figure 4.15(a) compares the experimental joint angles (filled symbols) of the index finger of design I with the simulated angular displacement (open symbols with trend lines). The theoretical results and experimental data contained a certain error due to the existence of the torsional springs, friction, and other dynamic effects. It can be seen that the simplified kinematic model of flexor tendon predicts very well the angular displacement of the index finger. Figure 4.15(b) shows that simulated X-Y trajectories of the joints in the index finger of design I, and they are in good agreement with the experimental values. Figure 4.15(c) shows the experimental angular displacement of the joints in the index finger of design II with 1 s pulse actuation, which is acceptable and in the range of 1-1.5 s [138]. Figure 4.15(a) and Figure 4.15(c) both show that the MCP joint ($\Delta\theta_1$) has the maximum angular displacement. Figure 4.15(d) shows the fingertip, DIP and PIP joints trajectories of the index finger of design II. The second prototype hand (design II) does not have the torsional springs found in the first prototype, and this enables the prototype to have the greater range of motion needed to achieve complete flexion.

Figure 4.16 shows the angular displacement of the index finger of design II during the continuous cycle of flexion-extension without active cooling. The narrow yellow shaded regions represent the pulse actuation of the flexor muscle for a duration of 1 s. The wide yellow shaded regions represent the low voltage actuation of the extensor muscle for a duration of 5 s. The actuation sequence is predefined in a similar way as shown earlier in Figure 4.4. First, the flexor muscle was actuated for 1 s. Then, the power was turned off for 7 s, and the extension spring on the palm side started contracting and facilitated the extension movement. After that, the power was switched to the extensor muscle at 0.25 W/cm for a duration of 5 s, which worked together with extension spring to complete the extension movement. Other tests were performed but only the

shortest duration is presented. This study indicates that the finger joints can operate at 20 s period (0.05 Hz frequency) without applying active cooling to the muscles.

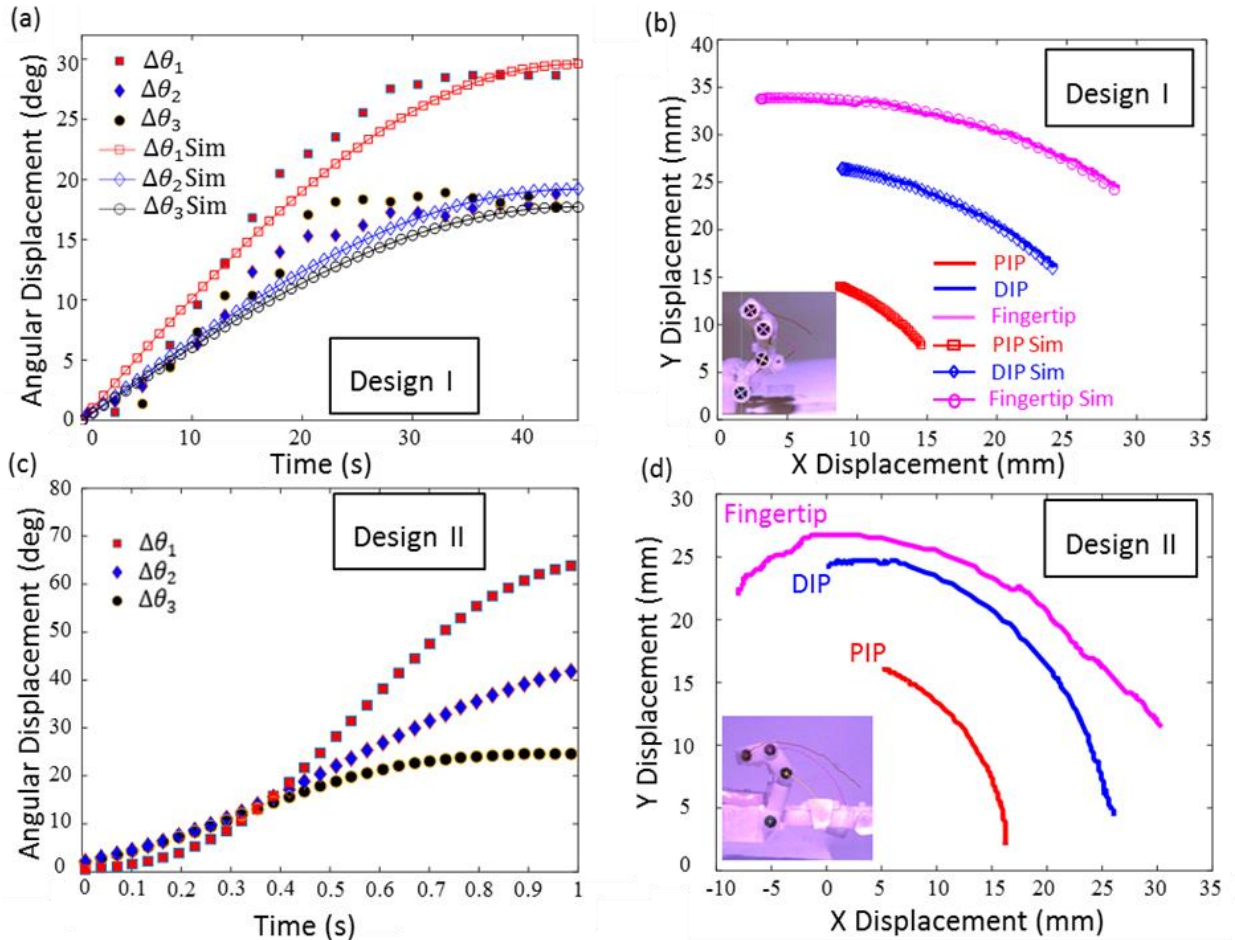


Figure 4.15. Characterization of the index finger of the prototype hands during flexion motion: (a) Comparison of experimental and simulated angular displacement of the joints in the index finger of design I (muscle's length of 100 mm) at low step input power 0.32 W/cm for 45 s. (b) Comparison of experimental and simulated joint trajectories of the index finger of design I; Inset: The humanoid hand prototype of design I with trajectories. (c) Experimental angular displacement of the joints in the index finger of design II (muscle length of 274 mm) at high pulsed power input of 2.12 W/cm for 1 s. (d) Experimental joint trajectories of the index finger of design II. Inset: The humanoid hand prototype of design II with trajectories. The experimental data were collected from high-speed camera data and processed in PCC software, and the theoretical data were obtained from Eq.4.1- 4.4 using Matlab.

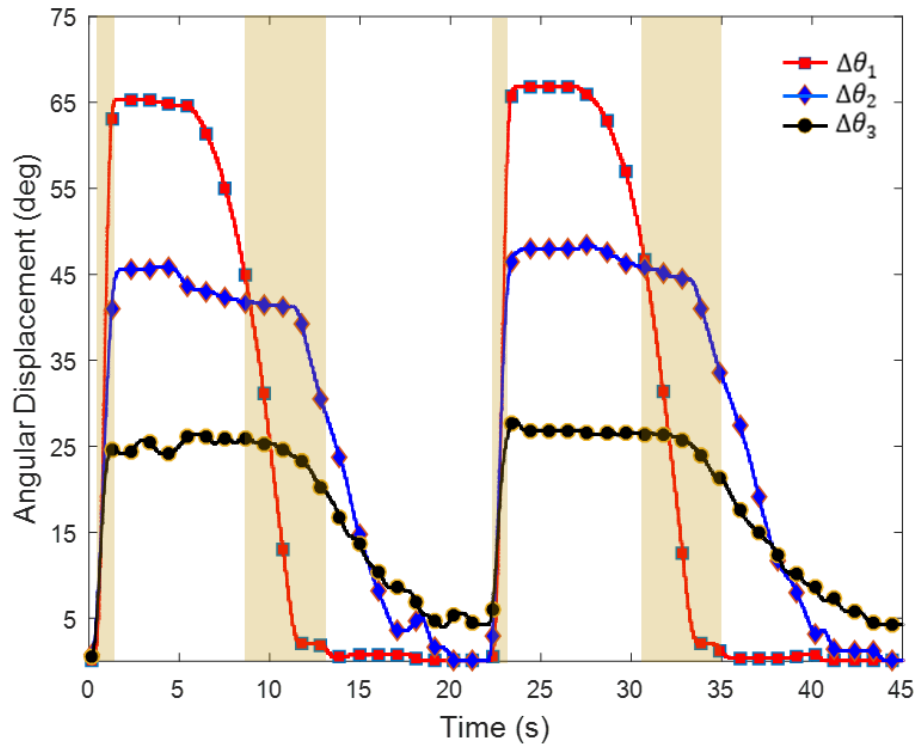


Figure 4.16. Angular displacement of the index finger in design II during the continuous cycle of flexion-extension. The narrow yellow shaded regions represent the heating stages of 1 s duration for flexor muscle at 2.12 W/cm; The wide yellow shaded regions represent the heating stages of 5 s duration for extensor muscle at 0.25 W/cm.

4.6 TCP Hand Grasping Experimental

Grasping experiments were conducted to demonstrate the performance of the second prototype hand (design II). The hand was oriented vertically so that it would grasp various objects against gravity (see examples in Figure 4.17). Voltage was provided to all flexor muscles by a DC power supply with multiple outputs (BK Precision 1687B). For actuation of the robotic finger, a microcontroller based circuit similar to the one demonstrated in Tadesse *et al.* [121] was constructed for controlling the sequence of finger motion as a preliminary testing. However, a DC power supply provided constant current input to the actuators and hence it was adapted to power

the robotic hand. Experimental results (Figure 4.17) show that the TCP hand has the ability to grasp different shaped objects, including a sphere, cylinder, cone and commonly used tools such as a stapler and syringe. Table 4.3 summarizes the objects the TCP hand could grasp. The TCP hand was capable of flexion, extension, and manipulation similar to that of a human by controlling the bending of each finger. The maximum fingertip force produced by the index finger in a maximum flexed posture was approximately 0.4 N for one 2-ply TCP muscle (measured at 0.21 W/cm power and at the end of the period of 30 s). However, the fingertip forces are not the potential upper limit of the robotic hand. The fingertip force could be improved by replacing the 2-ply muscles currently used with larger diameter muscles or by using multiple small diameter muscles in parallel. The robustness of grasping against resisting objects and the in-hand manipulation will be investigated in future work.

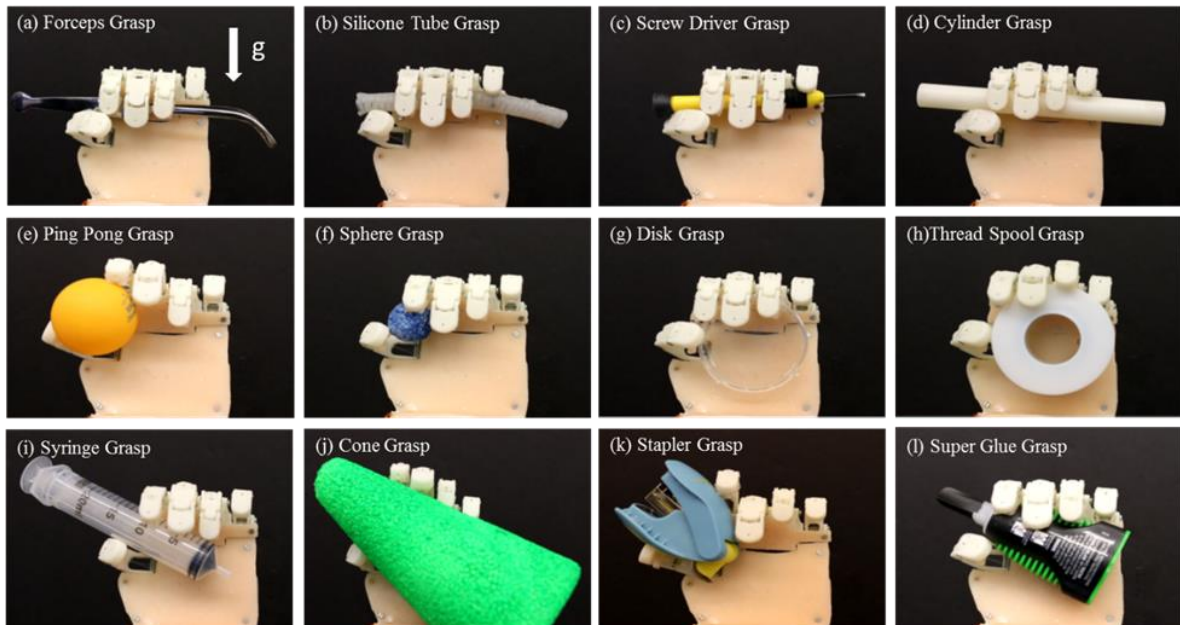


Figure 4.17. Grasping configurations on the TCP hand -prototype II: (a) forceps, (b) silicone tube, (c) screwdriver, (d) cylinder, (e) ping-pong, (f) sphere, (g) disk, (h) thread spool, (i) syringe, (j) cone, (k) stapler, (l) super glue. Gravity is in the same direction for all images as shown in (a).

Table 4.3. The various objects the TCP hand could grasp

Name	Forceps	Silicone Tube	Screw Driver	Cylinder Tube	Ping Pong	Sphere	Disk	Thread Pool	Syringe	Cone	Stapler	Super Glue
Mass (g)	26.0	8.0	7.0	7.0	2.7	0.5	4.5	33	14.0	4.0	38.0	26.0
Size (mm)	$L=150$	$L =115$ $D =10$	$L = 110$	$L = 130$ $D = 13$	$D = 40$	$D = 22$	$D = 60$ $T = 6$	$D = 56$ $T = 20$	$L = 125$ $D = 21$	$D_{\max} = 8$ $D_{\min} = 26$ $H = 155$	$LxWxH = 60x33x46$	$LxWxH: 13x44x63$

(L = length, W = width, H = height, T = thickness, and D = diameter).

4.7 Robotic Finger Actuated by Mandrel-Coiled Fishing Line Muscle via Fluidic method

Figure 4.18 shows hydrothermal actuation of a coiled 3.33-mm-diameter nylon 6 fishing line lifting a 200-gram load by 22% when switched between 21°C water and 99 °C water manually using the experimental setup shown in Figure 2.8. Hot water was used for the actuation of the muscle. This is different from Joule heating as the water directly heats the muscle. The monofilament reached the maximum displacement almost 37.5 mm at 200-gram external load.

Figure 4.19 shows the results with monofilament coiled fishing line muscles at 200 g and varying the heating source temperature between 60 °C and 100°C accordingly to experimental setup shown in Figure 2.8. The tensile actuation was calculated as the contraction displacement to the initial loaded length of the fishing line. The tensile actuation of the coiled muscle between 60 °C and 100°C increased from 8% to 22%. Monofilament coiled muscle actuation above 10% can be easily achieved at a temperature of 70°C. When the hot water passed through the channel, the coiled muscle only required 1.5 second to contract. Using active cooling method, in this study, 21°C water was used to provide the fast cooling speed. Without any active cooling, the cooling time is naturally longer than the heating time.

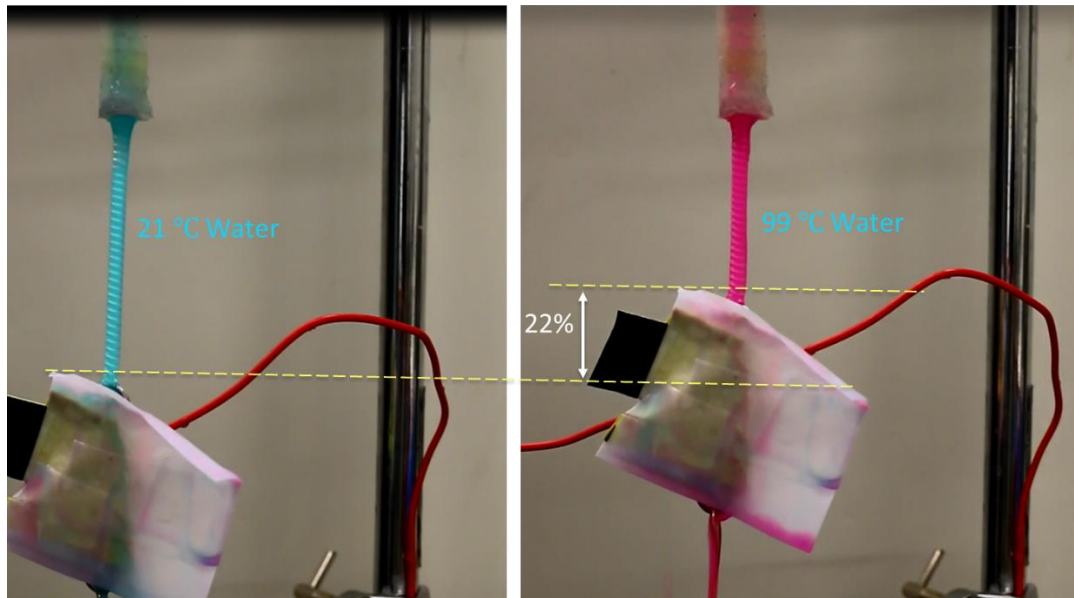


Figure 4.18. Hydrothermal actuation of a coiled 3.33-mm-diameter nylon 6 fishing line lifting a 200-gram load by 22% when switched between 21°C water and 99 °C water manually.

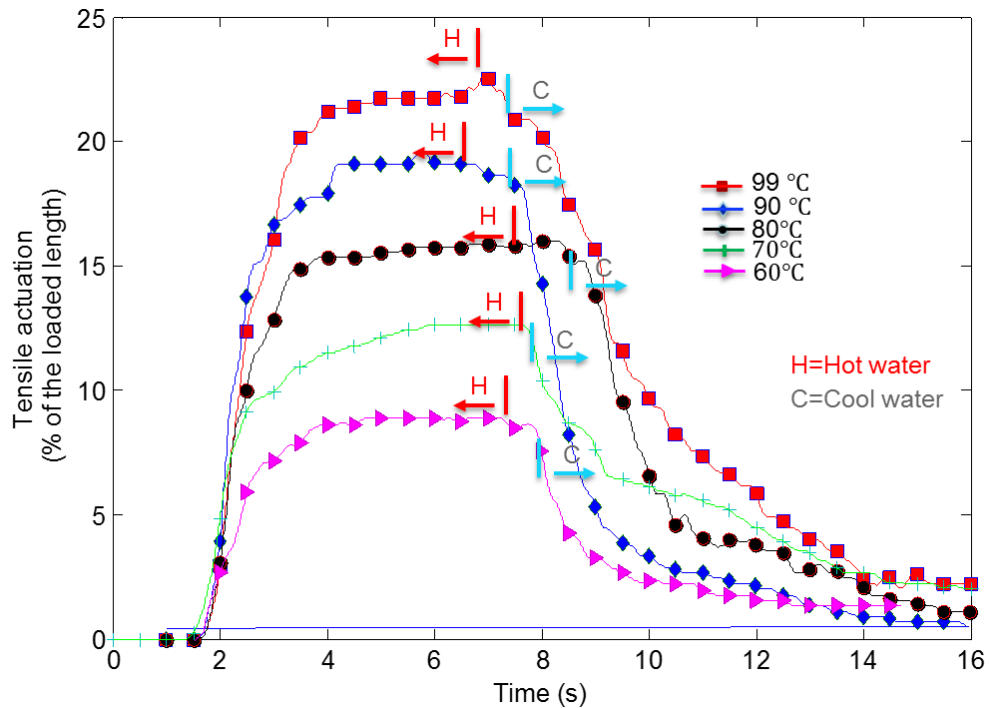


Figure 4.19. Tensile actuation for a coiled fishing line muscle as a function of the temperature of the hot water used to produce muscle contraction. A 200-gram weight was raised during muscle contraction.

In this section, the design of the fluidic actuation system is reported and illustrated in Figure 4.20(a). Matthew et al. proposed a wet shape memory alloy actuator in [13]. In that paper, they demonstrated that the compliant tube enables the actuator to expand and contract freely. In this study, to serve the requirement for pre-strain in the actuation of the coiled fishing line muscle, a spring was embedded in the silicone tube which provided the pre-strain without losing the tube's compliance. Figure 4.20(b) illustrates the actuator system composed of a silicone tube with embedded compression spring and a coiled fishing line muscle, and two 3D printed connectors which were attached to the two terminals of the silicone tube. Silicone was chosen for fabricating the tube to enable the actuator to have a soft and flexible body. The coiled fishing line muscle was employed as the contractile elements of the actuator system. The coiled muscle measures 3.33 mm in diameter and 86 mm in length, while the silicone tube is 8 mm in diameter and 112 mm in length. One end of the actuating system is fixed in the forearm while the other end was connected to the string which was fixed at the fingertip.

Next, the experimental setup used for testing the performance of the coiled muscle in the robot hand was described. A block diagram of the experimental setup is shown in Figure 4.20(c). The experimental setup consists of power supply (Topward 6306D), mini DC water pump (Size, L×W×D: 32 mm x 22 mm x 36 mm), water reservoir and 3D printed hand prototype. In Figure 4.20(d), two pumps that provided with hot water and cold water were connected to the fluid inlet of the actuator system. The fluid came out from the outlet terminal of the actuator and was taken to a reservoir. The water pump is capable of delivering hot water at high temperature 100°C which can generate a large tensile actuation. The water pump can also generate the necessary pressure to deliver the hot water through the silicone tube. The finger flexion motion operates as follows:

power is supplied to the hot water pump; the hot water passes through the silicone tube and across the coiled fishing line muscle resulting in longitudinal shortening. The soft compliant silicone tube is compressed due to the contraction of the coiled fishing line muscle while pulling the flexible string attached to the fingertip allowing the flexion of the index finger.

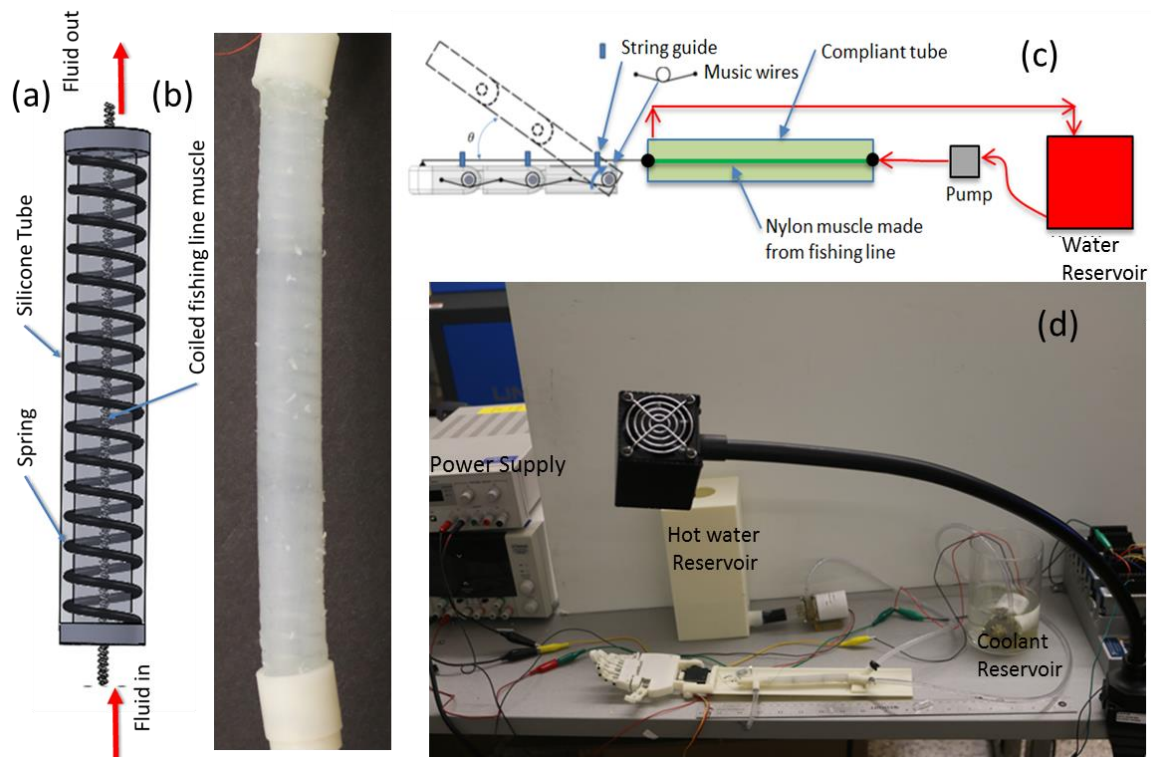


Figure 4.20. (a) Coiled fishing line actuator concept and (b) the assembled coiled fishing line actuator. (c) Schematic diagram of the experimental setup to test the performance of the coiled muscle in the application of robot hand and (d) picture of the laboratory experimental setup.

The trajectory of the index finger joints was also obtained by using a fast camera (Phantom Miro eX2). Four black rectangular marker papers were placed to index finger joints. In order to verify the feasibility of the design, the index finger was actuated as a representative model for actuation. Figure 4.21 shows the joint trajectories of the index finger for flexion. Figure 4.21(a) shows the initial position before actuation. Figure 4.21(b) shows the final position of the index

finger after actuation. From observation, the response was quite fast and it took less than two seconds for the flexion.

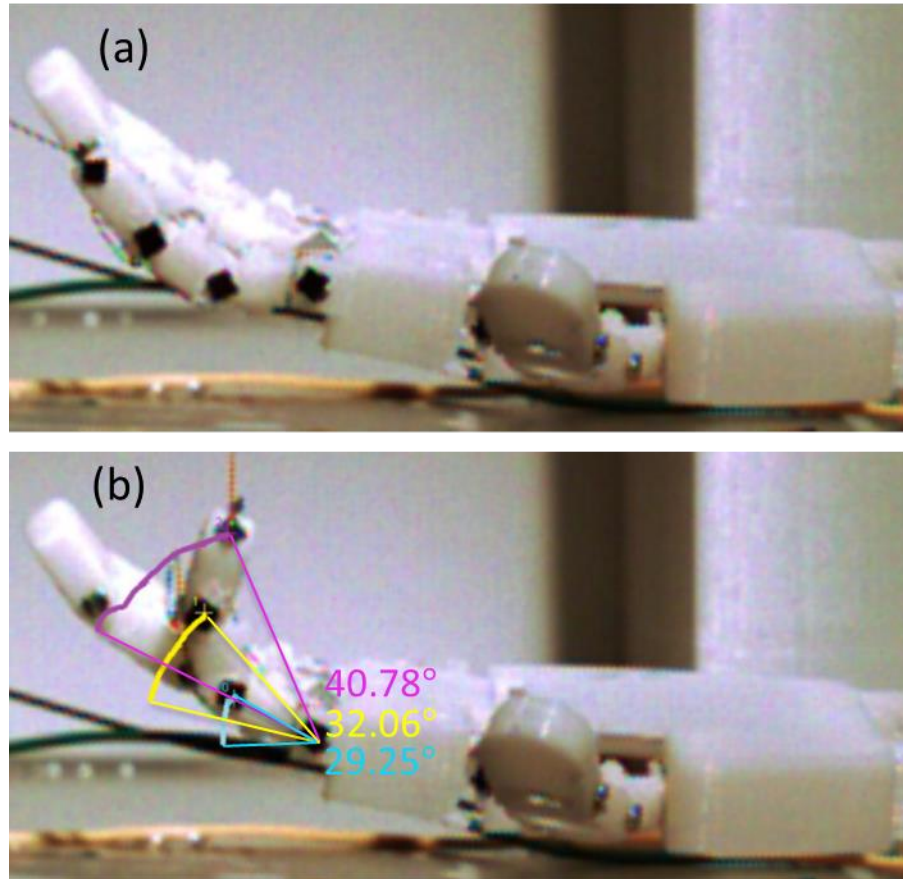


Figure 4.21. (a) Initial position of the index finger before actuation and (b) Final position of the index finger after actuation.

4.8 Summary

In this study, a biomimetic design and characterization of humanoid hands utilizing high-performance, low-cost artificial muscles based on twisted and coiled polymer (TCP) muscles were presented. Especially, the TCP hand with agonist and antagonist actuation system was extensively studied. The 3D printed hand has a total of 16 DOF (3 DOF per finger and 1 DOF at the palm) and

a kinematic structure similar to a natural hand featuring five articulated fingers, a hand size of 122 x 64 x 14 mm, overall arm length of 185 mm and a total weight of 140 g. The three phalanges of each finger in the hand are actuated by only one actuator for coupled motion.

The novel TCP muscles, unlike cumbersome servomotors, enable the placement of the actuators in a limited space resembling such as that of a 7-year-old child arm and hand. Thus, the mechanism can meet the strict size and weight constraints that are typically challenging requirements of robotic and prosthetic hands. The inexpensive actuators (2-ply) used in this study were able to deliver a tensile actuation stroke up to 14% for an applied power of 0.25W/cm square wave and a force of 4N for an applied power of 0.28W/cm square wave. In order to achieve fast motion, a short pulse with high electrical power of ~ 2.12 W/cm was supplied to TCP muscles that results in flexion of the hand within 1s without applying active cooling of the muscle. This is acceptable and in the range of 1-1.5s. A kinematic model of flexor tendons was developed and used to describe the finger motion. Results of grasping various objects with different size and weight for validating the performance of the TCP hand were also reported in the study.

Mandrel-coiled nylon muscle from fishing line was also tested via hydro-thermal actuation as an actuator in the robotic hand. The tendon string was tethered to the fingertip of the index finger and the other end was attached to the coiled fishing line actuator. The actuation system consists of a compliant silicone tube that houses a spring and a coiled muscle. The silicone tube allows the coiled muscle to contract when hot water is pumped through the channel. Experiments were carried out to investigate the characterization of the coiled fishing line muscle in embedded conditions. A strain magnitude of 22 % was obtained for a muscle made of fishing line of diameter 3.33 mm at an applied dead weight of 200 g. The hydrothermal-driven actuator took about only 1.5 seconds to

fully contract, and using cool water can provide fast reversible actuation. This muscle was able to actuate the fingertip of an index finger at an angle of 40.78° with a fast-responding speed and less than two seconds for the flexion. One challenge is the return motion (extension motion) of the robotic fingers, which requires longer time for cooling. This can be addressed by exploring various active cooling techniques. Another approach is to use antagonistic pair of muscles to facilitate the relaxation of muscles, which will be discussed in the next chapter.

CHAPTER 5

MUSCULOSKELETAL SYSTEM FOR SOFT ROBOTICS

5.1 Introduction

The musculoskeletal system (MS), which combines the muscular and skeletal systems together, is a vital biological system that enables humans and other animals to move and function in their daily lives. Comprised of bones, muscles, tendons, ligaments and other connective tissues [139], this system allows the contraction of muscles to maneuver the skeleton that supports and protects the body, allowing versatile movement of the body. Musculoskeletal system is the fundamental structure that allows complex mobility of biological systems. Therefore, the MS system is one of the most essential anatomical parts of humans and animals.

The combination of muscles, bones, cartilages and ligaments that are essential for mobility can result in different configurations of the musculoskeletal system design. The challenges for developing musculoskeletal structure in a robotic form to bring more advanced, safer, for other bio-inspired robotic systems include design and manufacturing, actuators integration, and control methods. A lot of efforts have been made in the past to mimic this structure using synthetic materials for use in robotic systems. Here, this chapter first describes the review of different artificial musculoskeletal systems and the actuators used in those systems, as actuators or muscles that drive the skeleton are the limiting elements. Several musculoskeletal model developments were presented in [140-142]. Unique design approaches were presented based on musculoskeletal system [143], such as Kotaro [144] (130cm, 69DOF), Kenzoh [145] (135cm, 58DOF) and Kenshiro [146] (90cm, 46DOF) robots. Damsgaard et al. [147] presented a review of one commercial musculoskeletal system simulation software, the AnyBody Modeling System (AMS). OpenSim is

another similar musculoskeletal systems modeling software [148]. However, to effectively address the challenging goals of musculoskeletal system, both the development of software and hardware devices need to be advanced. One of the most important elements of musculoskeletal system is artificial muscles or actuators utilized in the system. Many types of actuators such as shape memory alloy (SMA), dielectric elastomer, pneumatic muscle, conducting polymer muscle, ionic metal composite (IPMC) and servos are proposed in the literature [60, 149-152]. However, all of them have their own advantages and disadvantages. In their paper, Richter et al. [153] discussed the deployment of “Myrobotics”, which is a DC-motor-based actuator system that mimics the complex human arm. Easiness of integrating or replacing the muscle is another important issue that has been considered. Ikuo, et.al. [154] showed an advanced musculoskeletal humanoid called Kojiro, in which easily replaceable or modifiable “muscles” consisting of DC motors with gearheads were used. Researchers in [155] put an effort on developing a cable actuated 2 degrees of freedom (DOF) joint mechanism for surgical robotic application based on DC motor technology. Besides DC motors, pneumatic artificial muscles [102, 156-158] are of interest for biologically-inspired musculoskeletal system. Due to pneumatic muscles’ similarity to natural muscles in terms of length-load curves, their super compliance, rapid contraction, and the high power/weight ratio, Niiyama, et.al. [157] proposed an artificial musculoskeletal system for jumping robots based on a pneumatic system which consists of six McKibben actuators. Another application of pneumatic muscles into a musculoskeletal system for a biped robot was also reported in Niiyama and Kuniyoshi’s work [158]. Ikemoto et.al. [102], developed a linkage mechanism for a musculoskeletal robot arm using pneumatic artificial muscles to mimic the kinematic structure of humans. Ranzani et.al. [159] reported a soft manipulator based on a series of pneumatic chambers

for minimally invasive surgery. A flexible robotic spine actuated by shape memory alloy, which was able to achieve both bending motion and impact absorption was presented in [160]. However, actuators such as the electric motors and pneumatic artificial muscles used in the robots mentioned above have their own drawbacks. Although electric motors are energy efficient actuators, they require complex transmission system, resulting in limitations in terms of size and space. Above all, electric motors do not fit the bio-inspired design approach. On the other hand, pneumatic artificial muscles require a compressor to force a gas into the actuators to create a pressure difference between the inside and the ambient environment for actuation purpose. This makes pneumatic artificial muscles bulky in an overall system. The other major drawbacks are the requirement of solenoid valves and the large noise from the compressor during actuation. Reviews of actuation technologies suitable for humanoids and other robots are summarized in literature [104, 161, 162]. Most of actuator technologies do not match the performance of natural muscles in all metrics such as force generation, strain output, frequency, power density, ease of control and repeatability. In this chapter, a new bio-inspired approach was proposed to develop a musculoskeletal system which can serve as a building block for other biomimetic systems that can then be cascaded in various fashions to create advanced robots. Since the structures and principles found in nature are optimum for performance, nature is the best resource for inspiration and biomimicry. Figure 5.1 shows different animals, including those that can crawl, swim, walk and fly. Looking into the details of the skeletal system of these species, a unique structure that exists in the biological system of snake's vertebrae [163], fish's pivot [164], cat's hip [165], and bird's shoulder joint [166] is the ball-and-socket joint. Given the unique biological significance of this joint, an artificial musculoskeletal system based on the ball-and-socket joint for robotic systems

was proposed. The proposed ball-and-socket joint is actuated by tendon-like artificial muscles without any complex transmission system and resembles more biomimetic. In comparison with other assemblies, the proposed ball-and-socket joint is a promising solution to the diverse applications in robot joint, robot hands and other mechanisms that demand high performance, low cost and compact systems.

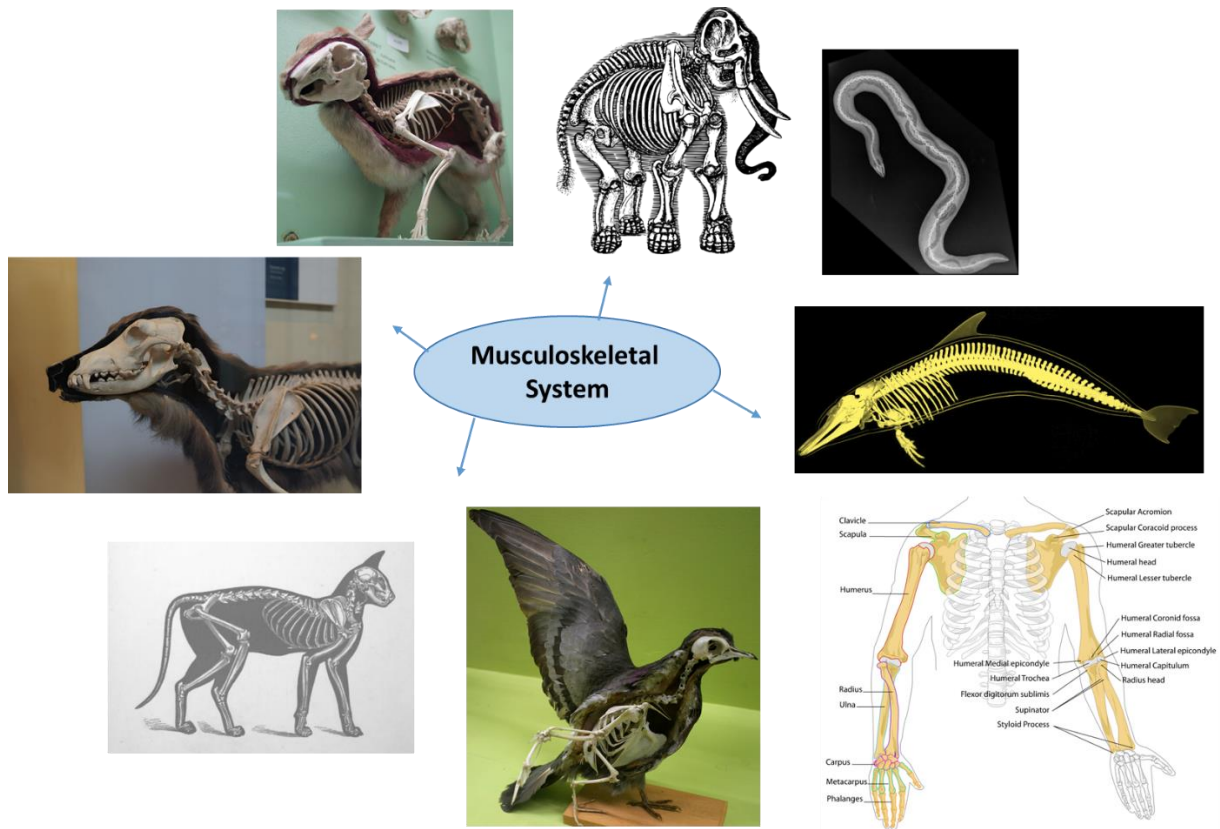


Figure 5.1. Musculoskeletal system in different species.

One of the key elements of musculoskeletal system is artificial muscles or actuators used in this system. In the proposed design of the joint structure, a new structure of twisted and coiled polymer (TCP) muscle from fishing line incorporating a nickel chromium resistance wire is developed as an actuator in the musculoskeletal system. This actuator can be referred as TCP_{NC}^{FL}

muscle hereinafter. This new version of the muscle is expected to overcome the limitations of motors and pneumatic artificial muscles and match some of the properties of natural. Human skeletal muscles provide 40% strain, 0.35MPa stress, 9-284 W/kg power output and life cycle of 10^9 cycles [122]. The recently emerged TCP muscle, can deliver a large strain of 49%, lift loads over 100 times heavier than those lifted by a human muscle of the same length and weight, generate 5.3 kW of mechanical work per kilogram of muscle weight, and undergo over 1 million life cycles. Compared with conventional actuators, the main advantages of TCP muscles are low-cost, minimal hysteresis, compact, lightweight and high power to weight ratio (the power per weight is about 7.1 horsepower per kilogram). These promising characteristics led to the widespread applications of these muscles in robotic hands [72, 128, 167], artificial skin[168], tensegrity robot[169], energy harvester [51], and other low-cost and high-performance robotic systems.

5.2 Design

5.2.1 Anatomy of the Human Shoulder

Detailed knowledge of biomechanical models is essential for improving the design and investigating biomechanical phenomena. It is not necessary to have bold engineering solutions to design a better musculoskeletal system, all that is required is to study nature and replicate the structure with synthetic materials. Figure 5.2 illustrates the structure of a human shoulder joint. As shown in the figure, the shoulder joint consists of rotator cuffs, a glenoid, a humeral head, a cartilage humerus, clavicle, acromion, scapula and synovium.

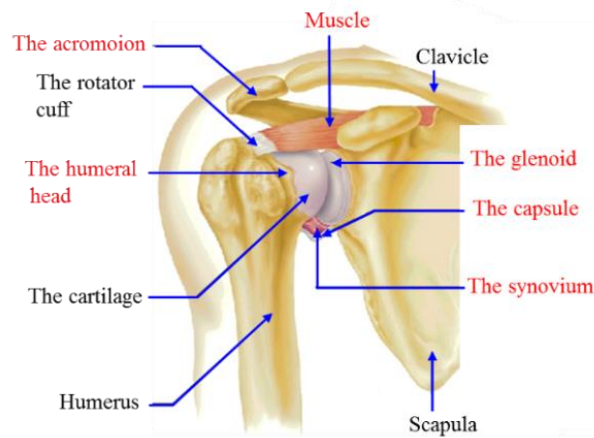


Figure 5.2. Structure of shoulder joint [170]

The shoulder joint is a ball-and-socket joint, which moves by contracting the muscles. The glenoid resembles a socket shape supporting the head of the arm bone, which looks like a ball. But only glenoid and humeral head are not enough to stabilize the motion of the shoulder. Therefore, a flexible sheet of fibers called capsule (not shown in the figure) surrounds the joint to stabilize the joint. The synovium produces a fluid to reduce the friction and avoid rubbing of bones during contact.

5.2.2 Biologically Inspired Joint Design

The first proof of concept design (design I) are illustrated in Figure 5.3. The prototype in design I has 136 mm in height and 59 mm in overall diameter. In this design, to mimic capsule's function, silicone elastomers (Ecoflex® 00-30 and Ecoflex® 00-10 shore hardness) were used to make the stabilization element to make the structure stand still. The structures were 3D printed with ABS-plus material in assembly mode (printed together as an assembly). The 2-ply twisted and coiled

polymer muscles from sewing thread were employed as the contractile actuators of the joint in the sides of the structure for inducing multidimensional actuation.

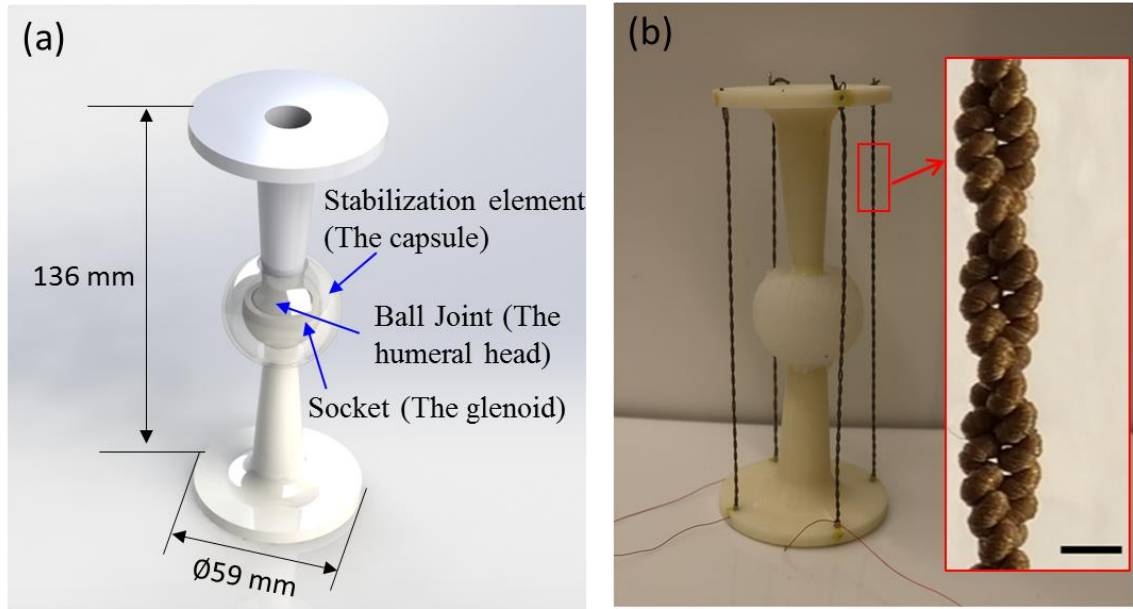


Figure 5.3. MS prototype in design I based on 3D printed ball and socket joint with stabilization element made of silicone: (a) CAD Design and (b) Prototype integrated with TCP muscles. The bar scale is 1 mm long.

The second design of musculoskeletal system consists of a 3D printed ball-and-socket joint, TCP_{NC}^{FL} muscles, a stabilization element made of silicone to serve as ligament, and soft silicone layer to embed the entire structure and serve as a tissue surrounding the joint. The entire system is designed to actuate in multidimensional fashion. Figure 5.4(c) shows the second prototype of the musculoskeletal system. The ball-and-socket joint will function as the skeletal system frame for biomimetic robots and other structures such as prosthetics. The ABS printed joint allows for the movement of the system through the contraction of the antagonistic pair of muscles. TCP_{NC}^{FL} muscles are used as actuators and make up the muscular system. Muscles of equal length are placed

in antagonistic pairs. The advantage of deploying antagonistic pairs of muscles is to facilitate the relaxation of the actuated muscle after contraction. As the actuated muscle contracts, the extension of the non-actuated muscle on the other side due to compliance can facilitate the relaxation of the actuated muscle.

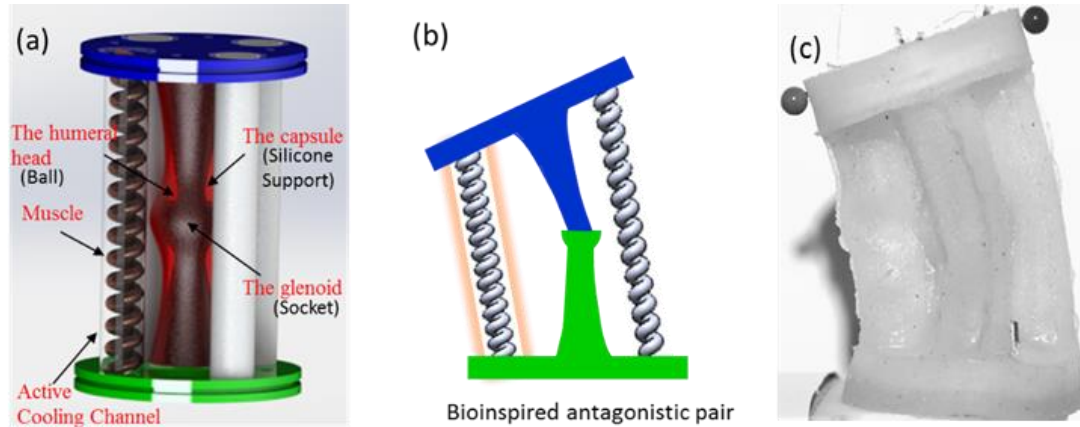


Figure 5.4. (a) Schematic diagram of the MS prototype in design II based on ball-and-socket joint structure using bioinspired antagonistic pairs of muscles. (b) The musculoskeletal system under actuated state, and (c) The final fabricated prototype of MS.

The fabricated muscle with the nichrome wire for the joint is shown in Figure 5.5A and the muscle capability of lifting a 100-gm load by a 53% tensile actuation is demonstrated in Figure 5.5(b). The CAD designs illustrated in Figure 5.4(a) were created in SolidWorks, and the ball-and-socket joint was 3D printed with ABS-plus material using Stratasys Fortus 250MC. To mimic the synovium's fluid and provide lubrication, jet-lube grease was added into the clearance between ball and socket joint. To replicate the capsule, silicone elastomer (Ecoflex® 00-10 shore hardness) was used to fabricate the stabilizing element. Finally, TCP_{NC}^{FL} muscles were employed as contractile actuators for the joint in four sides of the structure to provide multi-dimensional actuation. Figure

5.4(b) shows the schematic diagram of the ball-and-socket joint actuated using the bioinspired antagonistic pair of muscles.

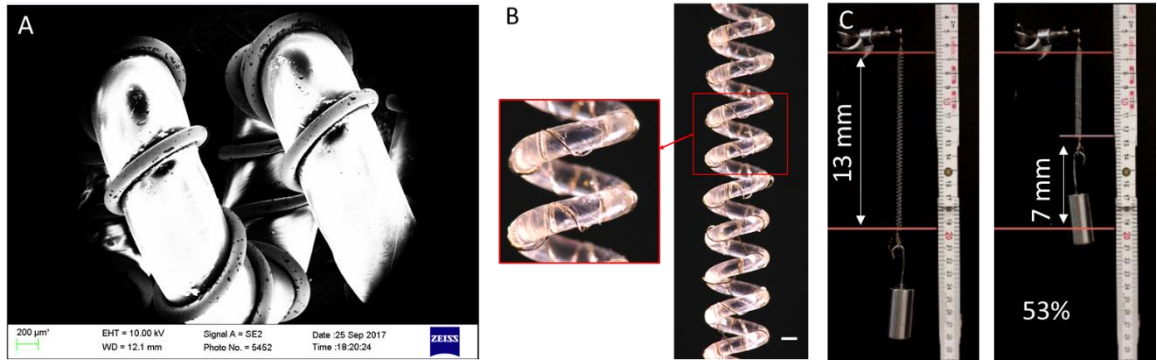


Figure 5.5. Muscle structures and implementation in musculoskeletal system. (A) A scanning electron microscope (SEM) image of TCP_{NC}^{FL} muscle. (B) Optical images of TCP_{NC}^{FL} muscle. (C) Electrothermal actuation of TCP_{NC}^{FL} muscle lifting a 100-gram load by 53% actuation stroke at a constant current 0.22A for a period of 6 seconds.

5.2.3 Kinematics of the Musculoskeletal System

The kinematic-specific models were used to locate the muscle attachment position and to estimate the maximal muscle moment-generating capacity for fulfilling rotational motion. Referring Figure 5.6(a) and (b), the position of the attachment point of the muscles to the plates can be calculated as follows:

$$(1 - \varepsilon) \cos \theta = \sin(90 - \theta - \beta/2) \quad (5.1)$$

Where ε is the muscle actuation stroke per length or strain, θ is the angle pointing to the muscle attachment from the center of the ball joint, β is the maximum bending angle of the joint and $\alpha = 90 - \theta - \beta/2$.

For specific actuators whose performance (strain, ε) have been determined, and the required bending angle (β), we can determine the muscle attachment position which is controlled by the

angle θ . In Eq.5.1, suppose the muscle has an average 12% actuation stroke ($\varepsilon = 0.12$), and the bending angle needed is 30° (β). Based on the equation (5.1), $\theta = 18.3^\circ$.

Moment of rotation M_z can be calculated as the product of force F and moment arm about the effective center of the rotation (CR, about z-axis). Let F be the force generated by the muscle. Assuming only one of the muscles is actuated to bend the joint, ignoring friction and damping, a simplified dynamic equation is given by:

$$M_z = F \left(\frac{l}{\cos\theta} \right) \cos\alpha = I_z \ddot{\beta} \quad (5.2)$$

Here l is the length of the upper and the lower ABS joint as shown in Figure 5.6, I_z is the moment of inertia of the moving joint about z-axis (the upper one) and $\ddot{\beta}$ is the angular acceleration of the joint.

In design I, the other dynamic motion of the joint is twisting motion about y-axis. Referring Figure 5.6(b)-(d), the moment M_y can be calculated as the product of force F_{ti} and moment arm $l * \tan\theta$, about the effective center of the rotation (CR, about y-axis). The moment is a summation of multiple actuators that should be summed up depending on their actuation conditions. Only the component F_t in the direction tangent to the radial direction contributes to the moment. F_{ti} is also determined by the muscle attachment position and the initial twisting angle of the ball-and-socket joint.

$$M_y = \sum_{i=1}^n F_{ti} (l \tan\theta) = I_y \ddot{\delta} \quad (5.3)$$

Where n is the total number of actuators triggered, I_y is the moment of inertia about y-axis and $\ddot{\delta}$ is the angular acceleration of the joint during twisting motion.

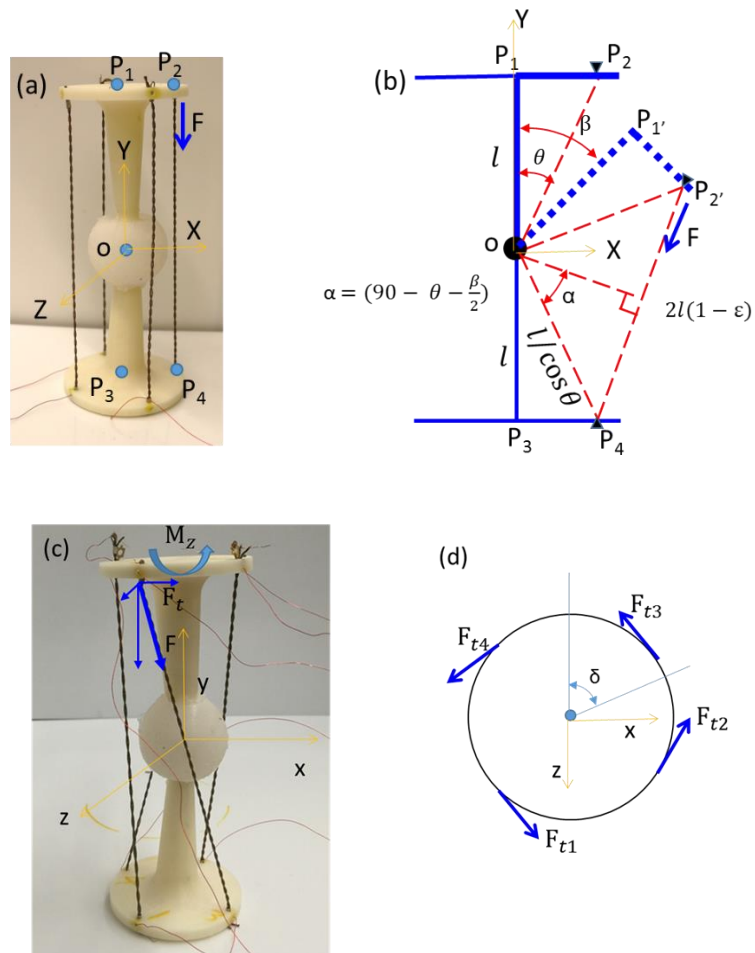


Figure 5.6. Modeling of the ball and socket joint (MS prototype in design I). (a) configuration of the prototype during bending motion about z axis and (b) schematic diagram of the bending motion, (c) the prototype during twisting motion about y-axis and (d) the top view of the joint during twisting motion.

The performance of the artificial muscle determines the working space of the final prototype of the MS joint. In the MS prototype in design II, position analysis was carried out to investigate the relationship between the pose of the top moving plate and the muscle tensile actuation. The kinematic diagram of the MS joint is shown in Figure 5.7. Coordinate system 1 and coordinate system 2 are attached to the base and moving plate, respectively. The origin of both these coordinate system is located at the center of the ball-and-socket joint, and both coordinate system

coincide with each other in the initial position where no muscle is actuated. The orientation of coordinate system 1 with respect to coordinate system 2 can be described by the rotation matrix $R \in SO(3)$. The orientation of the MS can also be described by XYZ Euler angles, ie., θ_1 , θ_2 , and θ_3 , where θ_1 is the angular displacement about the X axis of the coordinate system 1, θ_2 is the angular displacement about the Y axis of the previously rotated coordinate system, and θ_3 is 0 since in our case there is no rotation about the Z axis in the prototype of design II. In this case, the transformation matrix 1_2R can be represented by the following equation:

$$[{}^1_2R] = \begin{bmatrix} 1 & 0 & 0 \\ 0 & \cos \theta_1 & -\sin \theta_1 \\ 0 & \sin \theta_1 & \cos \theta_1 \end{bmatrix} \begin{bmatrix} \cos \theta_2 & 0 & \sin \theta_2 \\ 0 & 1 & 0 \\ -\sin \theta_2 & 0 & \cos \theta_2 \end{bmatrix} \begin{bmatrix} 1 & 0 & 0 \\ 0 & 1 & 0 \\ 0 & 0 & 1 \end{bmatrix} \quad (5.4)$$

Simplifying (5.4) gives

$$[{}^1_2R] = \begin{bmatrix} c\theta_2 & 0 & s\theta_2 \\ s\theta_1 s\theta_2 & c\theta_1 & -s\theta_1 c\theta_2 \\ -c\theta_1 s\theta_2 & s\theta_1 & c\theta_1 c\theta_2 \end{bmatrix} \quad (5.5)$$

Where $c\theta_i$ and $s\theta_i$ represent the cosine and sine of θ_i ($i = 1,2$).

Vector 1OP ($P=A, B, C, D$) denotes the position vector of the four-muscle's attachment point on the base in the coordinate system 1. Vector 2Op ($p=a, b, c, d$) denotes the position vector of the four-muscle's attachment point on the base in the coordinate system 2. Following similar approach in [171-173]. For the given orientation angles referring to the Figure 5.7, according to the vector loop-closure equation (vector addition), the analytical expressions for the artificial muscle length 1Pp , (1Aa , 1Bb , 1Cc , and 1Dd) can be written as:

$$[{}^1Pp] = [{}^1_2R][{}^2Op] - [{}^1OP] \quad (5.6)$$

Note that the coordinates of the muscle attachment points on the base and moving plate are expressed as:

$$\begin{aligned}
{}^1OA &= [r \ 0 \ -h]^T & {}^2Oa &= [r \ 0 \ h]^T \\
{}^1OB &= [0 \ r \ -h]^T & {}^1Ob &= [0 \ r \ h]^T \\
{}^1OC &= [-r \ 0 \ -h]^T & {}^1Oc &= [-r \ 0 \ h]^T \\
{}^1OD &= [0 \ -r \ -h]^T & {}^1Od &= [0 \ -r \ h]^T
\end{aligned} \tag{5.7}$$

Equation (5.6) can be rewritten as follows:

$$[{}^1Pp]^2 = ({}^1_2R[{}^2Op] - [{}^1OP])^2 \tag{5.8}$$

Equation (5.8) can be further rearranged in the following form:

$$[{}^1Pp]^2 = [{}^1Op]^2 + [{}^1OP]^2 - 2[{}^1OP^T][{}^1_2R][{}^2Op] \tag{5.9}$$

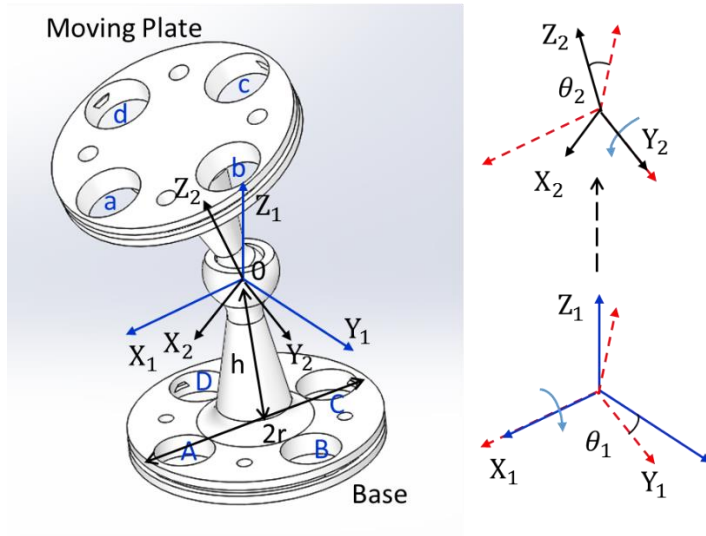


Figure 5.7. Position diagram of the MS.

The reachable workspace of the MS is defined here as all the positions that can be reached by any point at the outer circumference of the top moving plate with arbitrary orientation. The workspace was determined numerically using the equations for the position analysis. The result was generated using Matlab. The tensile actuation 12% was given as the input, and rotation matrix

was obtained by solving Eq. 5.9 using Fsolve function. The reachable positions are 13 to 22 mm in vertical Z axis, -17 to 17 mm in Y axis, -17 to 17 mm in X axis. This magnitude is with respect to the coordinate system 1. For design II, the prototype has 30 mm in diameter and 45 mm in height. The resulted total workspace is shown in Figure 5.8.

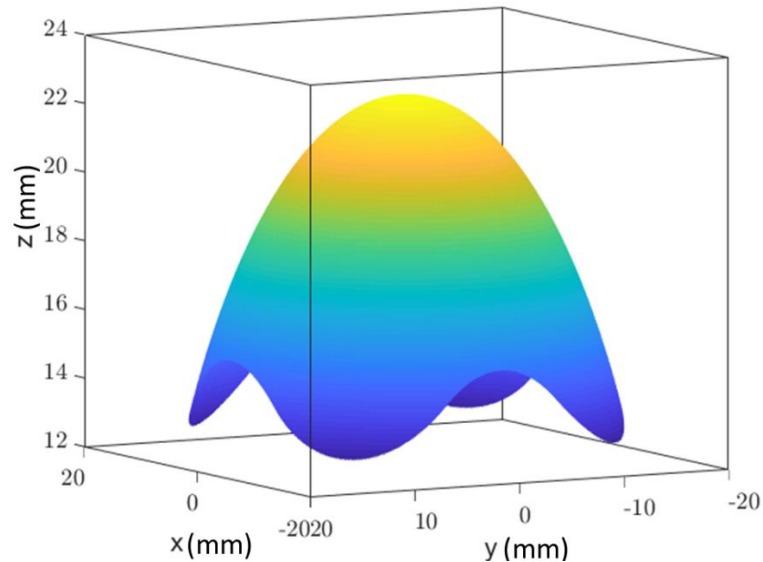


Figure 5.8. Dexterous workspace of the musculoskeletal system.

5.3 Manufacturing Method and Description

Figure 5.9 shows the workflow of the fabrication of the first prototype in step by step procedure. First, the CAD models were designed in SolidWorks and the parts were fabricated by 3D printing using Stratasys Fortus 250MC. The existing advanced multi-material 3D printer for soft materials cannot fabricate low shore hardness (below Shore 26A) [174]. Therefore, silicone casting was adapted as a prime choice for this study. Second, Novus plastic clean & shine and novus fine scratch remover were used to clean the surface of printed parts, and then the molds were assembled to the joint. Jet-lube grease was added into the clearance between ball and socket joint to provide

lubrication (Figure 5.9(b)). Figure 5.9(c) shows the sectional view of the joint. Two prototypes were fabricated with the same procedure except that different silicone materials were used. Platinum cured silicone rubber (Ecoflex® 00-30 & Ecoflex® 00-10 shore hardness) were used to fabricate the stabilization elements of the two prototypes in design I. Here the silicone fabrication procedure was briefly discussed. In the beginning, equal amount of part A and Part B were mixed thoroughly in a beaker for 3 minutes. Before pouring the silicone, the ball-and-socket joint was adjusted using the spirit level tool to keep the top surface of the structure horizontal, the bottom surface is kept in parallel to the table. After that procedure, the mixture is poured inside of the mold slowly and continuously using a syringe in order to get rid of air bubble as much as possible (Figure 5.9(d)). It took 4 hours for the rubber to cure at room temperature, and then to remove the mold. Figure 5.9(e) shows the fabricated silicone elements where half of the mold was removed. With the help of stabilization element, the ball-and-socket joint was able to stand freely.

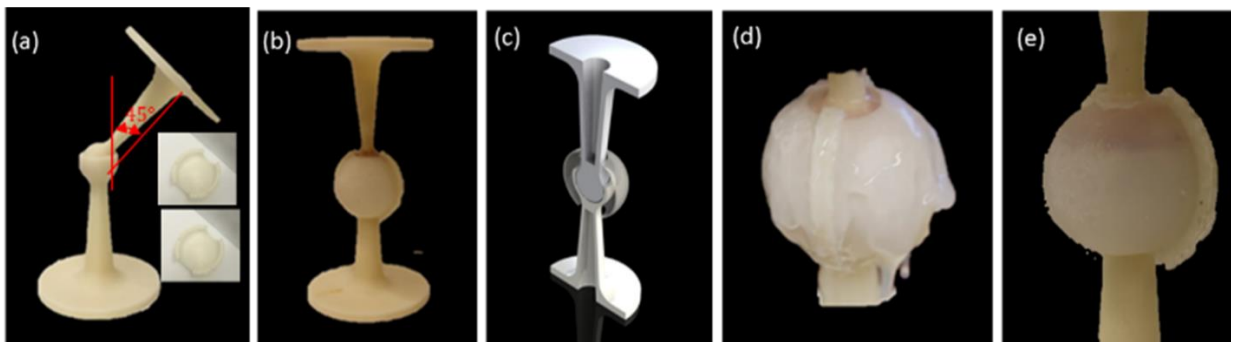


Figure 5.9. Manufacturing steps for creating of ball-and-socket joint (Design I): (a) 3D printed joint assembly mode, (b) surface polishing and adding grease into the clearance, (c) section view. (d) injecting the mixture of silicone, and (e) mold removed.

For design II, the prototype has 30 mm in diameter and 45 mm in height, and the channels diameter was set to be 6 mm. The bioinspired building block system features a ball & socket joint, hollow channels for artificial muscles insertion or to use it as cooling channels as well, and silicone

soft material to embed the bone-like ABS structures. Here, the musculoskeletal system prototype fabrication procedure was briefly discussed. Figure 5.10 shows the workflow of the fabrication in step by step procedure for design II. Ecoflex® 00-10 shore hardness was used to create the silicone parts. The ball-and-socket joint and molds were printed separately as shown in Figure 5.10(a) and assembled for silicone casting as shown in Figure 5.10(b), to create the stabilization elements and one pair of hollow channels as shown in Figure 5.10(c). The other pair of hollow channels were fabricated from silicone in a similar manner as shown from Figure 5.10(d) to (e). In order to secure the connection between the hollow channels and the ball-and-socket joint, another mold shown in Figure 5.10(f) was used to create the silicone layer covering the end caps as shown in (g) to connect the channels. The step in Figure 5.10(f) was repeated to cast the silicone layer on the other end.

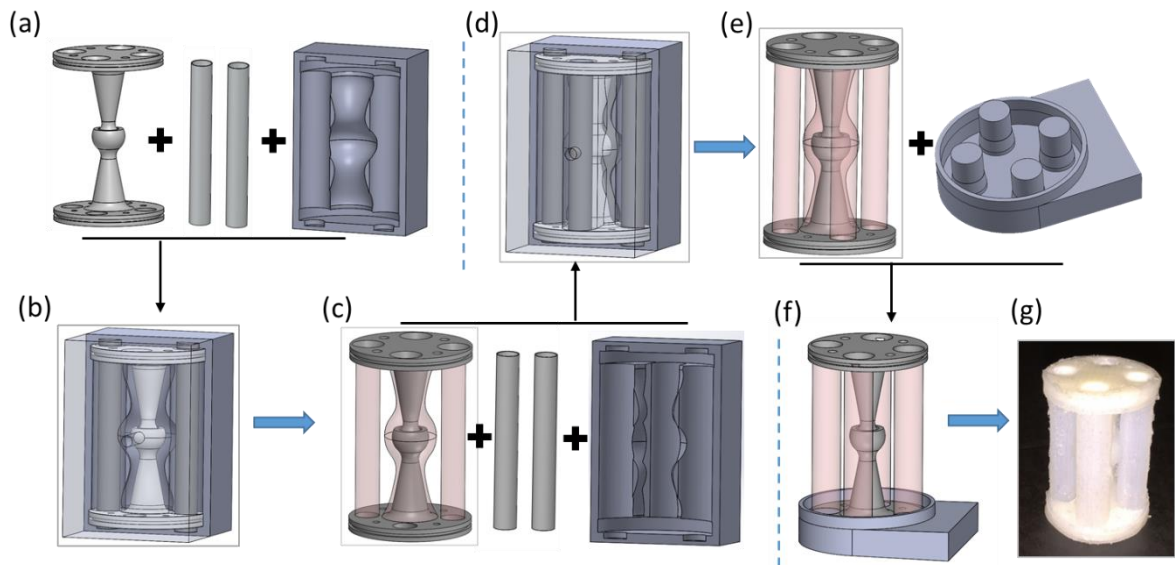


Figure 5.10. Fabrication procedures of the MS in design II: The ball-and-socket joint and mold in (a) was 3D printed using ABS plus material; The silicone ligament and one pair of channels were fabricated from step (b) to (c); The other pair of channels as shown in (e) could be added in step (d) from parts shown in step (c); Performing step (f) twice, a silicone layer was introduced to cover the top and bottom plates and secure the connection between four channels and the joint; (g) shows the final fabricated prototype.

5.4 Experimental Methods

5.4.1 Joint Stiffness and Muscle Stiffness

In an artificial musculoskeletal system, the contraction of muscles that pull on the skeletons allows for versatile movement. The pulling force and contraction of the muscles are two critical parameters affecting the performance of the musculoskeletal system in design II, where a large amount of silicone was used in the hollow channel. In order to determine how much force and contraction is required to achieve the maximum bending angle in design II, the force versus contraction of the joint structure was characterized using the experimental setup as shown in Figure 5.11. The setup consisted of a load cell (Futek LSB200), a laser displacement sensor (Keyence LK-G152), a power supply (BK Precision 1687B), a National Instrument DAQ, and home-made motorized linear stage. The base of the sample joint structure was secured to a fixture, and a string wire was attached to the other base of the joint through the hollow channel. The linear stage was driven at a constant speed of 0.12 mm/s until the traveling distance reached 7 mm, which was found to be sufficient to bend the joint at the maximum bending angle in our preliminary test. The length between the bases of the joint was 47 mm to accommodate the muscle, and the actuation stroke required for the muscle was at least 14.9% ($7/47$) at spring load condition. Due to the benefit of mandrel coiling, TCP_{NC}^{FL} muscle can get large actuation stroke even under spring load condition.

For design II, 3 different prototypes with the similar structure were fabricated. While prototype A and prototype B had the same volume of a silicone in the stabilization element, their side hollow channels had different thicknesses. On the other hand, prototype B and prototype C had the same channel thickness, but different volumes of silicone in the stabilization element. Prototype B was

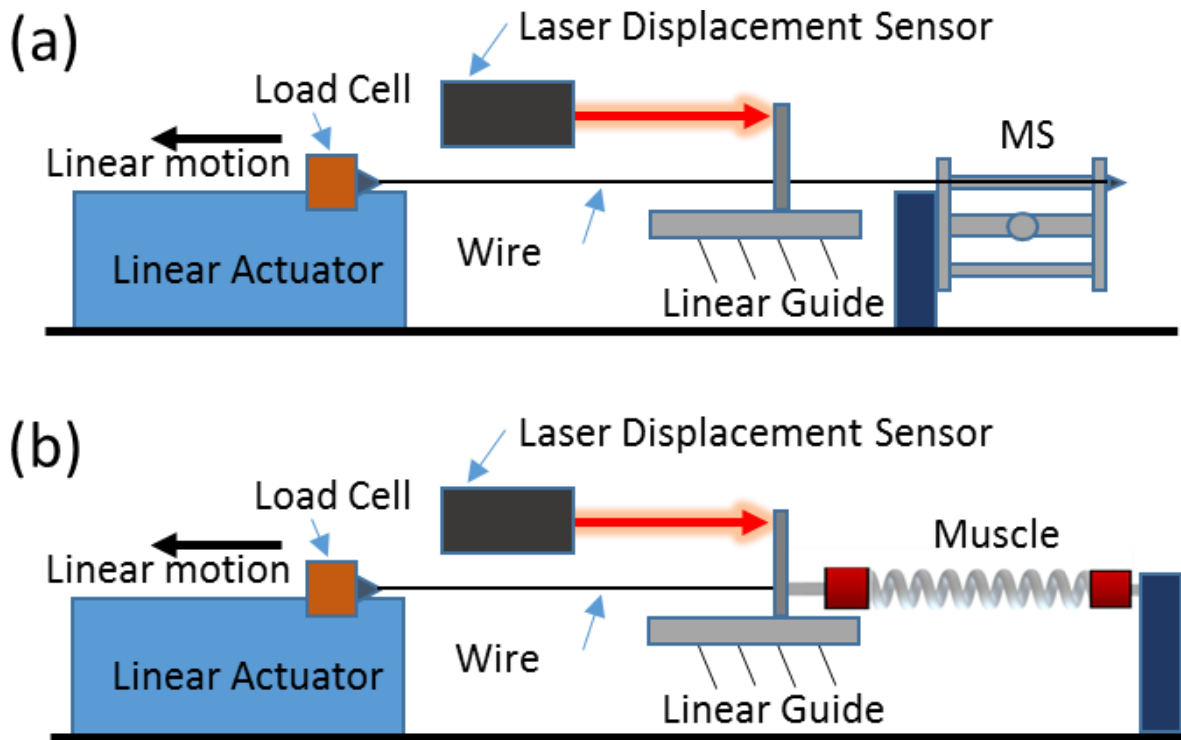


Figure 5.11. Schematic diagram of the experimental setup to characterize the stiffness of the joint (a) and muscle (b).

modified from prototype A by reducing the thickness of the channel from 1.5 mm to 0.9mm, and prototype C was modified from prototype B by reducing 15% of the silicone volume in the silicone ligament (stabilization element). For each prototype test, the force versus contraction displacement data was recorded and plotted in Figure 5.12. Comparing the slope of force versus displacement, it can be seen that the prototype C requires the least effective force (0.04N) to get the complete bending motion (7 mm displacement). The equivalent joint stiffness of prototype C was around 40 N/m. As discussed earlier, the MS comprises of a bio-inspired antagonistic pair of muscles. In this muscle arrangement, the actuated muscle not only must overcome the load exerted by the joint, but also the load exerted by the non-actuated muscle on the other side. Hence, the stiffness of the

muscle is also of great interest. The TCP_{NC}^{FL} muscle tested here was fabricated from an 860- μm -diameter nylon 6 monofilament that was mandrel coiled incorporating an 80- μm -diameter resistance wire, which resulted in spring index of 5.2. As shown by the magenta line in the Figure 5.12, the muscle stiffness is greater than that of prototype C and has an equivalent stiffness of 85 N/m. One assumption for the muscle characterization tests is that the muscle integrated in the MS will work similarly against a linear spring with a stiffness 125 N/m (the equivalent stiffness of the parallelly connected the non-actuated fishing line TCP muscle and the joint structure).

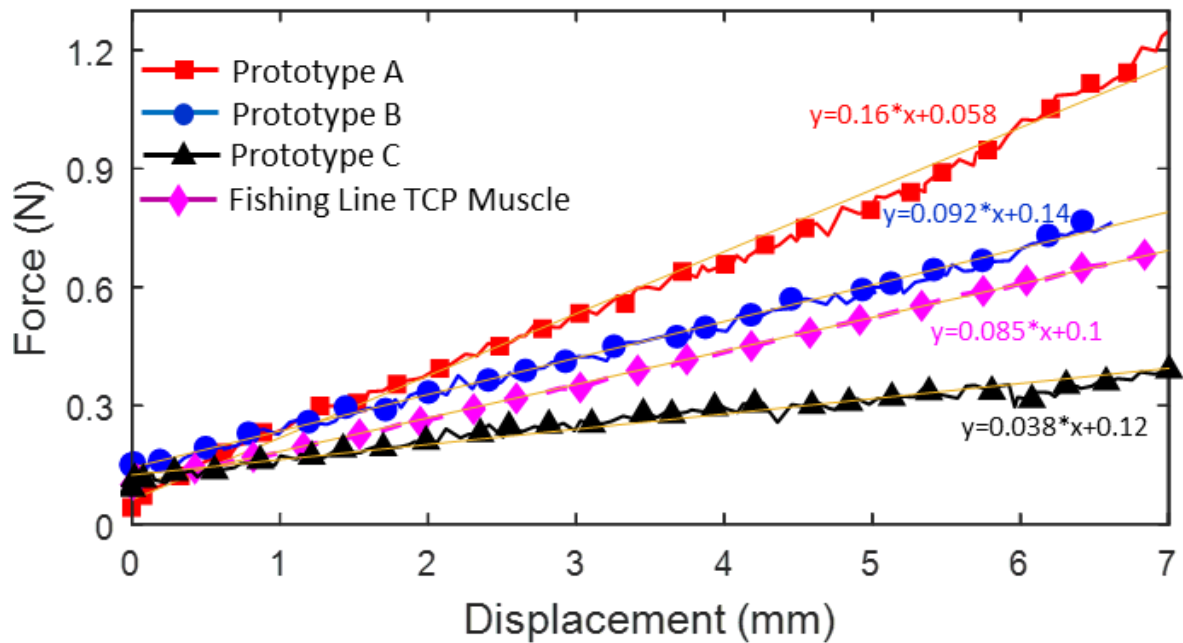


Figure 5.12. The measurement of force during stiffness test of the MS and TCP_{NC}^{FL} muscle.

5.4.2 Muscle Characterization

The experimental setups as shown in Figure 2.7 and Figure 2.9 were used to characterize the performance of TCP_{NC}^{FL} muscles as actuators. Figure 2.7 shows the schematic diagram of the setup

used in isotonic tests (constant load) and Figure 2.9 shows the muscle work against a linear spring (spring load). A linear spring with a stiffness 133N/m was selected considering the equivalent stiffness 125 N/m for the muscle and the joint. The lengthwise contraction displacement was measured via a laser displacement sensor (Keyence LK-G152), the pulling force was measured via a load cell (Futek LSB200), and the temperature was obtained by a type-E thermocouple. The power input waveforms were programmed and defined in a power supply (BK Precision 1687B) and current was set as a constant value. All the state variables of TCP_{NC}^{FL} muscle including pulling force, voltage, displacement and temperature were measured synchronously and stored in the master PC. Pre-stress was varied by translating the linear stage in discrete steps.

For isotonic tests, the constant load was varied from 10 g to 120 g. Figure 5.13 shows all the time domain state variables of the TCP_{NC}^{FL} muscle and the results are highly repeatable and consistent. Due to the friction induced by the pulley, some fluctuations in the measured force were observed in Figure 5.13(a), but the force magnitudes were nearly constant during the actuation period. In Figure 5.13(b), there was significant changes of the measured voltage because the neighboring coils, stretched under a low load condition, were in close contact during actuation such that the resistance wire between the coils interacted with itself, resulting in the decrease in resistance. The point at which the voltage drops reflects the time when the coils start contacting. Figure 5.13(c) and Figure 5.14 show the load dependence of absolute displacement. The maximum absolute displacement occurred at the constant load 30 g. Figure 5.13(d) and Figure 5.14 show the load dependence of the tensile actuation. The tensile actuation normalized to the loaded muscle length depends mainly on the applied load as the muscle elongates considerably under higher load as shown in Figure 5.14. The maximum tensile actuation, also realized at the constant load 30 g

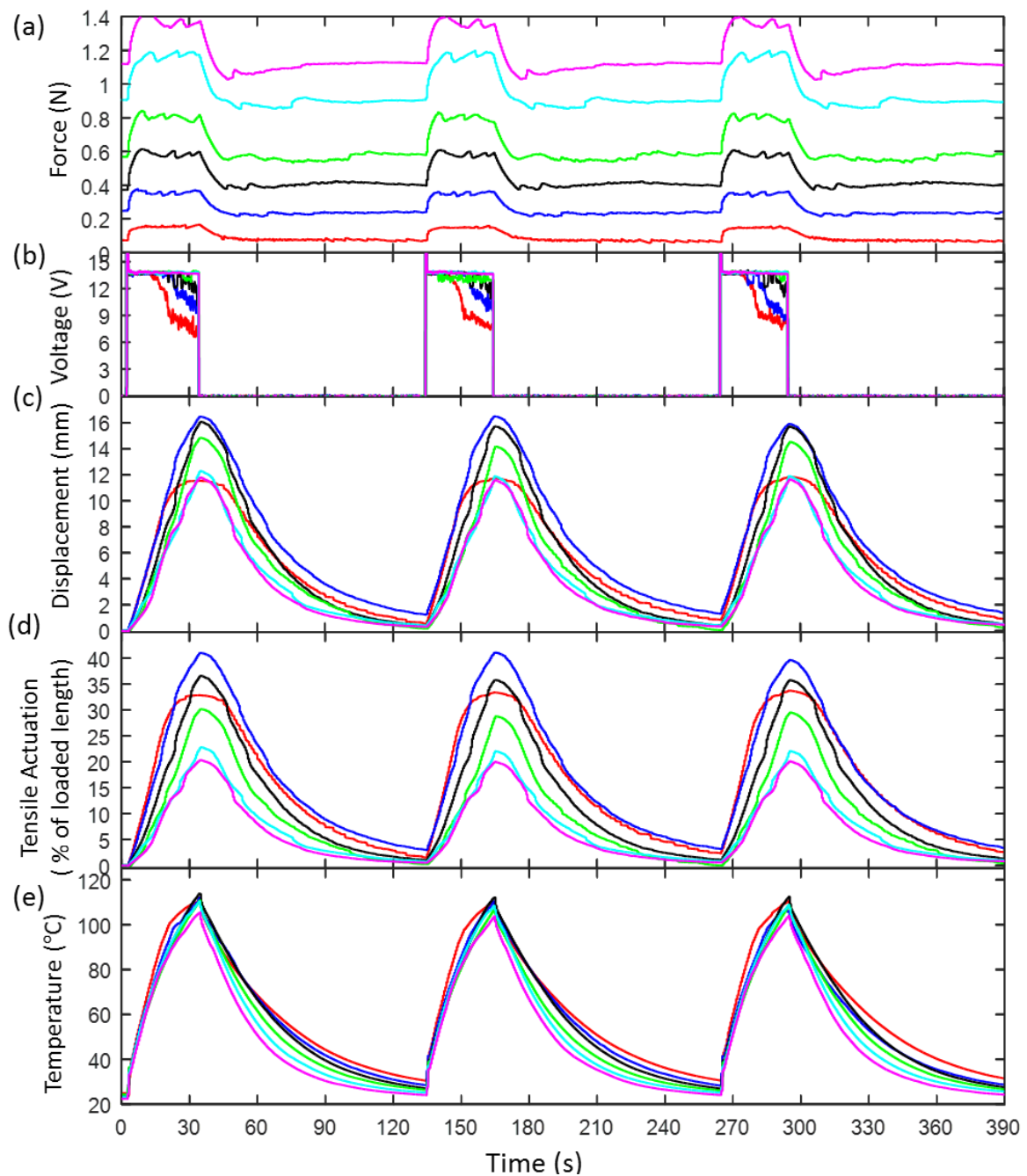


Figure 5.13. Characteristics of TCP_{NC}^{FL} muscle in an isotonic test fabricated from an 860- μ m-diameter nylon 6 monofilament that was mandrel coiled incorporating an 80- μ m-diameter resistance wire, which resulted in spring index of 5.2: (a) the measured force profile, (b) the measured voltage profile, (c) the measured absolute displacement profile, (d) tensile actuation stroke, as a percent of the loaded muscle length, (e) the measured temperature profile characteristics measured at different pre-stress levels,

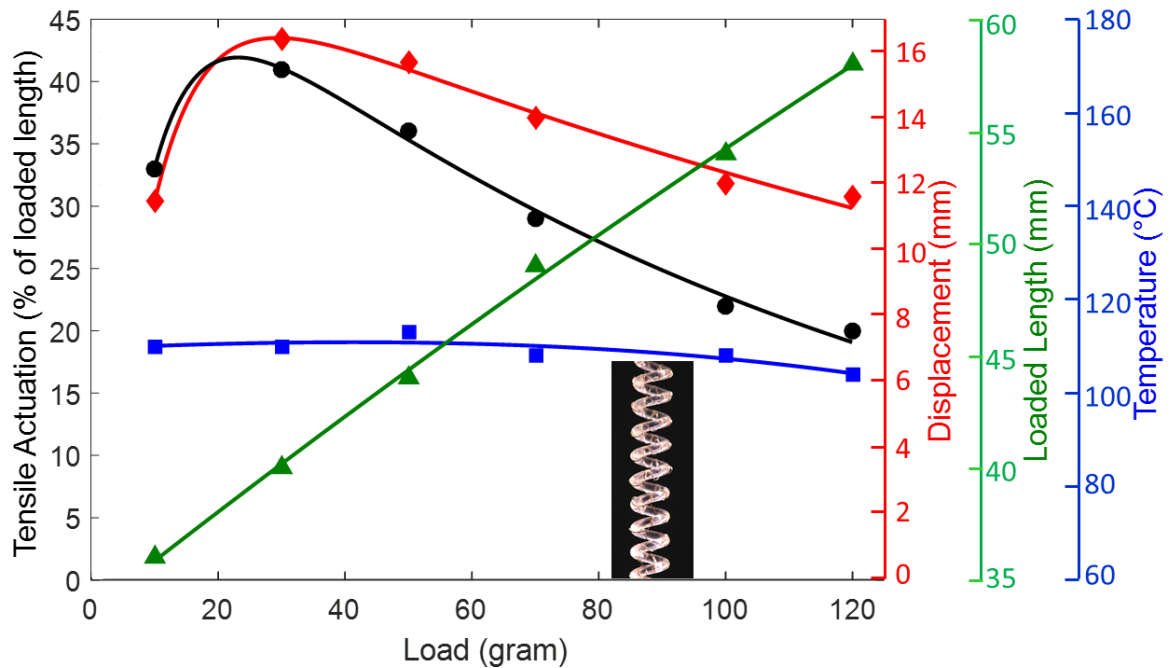


Figure 5.14. Average tensile actuation as a percent of the loaded length, the absolute contraction displacement during actuation, the loaded length and temperature of a TCP_{NC}^{FL} muscle fabricated from an 860- μ m-diameter nylon 6 monofilament that was mandrel coiled incorporating an 80- μ m-diameter resistance wire in a double spacing, which resulted in spring index of 5.2, in an isotonic test versus different load.

was 40 % stroke. This realized actuation stroke is significant and can be useful in many applications in robotics and other systems. The applied load which provides the maximum displacement or tensile actuation is called optimal load, and the optimal load of the investigated muscle is around 30 g. The temperature remained at around 110⁰C (max) for all different applied loads, as the current was kept constant all the time, Figure 5.13E and Figure 5.14.

For spring-load test, Figure 5.15 shows the performance of TCP_{NC}^{FL} muscle against a linear spring. The same TCP_{NC}^{FL} as the one used in the previous isotonic test was tested. Different magnitudes of pre-stress were used, starting from 0.11 to 0.71N. As the pre-stress is increased, the pulling force profile is shifted upwards accordingly as shown in Figure 5.15(a) and the max pulling

force is shown in Figure 5.16. In Figure 5.15(b), as the current was kept constant in all the experiments, the voltage magnitudes measured between the muscle's terminals in the first few seconds were the same until the neighboring resistance wire started contacting, which resulted in the fluctuation of voltage. Figure 5.15(c) and Figure 5.16, illustrates the contraction displacement at different pre-stress levels. The percentage of contraction was 15% at maximum and the maximum temperature was $\sim 110^{\circ}\text{C}$ (Figure 5.15(d) and (e)). The deduced result of displacement versus pre-stress is shown in Figure 5.16, the displacement at pre-stress 0.21N is the largest among the test results. It can be seen that the actuation stroke decreases with an increase in pre-stress beyond 0.21N, and actuation at pre-stress above 0.21N (16.6%) is less than that at pre-stress 0.11N (13%) because of the muscle lengthening. The temperature remains the almost same at pre-stress above 0.31N mainly due to the supplied constant current, and the temperature at pre-stress 0.11N is higher than the rest, which may result from the accumulated heat in local region because of the compact spacing between the neighboring coils at low pre-stress.

$\text{TCP}_{\text{NC}}^{\text{FL}}$ is also capable of fast actuation. Figure 5.17 demonstrated that it is possible to reach quick contraction (within 1 s) without sacrificing tensile actuation by using short pulse with high electrical power. The same $\text{TCP}_{\text{NC}}^{\text{FL}}$ muscle as the one used in the isotonic tests and the spring load tests, was used here as well. The experimental setup used for measurement of tensile actuation and pulling force here was also the same as shown earlier in Figure 2.9 (Chapter 2). The test was carried out by varying the high current pulse magnitude at 0.42 A, 0.46A and 0.50A for a short duration of 1s for all pulsed tests. As shown in Figure 5.17(a) and Figure 5.17(b), a pulsed current input of 0.50 A for only 1s results in 12 % actuation stroke, which is nearly 80% of the actuation stroke

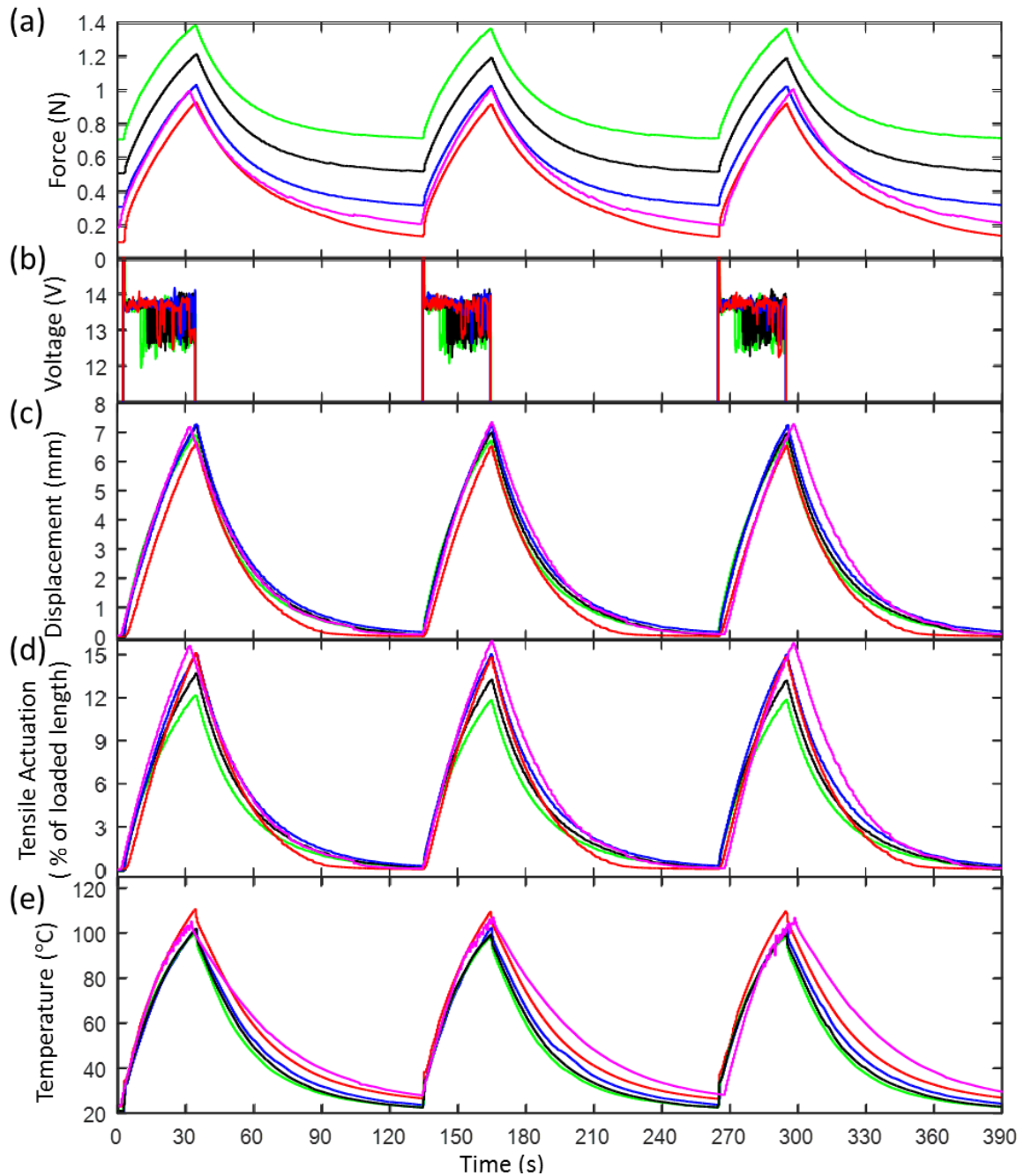


Figure 5.15. Characteristics of TCP_{NC}^{FL} muscle fabricated from an 860- μm -diameter nylon 6 monofilament that was mandrel coiled incorporating an 80- μm -diameter resistance wire, which resulted in spring index of 5.2, against a passive spring of stiffness of 133 N m^{-1} under different pre-stress: (a) the measured force profile, (b) the measured voltage profile, (c) the measured absolute displacement profile, (d) tensile actuation stroke, as a percent of the loaded muscle length, and (e) the measured temperature profile characteristics measured at different pre-stress levels.

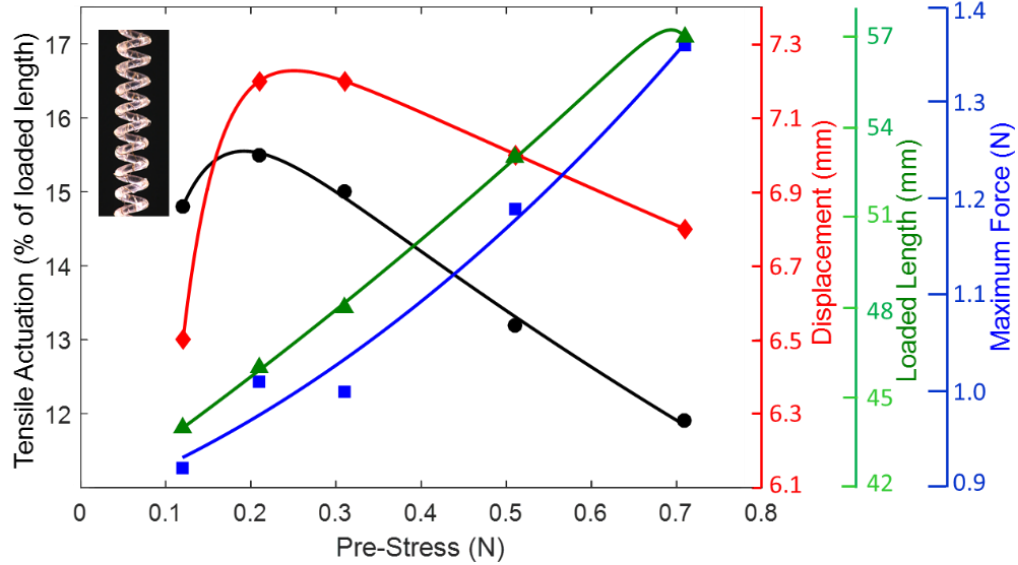


Figure 5.16. Average tensile as a percent of the loaded length, the absolute contraction displacement during actuation, the loaded length and maximum force of a TCP_{NC}^{FL} muscle fabricated from an 860-um-diameter nylon 6 monofilament that was mandrel coiled incorporating an 80-um-diameter resistance wire in a double spacing, which resulted in spring index of 5.2, in a spring load test against a passive spring of stiffness of 133 N m⁻¹ versus different pre-stress.

as that achieved by applying square-wave current input (0.12 A for 30 s at spring load test Figure 5.15). From the experimental results, we can see that a short pulse with high power improves the actuation frequency of the muscle. Figure 5.17(c) shows the results obtained for the pulling force of the fishing line TCP muscle under a spring load. The maximum force as shown in Figure 5.17(a) at 0.50A is 0.8 N.

5.4.3 Characterization of Musculoskeletal System

In MS (design I), the 2-ply TCP muscles from sewing thread were arranged in an agonist and antagonist manner for bi-directional bending motion. The muscle length was 13.6 cm and the silicone shore hardness was 00-10. To test the performance of the ball-and-socket joint, bending and twisting tests were carried out. Here, the results from the bending test was presented based on

the study of MS in design I. Figure 5.18 and Figure 5.19 show the obtained bending angles and experimental data. Figure 5.18 shows the maximum bending angles achieved by actuating the muscles in the blue blocks (side muscles) in sequence with a square-wave input power (33 % duty, 0.216 W/cm, 16.6 mHz). Figure 5.18(a) show the balanced initial position without actuating the muscles. Figure 5.18(b) shows the maximum angle obtained by first actuating the muscle in the right side, which resulted in around 25° . Then, the power was switch to the other muscle in left side muscle as shown in Figure 5.18(c). As can be seen in Figure 5.18(c), the maximum angle obtained towards to the left side is around 20° .

Quantitative actuation of the ball and socket joint was done using a video camera and applying power to the muscles to the right and left parts of the joint. The time domain angular displacement of the joint is provided in Figure 5.19 as a function of input power to the muscles. The shaded regions in Figure 5.19 indicate the heating cycles of the muscles due to joule heating and two cycles are shown in the figure.

As shown in Figure 5.19, the angular displacement about z-axis shows the maximum bending angle. It can be inferred from the slope of the curve that the muscle under higher power had fast response. After switching off power to the muscle in blue block (right side muscle) in Figure 5.18(b) during first bending towards to the right side, the muscle underwent natural cooling in the air and muscle elongated during this period. Therefore, from Figure 5.19, it was observed that after 25 seconds, the structure tried to return and the bending angle reached steady state at around 10° . However, around 42 seconds, the structure reached a balanced state until a power was delivered to the other side muscle at 65 seconds in blue block in Figure 5.18(c) (the left side muscle). Then the structure started bending towards to the left side.

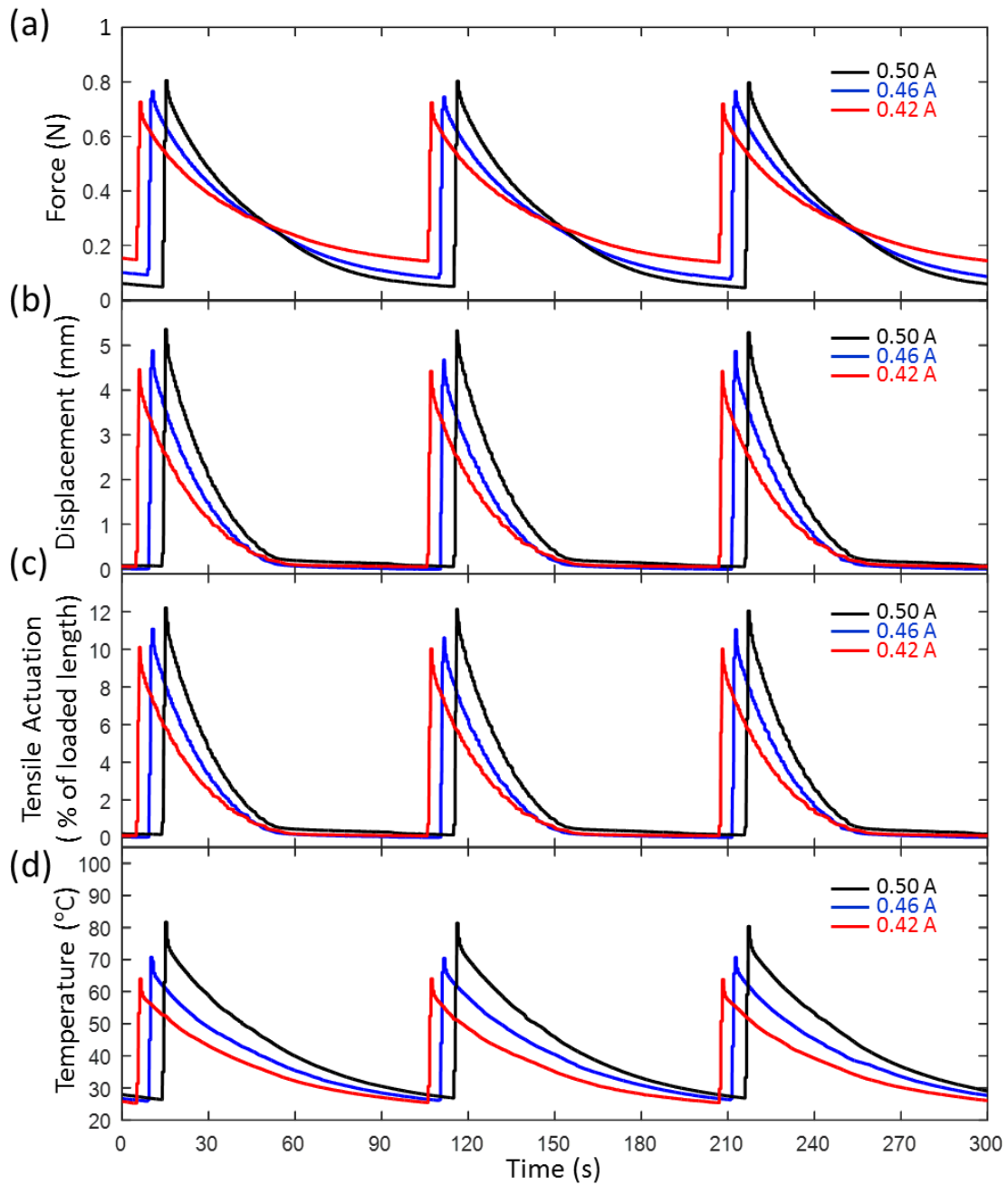


Figure 5.17. Pulsed actuation results for fishing line TCP muscle at different current. (a) Contraction absolute displacement of a fishing line TCP, (b) Tensile actuation as a percent of the loaded muscle length, (c) The measured force profile and (d) the measured temperature profile.

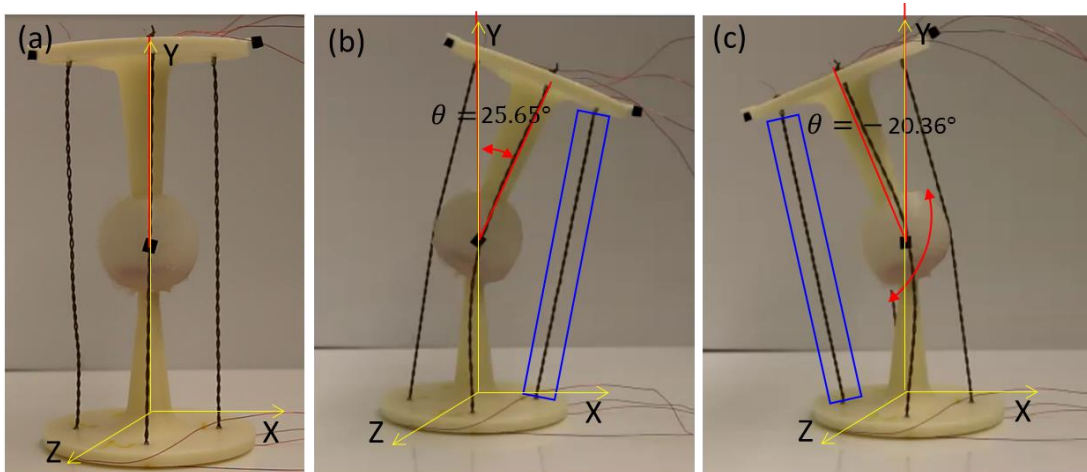


Figure 5.18. Bending test of the MS joint (Design I): (a) Initial position (no actuation), (b) The maximum angle bending towards to the right side (the muscle in the blue block was actuated, and θ represents the angle measured in the test), (c) The maximum angle bending towards to the left side (the muscle in the blue block was actuated).

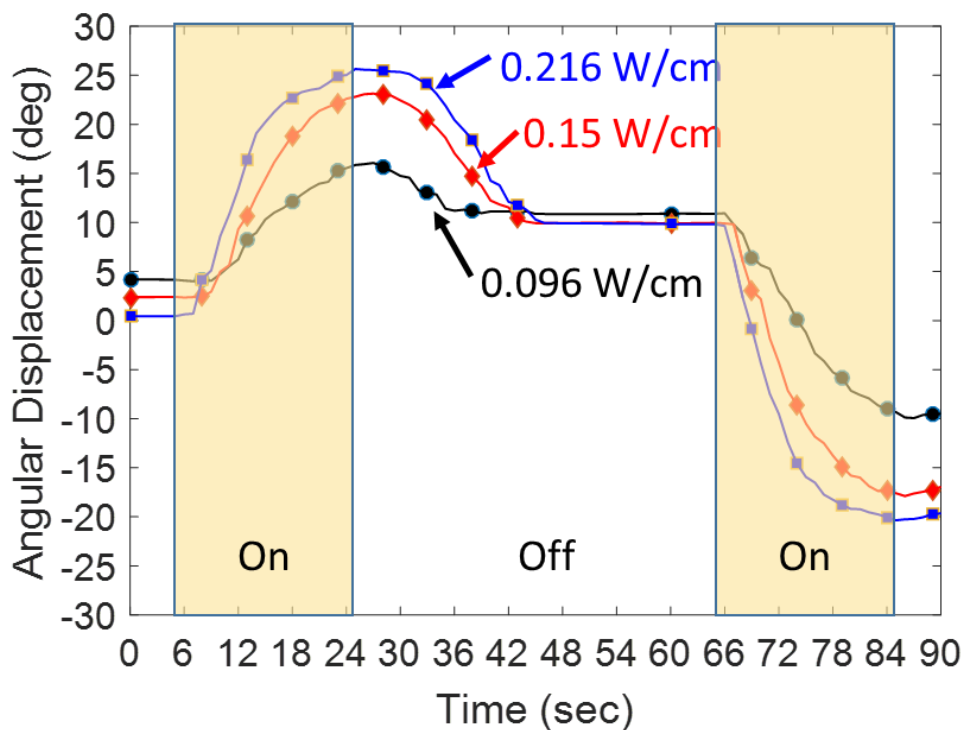


Figure 5.19. The angular displacement during the bending test of the joint integrated with TCP muscles (yellow highlighted regions indicate that the power is on).

For the twisting test of MS in design I, rotation test about y-axis (with respect to the axis indicated in Figure 5.18) was also carried out to evaluate the design as shown in Figure 5.3. For this test, another sample of the ball and socket joint was made using a silicone shore hardness of 00-30. Once the sample was fabricated, first, the ball-and-socket joint was twisted by hand manually to keep twisted state until the muscles were actuated. The angle was measured from the screen shots of the video recording the rotational motion from the top view. The maximum rotation angle obtained was 22.5° as shown in Figure 5.20. Since the muscles were inevitably different from each other, they delivered different response upon receiving power even though they were connected in parallel to twist the joint. Thus, during the rotation, the center of the rotation shifted somehow. But the rotation test demonstrated its potential application as a building block for spine structure and other biologically inspired robotic systems using torsional actuation.

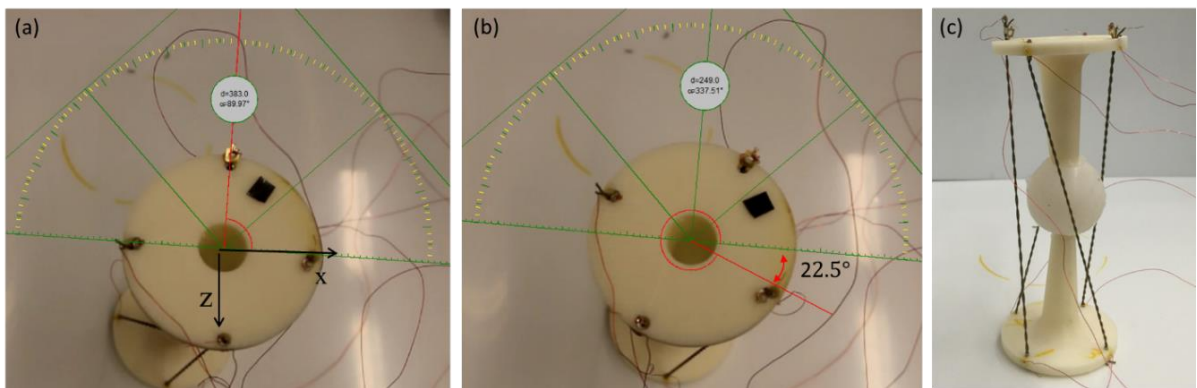


Figure 5.20. Rotation test about y-axis by twisting the ball-and-socket joint in Design I: (a) The initial state after twisting the ball-and-socket joint manually. (b) The final position after the rotation by actuating all the muscles, and (c) The twisted ball-and-socket joint as seen from side view.

For the characterization of musculoskeletal system in design II, both regular actuation as well as pulsed actuation tests were performed to characterize the second prototype of musculoskeletal system based on ball-and-socket joint. Before the muscles were integrated into the joint, they were

trained with a dead weight of 100 g at a current of 0.14 A for at least 4 cycles or until the actuation results were repeatable for 4 consecutive cycles. Each cycle consisted of 30 s for actuation and 100 s for relaxation. The training was performed using the experimental setup in Figure 2.7. The purpose of this training was to achieve consistency in stiffness, length, and actuation of the muscles at constant load. After the muscles were placed into the joint, they were then trained again for repeatability in a spring load setting. Subsequently, the base of the joint was fixed on a 3D printed support, and regular actuation and pulse actuation tests, which differed in terms of cycle frequency and current magnitudes, were performed. This regular actuation test was similar to the training cycle, 30 s for actuation and 100 s for relaxation. The joint was tested with three different currents ranging from 0.10 A to 0.14 A at an increment of 0.02 A. Figure 5.21 shows the different angular displacements at different constant currents for regular actuation. The pulsed actuation tests were performed to improve frequency of the MS. The actuation time was set to 1 s and the appropriate current was determined experimentally. A safe and optimum current was found to be 0.50 A, while the maximum current, which could break the muscle, was around 0.57A. Figure 5.21(a) shows the angular displacement at pulsed actuation with higher currents for 1 s actuation and 100 s for relaxation. One benefit of implementing the antagonistic pair of muscle is to increase the frequency by reducing the relaxation time. Based on angular displacement in Figure 5.21(b), the relaxation time was reduced to 30 s in Figure 5.21(c). For regular actuation, the maximum angular displacement was around 24°, whereas for pulse actuation, it was around 21°. During the pulsed actuation test, the frequency of the MS was increased from 0.008 Hz (regular actuation) to 0.03 Hz or by a factor of 3.75. This is a significant improvement from the previous joint [175] and broadens the scope for practical implementation. To explore the effect of change in current

magnitude on the actuation, three different currents ranging from 0.42 A to 0.50 A at an increment of 0.04 A were provided. Similar to other tests, pulsed actuation cycles were repeated at least 3 times to determine repeatability. Figure 5.21(c) further shows the bending angular displacement during the continuous cycle. All the angular displacement plots were obtained using an open source physics software called Tracker. Screenshots of the musculoskeletal system in the pulsed test (1 s for actuation and 30 for relaxation) is shown in Figure 5.22.

The MS characteristics are significantly improved by using pulsed actuation and antagonistic pair of muscles, and the design enables further improvements in terms of frequency by reducing the relaxation time. The addition of silicone channels around the muscles allows for different methods of both active and passive cooling, which will be carried out in future study. For instance, the joint frequency can be increased via active cooling by incorporating pumps to enable the flow of a fluid to quench the muscles. Apart from that, the channels can contain thermal grease to maximize heat transfer from the muscles and improve the response.

5.5 Power Source Design

The current MS is modular and constructed using ball-and-socket joint between two bone-like structures. In the current configuration, the MS is actuated via an external power supply through a wire connection. However, one limitation of using an external power supply is the portability of the MS which is limited by the length of the cord. For future application, the MS should also be able to operate in a cordless mode using a battery source for power. For instance, a snake robot built from the modular building block would be able to move freely on the ground. Here an approach utilizing the battery is proposed to

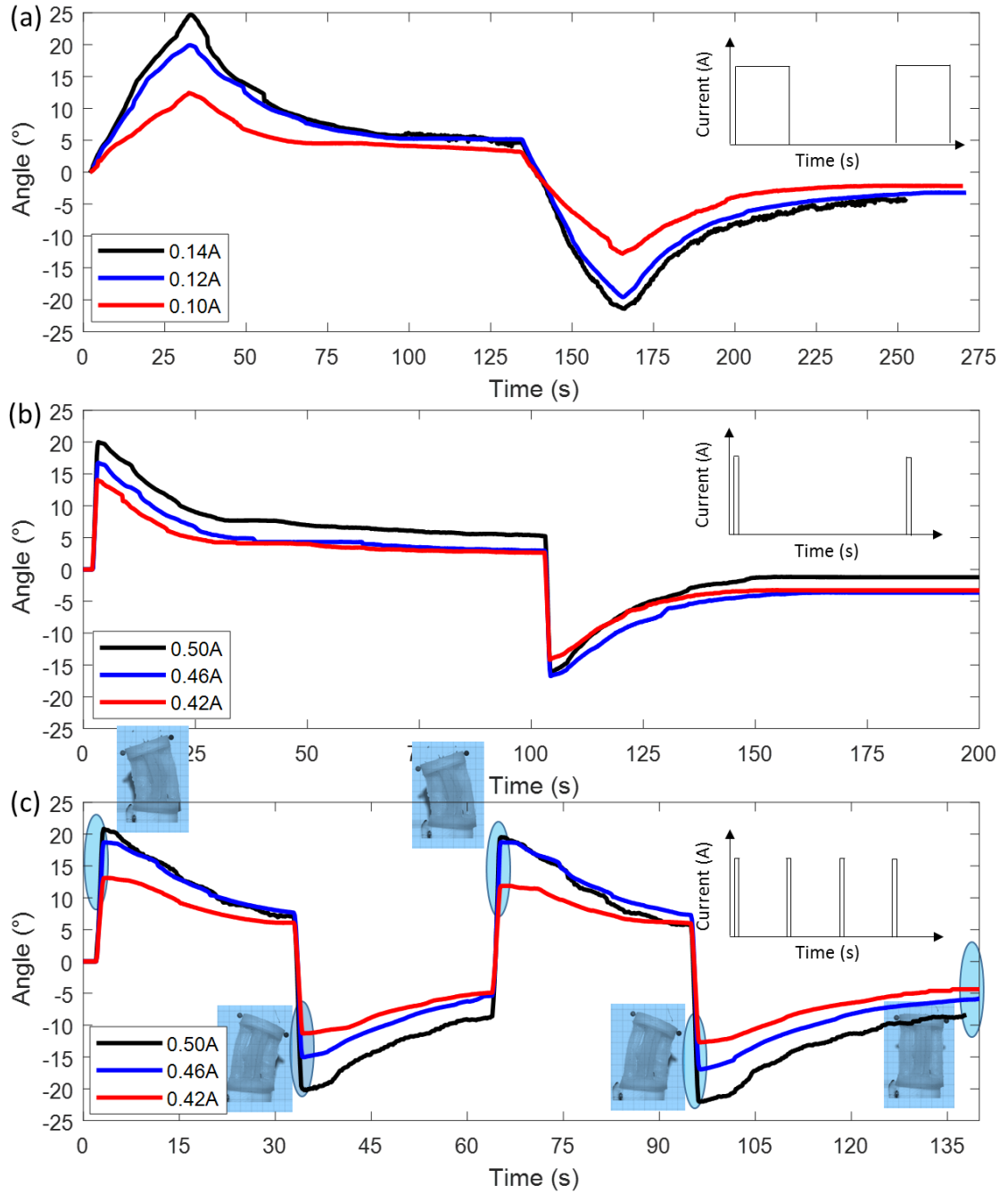


Figure 5.21. Performance of MS prototype (Design II): (a) Musculoskeletal system bending motion (Regular actuation with long duration 30 s, and cooling time is 100s); (b) Pulse actuation with short duration 1s, and cooling time is 100s. (c) Pulse actuation with short duration 1s, and cooling time is 30 s. The insets show the bending angle of the musculoskeletal skeletal system in the end of each actuation cycle.

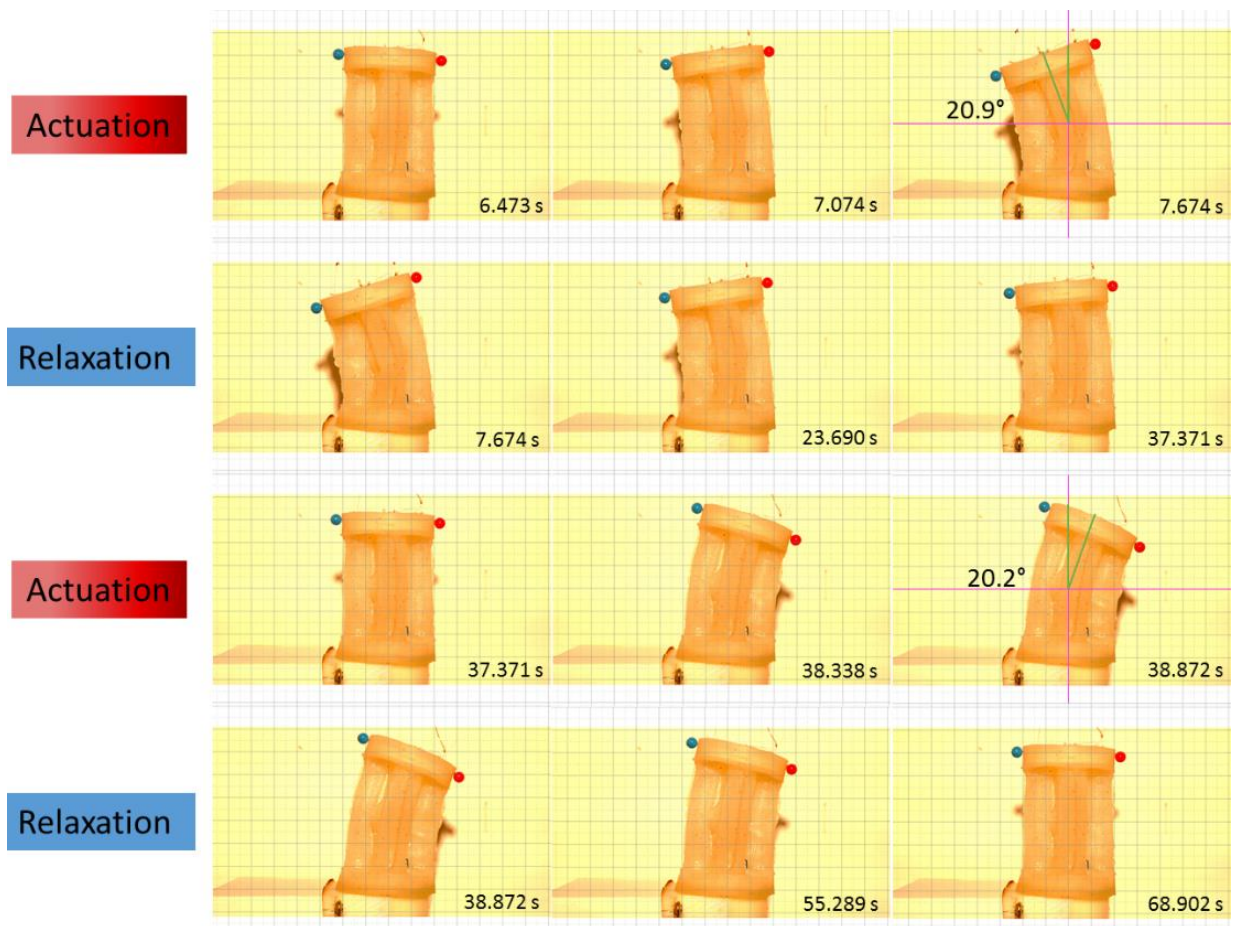


Figure 5.22. The bending motion of the musculoskeletal system (design II).

address the autonomous operation issue. The size of the MS is increased a little bit as shown in the Figure 5.23 to accommodate the battery. The top circular plate has a diameter of 60 mm and a height of 100 mm. In this design, a battery is directly embedded in the silicone which connects two modular MS prototypes when the silicone is casted in the mold. One advantage of using the silicone segments is to prevent the leakage and ensure the waterproof. To investigate the battery size and operation which can be implemented in the MS joint, analysis was carried out. Based on the preliminary test on a TCP muscle as shown in Figure 5.24, a length of 63 mm muscle can deliver a huge tensile actuation at a voltage 10V at a constant current 0.37A. If the battery is

powering the parallelly connected muscles (both have the equal length of 47 mm) shown in Figure 5.23, the current consumption will be 1.48A ($4 \times 0.37\text{A}$). Power cycle (on time) in one cycle of the MS bending motion takes 1 minutes and consumes 24.7 mAh. A commercially available battery (Item Number: 31866) was selected from all-battery.com that can deliver a high capacity and come in small size. The selected battery has a capacity of 4400 mAh. The MS can operate 178 cycles of two-sided bending motion and last around 6 hours for continuous two-sided bending motion. The battery can be recharged at charging current 1.0A for 4.4 hours. The battery technical data is listed in Table 5.1.

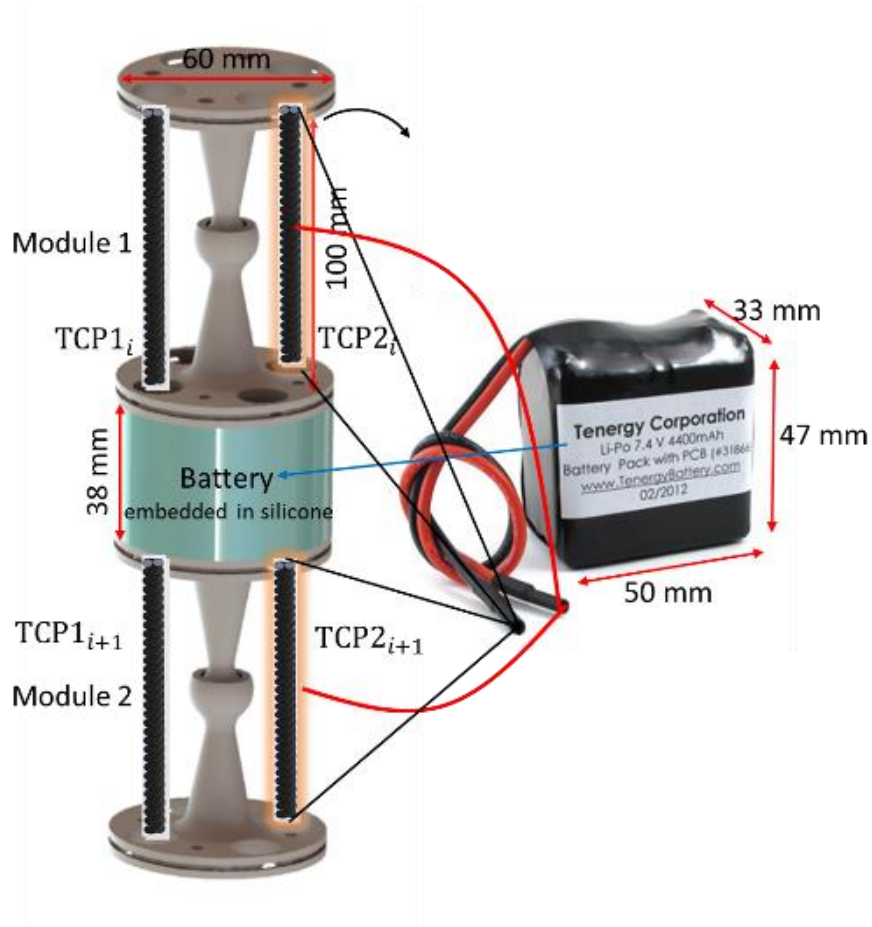


Figure 5.23. Concept design of MS which is operable in a cordless mode.

Table 5.1. The specification of the selected battery.

Model	Chemistry	Capacity (mAh)	Weight (gram)	Dimension(L*W*T)	Nominal Voltage (V)
Tenergy LiPo	Li-Polymer	4400	172	50*47*33	7.4

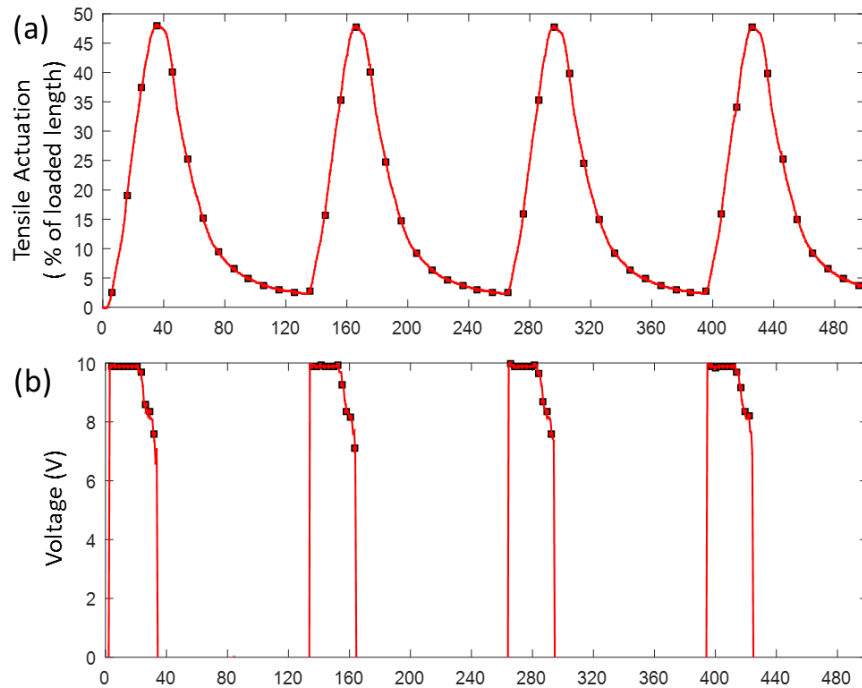


Figure 5.24. (a) The tensile actuation of a 2-ply TCP muscle (63 mm in length) at constant 100-gram load; (b) The measured voltage at a constant current input (0.37A).

5.6 Summary

In this study, a bio-inspired design of musculoskeletal system based on ball-and-socket joint powered by a novel high-performance, extremely low-cost artificial muscle was presented. Two antagonistic pairs of artificial muscles were employed as actuators while the 3D printed ABS ball-and-socket joint was used to mimic the musculoskeletal system found in nature. Silicone elastomer

(Ecoflex® 00-10 shore hardness) was used to cast a stabilization element to serve as ligament. Soft silicone layer was used to embed the entire structure and serve as a tissue surrounding the joint. Two prototypes with different size were made and extensively characterized. The prototypes in design I has 136 mm in height and 59 mm in overall diameter, and bending and rotation tests were carried out. In design I, the TCP muscle from sewing thread was selected as an actuator. The absolute angular displacement in the bending test of the first prototype was around 25° . The maximum rotation/twisting angle in the rotation test of the first prototype was around 22.5° . The prototypes in design II have 45 mm in height and 30 mm in overall diameter. TCP_{NC}^{FL} muscle was chosen as an actuator. The TCP_{NC}^{FL} muscle used in this study was fabricated from an 860-um-diameter nylon 6 monofilament that was mandrel coiled incorporating an 80-um-diameter resistance wire, which resulted in spring index of 5.2. The muscle could deliver a tensile actuation stroke up to 41% at a constant current of 0.12A for a period of 30s under a 0.5 MPa load. In spring load test, the muscle could deliver up to 15% actuation at a constant current of 0.12A for a period of 30s under a pre-stress of 0.21N against a linear spring of 133 N/m. The TCP_{NC}^{FL} muscle could also be actuated via pulsed actuation. A short pulse with high electrical current of 0.50A given as an input to the muscle resulted in a 1s response time for actuation, showing a 12% actuation. Once the muscles were integrated into the musculoskeletal system in the form of two antagonistic pairs (design II), the pulsed test reveals that the frequency of the operation can be increased by a factor of 3.75 (from 0.008 to 0.03 Hz). The continuous cycle test also shows that the joint bending motion in pulse test was highly consistent and repeatable. These results are significant because they broaden the scope of the applications of these muscles in the areas where modular articulated joints are employed, such as snake like robots, spine of biomimetic robots and others.

CHAPTER 6

CONCLUSION AND FUTURE WORK

6.1 Conclusion

Twisted and coiled polymer (TCP) muscles show large tensile actuation, produce significant mechanical power, and have a good dynamic range in a muscle-like form factor. TCP muscles are also beneficial from their diverse actuation methods, including hydrothermal actuation, electrothermal actuation and photothermal actuation. Among those actuation methods, electrothermal actuation is the most convenient method for practical actuation, especially in robotics application due to the easiness of delivering heat to the muscle via Joule heating. In Joule heating, a voltage or current is supplied to the muscle to raise the temperature, therefore it is easy to control voltage/current following certain control algorithm.

This PhD study aims to provide guidelines for actuator development for robotics application by extensively investigating the mechanical performance of TCP muscles. The aims of the dissertation are achieved in the following research activities. In the first chapter, a review of suitable actuator technologies for soft robotics is presented. First, a novel muscle fabrication setup as shown in Figure 6.1B is developed to produce TCP muscle from fishing line and resistance wire. The manufacturing method proposed in this study enables researchers to fabricate muscles with identical and repeatable characteristics easily. The unique feature of the muscle fabrication setup lies on the fact that the resistance wire is directly wrapped around the twisted monofilament nylon 6 fishing line fiber without applying twist in the resistance wire. Next, two test methods with an experimental apparatus are developed to obtain mechanical properties of TCP muscles, providing the insights on actuator development for robotics. Study of the electrical resistance of 1-ply TCP

muscle made from Ag-coated multifilament nylon is conducted via extensive experimental investigation. For applications of TCP muscles, a reconfigurable robot with tensegrity structure is developed for the first time using 2-ply TCP muscles from sewing thread as linear actuators. The low cost and high performance of TCP muscle also promotes the development of a compact and low-cost robotic hand for humanoid or prosthetic device, which is the second developed robotic system in this dissertation. The third application is a novel musculoskeletal system based on ball-and-socket joint that is proposed by utilizing the antagonistic pair of TCP muscles. A new type of muscle, TCP_{NC}^{FL} , twisted and coiled polymer (TCP) muscle with fishing line (FL, as superscript) and nickel chromium (NC, as subscript) is presented that can produce 53% strain under a 100-gram load.

Chapter 2 demonstrates a new artificial muscle (mandrel-coiled) fabrication apparatus to produce TCP_{NC}^{FL} . The unique advantage of this manufacturing system is the capability of incorporating a very thin resistance wire ($80 \mu m$) into the artificial muscle without affecting the mechanical properties of the fishing line as shown in Figure 6.1B. The benefit of bringing resistance wire into the artificial muscle is easiness of performing electrothermal actuation. The fabrication of self-coiled muscles is also shown in Figure 6.1A. In addition, two different test methods are designed to measure the properties of twisted and coiled polymer muscles, (1) when the muscle is subjected to a constant load (isotonic test) and (2) when the muscle is operating against a linear spring (variable load). This analysis suggests that all tensile actuation parameters and other state variables (absolute displacement, tensile actuation, pulling force, temperature, voltage and current) can be determined from the well-designed high-resolution experimental setup,

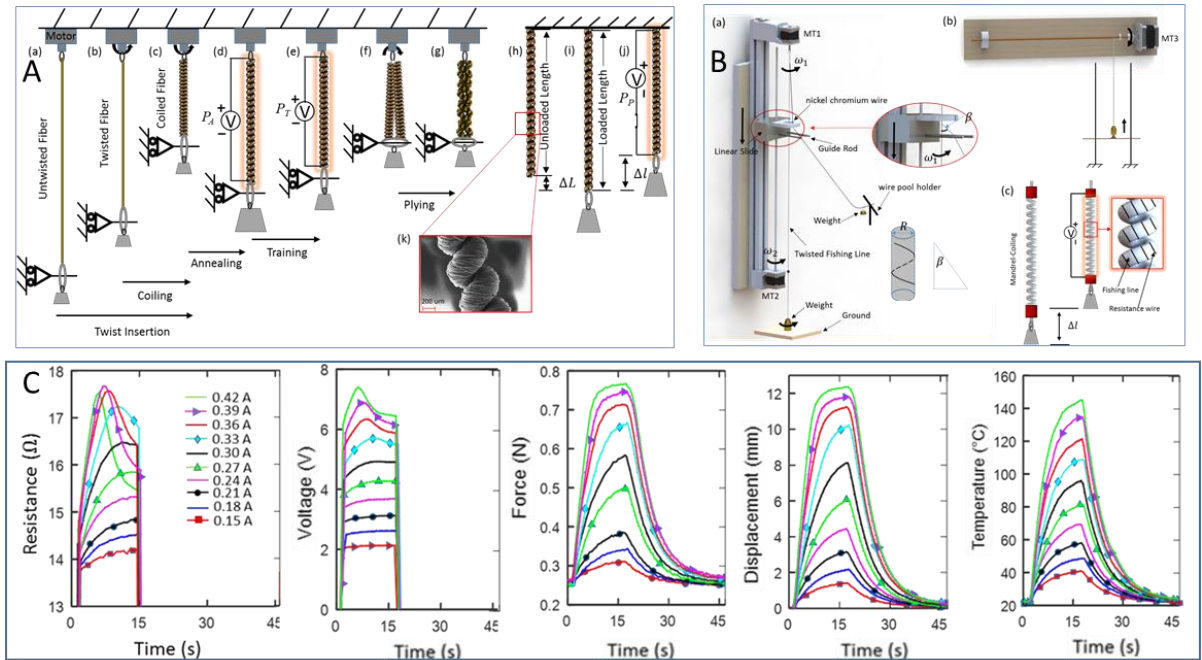


Figure 6.1. Overview of Chapter 2: Schematic diagram of self-coiled muscle (A) and mandrel-coiled muscle (B) fabrication setup, and (C) The resistance change of 1-ply TCP muscle in spring-load test, along with other state variables.

providing an insight for the development of actuator design for use in robotics. Since power is the key driving parameter determining the temperature, it is of great interest to investigate the resistance change of the TCP muscle from sewing thread. For this purpose, 1-ply TCP muscle from sewing thread was chosen as it is the simplest coiled structure. Change of resistance is a complicated non-monotonic function of temperature and length over a wider temperature range as shown in Figure 6.1C. A geometric model of the 1-ply TCP muscle was proposed to understand the underlying experimental phenomenon change of resistance in the 1-ply TCP muscle. A theoretical prediction of temperature and tensile actuation of the TCP muscle was developed using thermo-mechanical and thermo-electric models. The thermo-mechanical properties of the 1-ply TCP muscle were characterized using a spring-load test applied over a wide range of power input.

The presented thermo-mechanical model of the TCP muscle was validated by the experimental data. The thermo-electric model correlating the relationship of the power input and temperature was also developed. In this experiment, the temperature was directly measured from the surface of TCP muscle and used to validate the thermo-electric model. The simulated results showed a good agreement with experimental measurements for the spring-load test.

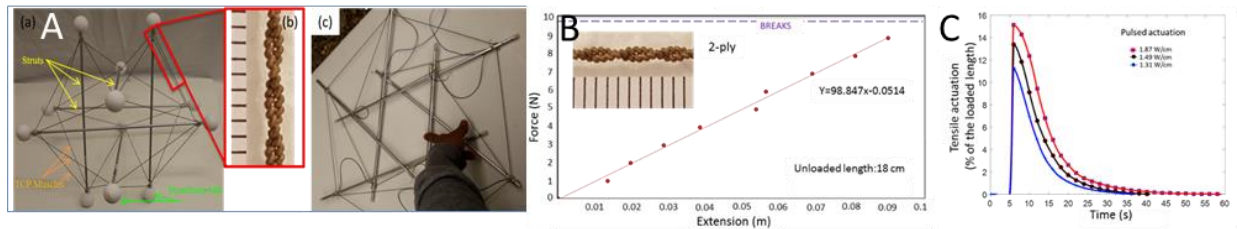


Figure 6.2. Overview of Chapter 3: (A) Tensegrity prototype, (B) Stiffness and (C) tensile actuation of 2-ply muscle.

The application of TCP muscles into robotics is still not well explored, and the area is becoming more and more active recently. In Chapter 3, a reconfigurable robot with tensegrity structure as shown in Figure 6.2A was developed using 2-ply TCP muscles from sewing thread. The artificial muscle was compact, lightweight and had high strain actuation (15.5% under 50 g at 1.87 W/cm, as shown in Figure 6.2 C). The stiffness of the 2-ply muscle was determined $\sim 98\text{N/m}$ as shown in Figure 6.2 B. The tensegrity structure had 24 TCP muscles and 6 rigid struts, and its weight was 69 g. A tensegrity structure always intends to reach an equilibrium configuration due to a balanced force between the tensile and compressive elements. As the muscle is silver plated, it also enables the convenient electrical-thermal actuation via Joule heating. Regular actuation and pulsed actuation were both explored to power the robot. Rolling motion of the tensegrity robot under a contact pattern 2 (contact with a ground in a non-regular, isosceles triangle) was also successfully demonstrated.

In Chapter 4, a compact and low-cost humanoid hand powered by nylon artificial muscle made from multifilament nylon 6 sewing thread was developed. The five-fingered humanoid hand was under-actuated and has 16 degrees of freedom (DOF) in total (15 for fingers and 1 at the palm). In the under-actuated hand designs, a single actuator provided coupled motions at the phalanges of each finger. Two different designs (Figure 6.3A, graphical abstract of Chapter 4) were presented along with the essential elements consisting of actuators, springs, tendons and guide systems. The chapter especially focused on the TCP hand with agonist and antagonist actuation system. It had a kinematic structure similar to a natural hand featuring five articulated fingers, a hand size of 122 x 64 x 14 mm, overall arm length of 185 mm and a total weight of 140 g (excluding the battery, sensors, and circuit). The stress and deformation analysis was also performed on the index finger (Figure 6.3D). The 2-ply TCP muscles developed for the hand could deliver actuation of 14% under 200 g at 0.25 W/cm. The 3-ply TCP muscles developed for the hand could deliver actuation of 13% under 200 g at 0.33 W/cm. Further, in the isotonic test of TCP muscle (multifilament nylon 6 sewing thread with silver plated), the load dependence of the tensile actuation was investigated in a wide load range from 50 g to 700 g. The load dependence of the tensile actuation revealed that the optimal load was around 100 g as shown in Figure 6.3C. In the spring-load test of TCP muscle (multifilament nylon 6 sewing thread with silver plated), the maximum pulling force of a 2-ply TCP muscle against a passive spring with stiffness of 50 N/m under a pre-stress 1.6 N was measured around 4.0 N; the maximum pulling force of a 3-ply TCP muscle against a passive spring with stiffness of 50 N/m under a pre-stress 1.7 N was measured around 4.7 N. Based on the results of fast actuation in Figure 6.3E, a short pulse with high electrical power of ~2.12 W/cm was supplied to TCP muscles that resulted in flexion of the hand within 1s without applying active

cooling of the muscle. This is acceptable and in the range of 1-1.5s, that is typical desired value for robotic hand [138]. A kinematic model of the flexor tendons as shown in Figure 6.3B was developed to simulate the flexion motion and compared with experimental results. Finally, grasping of various objects was demonstrated using the humanoid TCP hand showing an array of functions similar to a natural hand (Figure 6.3F).

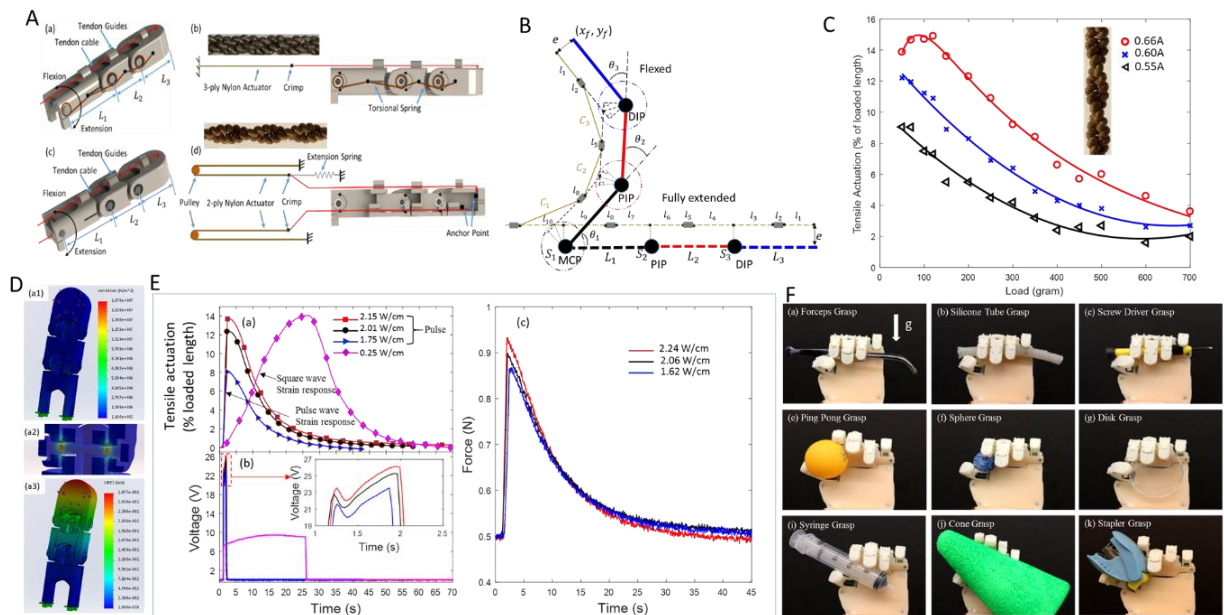


Figure 6.3. Graphical abstract of Chapter 4: (A) Schematic diagram of the finger actuation system. (B) Kinematic model of the finger. (C) Tensile actuation vs load at three different current input. (D) Stress analysis of the finger. (E) Tensile actuation and pulling force in pulsed actuation and (F) Grasping of various objects.

In Chapter 5, TCP muscles (both self-coiled TCP muscle from sewing thread and mandrel-coiled TCP muscle from fishing line) were explored for application in musculoskeletal system based on ball and socket joints (Figure 6.4C). The ball-and-socket joint functions as the skeletal system frame for biomimetic robots and other structures such as prosthetics. TCP muscles are used as actuators to mimic the muscular system. Especially, the TCP_{NC}^{FL} muscle (Figure 6.4A) which was fabricated from an 860-um-diameter nylon 6 monofilament that was mandrel coiled incorporating

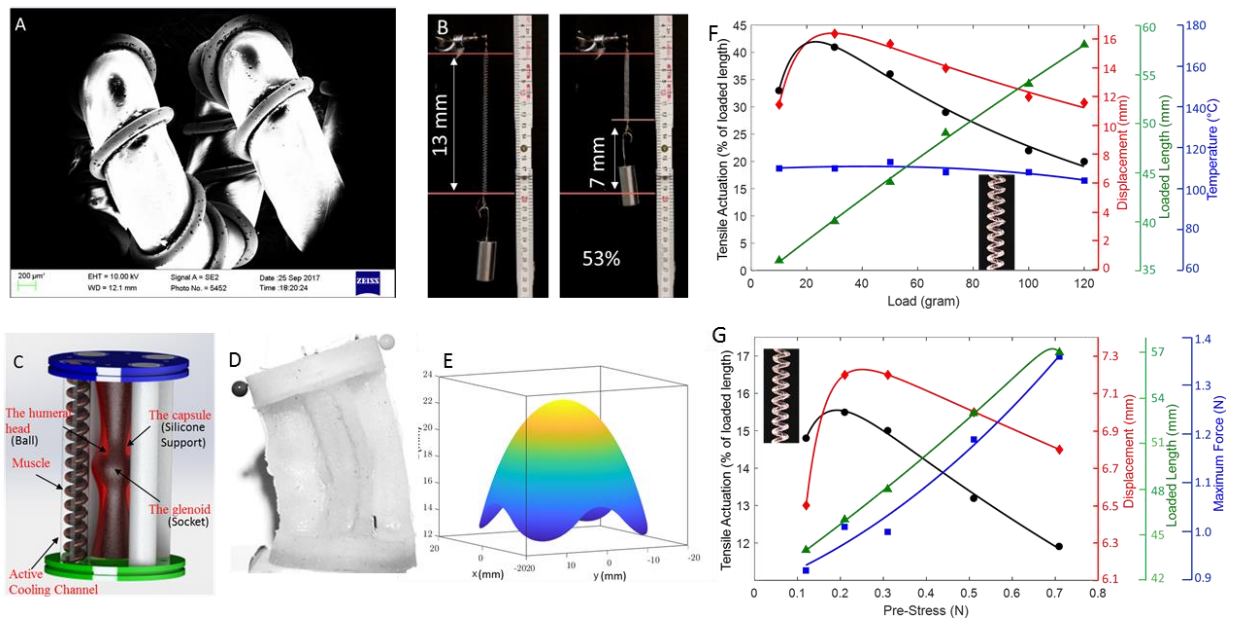


Figure 6.4. Overview of Chapter 5: Muscle structures and implementation in musculoskeletal system. (A) SEM image of TCP_{NC}^{FL} muscle. (B) Electrothermal actuation of TCP_{NC}^{FL} muscle lifting a 100-gram load by 53% actuation stroke. (C) Schematic diagram of the musculoskeletal system based on ball-and-socket joint structure using bioinspired antagonistic pairs of muscles. (D) The prototype of the musculoskeletal system. (E) Dexterous workspace of the musculoskeletal system. Mechanical performance of the TCP_{NC}^{FL} muscle in an isotonic test (F) and in a spring load test (G).

an 80- μm -diameter resistance wire, was presented for the first time. Extensive characterization of TCP_{NC}^{FL} muscles is also performed to provide some guideline for actuator development, including isotonic test (Figure 6.4F) and spring-load test characterization (Figure 6.4G). The muscle could deliver even larger tensile actuation stroke up to 53% at a constant current of 0.22A for a period of 6s under a 1.69 MPa load (100 g) as shown in Figure 6.4B). The reachable workspace of the MS is also presented in Figure 6.4E). The manufacturing method of the musculoskeletal system based on silicone casting and 3D printing technology was also described and the experimental results showed that the bio-inspired ball and socket joint could deliver a very good dynamic

response, promoting TCP muscle application in musculoskeletal system and other biologically inspired robotics system.

6.2 Future Recommendations

At the present stage, the principle of mandrel-coiled muscle with heating wire has been demonstrated, but further investigations are required to advance its practical application. For instance, the effect of the diameter of heating wire and the pitch of the wrapped heating wire on the resulting mandrel-coiling muscle need further exploration. Those two factors determine the heat transfer from the heat source to the fishing line fiber. Another future work is to explore alternative coil geometries as described by Spinks [176], such as cone structure, spiral structure [177]. The actuation stroke and stiffness of the mandrel-coiling muscle are highly dependent on the coil geometries, including the coil diameter and coil bias angle.

In the research project, TCP muscle was mainly used as an actuator for robotics application. Using TCP muscle as a sensor will advance the combined actuator-sensor integrated system development. In the future work, the strain sensing principle of TCP muscle based on electrical resistance change during actuation is a promising research topic. For example, in the robotic hand development, if TCP can not only function as an actuator, but also act as a sensor, that will further advance the development of a fully functional and dexterous robotic/prosthetic hand.

In the current design of musculoskeletal system for bio-inspired robotic systems based on ball and socket joint, a fundamental building block has been developed successfully. It is of great interest to develop more advanced and complicated robotic system based on the current design of musculoskeletal system all in a rapid prototyping system. For instance, the bio-inspired ball and

socket joint can be further cascaded to create complex robots such as underwater robotic fish and human spine structure.

REFERENCES

- [1] A. Ölander, "An electrochemical investigation of solid cadmium-gold alloys," *Journal of the American Chemical Society*, vol. 54, pp. 3819-3833, 1932.
- [2] W. J. Buehler, J. Gilfrich, and R. Wiley, "Effect of low-temperature phase changes on the mechanical properties of alloys near composition TiNi," *Journal of applied physics*, vol. 34, pp. 1475-1477, 1963.
- [3] L. Sun and W. Huang, "Nature of the multistage transformation in shape memory alloys upon heating," *Metal Science and Heat Treatment*, vol. 51, pp. 573-578, 2009.
- [4] T. Duerig and A. Pelton, "Ti-Ni shape memory alloys," *Materials properties handbook: titanium alloys*, pp. 1035-1048, 1994.
- [5] A. Potnuru and Y. Tadesse, "Characterization of coiled SMA actuators for humanoid robot," in *Active and Passive Smart Structures and Integrated Systems 2017*, 2017, p. 101640W.
- [6] J. M. Jani, M. Leary, A. Subic, and M. A. Gibson, "A review of shape memory alloy research, applications and opportunities," *Materials & Design*, vol. 56, pp. 1078-1113, 2014.
- [7] I. W. Hunter, J. M. Hollerbach, and J. Ballantyne, "A comparative analysis of actuator technologies for robotics," *Robotics Review*, vol. 2, pp. 299-342, 1991.
- [8] Y. Tadesse, N. Thayer, and S. Priya, "Tailoring the response time of shape memory alloy wires through active cooling and pre-stress," *Journal of Intelligent Material Systems and Structures*, vol. 21, pp. 19-40, 2010.
- [9] A. Lara-Quintanilla and H. Bersee, "Active cooling and strain-ratios to increase the actuation frequency of SMA wires," *Shape Memory and Superelasticity*, vol. 1, pp. 460-467, 2015.
- [10] A. Lara-Quintanilla and H. E. Bersee, "A study on the contraction and cooling times of actively cooled shape memory alloy wires," *Journal of Intelligent Material Systems and Structures*, vol. 27, pp. 403-417, 2016.
- [11] H. Rodrigue, W. Wang, M.-W. Han, T. J. Kim, and S.-H. Ahn, "An Overview of Shape Memory Alloy-Coupled Actuators and Robots," *Soft Robotics*, vol. 4, pp. 3-15, 2017.
- [12] A. Villoslada, A. Flores, D. Copaci, D. Blanco, and L. Moreno, "High-displacement flexible Shape Memory Alloy actuator for soft wearable robots," *Robotics and Autonomous Systems*, vol. 73, pp. 91-101, 2015.

- [13] Y. She, C. Li, J. Cleary, and H.-J. Su, "Design and fabrication of a soft robotic hand with embedded actuators and sensors," *Journal of Mechanisms and Robotics*, vol. 7, p. 021007, 2015.
- [14] K. Andrianesis and A. Tzes, "Development and control of a multifunctional prosthetic hand with shape memory alloy actuators," *Journal of Intelligent & Robotic Systems*, vol. 78, p. 257, 2015.
- [15] M. Bergamasco, F. Salsedo, and P. Dario, "Shape memory alloy micromotors for direct-drive actuation of dexterous artificial hands," *Sensors and Actuators*, vol. 17, pp. 115-119, 5/3/ 1989.
- [16] S. Dilibal, E. Guner, and N. Akturk, "Three-finger SMA robot hand and its practical analysis," *Robotica*, vol. 20, 2002.
- [17] A. Price, A. Jnifene, and H. Naguib, "Design and control of a shape memory alloy based dexterous robot hand," *Smart Materials and Structures*, vol. 16, p. 1401, 2007.
- [18] K. J. De Laurentis and C. Mavroidis, "Mechanical design of a shape memory alloy actuated prosthetic hand," *Technology and Health Care*, vol. 10, pp. 91-106, 2002.
- [19] J.-S. Koh and K.-J. Cho, "Omega-shaped inchworm-inspired crawling robot with large-index-and-pitch (LIP) SMA spring actuators," *IEEE/ASME Transactions On Mechatronics*, vol. 18, pp. 419-429, 2013.
- [20] M.-S. Kim, W.-S. Chu, J.-H. Lee, Y.-M. Kim, and S.-H. Ahn, "Manufacturing of inchworm robot using shape memory alloy (SMA) embedded composite structure," *International journal of precision engineering and manufacturing*, vol. 12, pp. 565-568, 2011.
- [21] J. Colorado, A. Barrientos, C. Rossi, and K. S. Breuer, "Biomechanics of smart wings in a bat robot: morphing wings using SMA actuators," *Bioinspiration & biomimetics*, vol. 7, p. 036006, 2012.
- [22] C. Laschi, M. Cianchetti, B. Mazzolai, L. Margheri, M. Follador, and P. Dario, "Soft robot arm inspired by the octopus," *Advanced Robotics*, vol. 26, pp. 709-727, 2012.
- [23] C. A. Daily-Diamond, A. Novelia, and O. O'Reilly, "Dynamical analysis and development of a biologically inspired SMA caterpillar robot," *Bioinspiration & Biomimetics*, 2017.
- [24] H. Jin, E. Dong, G. Alici, S. Mao, X. Min, C. Liu, *et al.*, "A starfish robot based on soft and smart modular structure (SMS) actuated by SMA wires," *Bioinspiration & biomimetics*, vol. 11, p. 056012, 2016.
- [25] C. Liu, H. Qin, and P. Mather, "Review of progress in shape-memory polymers," *Journal of Materials Chemistry*, vol. 17, pp. 1543-1558, 2007.

- [26] P. T. Mather, X. Luo, and I. A. Rousseau, "Shape memory polymer research," *Annual Review of Materials Research*, vol. 39, pp. 445-471, 2009.
- [27] M. Y. Razzaq and L. Frormann, "Thermomechanical studies of aluminum nitride filled shape memory polymer composites," *polymer composites*, vol. 28, pp. 287-293, 2007.
- [28] J. Xu, W. Shi, and W. Pang, "Synthesis and shape memory effects of Si–O–Si cross-linked hybrid polyurethanes," *Polymer*, vol. 47, pp. 457-465, 2006.
- [29] I. S. Gunes, F. Cao, and S. C. Jana, "Effect of thermal expansion on shape memory behavior of polyurethane and its nanocomposites," *Journal of Polymer Science Part B: Polymer Physics*, vol. 46, pp. 1437-1449, 2008.
- [30] P. T. Knight, K. M. Lee, H. Qin, and P. T. Mather, "Biodegradable thermoplastic polyurethanes incorporating polyhedral oligosilsesquioxane," *Biomacromolecules*, vol. 9, pp. 2458-2467, 2008.
- [31] S. Zhang, Z. Yu, T. Govender, H. Luo, and B. Li, "A novel supramolecular shape memory material based on partial α -CD–PEG inclusion complex," *Polymer*, vol. 49, pp. 3205-3210, 2008.
- [32] J. D. Merline, C. R. Nair, C. Gouri, T. Shrisudha, and K. Ninan, "Shape memory characterization of polytetra methylene oxide/poly (acrylic acid-co-acrylonitrile) complexed gel," *Journal of materials science*, vol. 42, pp. 5897-5902, 2007.
- [33] K. Ishida and N. Yoshie, "Two-way conversion between hard and soft properties of semicrystalline cross-linked polymer," *Macromolecules*, vol. 41, pp. 4753-4757, 2008.
- [34] R. Weiss, E. Izzo, and S. Mandelbaum, "New design of shape memory polymers: mixtures of an elastomeric ionomer and low molar mass fatty acids and their salts," *Macromolecules*, vol. 41, pp. 2978-2980, 2008.
- [35] H. Lv, J. Leng, Y. Liu, and S. Du, "Shape-memory polymer in response to solution," *Advanced Engineering Materials*, vol. 10, pp. 592-595, 2008.
- [36] M.-C. Chen, H.-W. Tsai, Y. Chang, W.-Y. Lai, F.-L. Mi, C.-T. Liu, *et al.*, "Rapidly self-expandable polymeric stents with a shape-memory property," *Biomacromolecules*, vol. 8, pp. 2774-2780, 2007.
- [37] J. M. Ortega, W. Small, T. S. Wilson, W. J. Benett, J. M. Loge, and D. J. Maitland, "A shape memory polymer dialysis needle adapter for the reduction of hemodynamic stress within arteriovenous grafts," *IEEE Transactions on Biomedical Engineering*, vol. 54, pp. 1722-1724, 2007.

- [38] W. M. Sokolowski and S. C. Tan, "Advanced self-deployable structures for space applications," *Journal of Spacecraft and Rockets*, vol. 44, pp. 750-754, 2007.
- [39] Q. Meng and J. Hu, "Study on poly (ε-caprolactone)-based shape memory copolymer fiber prepared by bulk polymerization and melt spinning," *Polymers for Advanced Technologies*, vol. 19, pp. 131-136, 2008.
- [40] T. Xie and X. Xiao, "Self-peeling reversible dry adhesive system," *Chemistry of Materials*, vol. 20, pp. 2866-2868, 2008.
- [41] F. Daerden and D. Lefeber, "Pneumatic artificial muscles: actuators for robotics and automation," *European journal of mechanical and environmental engineering*, vol. 47, pp. 11-21, 2002.
- [42] Y. Yang, Y. Chen, Y. Li, M. Z. Chen, and Y. Wei, "Bioinspired Robotic Fingers Based on Pneumatic Actuator and 3D Printing of Smart Material," *Soft Robotics*, vol. 4, pp. 147-162, 2017.
- [43] R. Deimel and O. Brock, "A compliant hand based on a novel pneumatic actuator," in *Robotics and Automation (ICRA), 2013 IEEE International Conference on*, 2013, pp. 2047-2053.
- [44] S. Wakimoto, J. Misumi, and K. Suzumori, "New concept and fundamental experiments of a smart pneumatic artificial muscle with a conductive fiber," *Sensors and Actuators A: Physical*, vol. 250, pp. 48-54, 2016.
- [45] C. S. Haines, M. D. Lima, N. Li, G. M. Spinks, J. Foroughi, J. D. Madden, *et al.*, "Artificial muscles from fishing line and sewing thread," *Science*, vol. 343, pp. 868-872, 2014.
- [46] J. Yuan and P. Poulin, "Fibers do the twist," *Science*, vol. 343, pp. 845-846, 2014.
- [47] L. Wu and Y. Tadesse, "Humanoid Robot Hand With SMA Actuators and Servo Motors," in *ASME 2014 International Mechanical Engineering Congress and Exposition*, 2014, pp. V04AT04A041-V04AT04A041.
- [48] G. Moretti, A. Cherubini, R. Vertechy, and M. Fontana, "Experimental characterization of a new class of polymeric-wire coiled transducers," in *SPIE Smart Structures and Materials+ Nondestructive Evaluation and Health Monitoring*, 2015, pp. 94320P-94320P-9.
- [49] J. van der Weijde, B. Smit, M. Fritschi, C. van de Kamp, and H. Vallery, "Self-Sensing of Displacement, Force and Temperature for Joule-Heated Twisted and Coiled Polymer Muscles via Electrical Impedance," *IEEE/ASME Transactions on Mechatronics*, 2016.

- [50] P. Zhang and G. Li, "Healing-on-demand composites based on polymer artificial muscle," *Polymer*, vol. 64, pp. 29-38, 2015.
- [51] S. H. Kim, M. D. Lima, M. E. Kozlov, C. S. Haines, G. M. Spinks, S. Aziz, *et al.*, "Harvesting temperature fluctuations as electrical energy using torsional and tensile polymer muscles," *Energy & Environmental Science*, vol. 8, pp. 3336-3344, 2015.
- [52] Y. Almubarak and Y. Tadesse, "Twisted and coiled polymer (TCP) muscles embedded in silicone elastomer for use in soft robot," *International Journal of Intelligent Robotics and Applications*, vol. 1, pp. 352-368, 2017.
- [53] L. Saharan, M. J. de Andrade, W. Saleem, R. H. Baughman, and Y. Tadesse, "iGrab: hand orthosis powered by twisted and coiled polymer muscles."
- [54] S. M. Mirvakili, A. R. Ravandi, I. W. Hunter, C. S. Haines, N. Li, J. Foroughi, *et al.*, "Simple and strong: Twisted silver painted nylon artificial muscle actuated by Joule heating," in *SPIE Smart Structures and Materials+ Nondestructive Evaluation and Health Monitoring*, 2014, pp. 90560I-90560I-10.
- [55] A. Cherubini, G. Moretti, R. Vertechy, and M. Fontana, "Experimental characterization of thermally-activated artificial muscles based on coiled nylon fishing lines," *AIP Advances*, vol. 5, p. 067158, 2015.
- [56] L. Wu, M. J. de Andrade, R. S. Rome, C. Haines, M. Lima, R. Baughman, *et al.*, "Nylon-muscle-actuated robotic finger," 2015.
- [57] C. Xiang, H. Yang, Z. Sun, B. Xue, L. Hao, M. A. Rahoman, *et al.*, "The design, hysteresis modeling and control of a novel SMA-fishing-line actuator," *Smart Materials and Structures*, vol. 26, p. 037004, 2017.
- [58] J. van der Weijde, B. Smit, M. Fritschi, C. van de Kamp, and H. Vallery, "Self-Sensing of Deflection, Force, and Temperature for Joule-Heated Twisted and Coiled Polymer Muscles via Electrical Impedance," *IEEE/ASME Transactions on Mechatronics*, vol. 22, pp. 1268-1275, 2017.
- [59] T. Arakawa, K. Takagi, K. Tahara, and K. Asaka, "Position control of fishing line artificial muscles (coiled polymer actuators) from nylon thread," *SPIE Smart Structures and Materials+ Nondestructive Evaluation and Health Monitoring*, pp. 97982W-97982W, 2016.
- [60] Z. F. Liu, S. Fang, F. A. Moura, J. N. Ding, N. Jiang, J. Di, M. Zhang . and *et al.*, "Hierarchically buckled sheath-core fibers for superelastic electronics, sensors, and muscles," *Science*, 2015.

- [61] J. Mu, C. Hou, G. Wang, X. Wang, Q. Zhang, Y. Li, *et al.*, "An Elastic Transparent Conductor Based on Hierarchically Wrinkled Reduced Graphene Oxide for Artificial Muscles and Sensors," *Advanced Materials*, vol. 28, pp. 9491-9497, 2016.
- [62] H. Yang, D. Qi, Z. Liu, B. K. Chandran, T. Wang, J. Yu, *et al.*, "Soft Thermal Sensor with Mechanical Adaptability," *Advanced Materials*, vol. 28, pp. 9175-9181, 2016.
- [63] M. Culebras, A. M. López, C. M. Gómez, and A. Cantarero, "Thermal sensor based on a polymer nanofilm," *Sensors and Actuators A: Physical*, vol. 239, pp. 161-165, 2016.
- [64] M. Arifuzzaman, C. Behrend, J. DesJardins, and J. N. Anker, "A smart polymer hydrogel as a chemical sensor on biomedical implant," 2016.
- [65] R. Ahmad, N. Tripathy, M.-S. Ahn, and Y.-B. Hahn, "Highly stable hydrazine chemical sensor based on vertically-aligned ZnO nanorods grown on electrode," *Journal of Colloid and Interface Science*, vol. 494, pp. 153-158, 2017.
- [66] T. Arakawa, K. Takagi, K. Tahara, and K. Asaka, "Position control of fishing line artificial muscles (coiled polymer actuators) from nylon thread," in *SPIE Smart Structures and Materials+ Nondestructive Evaluation and Health Monitoring*, 2016, pp. 97982W-97982W-12.
- [67] M. C. Yip and G. Niemeyer, "On the Control and Properties of Supercoiled Polymer Artificial Muscles," *IEEE Transactions on Robotics*, 2017.
- [68] J. Zhang, K. Iyer, A. Simeonov, and M. C. Yip, "Modeling and Inverse Compensation of Hysteresis in Supercoiled Polymer Artificial Muscles," *IEEE Robotics and Automation Letters*, vol. 2, pp. 773-780, 2017.
- [69] M. W. Shafer, H. P. Feigenbaum, D. Pugh, and M. Fisher, "First Steps in Modeling Thermal Actuation of Twisted Polymer Actuators Using Virgin Material Properties," in *ASME 2016 Conference on Smart Materials, Adaptive Structures and Intelligent Systems*, 2016, pp. V002T06A017-V002T06A017.
- [70] J. Zhao and A. Abbas, "A Low-Cost Soft Coiled Sensor for Soft Robots," in *ASME 2016 Dynamic Systems and Control Conference*, 2016, pp. V002T26A006-V002T26A006.
- [71] L. Wu, M. J. de Andrade, L. K. Saharan, R. S. Rome, R. H. Baughman, and Y. Tadesse, "Compact and low-cost humanoid hand powered by nylon artificial muscles," *Bioinspiration & Biomimetics*, vol. 12, p. 026004, 2017.
- [72] M. C. Yip and G. Niemeyer, "High-performance robotic muscles from conductive nylon sewing thread," in *Robotics and Automation (ICRA), 2015 IEEE International Conference on*, 2015, pp. 2313-2318.

- [73] B. F. Richard, "Tensile-integrity structures," ed: Google Patents, 1962.
- [74] K. Snelson, "Continuous tension, discontinuous compression structures," ed: Google Patents, 1965.
- [75] C. Sultan and R. Skelton, "Integrated design of controllable tensegrity structures," *Adaptive structures and material systems-1997*, pp. 27-35, 1997.
- [76] V. SunSpiral, G. Gorospe, J. Bruce, A. Iscen, G. Korbel, S. Milam, *et al.*, "Tensegrity based probes for planetary exploration: Entry, descent and landing (EDL) and surface mobility analysis," *International Journal of Planetary Probes*, 2013.
- [77] J. M. M. Tur and S. H. Juan, "Tensegrity frameworks: Dynamic analysis review and open problems," *Mechanism and Machine Theory*, vol. 44, pp. 1-18, 2009.
- [78] S. H. Juan and J. M. M. Tur, "Tensegrity frameworks: static analysis review," *Mechanism and Machine Theory*, vol. 43, pp. 859-881, 2008.
- [79] M. Shibata, F. Saijyo, and S. Hirai, "Crawling by body deformation of tensegrity structure robots," in *Robotics and Automation, 2009. ICRA'09. IEEE International Conference on*, 2009, pp. 4375-4380.
- [80] M. Shibata and S. Hirai, "Rolling locomotion of deformable tensegrity structure," in *12th International Conference on Climbing and Walking Robots and the Support Technologies for Mobile Machines, Istanbul, Turkey, Sept, 2009*, pp. 9-11.
- [81] Y. Koizumi, M. Shibata, and S. Hirai, "Rolling tensegrity driven by pneumatic soft actuators," in *Robotics and Automation (ICRA), 2012 IEEE International Conference on*, 2012, pp. 1988-1993.
- [82] K. Kim, A. K. Agogino, D. Moon, L. Taneja, A. Toghyan, B. Dehghani, *et al.*, "Rapid prototyping design and control of tensegrity soft robot for locomotion," in *Robotics and Biomimetics (ROBIO), 2014 IEEE International Conference on*, 2014, pp. 7-14.
- [83] *Pneumatic Bar Controlled Structure.* Available: http://maeresearch.ucsd.edu/skelton/laboratory/tensegrity_platform.htm
- [84] J. Bruce, K. Caluwaerts, A. Iscen, A. P. Sabelhaus, and V. SunSpiral, "Design and evolution of a modular tensegrity robot platform," in *Robotics and Automation (ICRA), 2014 IEEE International Conference on*, 2014, pp. 3483-3489.
- [85] A. P. Sabelhaus, J. Bruce, K. Caluwaerts, P. Manovi, R. F. Firoozi, S. Dobi, *et al.*, "System design and locomotion of SUPERball, an untethered tensegrity robot," in *Robotics and Automation (ICRA), 2015 IEEE International Conference on*, 2015, pp. 2867-2873.

- [86] F. A. dos Santos, A. Rodrigues, and A. Micheletti, "Design and experimental testing of an adaptive shape-morphing tensegrity structure, with frequency self-tuning capabilities, using shape-memory alloys," *Smart Materials and Structures*, vol. 24, p. 105008, 2015.
- [87] J. L. Rohmer, E. A. P. Hernandez, R. E. Skelton, D. J. Hartl, and D. C. Lagoudas, "An Experimental and Numerical Study of Shape Memory Alloy-Based Tensegrity/Origami Structures," in *ASME 2015 International Mechanical Engineering Congress and Exposition*, 2015, pp. V009T12A064-V009T12A064.
- [88] J. Aldrich and R. Skelton, "Backlash-free motion control of robotic manipulators driven by tensegrity motor networks," in *Decision and Control, 2006 45th IEEE Conference on*, 2006, pp. 2300-2306.
- [89] J.-P. Pinaud, S. Solari, and R. E. Skelton, "Deployment of a class 2 tensegrity boom," in *Smart structures and materials*, 2004, pp. 155-162.
- [90] H. Wang, S. Cai, F. Carpi, and Z. Suo, "Computational model of hydrostatically coupled dielectric elastomer actuators," *Journal of Applied Mechanics*, vol. 79, p. 031008, 2012.
- [91] N. Vyas and D. S. BHALLA, "Tensegrity based poultry shed," *Indian Institute of Technology, Delhi, project report*, 2009.
- [92] B. Di Carlo, "The wooden roofs of Leonardo and new structural research," *Nexus Network Journal*, vol. 10, pp. 27-38, 2008.
- [93] S. Deguchi, T. Ohashi, and M. Sato, "Tensile properties of single stress fibers isolated from cultured vascular smooth muscle cells," *Journal of biomechanics*, vol. 39, pp. 2603-2610, 2006.
- [94] A. Iscen, A. Agogino, V. SunSpiral, and K. Tumer, "Controlling tensegrity robots through evolution," in *Proceedings of the 15th annual conference on Genetic and evolutionary computation*, 2013, pp. 1293-1300.
- [95] K. Caluwaerts, J. Despraz, A. Işçen, A. P. Sabelhaus, J. Bruce, B. Schrauwen, *et al.*, "Design and control of compliant tensegrity robots through simulation and hardware validation," *Journal of The Royal Society Interface*, vol. 11, p. 20140520, 2014.
- [96] L. Wu, M. Larkin, A. Potnuru, and Y. Tadesse, "HBS-1: A Modular Child-Size 3D Printed Humanoid," *Robotics*, vol. 5, p. 1, 2016.
- [97] J. K. Salisbury and J. J. Craig, "Articulated hands force control and kinematic issues," *The International journal of Robotics research*, vol. 1, pp. 4-17, 1982.

- [98] G. Guo, W. Gruver, and X. Qian, "A robotic hand mechanism with rotating fingertips and motor-tendon actuation," in *Systems, Man, and Cybernetics, 1991. Decision Aiding for Complex Systems, Conference Proceedings., 1991 IEEE International Conference on*, 1991, pp. 1023-1028.
- [99] Y. Kurita, Y. Ono, A. Ikeda, and T. Ogasawara, "Human-sized anthropomorphic robot hand with detachable mechanism at the wrist," *Mechanism and Machine Theory*, vol. 46, pp. 53-66, 2011.
- [100] G. Jang, C. Lee, H. Lee, and Y. Choi, "Robotic index finger prosthesis using stackable double 4-BAR mechanisms," *Mechatronics*, vol. 23, pp. 318-325, 2013.
- [101] N. Thayer and S. Priya, "Design and implementation of a dexterous anthropomorphic robotic typing (DART) hand," *Smart Materials and Structures*, vol. 20, p. 035010, 2011.
- [102] S. Ikemoto, Y. Kimoto, and K. Hosoda, "Shoulder complex linkage mechanism for humanlike musculoskeletal robot arms," *Bioinspiration & biomimetics*, vol. 10, p. 066009, 2015.
- [103] K. Inoue, K. Nakamura, M. Suzuki, Y. Mori, Y. Fukuoka, and N. Shiroma, "Biological system models reproducing snakes' musculoskeletal system," in *Intelligent Robots and Systems (IROS), 2010 IEEE/RSJ International Conference on*, 2010, pp. 2383-2388.
- [104] J. Huber, N. Fleck, and M. Ashby, "The selection of mechanical actuators based on performance indices," in *Proceedings of the Royal Society of London A: Mathematical, Physical and Engineering Sciences*, 1997, pp. 2185-2205.
- [105] J. Ueda, M. Kondo, and T. Ogasawara, "The multifingered NAIST hand system for robot in-hand manipulation," *Mechanism and Machine Theory*, vol. 45, pp. 224-238, 2010.
- [106] F. Lotti, P. Tiezzi, G. Vassura, L. Biagiotti, G. Palli, and C. Melchiorri, "Development of UB hand 3: Early results," in *Robotics and Automation, 2005. ICRA 2005. Proceedings of the 2005 IEEE International Conference on*, 2005, pp. 4488-4493.
- [107] M. Diftler and R. O. Ambrose, "Robonaut: a robotic astronaut assistant," in *ISAIRAS conference*, 2001.
- [108] S. Schulz, C. Pylatiuk, and G. Bretthauer, "A new ultralight anthropomorphic hand," in *Robotics and Automation, 2001. Proceedings 2001 ICRA. IEEE International Conference on*, 2001, pp. 2437-2441.
- [109] C. Pylatiuk, S. Mounier, A. Kargov, S. Schulz, and G. Bretthauer, "Progress in the development of a multifunctional hand prosthesis," in *Engineering in Medicine and Biology Society, 2004. IEMBS'04. 26th Annual International Conference of the IEEE*, 2004, pp. 4260-4263.

- [110] J.-y. Nagase, S. Wakimoto, T. Satoh, N. Saga, and K. Suzumori, "Design of a variable-stiffness robotic hand using pneumatic soft rubber actuators," *Smart Materials and Structures*, vol. 20, p. 105015, 2011.
- [111] S. C. Jacobsen, J. E. Wood, D. Knutti, and K. B. Biggers, "The UTAH/MIT dextrous hand: Work in progress," *The International Journal of Robotics Research*, vol. 3, pp. 21-50, 1984.
- [112] D. Che and W. Zhang, "A dexterous and self-adaptive humanoid robot hand: GCUA hand," *International Journal of Humanoid Robotics*, vol. 8, pp. 73-86, 2011.
- [113] S. Dalley, T. E. Wiste, T. J. Withrow, and M. Goldfarb, "Design of a multifunctional anthropomorphic prosthetic hand with extrinsic actuation," *Mechatronics, IEEE/ASME Transactions on*, vol. 14, pp. 699-706, 2009.
- [114] L. U. Odhner, L. P. Jentoft, M. R. Claffee, N. Corson, Y. Tenzer, R. R. Ma, *et al.*, "A compliant, underactuated hand for robust manipulation," *The International Journal of Robotics Research*, vol. 33, pp. 736-752, 2014.
- [115] H. Liu, D. Yang, L. Jiang, and S. Fan, "Development of a multi-DOF prosthetic hand with intrinsic actuation, intuitive control and sensory feedback," *Industrial Robot: An International Journal*, vol. 41, pp. 381-392, 2014.
- [116] G. Palli, C. Melchiorri, G. Vassura, U. Scarcia, L. Moriello, G. Berselli, *et al.*, "The DEXMART hand: Mechatronic design and experimental evaluation of synergy-based control for human-like grasping," *The International Journal of Robotics Research*, vol. 33, pp. 799-824, 2014.
- [117] J. T. Belter, J. L. Segil, A. M. Dollar, and R. F. Weir, "Mechanical design and performance specifications of anthropomorphic prosthetic hands: a review," *J Rehabil Res Dev*, vol. 50, pp. 599-618, 2013.
- [118] J. S. Martell and G. Gini, "Robotic hands: Design review and proposal of new design process," *World Academy of Science, Engineering and Technology*, vol. 26, pp. 85-90, 2007.
- [119] J. Pons, R. Ceres, and F. Pfeiffer, "Multifingered dextrous robotics hand design and control: a review," *Robotica*, vol. 17, pp. 661-674, 1999.
- [120] A. Bicchi and V. Kumar, "Robotic grasping and contact: A review," in *ICRA*, 2000, pp. 348-353.
- [121] Y. Tadesse, D. Hong, and S. Priya, "Twelve degree of freedom baby humanoid head using shape memory alloy actuators," *Journal of Mechanisms and Robotics*, vol. 3, p. 011008, 2011.

- [122] Y. Tadesse, "Electroactive polymer and shape memory alloy actuators in biomimetics and humanoids," in *SPIE Smart Structures and Materials+ Nondestructive Evaluation and Health Monitoring*, 2013, pp. 868709-868709-12.
- [123] M. Bergamasco, F. Salsedo, and P. Dario, "Shape memory alloy micromotors for direct-drive actuation of dexterous artificial hands," *Sensors and Actuators*, vol. 17, pp. 115-119, 1989.
- [124] S. Dilibal, E. Guner, and N. Akturk, "Three-finger SMA robot hand and its practical analysis," *Robotica*, vol. 20, pp. 175-180, 2002.
- [125] F. Simone, A. York, and S. Seelecke, "Design and fabrication of a three-finger prosthetic hand using SMA muscle wires," in *SPIE Smart Structures and Materials+ Nondestructive Evaluation and Health Monitoring*, 2015, pp. 94290T-94290T-8.
- [126] E. D. Engeberg, S. Dilibal, M. Vatani, J.-W. Choi, and J. Lavery, "Anthropomorphic finger antagonistically actuated by SMA plates," *Bioinspiration & biomimetics*, vol. 10, p. 056002, 2015.
- [127] K. Garg, "BD Chaurasia's Human Anatomy—Regional and Applied Dissection and Clinical: Volume 1 Upper Limb and Thorax," ed: New Delhi: CBS Publishers and Distributors, 2004.
- [128] L. Wu, M. J. de Andrade, R. S. Rome, C. Haines, M. D. Lima, R. H. Baughman, *et al.*, "Nylon-muscle-actuated robotic finger," in *SPIE Smart Structures and Materials+ Nondestructive Evaluation and Health Monitoring*, 2015, pp. 94310I-94310I-12.
- [129] K. H. Cho, M. G. Song, H. Jung, J. Park, H. Moon, J. C. Koo, *et al.*, "A robotic finger driven by twisted and coiled polymer actuator," in *SPIE Smart Structures and Materials+ Nondestructive Evaluation and Health Monitoring*, 2016, pp. 97981J-97981J-7.
- [130] L. Saharan and Y. Tadesse, "Robotic hand with locking mechanism using TCP muscles for applications in prosthetic hand and humanoids," in *SPIE Smart Structures and Materials+ Nondestructive Evaluation and Health Monitoring*, 2016, pp. 97970V-97970V-9.
- [131] B.-H. Kim, "Analysis of Coordinated Motions of Humanoid Robot Fingers Using Interphalangeal Joint Coordination," *International Journal of Advanced Robotic Systems*, vol. 11, 2014.
- [132] E. L. Secco, A. Visioli, and G. Magenes, "Minimum jerk motion planning for a prosthetic finger," *Journal of Robotic Systems*, vol. 21, pp. 361-368, 2004.
- [133] B.-H. Kim, "A bio-mimetic inter-articular coordination model for humanoid graspings," in *Robotics, Automation and Mechatronics, 2006 IEEE Conference on*, 2006, pp. 1-6.

- [134] N. M. Kakoty and S. M. Hazarika, "Local Hand Control for Tezpur University Bionic Hand Grasping," in *Proceedings of Conference on Advances In Robotics*, 2013, pp. 1-7.
- [135] V. Bundhoo, E. Haslam, B. Birch, and E. J. Park, "A shape memory alloy-based tendon-driven actuation system for biomimetic artificial fingers, part I: design and evaluation," *Robotica*, vol. 27, pp. 131-146, 2009.
- [136] K. Masuya, S. Ono, K. Takagi, and K. Tahara, "Modeling Framework for Macroscopic Dynamics of Twisted and Coiled Polymer Actuator Driven by Joule Heating Focusing on Energy and Convective Heat Transfer," *Sensors and Actuators A: Physical*, 2017.
- [137] T. A. Luong, S. Seo, J. C. Koo, H. R. Choi, and H. Moon, "Differential hysteresis modeling with adaptive parameter estimation of a super-coiled polymer actuator," in *Ubiquitous Robots and Ambient Intelligence (URAI), 2017 14th International Conference on*, 2017, pp. 607-612.
- [138] N. Dechev, W. Cleghorn, and S. Naumann, "Multiple finger, passive adaptive grasp prosthetic hand," *Mechanism and machine theory*, vol. 36, pp. 1157-1173, 2001.
- [139] L. Ren, Z. Qian, and L. Ren, "Biomechanics of musculoskeletal system and its biomimetic implications: a review," *Journal of Bionic Engineering*, vol. 11, pp. 159-175, 2014.
- [140] M. Kia, T. M. Guess, and A. P. Stylianou, "Musculoskeletal Model During Treadmill Gait," in *ASME 2013 Summer Bioengineering Conference*, 2013, pp. V01BT27A004-V01BT27A004.
- [141] M. D. Harris, R. S. Davis, B. A. MacWilliams, C. L. Peters, and A. E. Anderson, "Musculoskeletal modeling of acetabular dysplasia-kinematics, muscle and joint reaction forces," in *ASME 2010 Summer Bioengineering Conference*, 2010, pp. 795-796.
- [142] M. M. Kayo and Y. Ohkami, "Multi-Body Modeling of Human Musculoskeletal System for an Exercise Therapy Method and its Verification," in *ASME 2013 Conference on Frontiers in Medical Devices: Applications of Computer Modeling and Simulation*, 2013, pp. V001T10A023-V001T10A023.
- [143] Y. Nakanishi, S. Ohta, T. Shirai, Y. Asano, T. Kozuki, Y. Kakehashi, *et al.*, "Design Approach of Biologically-Inspired Musculoskeletal Humanoids," *Int J Adv Robot Sy*, vol. 10, 2013.
- [144] I. Mizuuchi, T. Yoshikai, Y. Sodeyama, Y. Nakanishi, A. Miyadera, T. Yamamoto, *et al.*, "Development of musculoskeletal humanoid kotaro," in *Robotics and Automation, 2006. ICRA 2006. Proceedings 2006 IEEE International Conference on*, 2006, pp. 82-87.

- [145] Y. Nakanishi, T. Izawa, M. Osada, N. Ito, S. Ohta, J. Urata, *et al.*, "Development of musculoskeletal humanoid kenzoh with mechanical compliance changeable tendons by nonlinear spring unit," in *Robotics and Biomimetics (ROBIO), 2011 IEEE International Conference on*, 2011, pp. 2384-2389.
- [146] T. Kozuki, Y. Motegi, T. Shirai, Y. Asano, J. Urata, Y. Nakanishi, *et al.*, "Design of upper limb by adhesion of muscles and bones—Detail human mimetic musculoskeletal humanoid kenshiro," in *Intelligent Robots and Systems (IROS), 2013 IEEE/RSJ International Conference on*, 2013, pp. 935-940.
- [147] M. Damsgaard, J. Rasmussen, S. T. Christensen, E. Surma, and M. De Zee, "Analysis of musculoskeletal systems in the AnyBody Modeling System," *Simulation Modelling Practice and Theory*, vol. 14, pp. 1100-1111, 2006.
- [148] S. L. Delp, F. C. Anderson, A. S. Arnold, P. Loan, A. Habib, C. T. John, *et al.*, "OpenSim: open-source software to create and analyze dynamic simulations of movement," *Biomedical Engineering, IEEE Transactions on*, vol. 54, pp. 1940-1950, 2007.
- [149] T. W. Duerig, K. Melton, and D. Stöckel, *Engineering aspects of shape memory alloys*: Butterworth-Heinemann, 2013.
- [150] A. O'Halloran, F. O'malley, and P. McHugh, "A review on dielectric elastomer actuators, technology, applications, and challenges," *Journal of Applied Physics*, vol. 104, p. 071101, 2008.
- [151] M. De Volder and D. Reynaerts, "Pneumatic and hydraulic microactuators: a review," *Journal of Micromechanics and microengineering*, vol. 20, p. 043001, 2010.
- [152] M. Shahinpoor, Y. Bar-Cohen, J. Simpson, and J. Smith, "Ionic polymer-metal composites (IPMCs) as biomimetic sensors, actuators and artificial muscles—a review," *Smart materials and structures*, vol. 7, p. R15, 1998.
- [153] C. Richter, S. Jentsch, R. Hostettler, J. A. Garrido, E. Ros, A. Knoll, *et al.*, "Musculoskeletal robots: scalability in neural control," *IEEE Robotics & Automation Magazine*, vol. 23, pp. 128-137, 2016.
- [154] I. Mizuuchi, Y. Nakanishi, Y. Sodeyama, Y. Namiki, T. Nishino, N. Muramatsu, *et al.*, "An advanced musculoskeletal humanoid kojiro," in *Humanoid Robots, 2007 7th IEEE-RAS International Conference on*, 2007, pp. 294-299.
- [155] M. Zimmermann, T. Ranzani, A. Menciassi, and B. Kellner, "Development of a Cable Actuated Joint for a Surgical Robotic Flexible Arm," *Biomedical Engineering/Biomedizinische Technik*, 2013.

- [156] S. Kurumaya, K. Suzumori, H. Nabae, and S. Wakimoto, "Musculoskeletal lower-limb robot driven by multifilament muscles," *Robomech Journal*, vol. 3, p. 18, 2016.
- [157] R. Niiyama, A. Nagakubo, and Y. Kuniyoshi, "Mowgli: A bipedal jumping and landing robot with an artificial musculoskeletal system," in *Robotics and Automation, 2007 IEEE International Conference on*, 2007, pp. 2546-2551.
- [158] R. Niiyama and Y. Kuniyoshi, "Design principle based on maximum output force profile for a musculoskeletal robot," *Industrial Robot: An International Journal*, vol. 37, pp. 250-255, 2010.
- [159] T. Ranzani, M. Cianchetti, G. Gerboni, I. De Falco, and A. Menciassi, "A soft modular manipulator for minimally invasive surgery: design and characterization of a single module," *IEEE Transactions on Robotics*, vol. 32, pp. 187-200, 2016.
- [160] S. Wang, Q. Zhu, R. Xiong, and J. Chu, "Flexible Robotic Spine Actuated by Shape Memory Alloy," *International Journal of Advanced Robotic Systems*, vol. 11, 2014.
- [161] J. D. Madden, "Mobile robots: motor challenges and materials solutions," *science*, vol. 318, pp. 1094-1097, 2007.
- [162] Y. Tadesse, "Actuation technologies for humanoid robots with facial expressions (hrwfe)," *Transaction on Control and Mechanical Systems*, vol. 2, 2013.
- [163] W. Mosauer, "On the locomotion of snakes," *Science*, vol. 76, 1932.
- [164] T. H. Eaton, "Evolution of the upper jaw mechanism in teleost fishes," *Journal of Morphology*, vol. 58, pp. 157-172, 1935.
- [165] A. Rossi and P. Grigg, "Characteristics of hip joint mechanoreceptors in the cat," *Journal of Neurophysiology*, vol. 47, pp. 1029-1042, 1982.
- [166] D. L. Raney and E. C. Slominski, "Mechanization and control concepts for biologically inspired micro air vehicles," *Journal of Aircraft*, vol. 41, pp. 1257-1265, 2004.
- [167] L. Wu, M. J. de Andrade, L. K. Saharan, R. S. Rome, R. H. Baughman, and Y. Tadesse, "Compact and Low-cost Humanoid Hand Powered by Nylon Artificial Muscles," *Under Review*, 2016.
- [168] A. Tomar and Y. Tadesse, "Multi-layer robot skin with embedded sensors and muscles," 2016, pp. 979809-979809-12.
- [169] L. Wu, M. J. de Andrade, T. Brahme, Y. Tadesse, and R. H. Baughman, "A deformable robot with tensegrity structure using nylon artificial muscle," in *SPIE Smart Structures and Materials+ Nondestructive Evaluation and Health Monitoring*, 2016, pp. 97993K-97993K-12.

- [170] J. Di, S. Fang, F. A. Moura, D. S. Galvão, J. Bykova, A. Aliev, *et al.*, "Strong, Twist-Stable Carbon Nanotube Yarns and Muscles by Tension Annealing at Extreme Temperatures," *Advanced Materials*, vol. 28, pp. 6598-6605, 2016.
- [171] Y. Zhang, C. D. Crane, and J. Duffy, "Determination of the unique orientation of two bodies connected by a ball-and-socket joint from four measured displacements," *Journal of Field Robotics*, vol. 15, pp. 299-308, 1998.
- [172] G. Alici and B. Shirinzadeh, "Loci of singular configurations of a 3-DOF spherical parallel manipulator," *Robotics and Autonomous Systems*, vol. 48, pp. 77-91, 2004.
- [173] G. Alici and B. Shirinzadeh, "Topology optimisation and singularity analysis of a 3-SPS parallel manipulator with a passive constraining spherical joint," *Mechanism and Machine Theory*, vol. 39, pp. 215-235, 2004.
- [174] X. Jiang and P. B. Lillehoj, "Pneumatic microvalves fabricated by multi-material 3D printing," in *Nano/Micro Engineered and Molecular Systems (NEMS), 2017 IEEE 12th International Conference on*, 2017, pp. 38-41.
- [175] L. Wu and Y. Tadesse, "Musculoskeletal System for Bio-Inspired Robotic Systems Based on Ball and Socket Joints," in *ASME 2016 International Mechanical Engineering Congress and Exposition*, 2016, pp. V04AT05A020-V04AT05A020.
- [176] G. M. Spinks, "Stretchable artificial muscles from coiled polymer fibers," *Journal of Materials Research*, vol. 31, pp. 2917-2927, 2016.
- [177] C. S. Haines, N. Li, G. M. Spinks, A. E. Aliev, J. Di, and R. H. Baughman, "New twist on artificial muscles," *Proceedings of the National Academy of Sciences*, p. 201605273, 2016.

BIOGRAPHICAL SKETCH

Lianjun Wu was born in Yangzhou, Jiangsu Province in China. He received his BS degree in Mechanical Engineering from Chongqing University, and his MS degree in Mechanical Engineering from Xi'an Jiaotong University. Currently, he is working towards his PhD at The University of Texas at Dallas. His research is focused on bioinspired robotics design and smart actuators. He has published three journal/magazine papers and five conference papers in humanoid and bio-inspired areas. He is also a teaching assistant for Computer Aided Design (CAD) graduate and undergraduate courses.

CURRICULUM VITAE

Lianjun Wu

November 02, 2017

CONTACT INFORMATION:

Department of Mechanical Engineering
The University of Texas at Dallas
800 W. Campbell Rd.
Richardson, TX 75080-3021, U.S.A

Email:
Lxw132630@utdallas.edu
campusjun@gmail.com

EDUCATION:

Ph.D. Candidate in Mechanical Engineering, Sep. 2013 - Dec. 2017
The University of Texas at Dallas, Richardson, TX, USA

Dissertation Title: Twisted and Coiled Polymer Muscle and Structure for Robotics Application

M.S. in Mechanical Design and Theory, Sep. 2012 - May 2013
Xi'an Jiaotong University, Xi'an, China

Thesis: Simulation of a Bearing-Rotor-Seal System in Water-lubricated High-Speed Spindle Based on CFD

B.S. in Mechanical Design and Manufacturing, Sep. 2006 - May 2010
Chongqing University, Chongqing, China

PEER-REVIEWED JOURNAL PUBLICATIONS

1. **Lianjun Wu**, Monica Jung de Andrade, Lokesh Kumar Saharan, Richard S. Rome, Ray H Baughman and Yonas Tadesse. "Compact and low-cost humanoid hand powered by nylon artificial muscles." *Bioinspiration & biomimetics* 12, no. 2 (2017): 026004. doi:10.1088/1748-3190/aa52f8
2. **Lianjun Wu**, Miles Larkin, Akshay Potnuru, and Yonas Tadesse. "HBS-1: A Modular Child-Size 3D Printed Humanoid." *Robotics* 5.1 (2016): 1. doi:10.3390/robotics5010001
3. Yonas Tadesse, **Lianjun Wu**, and Lokesh Saharan. "Musculoskeletal System for Bio-inspired Robotic Systems." *Mechanical Engineering* 138, no. 3 (2016): S11.
4. Wei Chen, Hongjie Fan and **Lianjun Wu**. Review of Water Lubricated Bearing for high speed spindle (*Chinese Engineering Science*) (Published, 01/2013). doi:009-1742 (2013) 01-0021-07
5. Lokesh Kumar Saharan, **Lianjun Wu**, and Yonas Tadesse. "Modeling and Simulation of Three Link Biomimetic Finger Powered by Nylon Artificial Muscles - Euler-Lagrangian Approach." *Journal of Mechanisms and Robotics*. Submitted 2017.
6. **Lianjun Wu**, Indrajeet Samratsingh Chauhan, and Yonas Tadesse. "A novel soft actuator for musculoskeletal system." *Advanced Materials*, Submitted 2017.

7. **Lianjun Wu** and Yonas Tadesse. "Characterization and Modeling of the electrical resistance of Twisted and Coiled muscle." Smart Material and Structure. In Preparation 2017.

PEER-REVIEWED CONFERENCE

1. **Lianjun Wu** and Yonas Tadesse. "Musculoskeletal System for Bio-Inspired Robotic Systems Based on Ball and Socket Joints". ASME International Mechanical Engineering Congress and Exposition, Volume 4A: Dynamics, Vibration, and Control: IMECE2016-67394.
2. **Lianjun Wu**, Monica Jung de Andrade, Tarang Brahme, Yonas Tadesse and Ray H Baughman. "A reconfigurable robot with tensegrity structure using nylon artificial muscle." In SPIE Smart Structures and Materials+ Nondestructive Evaluation and Health Monitoring, pp. 97993K-97993K. International Society for Optics and Photonics, 2016.
3. **Lianjun Wu**, Monica Jung de Andrade, Richard S Rome, Carter Haines, Marcio D Lima, Ray H Baughman and Yonas Tadesse. "Nylon-muscle-actuated robotic finger." SPIE Smart Structures and Materials+ Nondestructive Evaluation and Health Monitoring. International Society for Optics and Photonics, 2015.
4. **Lianjun Wu** and Yonas Tadesse. "Humanoid Robot Hand With SMA Actuators and Servo Motors." ASME 2014 International Mechanical Engineering Congress and Exposition. American Society of Mechanical Engineers, 2014.
5. Akshay Potnuru, **Lianjun Wu**, and Yonas Tadesse. "Artificial heart for humanoid robot." SPIE Smart Structures and Materials+ Nondestructive Evaluation and Health Monitoring. International Society for Optics and Photonics, 2014.
6. **Lianjun Wu** and Yonas Tadesse. "Modeling of the electrical resistance of TCP muscle. " In ASME 2017 International Mechanical Engineering Congress and Exposition
7. Mohsen Jafarzadeh, **Lianjun Wu** and Yonas Tadesse. "System Identification of force of a silver coated twisted and coiled polymer muscle." In ASME 2017 International Mechanical Engineering Congress and Exposition

PATENT

Wei Chen, **Lianjun Wu** and Hongjie Fan. Sealing System of Water-Lubricated hybrid bearing for Ultra-Speed Motorized Spindle. In China, Application No.:201210361483.9.

PROFESSIONAL MEMBERSHIP

The American Society of Mechanical Engineers

PROFESSIONAL SERVICE

Topic Co-organizer, 2017 American Society of Mechanical Engineers (ASME), International Mechanical Engineering Congress & Exposition (IMECE) Conference

HONORS AND AWARDS

IAC Graduate Fellowship at The University of Texas at Dallas

ASME Outstanding Graduate Student (ASME North Texas Section)

Jonsson School Graduate Study Scholarship at The University of Texas at Dallas